UNIVERSITAT POLITÈCNICA DE CATALUNYA BARCELONATECH

Catalytic hydrogen production over $RhPd/CeO_2$ catalysts and CO purification over Au/TiO_2 catalysts

Núria Jiménez Divins

Tesi presentada per obtenir el títol de Doctora per la Universitat Politècnica de Catalunya

Director: Dr. Jordi Llorca Piqué

Programa de doctorat d'Enginyeria Nuclear i de les Radiacions Ionitzants

Institut de Tècniques Energètiques
Universitat Politècnica de Catalunya

Barcelona, febrer de 2015

UNIVERSITAT POLITÈCNICA DE CATALUNYA
BARCELONATECH
Escola de Doctorat

Acta de qualificació de tesi doctoral	**Curs acadèmic:**

Nom i cognoms

Programa de doctorat

Unitat estructural responsable del programa

Resolució del Tribunal

Reunit el Tribunal designat a l'efecte, el doctorand / la doctoranda exposa el tema de la seva tesi doctoral titulada _____ _____.

Acabada la lectura i després de donar resposta a les qüestions formulades pels membres titulars del tribunal, aquest atorga la qualificació:

☐ NO APTE ☐ APROVAT ☐ NOTABLE ☐ EXCEL·LENT

(Nom, cognoms i signatura) President/a		(Nom, cognoms i signatura) Secretari/ària
(Nom, cognoms i signatura) Vocal	(Nom, cognoms i signatura) Vocal	(Nom, cognoms i signatura) Vocal

_____, _____ d'/de _____ de _____

El resultat de l'escrutini dels vots emesos pels membres titulars del tribunal, efectuat per l'Escola de Doctorat, a instància de la Comissió de Doctorat de la UPC, atorga la MENCIÓ CUM LAUDE:

☐ SÍ ☐ NO

(Nom, cognoms i signatura) President de la Comissió Permanent de l'Escola de Doctorat	(Nom, cognoms i signatura) Secretari de la Comissió Permanent de l'Escola de Doctorat

Barcelona, _____ d'/de _____ de _____

Printed in: Format Digital S.L.

This thesis was supported in part by a:

PhD fellowship of
Universitat Politècnica de Catalunya

Mobility support grant:
Beques per a estades de recerca a l'estranger of
Generalitat de Catalunya

A la meva família

What is a scientist after all?
It is a curious person looking through a keyhole,
the keyhole of nature, trying to know what's going on.

Jacques-Yves Cousteau (France 1910-1997)

Acknowledgements

I want to express my most sincere gratitude to many people. For that, let me use the language closer to them.

Per fi ha arribat el moment de donar les gràcies i sou molts els que m'heu acompanyat durant aquest llarg camí de més de 5 anys.

En primer lloc, vull donar les gràcies al meu director de tesi, el Dr. Jordi Llorca, per tot el que m'ha ensenyat, però també per donar-me les eines per seguir aprenent. Vaig tenir la gran sort d'anar a parar al seu grup de recerca i he de dir que em sento afortunada d'haver estat guiada per ell. Jordi, gràcies per estar sempre disponible per nosaltres, per aportar llum quan em semblava que no n'hi havia, per totes les grans estones de ciència compartides arreu del món. En definitiva, gràcies per tot!

También quiero agradecer al Dr. Eduardo López todo lo que me enseñó cuando llegué al laboratorio. No sabía nada y me pegué a ti para aprender a montar sistemas de reacción, para analizar los datos, etc.

També m'agradaria donar les gràcies a la Dra. Inma Angurell i al Ferran Gonzàlez per sintetitzar les nanopartícules que es descriuen en aquesta tesi. Sempre que n'he necessitat, en menys d'una setmana he tingut les nanopartícules disponibles.

I also want to thank the group and researchers that hosted me during my visit at Brookhaven National Laboratory. Thanks to Dr. Jose Rodriguez for accepting me to do a PhD stay at his laboratory and, in particular, to Sanj and Alba for making my stay at BNL warmer.

A tots els companys amb qui he compartit despatx al llarg d'aquests anys: amb els que vaig començar i amb els qui ara acabo aquesta etapa. Cristian, Montse, Elena, Vanessa, Raúl, Leonor, Andrea, Edu, Estel i Albert, Alejandra, David, Lluís, Erika, Ali, Raquel i Adrian: gràcies per fer la vida al despatx més amena i per totes les es-

tones compartides! Lluís, gràcies per la paciència de llegir-te la tesi! Elena, gracias a ti también por leer esta tesis y por los grandes ratos que en su día compartimos. Sé que amb alguns de vosaltres seguirem en contacte des d'allà on ens trobem.

També vull donar les gràcies als companys del Centre de Recerca en Nanoenginyeria, altra vegada a la Montse en aquesta etapa, i al Trifon.

I als amics de Barcelona, d'Alella i rodalies, de la carrera i als que esteu repartits pel món! Gràcies per les bones estones que seguim compartint, perquè cada vegada que ens retrobem, és com si no hagués passat el temps.

I per últim vull donar les gràcies a la meva família, el meu gran pilar. Als que esteu a prop i als que sou lluny, però que m'acompanyeu igualment. A la Toni i al Salvador, per cuidar-me i recolzar-me. A la meva àvia, per cuidar-me i transmetre'm la seva força i energia positiva. I en especial, als meus pares i a la meva germana: per estar sempre al meu costat, per donar-me les oportunitats i valors amb què he crescut, per ajudar-me sempre en tot i per creure en mi quan ni tan sols jo ho feia. I, finalment, a tu Raül: per ser la meitat perfecte d'aquest equip que formem. Per cuidar-me sempre, pel teu suport i ajuda incondicionals, per totes les hores que t'he robat durant aquests últims mesos, ... En definitiva, per tot el que hem viscut junts i, sobretot, per totes les aventures que ens queden per viure! Espero que tingueu present que si he arribat fins aquí també és gràcies a vosaltres. En aquesta tesi també hi ha una petita part vostra. Gràcies per haver-me encoratjat a seguir endavant!

Barcelona, 15 de febrer de 2015.

Contents

List of Figures

List of Tables

List of Abbreviations

µGC	Gas micro-chromatograph
450 PS	450 PS scenario
AFC	Alkaline Fuel Cell
AFM	Atomic force microscopy
AP-XPS	Ambient pressure X-ray photoelectron spectroscopy
ATR	Autothermal regime
Au@D	Preformed Au nanoparticles encapsulated in dodecanethiols ligands
Au@G0	Preformed Au nanoparticles encapsulated in G0 dendrons
Au@G1	Preformed Au nanoparticles encapsulated in G1 dendrons
Au@G2	Preformed Au nanoparticles encapsulated in G2 dendrons
AuC	Au nanoparticles synthesized from $HAuCl_4$
BE	Binding energy
BNL	Brookhaven National Laboratory, USA
CFN	Center for Functional Nanomaterials, Brookhaven National Laboratory
CMR	Catalytic membrane reactor
CM	Cordierite monolith
CO-PrOx	CO preferential oxidation
cpsi	Cells per square inch
CRnE	Centre de Recerca en Nanoenginyeria
D	Dodecanethiol

DRIFTS	Diffuse reflectance infrared Fourier transform spectroscopy
EDX	Energy dispersive X-ray
EELS	Electron energy loss spectroscopy
EIA	Energy Information Agency of United States
ESR	Ethanol steam reforming
fcc	Face-centered cubic
FC	Fuel Cell
FIB	Focused ion beam
FT	Fourier transform
G8	Group of Eight
GHG	Green house gases
GHSV	Gas hourly space velocity
HF	Hydrofluoric acid
HRTEM	High resolution transmission electron microscopy
IEA	International Energy Agency
IMFP	Inelastic mean free path
IMM	Mainz Institute of Microtechnology, Germany
IPCC	Intergovernmental Panel on Climate Change
IR	Infrared
KE	Kinetic energy
MCFC	Molten Carbonate Fuel Cell
MDGs	Millennium Development Goals
MSR	Methane steam reforming
MTC	Metric tonnes of carbon
Mtoe	Million tonnes of oil equivalent
NCD	Nanoparticle-cored dendrimers
NM	Noble metals
NPs	Nanoparticles
O/E	Oxygen-to-ethanol ratio

OPEC	Organization of the Petroleum Exporting Countries
OSC	Oxygen storage capacity
OSR	Oxidative steam reforming
P	Pressure
Pd@Rh	Preformed nanoparticles composed of a Pd core encapsulated in Rh-functionalized ligands
PEMFC	Polymer Electrolyte Membrane Fuel Cell
PGM	Platinum group metal
POX	Partial oxidation
PSS	Porous stainless steel
PVA	Polyvinyl alcohol
RhPd@D	Preformed nanoparticles composed of a RhPd core encapsulated in dodecanethiol ligands
rWGS	Reverse water gas shift
S/C	Steam-to-carbon ratio
S/E	Steam-to-ethanol ratio
SEM	Scanning electron microscopy
SiM	Silicon micromonolith
SOFC	Solid Oxide Fuel Cell
SR	Steam reforming
SSM	Stainless steel microreactor
STEM	Scanning transmission electron microscopy
STEM-HAADF	STEM-High angle annular dark field
STO	$SrTiO_3$
T	Temperature
TCD	Thermal conductivity detector
TEM	Transmission electron microscopy
TGA	Thermogravimetric analyses
TOX	Total oxidation
TPD	Temperature programmed desorption

TPO	Temperature programmed oxidation
TPR	Temperature programmed reduction
UB	Universitat de Barcelona
UHV	Ultra-high vacuum
UN	United Nations
UPC	Universitat Politècnica de Catalunya
WGS	Water gas shift
WHSV	Weight hourly space velocity
XPS	X-ray photoelectron spectroscopy
XP	X-ray photoelectron
XRD	X-ray diffraction

Outline of the Thesis

The main goal of this Thesis is to generate hydrogen for energy purposes. To achieve this broad goal, two main objectives were defined: the hydrogen generation by means of steam reforming, a well-known catalytic route, and the purification of the reformate streams to power fuel cells. These two main objectives are the focus of Part I and Part II, respectively.

For the sake of simplicity, this Thesis is organized in four blocks: first a general introduction provides the background and sets the context of this Thesis. Then, in Part I we focus on $RhPd/CeO_2$ catalysts to produce hydrogen from the ethanol steam reforming reaction. In Part II we move our attention to the study of Au/TiO_2 catalysts to reduce the carbon monoxide concentration of pre-cleaned reformate streams via its preferential oxidation. Finally, we end this Thesis with the conclusions of both Parts. These four blocks are broken down as follows:

In Chapter 1, the general introduction sets the current energy scenario and the role that hydrogen may play in a new energy system. It also describes different existing routes to produce hydrogen and provides the reader with some concepts used throughout this Thesis.

Then Part I starts. In Chapter 2 we first introduce different routes to produce hydrogen from ethanol and we review different types of catalysts reported in the open literature to produce hydrogen through the ethanol steam reforming. Finally, the objectives of Part I are described.

Chapter 3 describes the synthesis of the different $RhPd/CeO_2$ catalysts studied and their morphology and structural properties are detailed in Chapter 4. The influence of several operational parameters on the ethanol steam reforming performance of $RhPd/CeO_2$ catalysts is investigated in Chapter 5. Chapter 6 is devoted to the characterization of post-reacted catalysts and to the investigation of catalysts while they are under reaction conditions. In Chapter 7, the integration of $RhPd/CeO_2$ catalysts with a metallic membrane to obtain pure hydrogen streams is addressed.

Part I ends with Chapter 8, where we miniaturize the hydrogen generation scale by supporting our $RhPd/CeO_2$ catalysts in novel silicon micromonoliths.

Part II is organized following the same structure as Part I. It starts with an overview of the requirements of the CO preferential oxidation (CO-PrOx) reaction and of suitable catalysts for the CO-PrOx described in the literature. Finally, Chapter 9 ends describing the specific objectives of Part II.

In Chapter 10 the synthesis of the different Au/TiO_2 catalysts investigated is described and their characterization is discussed in Chapter 11.

The influence of different reaction parameters on the performance of the developed Au catalysts supported on cordierite monoliths is presented in Chapter 12. In the subsequent Chapters 13 and 14, the CO abatement scale is reduced. In Chapter 13, the best Au/TiO_2 catalysts developed are supported on stainless steel microreactors and their performance is evaluated. In Chapter 14 we further reduce the scale of the CO-PrOx reaction by supporting a stable Au/TiO_2 catalyst on a silicon micromonolith. Chapter 14 ends with a comparison of the different purification scales investigated.

Finally, the conclusions of the Thesis are drawn in Chapter 15.

This dissertation also includes a list of the publications produced during this Thesis and the original papers published.

1 Introduction

1.1 The energy scenario

At the beginning of the millennium, the United Nations (UN) identified the most urgent problems of the world population and marked a horizon of 15 years to solve them. This challenge took shape in eight goals: the Millennium Development Goals (MDGs) [1]; the fulfillment of some of them, such as the eradication of extreme poverty and hunger, ensuring environmental sustainability and encourage global partnership for development will be closely linked to a change in the energy model.

The current energy system is based primarily on the burning of fossil fuels -oil, natural gas and charcoal- and only 13% comes from the use of clean energy sources. The world's energy supply between 1973 (at that time it was 6106 million tonnes of oil equivalent, Mtoe) and 2012 (13371 Mtoe) has been increased by more than 100% in this 40-years period, as reported by the International Energy Agency (IEA) [2]. Figure 1.1 shows the world's energy supply increase and details its distribution by fuel. It can be seen the large increase experienced by natural gas (from 16.0 to 21.3%) and coal (from 24.6 to 29.0%), whereas renewable energy sources together: solar, geothermal, wind, hydro, marine (tides and waves) represent only a 3.5% of the total supplied worldwide energy during 2012.

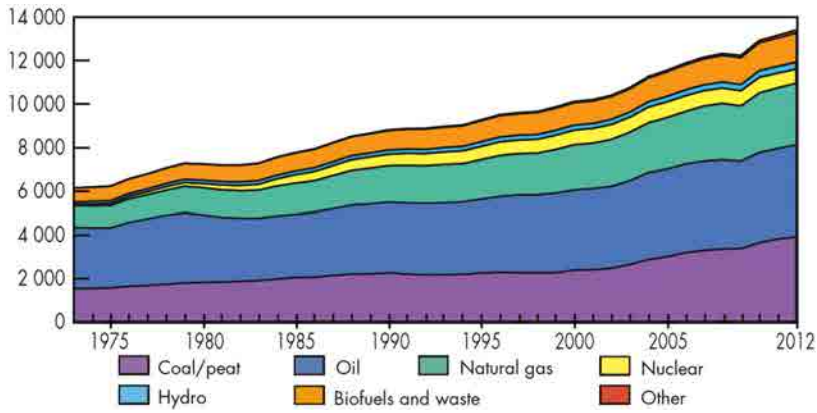

Figure 1.1: World energy supply from 1973 to 2012 by fuel. Other includes geothermal, solar, wind, etc. Adapted from IEA [2].

The wide availability of energy from fossil fuels allowed for the twentieth century the rapid development of sectors such as industry and transport and improving the quality of life of million people. This development led to spectacular growth in energy consumption, evidenced by the 911 Mtoe consumed in 1900, compared with the 9342 Mtoe in 2000 or the 12483 Mtoe consumed in 2012, as shown in table 1.1 [3, 4]. In the twentieth century, humans have consumed 10 times more energy than they ancestors had used in the 1000 years preceding 1900 [5].

When the hydrocarbon age was being developed at the beginning of the twentieth century, few people could imagine the huge economic, political and ecological impact that this new energy source would achieve in the following decades. Fossil fuels have shaped and have irrevocably altered the wars, politics, business, lifestyle and natural environment. Because of this, some historians call the twentieth century as the century of oil [5].

Table 1.1 shows the increase in worldwide energy consumption, the different sources of consumed energy, the world population and energy consumption per capita, comparing 1900 with 2012. The global carbon dioxide emissions arisen from fossil fuels burning, cement production and gas flaring are also listed.

Table 1.1: Worldwide energy use in Mtoe, world population and per capita energy consumption comparing years 1900 and 2012. Adapted from [3]. Data extracted from [4, 6, 7].

	1900		2012	
Energy source	Mtoe	%	Mtoe	%
Oil	18	2	4139	33
Natural gas	9	1	2986	24
Coal	501	55	3724	30
Nuclear	0	0	560	4
Renewable	383	42	1074	9
Total	911	100	12483	100
Population (million)	1762		7100	
Per capita energy use (toe)	0.517		1.758	
Global CO_2 emission (MMTC*)	530		9600	
Per capita CO_2 emission (MTC)	0.30		1.35	
Atmospheric CO_2 (ppm)	295		393	
Life expectancy (years)	47		71	

*MTC: Metric tonnes of carbon. MMTC: MTC given in million.

These data show that global emissions of CO_2 have increased 10 times during the last century, in clear and direct relationship with the sharp increase in worldwide fossil energy consumption [3]. In November 2014, the global atmospheric concentration of CO_2 was 398.3 ppm [6].

Following the increasing trend of atmospheric concentrations of CO_2 and other green house gases (GHG), the surface temperature of the Earth has been increasing since 1861, being greater warming since 1970 [8]. Most of the scientific community agrees that climate change has an anthropogenic origin and, therefore, the Intergovernmental Panel on Climate Change (IPCC) from UN and the Group of Eight (G8) have recognized that global average temperature should not exceed 2°C the global pre-industrial levels, thus avoiding irreversible loss of ice sheets and species caused by human footprint [9].

Some of the most influential scientists in the field of climate change have predicted that if the concentration of GHG exceeds 450 ppm, it could reach a critical point of global warming, intensified by a strong positive feedback. That will seriously affect the climate for centuries and exceed the 2°C identified as a limitation, indicating that it is necessary to reduce the current concentration of CO_2, for keeping the climate in which humanity, wildlife and the rest of the biosphere are adapted [10]. At the current rate it would happen in the next 25 years.

In this context, the International Energy Agency has presented the 450 PS scenario (450 PS), where certain requirements are defined to achieve stabilization of GHG concentrations at 450 ppm in 2035. To accomplish this milestone, the policies must be strongly determined to reduce the current rate of GHG emissions [11]. The most important and urgent of these policies is the reduction of global energy consumption, which should not exceed 14.920 Mtoe in 2035, according to the projections from the IEA. This clearly contrasts with the predictions of the Energy Information Agency of United States (EIA), which indicate that with current policies, consumption in 2035 will be 19.404 Mtoe. Furthermore, the contribution of renewable and nuclear energies should be duplicated and fossil energy reduced to 62%. At the same time, the proportion of natural gas should increased, because it is the fossil fuel which has lower carbon content [11, 12]. The energy demand in 2035 would be even greater if the Millennium Development Goals were achieved.

Responding to the commitment made by the G8, the European Union has launched a series of ambitious initiatives and has developed a roadmap (*Roadmap 2050: a practical guide to a prosperous, low-carbon Europe* [13]), which defines plausible and urgent ways to reduce GHG emissions. One of the most remarkable aspects of this document is to achieve that reduction of emissions will be difficult to accomplish if they do not start a transition to a new energy system before 2015, in the

sense that energy is produced and also consumed. In this document, a minor role is given to hydrogen.

In parallel, the air pollution in large cities can also be an important stimulus to promote a transition to a new energy system. The transport sector is one of the most important contributors to the emission of particles and pollutant gases to the atmosphere and, moreover, they are delocalized issuers. This particularity makes difficult the treatment of emitted gases and makes essential the use of catalysts in vehicles, in order to make an on-site treatment of emissions from combustion engines. However, many industrialized nations often exceed the limits on concentrations of ozone and nitrogen dioxide, and in some developing nations, emissions of polluting gases and particles are even higher [5]. In 2000, it was estimated that local pollution produced by transport caused 1.1% of world deaths annually, rising in Europe up to ca. 6% [14].

In spite of the scenario presented above, the most important transition drivers to a new energy model will be possibly the problems related with energy security. Energy security refers to the loss of economic welfare that may occur as a result of a change in the price or availability of energy [15]. In fact, to a large extent, global economic stability depends on abundant energy. And precisely for economic reasons the energy supply has been dominated by fossil fuels, and very probably will remain dominant [16]. However, it should be mentioned that fossil fuels are finite resources and, if its exploitation exceeds the regenerative capacity of the Earth, its exhaustion will be produced.

Fossil resources duration is a widely debated issue, because it involves several disciplines and different approaches to the problem. The discovery and the extraction of oil and natural gas as well as less conventional resources (such as shale gas, oil sands, sand tars, pitch) are determined by multiple geological, technical, economic and political factors. Their combination adds uncertainty to the medium- and long-term forecasts [17].

Moreover, the geopolitical implications of fossil fuels use are very important. As it is well known, access to oil unevenly distributed and geographically concentrated has influenced the World Wars, the Gulf Wars and relationships between western economies, and also between the West and the Middle East and the developing countries.

According to the drawn scenarios, where world energy demand increases significantly, this uneven distribution may contribute to augment insecurity energy in the near future, due to the dependency of many nations on imports of oil and natural gas and the expected increase in their prices. Currently, 81% of world oil

reserves are in countries of the Organization of the Petroleum Exporting Countries (OPEC)[1] [18]. While, for instance, in 2009, the European Union (EU) (comprised by 27 countries) imported ca. 50% of its primary energy and, if no additional measures are taken, dependency on imports will increase to about 70% by 2030. The EU also imports 35% of coal consumed and 100% of uranium [19].

Therefore, from the review of the current energy scenario, it seems clear that we have enough elements that demonstrate the need to define a new energy system for the XXI century, ensuring the availability of energy (essential for social and economic development) and respecting the environment. In this context, hydrogen is often presented as a valuable piece of a new energy system.

1.2 Hydrogen economy

1972 was the first time that the idea of *Hydrogen Economy* was published in a paper. Bockris and Appleby presented the idea of a new energy system where hydrogen replaces fossil fuels [20].

Hydrogen is not a primary energy source, but an energy vector, as electricity or gasoline. Therefore it transports or stores the chemical energy contained in its H-H bonds, which can be released or processed as required. Furthermore, the energy content of H_2 is very high: 141.6 MJ/kg (39.3 kWh/kg), compared with 44.4 MJ/kg (3.12 kWh/kg) of gasoline. Maybe, in the peak of the oil age, the transition to a new energy system based on hydrogen seems unfeasible, but looking at the history of energy from the atoms point of view, then it seems more plausible. From the mid-nineteenth century, the world has been changing the form of energy. Wood was the most used fuel until mid-nineteenth century. But in Britain, due to the growth in population and in energy demand, they began to use the coal. Coal has a higher energy density than wood and is less heavy and difficult to transport, so it was widely used during the nineteenth and beginning of the twentieth century. But around 1900, the transport system began to change trains with automobiles, so liquid fuels became more attractive than solids. In this context, oil was gaining prominence because of its high energy density and possibility of transporting it to pipes. In the mid-twentieth century, oil had already become the world's dominant energy source [5].

Today, natural gas is the fossil fuel that is growing faster and the third source of energy used worldwide. This is because natural gas burns more efficiently, it is lighter and less polluting than other fossil fuels and the distribution network required is more efficient, discreet and extensive than the oil's one.

[1] OPEC is made up of 12 countries: Algeria, Angola, Ecuador, Iran, Iraq, Kuwait, Libya, Nigeria, Qatar, Saudi Arabia, United Arab Emirates and Venezuela.

This transition from solid to liquid and finally to gas, looking for higher energy densities and easier distribution and transportation fuels, implies another transition less visible, the decrease in carbon content [5]. Figure 1.2 shows the relationship between carbon and hydrogen atoms of every previous fuel. It makes visible that, at every change, the proportion of H has increased and, therefore, the world has followed a trend towards *decarbonization*. Following this trend, the next fuel of this progression should be hydrogen.

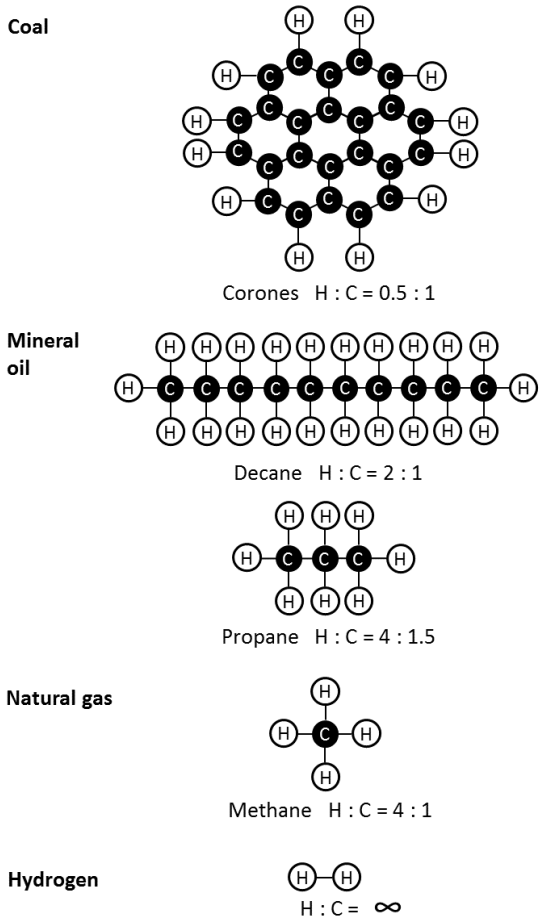

Figure 1.2: Atomic hydrogen/carbon ratio of different fuels. Extracted from [21].

1.2.1 Hydrogen

Hydrogen constitutes 93% of our universe, therefore being the most abundant element, and it is the tenth most abundant element on the Earth's crust [22]. However, due to its reactivity, under normal conditions on Earth, hydrogen is only part of a variety of compounds, mostly water or hydrocarbons. Indeed the existence of

this variety of hydrogenated compounds permits the extraction of hydrogen from different sources and therefore, it is considered a very versatile energy vector for the future. Furthermore, the selected source to produce it is the determining factor of its footprint and of CO_2 emissions. It can become a clean energy carrier, inexhaustible, efficient and attractive respect costs [16].

When hydrogen reacts with oxygen from the air, the products resulting are only water and heat (see equation 1.1). Also nitrogen oxides can be formed due to the high temperatures reached during combustion.

$$H_{2(g)} + \frac{1}{2} O_{2(g)} \longrightarrow H_2O_{(l)} + 286 \text{ kJ mol}^{-1} \qquad [23] \tag{1.1}$$

But to achieve an economy based on H_2, that feeds the homes, industries, trades and transports, requires its production, distribution, storage and exploiting it in economic ways. Theses ways must be equal or more competitive than the ones used today with fossil fuels. It should be mentioned that most problems of creating an infrastructure for the complete hydrogen operation as an energy carrier, have been identified and have obtained considerable progress; moreover they are not completely new, because now hydrogen is a gas commonly used in the industry.

One of the central problems for the establishment of this new economy is hydrogen storage. Hydrogen has a high energy density per unit mass (141.6 MJ/kg), but per unit volume is very small (12.8 MJ/m^3). And, thus, usually it is stored under high pressure or liquefied, with associated risks. While these two techniques have almost reached their physical limits, there is still potential for development in the field of solid materials such as metal hydrides. Currently, automotive industry considers that hydrogen storage on board vehicles is one of the technological bottlenecks [19].

Another critical point in the hydrogen economy is that it practically does not exist in free form on Earth and, therefore, it must be generated from hydrogen-rich sources consuming energy.

1.2.2 Hydrogen production

Regarding hydrogen production, which is one of the central goals of this Thesis, in 2009, 60 million tonnes were generated worldwide, mainly to synthesize ammonia, to refine fossil fuels and to produce various chemical products such as methanol, plastics, ... But rarely to be used for energy purposes (except in the case of spatial tasks that have been using hydrogen as an energy source from years ago).

Currently, the main ways to produce H_2 include non-renewable energy sources (fossil fuels and nuclear energy) and only 4% is generated by electrolysis of water.

Hydrogen is mainly obtained from the steam reforming of natural gas (or methane, which is the main component of natural gas): 48%, that is the same as $6{\cdot}10^{11}$ Nm^3/year; another 30% from the steam reforming or partial oxidation of petroleum fractions; and 18% of coal gasification, all of them well-established processes, but which also produce CO_2 in parallel [19, 23].

A strategy based on biomass (obtained from agricultural, forestry or municipal waste, algae and/or crops that do not compete with food) to produce hydrogen is also presented as very plausible process. Biomass can be gasified as coal to obtain a H_2-rich mixture, or fermented to obtain biofuels, from which H_2 is then extracted by reforming reactions. However, this strategy, despite being based on a renewable source, presents certain drawbacks related to the exploitation of land, its transport and the large energy required for the whole process. On the other hand, in gasification and reforming reactions CO_2 is generated. Nevertheless, in the case of biomass, it is considered that the net balance of emissions of this gas is lower or almost zero, because the plants consume CO_2 for photosynthesis during its growth [24].

For this reason, fermentation of biomass is presented as a very plausible path to produce biofuels, as for example, ethanol. Today, ethanol is obtained from a very effective process, the fermentation of starch or sugar, but it seems likely that it can be produced from cheaper vegetables, as agricultural waste, making it more attractive, and solving some of the issues above-mentioned. Bioethanol is a fuel already available and increasingly used because countries like Brazil use it as fuel for vehicles and the United States have adopted regulations requiring to put it as an additive to gasoline. In addition to its direct use as fuel, it has been demonstrated that through its reforming with steam, H_2 can be extracted quickly and efficiently [25]. Even more, this method enables the production of H_2 when it is required, avoiding key issues, such as storage and related security problems. Part I of this Thesis is devoted to the production of hydrogen by ethanol steam reforming.

Hydrogen can also be produced in nuclear plants by thermochemical cycles, but problems associated with nuclear power generation should be considered. On the other hand, biological production and photocatalysis are still in a very experimental stage.

The most widespread view is that, for a new energy model based on the hydrogen, in the long term, hydrogen should be mainly produced from electrolysis of water using renewable energy sources, and thus avoiding GHG emissions. The breaking of the water molecule should be done by the electricity generated from solar, wind, marine, geothermal, hydro, biomass energies, ... It is noteworthy that this would store the excess of intermittent renewable energies such as wind or the sun in hy-

drogen form. This would allow for the consumption of the stored energy when required. Nowadays, this issue is not possible because electricity storage is still not a solved problem [24]. As highlighted, hydrogen can be produced from a variety of energy sources and, consequently, each country could exploit their renewable resources more profitably. The implications of this are very powerful because it offers the possibility of decentralized energy production, from the primary energy sources and geographic locations point of view, and moreover, from inexhaustible resources. At the same time, the hydrogen economy also would allow the energy access in remote areas or sparsely populated, because it can be generated in distributed small stations [19]. Figure 1.3 describes the different stages comprising an energy system based on hydrogen and its potential uses.

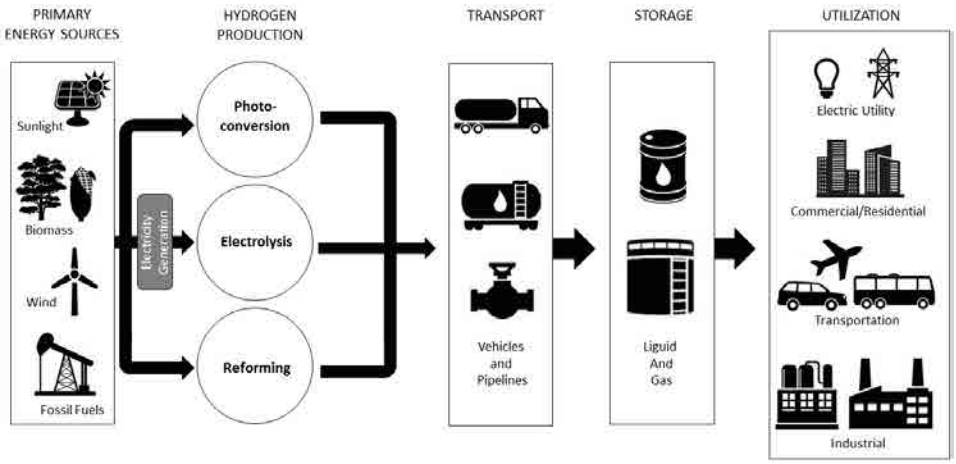

Figure 1.3: Hydrogen energy system. Extracted from [21].

The stored energy in the hydrogen produced can be removed in several ways: it can be used as a fuel in internal combustion engines, in conventional combustion turbines or in fuel cells. Most authors, however, agree that the long-term goal is to use hydrogen for producing electricity in fuel cells.

1.3 Fuel cells

Fuel cells (FC) are electrochemical devices that convert the chemical energy of a fuel directly into electricity. This is achieved through two chemical semireactions occurring in two electrodes separated by an ion conductive electrolyte: at the anode the fuel is oxidized and at the cathode, the oxidant (usually oxygen in the air) is reduced. The exact reactions depend on the electrolyte type of each FC, as is explained in section 1.3.1. In this redox process ions generated are transferred between the electrodes through the electrolyte, while the electrons travel through an external circuit generating electricity directly.

Conventional methods to produce kinetic energy or electricity involve two or three stages: first obtaining heat (by using different energy sources) to generate mechanical or kinetic energy. And finally, they are transformed again to generate electrical energy. Therefore, its performance is limited by thermodynamics according to Carnot's theorem. As a result of this thermodynamic limitation, an ideal gasoline car without any loss (at the usual working temperatures of cars) would have a performance between 40-50%. But, due to the not ideal behavior of engines, they only use ca. 20% of the energy released in the explosions to move the car wheels [23, 26].

As efficient energy usage is a matter of high urgency, one way to improve resources utilization is to change from combustion engines to engines based on fuel cell technology [27], as fuel cells are energetically more efficient and the only byproducts of their utilization are water and heat. In FC electrical energy is obtained directly from the chemical energy stored in fuels, not from the stages above-mentioned, so its efficiency is determined by equation 1.2.

$$\eta_{FC} = \frac{\Delta G}{\Delta H} = 1 - T\frac{\Delta S}{\Delta H} \tag{1.2}$$

In this equation ΔG is the change in Gibbs free energy, ΔH the change in enthalpy and ΔS the change in entropy of the chemical reaction.

In real fuel cells powered by H_2, working with common electric potentials between 0.6-0.8 V, the obtained yields range 45-65%, two to three times greater than yields achieved with thermodynamic-limited methods.

1.3.1 Fuel cell types

There are different types of fuel cells, depending on the electrolyte that they are composed of. This determines the fuel that the FC admits, the ions formed in the redox reactions, the catalysts that coat electrodes and the working temperature of fuel cells. Figure 1.4 presents the outline of the existing different types of FC, the transferred ions, the working temperatures and the power range that they can generate.

As seen in figure 1.4, not all the existing FC must be powered by pure hydrogen. For example, Phosphoric Acid Fuel Cells (PAFC) and Molten Carbonate Fuel Cells (MCFC) can be fed with natural gas. The Solid Oxide Fuel Cell (SOFC) stands H_2 with CO as a fuel, and the Direct Methanol Fuel Cell (DMFC) can be powered directly by methanol. Conversely, Polymer Electrolyte Membrane Fuel Cells (PEMFC) must be fed with high-purity hydrogen. Likewise, Alkaline Fuel Cells (AFC) are poisoned by CO_2, and thus purified air or pure oxygen have to be supplied.

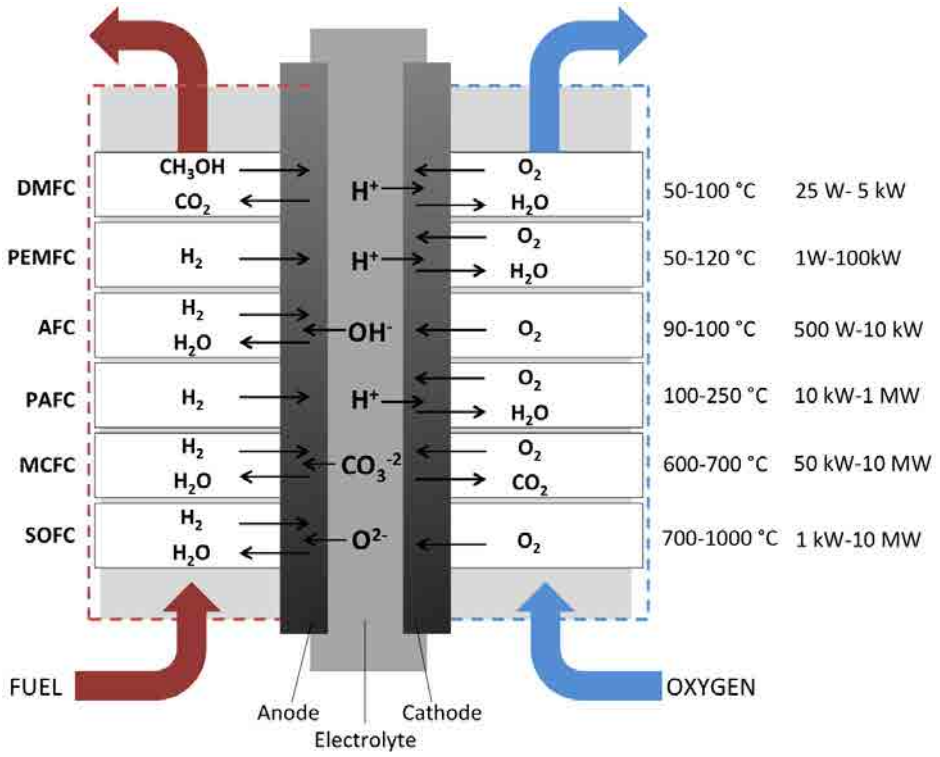

Figure 1.4: Different types of FC. Their corresponding working temperature and power range are listed. Extracted from [28].

FCs do not contain moving parts and this makes them very robust, compact, quiet and reliable (currently sensitive facilities to power outages such as hospitals, banks, schools, database centers, ... are already using them). Therefore, they can be installed inside buildings. In addition, its modular nature makes them very attractive, because a single cell can produce about 0.7 V and stacking them in series allows for obtaining FC for any applications, from the range of watts to megawatts [28].

For example, MCFC and SOFC are designed for applications with high power demand, in the range of hundreds of kW to MW and work at high temperatures, above 650℃. Due to the high working temperatures, these fuel cells have a slow start up, manufacturing materials must withstand thermal stress and need a continuous energy supply. Nevertheless, the exhaust gases have high energy content. These gases can be used to operate turbines and to heat water, increasing their efficiencies up to 80-90%, thanks to cogeneration. These high working temperatures make these types of FC not requiring electrodes composed of expensive catalysts, but they are difficult to manipulate and maintain. So, these two types of FC are designed for high power stationary applications.

On the other hand, PEMFC appear attractive for small-scale power generation. Thus, nowadays they arise, among the different fuel cells categories, as the most promising for small-scale portable and mobile applications, such as electric vehicles and residential power generators, as a consequence of their advantageous features. Hence, a major part of the research (for small-scale applications) is being directed towards low temperature fuel cells [29].

1.3.2 PEM fuel cells

PEMFC offer many advantageous features for small-scale electricity generation, such as [3, 26]:

- Operation at low temperature, around 70-90°C, which results in increased safety and low cost.
- Fast response times, reaching half of its power almost instantly at room temperature and 100% in just 3 minutes.
- They provide current densities one order of magnitude greater than other types of FC (up to 1 $A{\cdot}cm^{-2}$).
- They can work in any orientation.
- They are suitable for discontinuous operation.

The PEMFC electrolyte is a proton-conductive polymeric membrane. Both semireactions occurring at each PEMFC electrode are presented in equations 1.3 i 1.4.

$$\text{Anodic reaction: } H_2 \longrightarrow 2\,H^+ + 2\,e^- \tag{1.3}$$

$$\text{Cathodic reaction: } \frac{1}{2}\,O_2 + 2\,H^+ + 2\,e^- \longrightarrow H_2O \tag{1.4}$$

$$\text{Overall reaction: } \frac{1}{2}\,O_2 + H_2 \longrightarrow H_2O + \text{⚡} \tag{1.5}$$

First, hydrogen is dissociated in protons and electrons in the anode, which is coated with a Pt-based catalyst (equation 1.3). The generated protons migrate to the cathode through the membrane and the electrons are forced to circulate through an external circuit producing electricity. Finally, in the cathode the electrons and the protons are recombined and oxidized with the oxygen of air, producing water and heat (see equation 1.4) [26]. Therefore, the only products of the global reaction between hydrogen and oxygen are water, electricity and heat (equation 1.5). This mechanism is schematically represented in figure 1.5.

The PEMFC limitations are the high prices of the polymeric membrane and the platinum catalyst on one hand and, on the other hand, the loss of activity of Pt

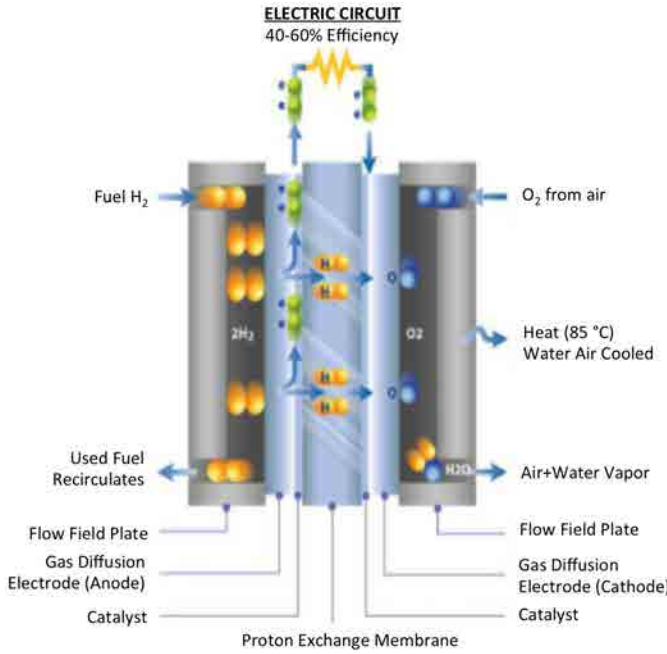

Figure 1.5: PEMFC scheme. Extracted from [28].

catalysts in presence of very low concentrations of carbon monoxide. In the working temperature range of the PEMFC, Pt catalysts are poisoned with CO concentrations ranging from 10 to 50 ppm, because CO coordinates strongly with Pt. So, the PEMFC must be powered by high purity H_2 [30].

Despite the advantages of fuel cells against traditional methods to produce energy, there are some disadvantages and challenges to overcome to achieve their widespread use. Mainly, the kW cost is still high in comparison with conventional methods and also its durability and non-availability of a hydrogen network. Currently, FC can be powered by hydrogen, by reforming currents or by methanol directly (only in case of DMFC). So, H_2 must be produced on-site or on-board from reforming reactions [3, 31].

1.4 Reformers

1.4.1 Hydrogen generation

Steam reforming reactions consist in the reaction between organic molecules, such as hydrocarbons or alcohols, and water vapor to obtain a rich mixture in H_2 and CO, according to the general reaction **1.6**; where the hydrogen generated not only comes from organic molecules, but also from water. The steam reforming reactions

are endothermic reactions and, therefore, a heat input is required [32]. Supplying external heat is critical for efficient use of the catalyst.

$$C_xH_yO_z + (x - z)\,H_2O \longrightarrow xCO + (x - z + \frac{y}{2})\,H_2 \tag{1.6}$$

Typically, reformate streams contain, in conjunction with H_2, between 8-12% CO (depending on the reaction conditions and catalyst used). This CO can react with steam via the water gas shift reaction (WGS), yielding more hydrogen (see equation 1.7) [30].

$$CO + H_2O \longleftrightarrow CO_2 + H_2 \qquad \Delta H^0_{298K} = -44 \text{ kJmol}^{-1} \tag{1.7}$$

Currently, natural gas steam reforming is the most energetically efficient process available to generate hydrogen and, also, the most developed. In this context, ethanol steam reforming appears as a promising route to generate H_2 from renewable sources [33], as already mentioned in section 1.2.2. The ideal ethanol steam reforming reaction is shown in equation 1.8.

$$C_2H_5OH_{(l)} + 3\,H_2O_{(l)} \longrightarrow 2\,CO_{2(g)} + 6\,H_{2(g)} \quad \Delta H^0_{298K} = +347.4 \text{ kJmol}^{-1} \tag{1.8}$$

Nevertheless, ethanol and water vapor can react through several reaction pathways, depending on the catalyst and the reaction conditions employed, and thus CH_4, acetaldehyde and up to a dozen byproducts [33] can be produced along with H_2 and CO_2. This is described in detail in Chapter 5. However, the purpose of the reforming process is to maximize the H_2 yield and to eliminate compounds that can poison FCs, as for example, CO in PEMFC. Therefore, reformers generally include the stages shown in figure 1.6.

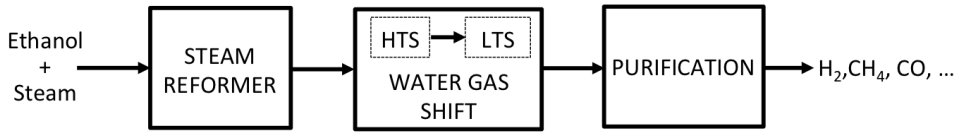

Figure 1.6: Reforming process scheme to power PEMFCs. Abbreviations legend: HTS-high temperature WGS reactor; LTS-low temperature WGS reactor.

WGS reactions are favored at low temperature, but reaction kinetics are very slow, so very large volumes are required. Generally, the WGS reactor is the bulkiest of the reforming system. It is for this reason that normally two WGS reactors in series are used [29]:

- The high-temperature WGS reactor (HTS) is located downstream the reformer and works at temperatures between 823-623 K with catalysts based on Fe and Cr oxides.

- Low temperature WGS reactor (LTS) operates at temperatures between 573-473 K, with catalysts based on Cu and Zn.

In each WGS reactor, ca. 90% of present CO is converted and downstream of WGS reactors the CO concentration is reduced to 0.5-2%, depending on the operation conditions [33]. However, hydrogen purity demands for PEMFC feeding require further CO removal. In fact, CO levels under 10 ppm in the hydrogen stream feeding the fuel cell are required to avoid the irreversible poisoning of the Pt catalyst of the PEMFC anode. Therefore, purifying stages are unavoidable.

1.4.2 Catalytic hydrogen purification

Three catalytic approaches have been proposed and investigated thoroughly to purify reformate currents, aimed at reducing the CO concentration and obtaining pure H_2 streams. They are: Pd-membrane separation, catalytic methanation and CO preferential oxidation in the presence of a large H_2 excess [34].

1.4.2.a Methanation

In the methanation reactor carbon oxides are hydrogenated, consuming hydrogen according to the following reactions:

$$CO + 3\,H_2 \longrightarrow CH_4 + H_2O \qquad \Delta H^0_{298K} = -251 \text{ kJmol}^{-1} \tag{1.9}$$

$$CO_2 + 4\,H_2 \longrightarrow CH_4 + 2\,H_2O \qquad \Delta H^0_{298K} = -253 \text{ kJmol}^{-1} \tag{1.10}$$

In these reactions it is not necessary to add new reactants to the reformate stream, and thus increasing the complexity of the system is avoided, but, on the contrary, it consumes part of the H_2 generated. The methanation reaction is the inverse of methane steam reforming.

1.4.2.b Carbon monoxide preferential oxidation

The CO selective or preferential oxidation (CO-PrOx) is one of the most effective methods to reduce CO concentration below 10 ppm. CO-PrOx catalysts must be very active to oxidize CO (equation 1.11), which is found in concentrations between 0.5-2%. On the other hand, they should not be active for H_2 oxidation (equation 1.12) in order to avoid losing fuel, even though its concentration is between 40-70%. Both oxidation reactions compete and, consequently, the catalysts have to be very selective [30]. To perform the CO-PROX reaction, it is necessary to add oxygen to the pre-cleaned WGS stream, usually from the air.

$$CO + \frac{1}{2}\,O_2 \longrightarrow CO_2 \qquad \Delta H^0_{298K} = -285 \text{ kJmol}^{-1} \quad \text{Desired reaction} \tag{1.11}$$

$$H_2 + \frac{1}{2} O_2 \longrightarrow H_2O \qquad \Delta H^0_{298K} = -243 \text{ kJmol}^{-1} \quad \text{Undesired reaction} \qquad (1.12)$$

Purification of pre-cleaned reformate streams by means of CO-PrOx reaction is the second main objective of this Thesis. Part II is dedicated to CO abatement through its preferential oxidation, where the main results achieved are detailed.

1.4.2.c Hydrogen separation with membranes

The use of H_2-selective membranes coupled to the reforming stage allows for continuous hydrogen removal from the reformate stream and for obtaining ultra pure hydrogen streams, which can be directly used to feed PEMFC. In addition, the continuous removal of one of the reaction products, the hydrogen, promotes the reactions extension beyond equilibrium values, as the equilibria of reactions are shifted. Hence, this shift results in even higher hydrogen yields, because higher conversion values and improved hydrogen selectivities are achieved in comparison with traditional reactors under the same operative conditions [35].

Moreover, in comparison with the classical configuration depicted in figure 1.6, which consisted of a H_2 generation unit in series with several purification units, the coupling of a reformer to catalytic membranes represents a modern configuration, in which hydrogen production and purification take place simultaneously in a single unit. An integrated reaction-separation unit considerably simplifies the reformers design, because the requirement of purification stages and even of bulky WGS reactors can be avoided, leading to a process intensification. This is schematically represented in figure 1.7.

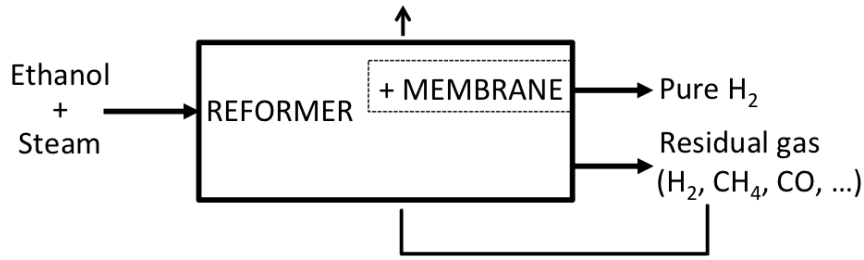

Figure 1.7: Simplification of the reforming process coupling a steam reformer with a H_2-selective membrane.

Such a unit has many potential advantages over traditional reactors due to the reduction of the number of catalytic stages required and the better heat transfer management. Namely, these advantages are reduced capital costs, improved hydrogen yield and selectivities, drastically reduced downstream separation costs and improved reliability [36, 37].

The implementation of membranes to purify hydrogen results in a simplified and more compact process and allows to operate the system at lower temperatures while obtaining the same performance of traditional configurations, which is particularly attractive and even more important for small-scale, decentralized hydrogen production units [35], such as on-site or on-board reformers.

The most widely used membranes are formed by Pd or Pd alloys, as they provide a very high selectivity to H_2 (only H_2 can diffuse across them). In fact, Pd membranes are those that provide greater selectivity and permeability of hydrogen. Typically, the membranes used have a <50 µm thickness, to reach an equilibrium between hydrogen permeate flux and their mechanical strength [38].

The H_2 permeation through membranes not only depends on their physical properties, but also on the difference between the partial pressures of H_2 on each side of the membrane, which is its driving force, according to Sievert's law (equation **1.13**). The membrane thickness plays an important role: the thinner the membrane the higher the hydrogen permeation and the lower the costs, however the membrane's mechanical resistance can be compromised. Therefore, for practical applications, thicker membranes are necessary to ensure the mechanical resistance and strength of the membrane. They are generally deposited on porous supports such as SiO_2, Al_2O_3, B_2O_3 and porous stainless steel (PSS) [39].

$$F_{H_2,permeate} \propto \frac{e^{(-E_a/RT)}}{d}\left(\sqrt{P_{H_2,retentate}} - \sqrt{P_{H_2,permeate}}\right), \quad [40]$$
$$P_{H_2} = P \cdot y_{H_2} \tag{1.13}$$

In Chapter 7, a pure hydrogen generation device is presented. In this Chapter, the performance of a Pd-Ag membrane placed in series with an ethanol steam reforming stage comprised of the $RhPd/CeO_2$ catalysts developed in this Thesis is evaluated.

1.5 Structured catalysts

Catalysts deposition on monolithic structures presents advantages over traditional catalysts in powder or pellets. The monoliths are single-body structures that comprise the structural support (or substrate) where the catalysts are deposited. They can be ceramics (usually cordierite), metallics or made of catalytically active materials, such as stabilized alumina. Usually, they are formed by parallel channels or cavities (as sponges), among others, in order to obtain large surface areas.

The catalyst is deposited directly on the monoliths' walls forming a thin layer that covers them. The use of structured catalysts (catalysts supported on monoliths) has the following advantages over the catalysts in powder or pellets [41]:

- The catalytic layers have enhanced mechanical and chemical stability and durability.
- They have higher surface areas.
- Catalyst deposition as thin layers allows the use of less amount of catalyst.
- The catalytic phase is immobilized.
- They avoid reactor blockage due to the agglomeration of catalytic material.
- They have a low-pressure drop (2-3 orders of magnitude lower than the corresponding pellets).
- They have higher heat and mass transfer.
- They present a modular nature that allows the direct increase or reduction of the scale.
- They have fast response to operational changes.
- They allow the size and weight of reactors to be reduced.

This group of features makes the structured catalysts very suitable for reformers coupled to low-temperature FCs (such as PEMFC) and autonomous hydrogen generators.

On the other hand, it is considered that fuel cells for low-power portable and mobile applications (from less than 1 W to several hundred watts) will be the first to enter into the market and, therefore, research has been directed towards the development of miniaturized reformers to produce H_2 on-site and on-demand [32]. The reduction of the scale required by these devices and safety in the handling and storage of H_2 make unfeasible the implementation of catalytic fixed bed reactors in this type of applications. In this context, the use of structured catalysts with channel dimensions in the micrometers range (up to 1000 µm) is advantageous.

1.5.1 Microreactors

The main advantages of using microreactors derive from their geometry. The small size of the microreactor channels and their homogeneous distribution offer high area-to-volume ratios, short transfer and diffusion distances, homogeneous flows and very small residence times [42]. As a result, mass and heat transfers are significantly enhanced and thus reactions can be better controlled [43]. For these reasons, microreactors are increasingly used as they have capabilities exceeding those of their conventional macroscopic counterparts [44].

Microreactors present large surface areas per unit of volume, which reduces the size of the reactors and leads to higher amounts of catalyst exposed to reactants. Generally, the catalysts are deposited directly on the microchannels walls, forming thin catalytic layers, which also help to improve heat transfer and to reduce the amount of required catalyst.

The better heat management in microreactors makes them very interesting for strongly exothermic reactions, as the heat generated can be better extracted, maintaining the reaction in suitable temperature range, thus avoiding the formation of hot spots. Similarly, the heat input can also be performed more efficiently in the case of endothermic reactions, such as reforming reactions. In addition, the combination of an endothermic and an exothermic reaction in adjacent channels of a single device, designed as a heat exchanger, allows to take advantage of the excellent heat transfer of microreactors and to achieve an autothermic system, at least once the process has started and has reached the steady state.

The better mass transfer compared with conventional reactors, is mainly due to the small size of microchannels. So the mass transfer is basically limited by the rate of reactants adsorption and desorption, not by their diffusion.

Finally, it should also be mentioned that microreactors allow the scale-up of applications by directly increasing the number of microreactors, as it is not necessary to change the microreactor geometry, which could be considered the *unit cell*. However, the periphery of microreactors must be redesigned, such as the reactants feeding, the system encapsulation and the increased initial energy demand for feeding larger devices [44, 45].

Numerous methanol microreformers working in the temperature range 533-723 K have been reported in the literature. However, due to the higher temperatures required for ethanol steam reforming, ethanol microreformers have not been as widely studied as the methanol-based. In Chapter 8, a survey of ethanol microreformers reported in the literature is performed.

The use of microreactors in H_2 technology provides safer operational conditions than conventional reformers in the management of H_2-rich streams, avoiding the storage of large volumes of hydrogen, and allows the use of process parameters that otherwise would be explosive [39]. Therefore, microreactors appear as an invaluable technology for boosting the implementation of on-site and on-demand generation of hydrogen for portable applications, thus avoiding limitations imposed by hydrogen storage. However, the natural trend in miniaturization of fuel cell systems is followed with increasing difficulty by present micro-reforming/micro-cleaning units. To further reduce the hydrogen generation scale while maintaining system efficiency

is hardly attained using conventional geometries and/or manufacture techniques of present microreactors. Therefore, the development of breakthrough technologies capable of providing higher hydrogen generation rates per unit volume and, at the same time, enable downscaling is required. In a pioneering publication, our research group reported a new turn of the screw in miniaturization of systems for hydrogen production. It was accomplished using novel silicon micromonoliths with millions of regular and parallel microchannels per square centimeter with a diameter of only ∼3-4 µm [46]. In this publication, Llorca et al. evaluated the ESR performance of a Si micromonolith coated with a Co/ZnO catalyst.

1.5.1.a Silicon micromonoliths

The Si micromonoliths exhibit a unique geometry that was achieved by photo-assisted electrochemical etching in a ∼0.2 mm thickness silicon wafer. The microfabrication process started pre-structuring a ⟨100⟩ n-type silicon wafer by lithography and tetramethylammonium hydroxide (TMAH) etching to create a square array of inverted pyramids. These pyramids pointed toward the bulk of the wafer and defined the positions of pore growth. The electrochemical etching was then carried out at 288 K in 5 wt.% hydrofluoric acid (HF) solution, using a wetting agent. The structured (front) side of the wafer was in contact with the electrolyte, while the backside was illuminated through an array of LEDs with an 880-nm peak emission wavelength. A constant anodic potential of 2 V was applied. The etching current was computer-controlled and was reduced as a nonlinear function of the etching time, to compensate for the effects of limited HF diffusion in the narrow pores [47, 48]. Under these conditions, about 330 min of etching time was required to achieve a pore depth of 220 µm. After the electrochemical etching, the macroporous samples were oxidized in dry O_2 at 1373 K for 30 min. The oxide layer on the backside was removed, and the remaining backside silicon was etched off in 25 wt.% TMAH solution at 358 K until the pore tips were reached. Finally, the samples were dipped in 5 wt.% HF to remove any oxide remaining on the pore walls and on the wafer's front side. This process is carried out at the Departament d'Enginyeria Electrònica from the Universitat Politècnica de Catalunya (UPC) and they provided us with the Si micromonoliths. Figure 1.8 shows on the left side a picture of a conventional cordierite monolith (center) and of a Si micromonolith (right) compared to a 1 euro coin. On the right side of figure 1.8, a SEM image of the 5-million microchannels array developed over the Si wafers is shown.

The resulting Si micromonoliths of ∼0.2 mm length and 13 mm in diameter contained ca. $5{\cdot}10^6$ channels of 3.3 µm in diameter, perfectly cylindrical and parallel, opened at both sides and arranged in a square lattice with 4 µm periodicity, as seen in figure 1.9.

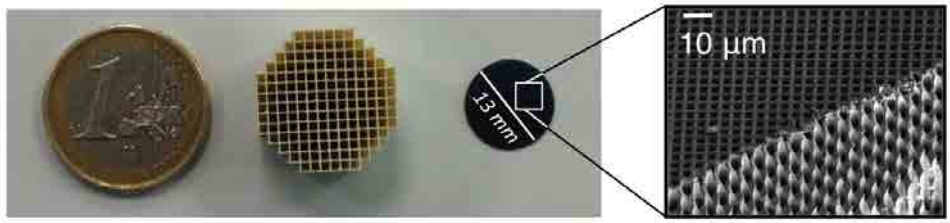

Figure 1.8: Scale comparison between a conventional cordierite monolith and a Si micromonolith. Left: Picture of a conventional cordierite monolith and of a Si micromonolith compared with a 1 euro coin. Right: SEM image showing the detail of the Si microchannels array.

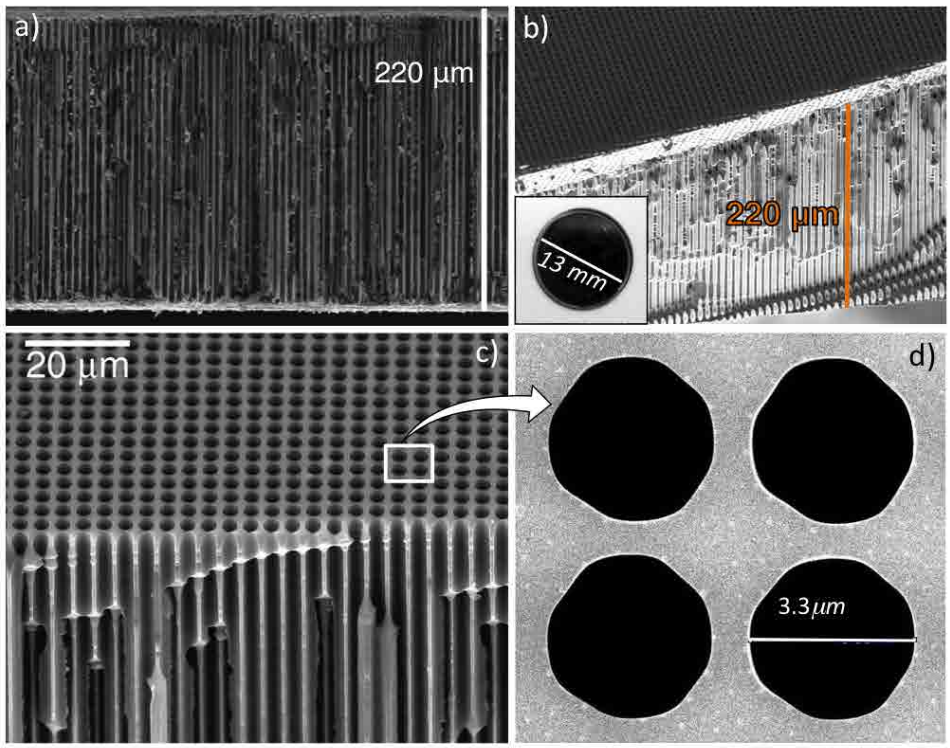

Figure 1.9: SEM images of the Si micromonolith structure. a) Frontal view of the micromonolith where the length of the microchannels is measured. b) and c) View of the microchannels array structure. d) Top view of 4 microchannels.

Figure 1.9 shows SEM images of the Si micromonolith. In figure 1.9a a cross-sectional view of the micromonolith is given, where the channels length was measured. The length of the channels, which coincides with the Si micromonolith thickness, was 220 µm. SEM images 1.9b and 1.9c show low-magnification images of the array of Si channels. Figure 1.9c shows the detail of the perfect regular matrix of parallel microchannels; being the channels density of the matrix $4{\cdot}10^6$

channels/cm^2. Finally, the detail of 4 microchannels is given in top view in figure 1.9d.

The open frontal area of such a microstructure was 34% and the corresponding pressure drop measured flowing 60 mL/min N_2 at room temperature was only ca. 170 Pa, which was virtually identical to the value predicted by the Poiseuille law (165 Pa) [49]. Such a geometry led to a specific contact area of $4.1 \cdot 10^5$ m^2/m^3.

Figure 1.10 shows the three types of structured monoliths reviewed throughout this Introduction: conventional cordierite monoliths, conventional microreactors and the Si micromonolith developed at UPC. The scale reduction involved in the miniaturization of the cordierite monolith brings along an increase in the specific contact area (exposed area per unit volume of monolith, m^2/m^3) of two orders of magnitude.

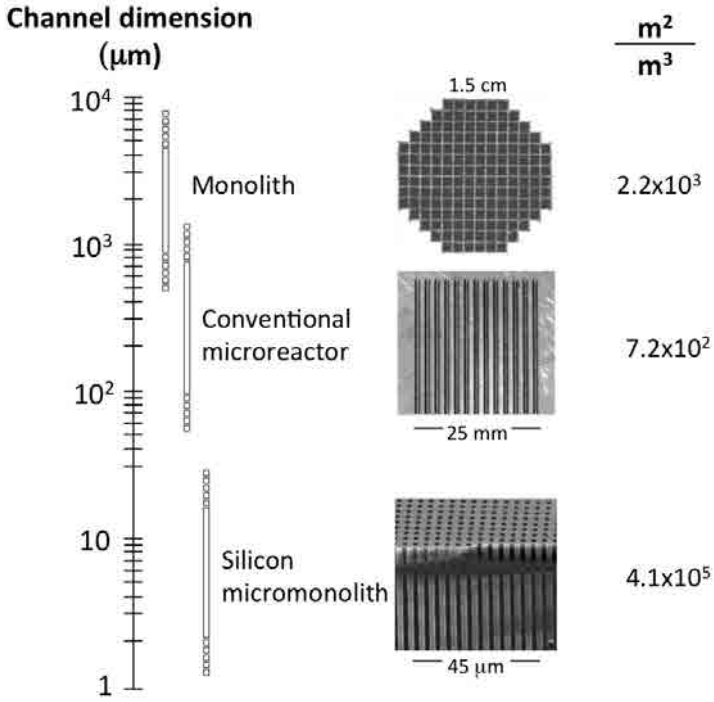

Figure 1.10: Scale comparison of the different structured monoliths used in this Thesis.

Given the small dimensions of the microchannels and their high depth/diameter ratio (depth/diameter>65), new catalysts synthesis methods had to be precisely designed in order to successfully coat the channels' walls with homogeneous thin layers of appropriate catalysts. Different synthesis methods were designed and Si microchannels have been successfully coated with a Co_3O_4/ZnO catalyst for ESR as reported in [46], where the functionalized micromonolith performance is also de-

scribed. The Si micromonoliths have also been coated with a $RhPd/CeO_2$ catalyst aimed also at ESR, which is the subject of Chapter 8, and with Au/TiO_2 catalysts intended for CO-PrOx, which is the subject of Chapter 14. The increasing specific contact areas led to increasing catalytic activities per unit volume and to decreasing amounts of catalyst needed, as explained in the corresponding Chapters above-mentioned.

1.6 Aims of this Thesis

The main objective of this thesis is the hydrogen generation for energy purposes. To achieve this general goal, three main objectives were defined, that can be broken down as follows:

1. Development of an effective $RhPd/CeO_2$ catalyst to produce hydrogen through ethanol steam reforming:
   (a) To synthesize new $RhPd/CeO_2$ catalysts.
   (b) To fundamentally characterize the synthesized catalysts.
   (c) To study the catalytic performance of the developed catalysts for the ethanol steam reforming reaction.
   (d) To characterize the $RhPd/CeO_2$ catalysts under reaction conditions.
   (e) To evaluate the catalytic performance of a unit composed of a Pd-Ag membrane coupled to a reforming stage based on the $RhPd/CeO_2$ catalysts synthesized.
2. Development of a robust Au/TiO_2 catalyst to purify hydrogen streams through the preferential oxidation of carbon monoxide:
   (a) To synthesize new Au/TiO_2 catalysts.
   (b) To fundamentally characterize the synthesized catalysts.
   (c) To evaluate the reaction performance and stability of the Au/TiO_2 catalysts synthesized for the preferential oxidation of carbon monoxide.
3. Miniaturization of the hydrogen production and purification scales by testing the catalytic performance of the $RhPd/CeO_2$ and Au/TiO_2 catalysts developed loaded on microreactors:
   (a) To develop new synthesis methods to functionalize Si micromonoliths with $RhPd/CeO_2$ and Au/TiO_2 catalysts.
   (b) To implement the needed periphery and assembly to evaluate the catalytic performance of the functionalized microreactors.
   (c) To characterize the catalytic layers developed on the Si micromonoliths.

Part I.

RhPd/CeO_2 catalysts for ethanol steam reforming

2 Hydrogen production with $RhPd/CeO_2$ catalysts: An overview

After the overview of the energy scenario and the important role that hydrogen may play as an energy carrier in a new energy system given in the Introduction, the present Part focuses on the catalytic production of hydrogen.

As already mentioned in the Introduction, in nature, hydrogen is always found in bound form, being part of a wide variety of compounds. Thus H_2 can be obtained from several hydrogen-containing sources by using different extraction processes. These two facts greatly influence its environmental and carbon footprints.

Generally, H_2 production technologies fall into three broad categories: (i) photoconversion, (ii) electrolysis and (iii) thermochemical processes. Photobiological and photocatalytic technologies still render low H_2 yields and are in the early stages of development. In contrast, the electrolysis of water is a mature technology. However, the overall efficiency of water electrolyzers only reaches $\sim$25%, as electrolysis is an energy-intensive process and its main drawback is economic. Nevertheless, thermochemical processes are commercially available and are the most widely used for H_2 production. Among thermochemical processes, gasification and pyrolysis are commonly used for hydrogen extraction from solid feedstocks (such as coal, wood or other biomass). On the other hand, steam reforming is chosen for liquid and gaseous materials such as natural gas, methanol or even gasoline. Currently, catalytic methane steam reforming (MSR) is the most energy-efficient and commonly used technology available and it is specially mature [11, 33].

Steam reforming reactions are particularly attractive for H_2 production and render the highest H_2 yields, as hydrogen is not only extracted from the fuel, but also from water. In addition, in order to reduce the environmental impact and carbon footprints of the reforming processes, fossil fuels can be replaced by environmentally friendly fuels such as bioethanol.

2.1 Hydrogen from ethanol

Ethanol offers numerous advantages among other fuels: (i) it can be produced from renewable sources, (ii) it has a relative high hydrogen content per unit volume in the liquid phase and a high hydrogen-to-carbon ratio (H/C=3), (iii) it is non-toxic, (iv) it can be transported, stored and handled safely and easily and (v) it is already available in the distribution networks of some countries. Its energy content is 21.5 MJ/L or 27.2 MJ/kg of liquid ethanol [50].

Ethanol can be produced renewably from the fermentation of a large variety of sources, mainly corn, sugarcane and starch. But other non edible sources, which do not compete with food, such as cellulose, wood, agricultural and forest residues can also be used as a source of bioethanol; these lignocellulosics increase the availability of raw materials and reduce the production costs of bioethanol [51]. The fermentation process produces an aqueous mixture where the steam-to-ethanol (S/E) ratio is between 7:1 and 13:1, the so-called bioethanol.

There are three main catalytic processes to directly produce hydrogen from ethanol, namely steam reforming (SR), partial oxidation and its combination, oxidative steam reforming. These catalytic routes differ by the co-reactant used, the process chemistry and the maximum hydrogen yield rendered. These three catalytic pathways are described in sections 2.1.1 to 2.1.3.

2.1.1 Steam reforming

The ethanol steam reforming (ESR) reaction (equation 2.1) ideally produces 6 moles of H_2 per mol of ethanol reacted, where half of the H_2 produced comes from water, and 2 moles of CO_2.

$$C_2H_5OH_{(g)} + 3\,H_2O_{(g)} \longrightarrow 6\,H_{2(g)} + 2\,CO_{2(g)}\ \Delta H^0_{298K} = 173.3\ \text{kJmol}^{-1} \qquad (2.1)$$

The main drawback of ESR is its high endothermicity. Consequently, a continuous energy supply is required to run the reaction (the ESR operating temperature is usually in the range of 700-1000 K), which is added to the energy needed to evaporate the liquid reactants and to heat up the gaseous mixture. Moreover, hydrogen formation is limited by the thermodynamic equilibrium; nevertheless, equilibrium can be shifted by increasing the steam-to-ethanol ratio. Usually S/E ratios higher than the stoichiometric (S/E=3) are preferred for operation, as they also prevent carbon deposition (or gasify carbon deposits). The use of S/E higher than 3 increases the energy input related to water evaporation, but it allows the direct use of the bioethanol produced by fermentation. Bioethanol reforming allows for reducing or eliminating the distillation process of synthetic ethanol, with the subsequent reduction of energy consumption and associated costs of this process.

Furthermore, the use of bioethanol leads to an almost-closed CO_2 cycle, because the CO_2 released during ESR performance has been previously consumed by the biomass during the photosynthesis.

2.1.2 Partial oxidation

In the partial oxidation of ethanol (POX), ethanol is partially oxidized with oxygen to produce H_2 and CO_2 (equation 2.2).

$$C_2H_5OH_{(g)} + \frac{3}{2}\,O_{2(g)} \longrightarrow 3\,H_{2(g)} + 2\,CO_{2(g)} \quad \Delta H^0_{298K} = -552 \text{ kJmol}^{-1} \tag{2.2}$$

For low oxygen-to-ethanol (O/E) ratios, CO can be also produced, although the reaction is thermodynamically unfavored (equation 2.3).

$$C_2H_5OH_{(g)} + \frac{1}{2}\,O_{2(g)} \longrightarrow 3\,H_{2(g)} + 2\,CO_{(g)} \quad \Delta H^0_{298K} = 14 \text{ kJmol}^{-1} \tag{2.3}$$

In POX reactions the heat is provided by the oxidation, thus there is no need for external energy input, and the presence of oxygen can contribute to decrease the formation of carbon deposits. Despite this advantages, the maximum hydrogen yield achievable is lower (3 mol H_2/mol ethanol reacted) than in ESR and the total oxidation (combustion) is much more favored by thermodynamics (equation 2.4).

$$C_2H_5OH_{(g)} + 3\,O_{2(g)} \longrightarrow 3\,H_2O_{(g)} + 2\,CO_{2(g)} \quad \Delta H^0_{298K} = -1293 \text{ kJmol}^{-1} \tag{2.4}$$

As a consequence, hydrogen selectivity is low. In addition, the mixture of ethanol with oxygen entails risk of explosion and operation outside the flammability range (3.5-19 vol.% in air) is required.

2.1.3 Oxidative steam reforming

Ethanol oxidative steam reforming (OSR, equation 2.5) is a combination of ESR and POX, where the heat released in POX is used to run the ESR reaction. The reactants mixture consists of ethanol, water and oxygen whose concentrations have to be adjusted to ensure reaction enthalpy close to zero (thermal neutrality).

$$\begin{gathered} C_2H_5OH_{(g)} + (3-2x)\,H_2O_{(g)} + x\,O_{2(g)} \longrightarrow (6-2x)\,H_{2(g)} + 2\,CO_{2(g)}, \\ \Delta H^0_{298K} = (173.3 - 483x) \text{ kJmol}^{-1} \end{gathered} \tag{2.5}$$

where x is the oxygen-to-ethanol (O/E) molar ratio.

The main advantage of OSR is that it does not require an external heat supply, once the steady state is achieved, provided that the reactants concentration

is properly adjusted. Also, it may be operated at much lower temperatures than ESR, thus offering a favorable energy balance. Furthermore, the presence of water in the feed mixture inhibits flammability and explosion risks of ethanol-oxygen mixtures, overcoming one of the major drawbacks of POX and producing higher H_2 yields. The presence of steam also decreases combustion selectivity and retards carbonaceous deposits formation. However, the reaction is difficult to control and two catalytic regimes may appear: one driven by POX followed by pure ESR.

In this Thesis, ethanol steam reforming and oxidative steam reforming are the chosen routes for hydrogen production. Chapter 5 describes the ESR results obtained over the RhPd/CeO_2-based catalysts investigated and Chapter 8 (section 8.3.2) describes results regarding OSR.

2.2 ESR catalytic pathways

Ethanol steam reforming proceeds through a complex series of steps that involve several reaction pathways, depending on the catalyst and the reaction conditions tested (such as temperature, S/E ratio, residence time, ...), which modify the theoretical products distribution and the H_2 yield. Several reaction mechanisms have been proposed in the literature and can be summarized as follows: firstly ethanol adsorbs on the catalyst surface and may undergo dehydration to ethylene (equation 2.6), dehydrogenation to acetaldehyde (equation 2.7), decomposition to CH_4, CO and H_2 (equation 2.8) or acetone formation (equation 2.9).

$$\text{Dehydration: } C_2H_5OH \longrightarrow C_2H_4 + H_2O \tag{2.6}$$

$$\text{Dehydrogenation: } C_2H_5OH \longrightarrow H_2 + CH_3CHO \tag{2.7}$$

$$\text{Decomposition: } C_2H_5OH \longrightarrow H_2 + CO + CH_4 \tag{2.8}$$

$$\text{Acetone formation: } 2\,C_2H_5OH + H_2O \longrightarrow (CH_3)_2\,CO + CO + CH_4 \tag{2.9}$$

Products formed in the first step can further react through a network of interrelated reactions. Acetaldehyde can undergo steam reforming (equation 2.10) or further decompose (equation 2.11).

$$\text{Acetaldehyde SR: } CH_3CHO + H_2O \longrightarrow 3\,H_2 + 2\,CO \tag{2.10}$$

$$\text{Acetaldehyde decomposition: } CH_3CHO \longrightarrow CH_4 + CO \tag{2.11}$$

Also methane formed in equations 2.8, 2.9 and 2.11 can further react and undergo SR (equation 2.12) or decompose to form coke (equation 2.13).

$$\text{Methane SR: } CH_4 + H_2O \leftrightharpoons 3\,H_2 + CO \tag{2.12}$$

$$\text{Methane decomposition: } CH_4 \longrightarrow 2\,H_2 + C \tag{2.13}$$

Carbon monoxide and CO_2 produced in the previous reactions can also react through the water gas shift reaction (WGS, equation **2.14**) and produce more H_2 or via the Boudouard reaction (equation **2.15**) that also leads to carbon deposition.

$$\text{WGS reaction: } CO + H_2O \leftrightharpoons H_2 + CO_2 \tag{2.14}$$

$$\text{Boudouard reaction: } 2\,CO \longrightarrow C + CO_2 \tag{2.15}$$

Ethanol dehydration is usually followed by ethylene polymerization (equation **2.16**), which forms coke that blocks the active sites of the catalysts.

$$\text{Polymerization: } C_2H_4 \longrightarrow Polymers \longrightarrow 2\,C + 2\,H_2 \tag{2.16}$$

One problem in the elucidation of the reaction mechanism is that most of the ethanol reaction mechanisms proposed in the literature rely on different reaction conditions and are mainly based on temperature programmed desorption of ethanol or temperature programmed reaction under diluted steam reforming conditions, which do not represent realistic reaction conditions.

The purpose of the ESR process is to maximize H_2 and CO_2 production and, specially, hinder the formation of intermediate compounds that lead to coke formation, which finally deactivates the catalysts. But, as seen, the ESR reaction network is complex and involves a variety of reaction types occurring simultaneously. These reactions have different dependencies on reaction conditions and their promotion depends on different functionalities of the catalysts, thus the role of the catalyst is crucial. All these factors contribute to the need for extensive research of catalysts as well as reactors and process engineering. The following section (**2.3**) reviews the catalysts reported so far in the literature for ESR.

2.3 Ethanol steam reforming catalysts

Many studies have focused on catalysts based on nickel, cobalt and noble metals for ESR. An efficient catalyst for hydrogen production from ethanol has to efficiently dissociate the C-C bond (at reasonably low temperatures), keep CO concentration low and be stable under catalytic operation. Catalyst deactivation related to coke and carbonaceous compounds deposition is the major drawback of catalytic systems based on transition metals. Among transition metals, noble metals and, in particular, Rh and Ru are known to successfully break the C-C bond leading to less coke deposition and thus to more stable catalysts, provided that high enough temperatures are selected for operation (T>850 K).

2.3.1 Noble metal catalysts

In an early work by Cavallaro in 2000 [52], catalysts with different Rh contents supported on Al_2O_3 were investigated for ESR with S/E=8.4. The proposed reaction mechanism started with the dehydrogenation and/or dehydration of ethanol followed by rapid conversion of the products into CH_4, CO and CO_2. The acid sites of Al_2O_3 promoted ethanol dehydration, whereas the other reactions were catalyzed by Rh. The increase in Rh content resulted in higher C_1 (CH_4, CO and CO_2) concentrations while C_2 (ethylene, ethanol and acetaldehyde) disappeared gradually from the reformate stream. High Rh loadings (Rh $\geq$ 5 wt.%) supported on an acid support and high operation temperatures (T=923 K) led to up to four hours of maintained catalytic activity. After this investigation, in 2002 Auprêtre et al. [53] and Breen et al. [54] tested a wide range of catalysts in order to elucidate the best ESR catalytic system. The former studied different active phases (Rh, Pt, Pd, Ru, Ni, Cu, Zn, Fe) as well as supports (Al_2O_3, CeO_2-Al_2O_3, CeO_2, CeO_2-ZrO_2, ZrO_2) in order to obtain highly active catalysts for ESR, which rendered high H_2 yields, and selective to the formation of CO_2 both in the ESR and the WGS reactions. The authors concluded that the most active and selective catalysts were the Rh and Ni-based ones, achieving the highest H_2 yield with a Rh/$CeZrO_2$ catalyst. On the other hand, Breen et al. [54] studied Rh, Pt, Pd and Ni supported on Al_2O_3 and CeO_2-ZrO_2 and obtained that Rh- and Pt-based catalysts exhibited better performance and were more active when supported on ceria-zirconia mixed oxides.

2.3.1.a Active phases

Since these initial works, considerable effort has been made on the research of ESR over noble metals, and Rh, Pt, Pd, Ru, Ir and Ag-based catalysts have been investigated. In more than 40% of the published works, Rh-based catalysts have been used, since this metal is the most effective with respect to ethanol conversion and hydrogen selectivity, due to its superior capacity to successfully dissociate the C-C and H-C bonds of ethanol and reaction intermediates such as acetaldehyde [55,56]. In addition, their resistance to particle sintering leads to stable catalysts. Nearly 30% of publications corresponds to Pt-based catalysts, which take advantage of the strong oxidation activity and the WGS reaction promotion of Pt and its high activity and selectivity to H_2 production [57]. To a lesser extent, Pd-based catalysts have been used due to its known dehydrogenation and methane steam reforming catalytic activity. Also, some works report on the use of Ru-based catalysts because their H_2 production is comparable to that of Rh, but at high Ru loading. Nevertheless, whereas Rh catalysts are stable, Ru induces dehydration of ethanol to form ethylene, leading to coke formation via polymerization [58,59]. Iridium has been tested in few works [60,61] and it was found that Ir particles are responsible for the acetaldehyde C-C bond cleavage, which mainly decomposes to CO and CH_4 at tem-

peratures above 673 K or it is converted to acetone at lower temperatures. Finally, Ramos et al. [59] also tested Ag/CeO_2 for the ESR obtaining poor activity of the catalyst and being the main products H_2 and acetaldehyde between 373 and 873 K.

The combination of two or more metals has synergetic effects and bimetallic catalysts show enhanced activity than the metals alone in bond dissociation, dehydrogenation and oxidation processes, however few authors have studied them [62]. Idriss et al. [63] and Scott el al. [64] studied $Rh\text{-}Pd/CeO_2$, obtaining that the direct oxidation route to acetate over CeO_2 is suppressed by the presence of the metals and the dehydrogenation reaction temperature is lowered by about 100 K in comparison with CeO_2 alone. Additionally, by in-situ infrared (IR) studies, they inferred that the bimetallic catalysts break ethanol's C-C bond at temperatures below 400 K. Rh-Pt and Pt-Pd supported on CeO_2 were studied by Idriss [65]. Rh-Pt was also tested by Simson et al. [66] for SR of 85% pure ethanol mixed with 15% gasoline (defined as E85). More recently, Cobo et al. [67] studied a Rh_6Pt_2/La_2O_3 catalyst. They obtained full ethanol conversion and an active catalyst for 120 h under the reaction conditions tested (873 K, S/E=7 diluted in 76% Ar) performing two types of catalyst regenerations: (i) after a H_2 treatment the catalytic activity was recovered, but a fast deactivation occurred; (ii) after a regeneration treatment with air the catalyst completely recovered its activity most likely due to both the oxidation of the carbonaceous deposits and the regeneration of the identified $Rh\text{-}Pt\text{-}Rh_2O_3$ active sites. The alloy of a noble metal with a non-noble metal has also been investigated. Platinum-Ni and Pt-Co supported on CeO_2 were evaluated for ESR in the low temperature regime [68]. The $Pt\text{-}Ni/CeO_2$ catalyst showed at 623 K a performance closed to the thermodynamic equilibrium but large quantities of carbon deposits that blocked the reactor were detected. On the other hand, the $Pt\text{-}Co/CeO_2$ catalyst exhibited H_2 yields higher than thermodynamic values and scarce coke selectivity.

Platinum-based catalysts have been studied by De Lima et al. The ESR reaction performance of Pt/CeO_2 and $Pt/CeZrO_2$ catalysts was investigated in [69] and [70], respectively. The authors concluded that the presence of the metal improved ethanol conversion and resulted in high selectivity to H_2, CO and CO_2, however the Pt-support interfaces were quickly lost due to the formation of carbonaceous species which led to catalysts deactivation. Chen et al. [71] performed ESR at 623-823 K over $Pt/Ce_xZr_{1\text{-}x}O_2$ catalysts (x=0.2, 0.4, 0.6 or 0.8). The catalysts showed good initial stability and were highly active at low temperatures, only yielding H_2, CO, CH_4 and CO_2 as products. At 723-823 K, the selectivity was close to thermodynamic equilibrium.

Ethanol steam reforming performed over 5 wt.% Pd supported on commercial γ-alumina using biomass-derived ethanol was investigated by Goula et al. [72]. The

catalytic tests were performed with S/E=3, 4.5, 9 and 15 at different values of flow rates and temperatures ranging between 493 and 973 K. They attained full ethanol conversion at temperatures higher than 573 K. At temperatures close to 923 K, hydrogen selectivity up to 95% was obtained; indeed, they noticed that in this temperature region the products mixture was controlled by methane steam reforming (equation **2.12**) and WGS (equation **2.14**) reactions. During their experiments, only traces of acetaldehyde and ethylene were detected and no carbon formation was found, achieving a stable catalyst. Galvita et al. [73, 74] studied ESR over 1 wt.% Pd supported on a porous carbonaceous material. For S/E=8.1 and atmospheric pressure, the catalyst exhibited full ethanol conversion at 600 K and high activity and long-term stability for the decomposition of ethanol into CO, CO_2, CH_4 and H_2.

In the literature, the effect of the noble metal content has also been evaluated. Liguras et al. [58] examined the performance of Rh, Ru, Pt and Pd supported on Al_2O_3, MgO and TiO_2 by changing the metal loading between 0 and 5 wt.%, in the 873-1123 K temperature range. They concluded that for low-loaded catalysts, Rh is the most active and selective noble metal towards hydrogen production. Ru, particularly, and Rh performance improved increasing the metal content which led to higher ethanol conversions and H_2 selectivity. Gucciardi et al. [75] tested Rh/Al_2O_3 catalysts with different Rh loadings (0, 0.2 and 2 wt.% Rh) for ESR at 823 and 923 K under S/E=6 and diluted conditions. The maximum H_2 yield was obtained for the highest Rh-loading and it was nearly negligible for the low-content Rh catalyst, nevertheless ethanol conversion decayed faster on the former (mainly at low temperatures), which was ascribed to coke deposition on the active sites.

Rhodium-based catalysts are the most widely used and its activity has been investigated along with the activity of the support. It should be stressed that the nature of the support may strongly influence the catalytic performance of ESR catalysts and even participate in the reaction by activating certain reactants and by providing new active sites. Furthermore, the strong metal-support interaction prevents metal particle sintering and diminishes the formation of carbonaceous deposits and, consequently, more stable catalysts are obtained.

2.3.1.b Effect of the support

From the investigations of Noronha's group and Idriss of Pt/CeO_2 [76] and Rh-Pd/CeO_2 [63] catalysts, respectively, the main reaction mechanism of ESR over CeO_2-based catalysts was found to start with a dissociative adsorption of ethanol to ethoxy (CH_3CH_2O-) species, which react with the surface and undergo dehydrogenation to form adsorbed acetaldehyde (equation **2.7**). Acetaldehyde may then be oxidized in the presence of hydroxyl groups to adsorbed acetate (CH_3COO-) or acetyl (CH_3CO-) intermediates. Finally, the process follows with C-C bond

scission and acetates suffer demethanation to CH_x groups and carbonate (-CO_3) species which decompose to CO_2. These CH_x groups may then hydrogenate to CH_4 and a fraction decomposes to adsorbed C and H. Ceria (CeO_2) promotion of ethanol dehydrogenation to acetaldehyde rather than dehydration to ethylene is one of the reasons why ceria has been extensively used as a support, but other properties of ceria also make it attractive. Namely, its remarkable oxygen storage/release capacity (OSC) and high oxygen mobility which allow gasification/oxidation of carbon deposits [77]. In addition, noble metals supported on ceria are active for the WGS reaction [78], one of the steps through which ESR proceeds, and the strong metal-support interaction and dispersion of noble metals improve catalysts activity [79].

Noble metals supported on alumina (Al_2O_3) are often used due to alumina chemical and mechanical resistance under reaction conditions, although it is known that acid supports assist ethanol dehydration to ethylene (equation 2.8) at low temperatures, which in turn facilitates the formation of C deposits [52, 80]. Ciambelli et al. [81] carried out temperature programmed desorption (TPD) experiments concluding that under reaction conditions Al_2O_3 is not able to promote desorption of secondary reaction products, poisoning the surface catalyst and hindering the decomposition process, which finally leads to a marked decay in H_2 and CO_2 selectivity. From temperature programmed oxidation (TPO) studies they found that stable carbonaceous species and coke residues formed on both Al_2O_3 and Pt/Al_2O_3. Erdohelyi et al. [82] carried out IR and TPD measurements on Pt, Rh, Pd, Ir and Ru supported on Al_2O_3 and reported that the accumulation of surface acetate species may deactivate the catalytic systems.

Although cerium and aluminum oxides are the most widely used supports, other elements and oxides have also been investigated. ZrO_2, SiO_2, Y_2O_3, C, Nb_2O_5, $MgAl_2O_4$, MgO, TiO_2 and also zeolites have been tested as noble metal supports. Among these, ZrO_2 is the most frequently used due to its large OSC, high oxygen mobility and steam activation. Ceria-zirconia solid solutions have been widely used because the addition of ZrO_2 to the ceria lattice results in enhanced ceria redox properties. Furthermore, its basicity is reduced as the ZrO_2 content increases, its thermal resistance is improved and it also helps to increase metal dispersion [79, 83, 84]. Roh et al. [84] designed Rh/CeO_2-ZrO_2 catalysts in order to attempt to kinetically control H_2 selectivity against CH_4 formation by increasing the metal-support interaction. Diagne et al. [55] investigated the performance of Rh supported on CeO_2, ZrO_2 and Ce-Zr solid solutions for ESR under S/E=8. At 673 and 773 K the catalysts showed similar behavior with respect to H_2 production with values close to thermodynamic equilibrium; the main difference noticed was in CO_2 and CO distribution which was found to be sensitive to reaction temperature and to the relative amount of ZrO_2 and CeO_2. Interestingly, they performed temperature programmed reductions (TPR) experiments finding large variations of

Rh dispersion between all catalysts and concluding that this had a small effect on H_2 production. Birot et al. [83] achieved the best performance (highest hydrogen yield and less coke deposition) for a 1 wt.% Rh/$Ce_{0.5}Zr_{0.5}O_2$ catalyst under S/E=4 without carrier gas at 873 K, which produced up to 3.63 moles of H_2 per mole of ethanol. The inclusion of ZrO_2 to alumina supports has also been tested and its presence led to the detection of smaller amounts of acetate species. From diffuse reflectance infrared Fourier transform spectroscopy (DRIFTS) and TPD experiments, Dömök et al. [57] concluded that the formation of H_2, CO_2 and CH_4 increased as the zirconia content of the catalyst increased. The previous supports have also been combined and supports based on CeO_2/Al_2O_3 and CeO_2-ZrO_2/Al_2O_3 have been investigated. Peela et al. [85] obtained that Rh/CeO_2/Al_2O_3 showed higher activity and selectivity than Rh/Al_2O_3 for ESR under S/E=6 at temperatures ranging from 673 to 873 K. De Rogatis et al. [86] synthesized Rh/$Ce_{0.2}Zr_{0.8}O_2/Al_2O_3$ nanocomposites and characterized and tested them for ESR. These materials favored methane formation at moderated temperatures while they also inhibited the formation of ethylene and acetaldehyde, contrary to the behavior of their counterpart without the ceria-zirconia solid solution. Roh et al. [87] studied Rh-based catalysts dispersed over various supports: 1 wt.% Rh supported on Al_2O_3, $MgAl_2O_4$, ZrO_2, and ZrO_2-CeO_2 were tested for ESR at T<723 K. The catalytic activity exhibited followed the order: Rh/ZrO_2-CeO_2>Rh/Al_2O_3>Rh/$MgAl_2O_4$>Rh/ZrO_2. Moura et al. [88] tested Rh supported on different oxides, namely, alumina, magnesia and Mg-Al oxide obtained from hydrotalcite; and attained that magnesium-containing catalysts showed low ethane selectivity and high H_2 selectivity.

2.3.1.c Promoters

To improve the performance of the catalysts and block coke deposition different dopants have been tested. Dömök et al. [89] incorporated K (up to 0.4 wt.%) into Pt/Al_2O_3, which was found to destabilize surface acetate groups; the ESR activity and stability were improved proportionally to the K content. De Lima et al. [90] incorporated Sn into Pt/CeO_2 achieving improved stability. Yaseneva et al. [91] doped a CeO_2-ZrO_2/Al_2O_3 support with La, Pr and Sm. The general formula of the catalysts tested was: M/$Ce_xZr_{1-x}Y_{1-2x}O_2/\gamma$-$Al_2O_3$, Y=(La,Pr,Sm) and the metals supported were M= 7 wt.% Cu, 1.4 wt.% Pt or Ru, 10 wt.% Cu-Ni or Cu-Ni-Cr (x=0.5-0.35). The authors expected that incorporation of low-valence cations (such as La, Gd, Pr) into the lattice of ceria-zirconia solutions stabilizes it and improves the lattice oxygen mobility, as previously reported by [92]. Their results showed that Ru-containing catalysts doped with Sm were the most effective while among the Pt-based ones, La-doping led to the most active catalyst. Can et al. [93] and Le Valant et al. [94] added 10 wt.% Sc, Y, La, Er and Gd to 1 wt.% Rh/Al_2O_3 catalysts. On these modified supports, the dehydration reaction, leading to olefins which are coke precursors, was disfavored and consequently the ethanol conversion and the hydrogen yield were increased. Le Valant et al. emphasized

that the addition of rare earth elements instead of magnesium to alumina supports leads to a rearrangement of the acidity and basicity of alumina [94]. The higher hydrogen production was achieved with Rh/Y-Al_2O_3, which was found to be the less acidic support and one of the most basic supports performing IR spectroscopy of adsorbed pyridine and CO_2.

2.3.1.d Impurities in the feed mixture

It is well-known that the presence of some impurities, such as sulfur, in the feed mixture may poison the active sites of the catalysts. Duprez's group has done extensive research on the addition of impurities to pure ethanol-water mixtures in order to simulate raw bioethanol, which is of major importance for a cost effective industrial application [94–96]. Raw bioethanol contains higher alcohols and also aldehydes, amines, acids and esters. Over Rh/$MgAl_2O_4$, esters, ethers, acetic acid, ethylacetate, C_4 alcohols and branched alcohols had a poisoning effect on the catalyst which was strongly deactivated after only 2h on-stream due to coke production. Simson et al. [66] studied 4 wt.% Rh-Pt on a zirconia-based support for the SR of E85 with and without sulfur. The tests performed showed that full ethanol and gasoline conversion and equilibrium concentrations of H_2, CO_2, CO and CH_4 could be achieved with the S-free mixture for at least 110 h of performance. In the presence of only 5 ppm of S, after 22 hours on-stream the catalyst underwent a strong deactivation. After TPO analysis, the authors concluded that large carbon deposits were formed, demonstrating that sulfur promotes C formation and was responsible for catalyst deactivation.

Although this Thesis is focused on the study of noble metal-based catalysts, a brief review of other metallic systems commonly used for ESR is given in next sections [39].

2.3.2 Nickel catalysts

Nickel-based catalysts are the most frequently used in reforming reactions due to its C-C bond cleavage capability and low cost. In contrast to noble metals, ESR over Ni-based catalysts takes place at moderate temperatures, even though the reaction mechanism over Ni-based catalysts follows the same steps as over noble metals-based catalysts [97,98]. It has been generally observed that their selectivity to hydrogen is increased at increasing temperatures, steam-to-ethanol ratio and Ni loading [99–101]. The major drawbacks of Ni-based catalysts are that under ESR conditions Ni particles tend to sinter and they are vulnerable to carbon deposition, which finally deactivate the catalysts. As in the case of noble metal-based catalysts, several promoters have been added to Ni-based catalysts in order to circumvent these inconveniences.

Copper is the most efficient dopant to promote hydrogen production [102]. Copper species are active for the WGS reaction to produce hydrogen and avoid growth of Ni particles [103]. The effect of Mo has also been studied and was found that it reduces the interaction between Ni particles and the alumina support, increasing the reducibility of Ni species and preventing the growth of Ni particles [104]. Calcium and Mg have also been added to neutralize alumina acid sites, which prevents ethylene formation and thus coke deposition [105].

2.3.3 Cobalt catalysts

Cobalt-based catalysts are less active for ESR than noble metals-based catalysts, but they are cheaper and very selective to H_2 and CO_2 generation. Since the reforming temperature can be as low as 623 K, the WGS reaction, which occurs simultaneously with the reforming process, is promoted. As a consequence, CO concentration is kept low and high H_2 yields are achieved. In addition, the ESR reaction mechanism over cobalt-based catalysts follows different paths than over noble metal-based catalysts and methane is not an intermediate of the reforming process. Therefore, the high temperatures required for MSR are not necessary.

Over cobalt-based catalysts, ethanol is first adsorbed to yield ethoxy species, which undergo dehydrogenation and transform into acyl species (rate-determining step [106]) which, in turn, react with activated water to yield hydrogen and carbon oxides. Methane is a secondary product formed through the methanation reaction [107]. Carbonates are formed at the surface of the catalyst and also carboxylates are detected, which are believed to be spectator species. Dimethyl ketone can also be formed via condensation of acetaldehyde. A complete network of reactions can be found in Song et al. [108]. The mechanism of the ethanol reforming reaction is accompanied by a simultaneous transformation of the cobalt phase. High resolution transmission electron microscopy, X-ray diffraction (XRD), Raman spectroscopy and *in situ* magnetic measurements showed that Co_3O_4 is active for ethanol dehydrogenation and it is progressively reduced by the hydrogen generated during the first step of the reaction to CoO and metallic Co [109]. The same transformation has been shown to occur over Co/CeO_2 by using *in situ* XRD, controlled-atmosphere X-ray absorption fine structure and X-ray photoelectron spectroscopy [110]. Once metallic cobalt is formed, the catalyst becomes very active for the ESR and the hydrogen yield increases sharply. However, a consequence of this reaction scheme is that extensive carbon deposition occurs under reaction conditions upon formation of metallic cobalt nanoparticles [111], which certainly constitutes the major drawback of cobalt-based catalysts.

2.4 From words to action

This Part is dedicated to hydrogen generation via ethanol and bioethanol steam reforming for energy applications. Thus highly active, selective and especially stable catalysts under operation conditions are required.

From the literature review, the catalysts chosen to develop in this Thesis are composed of a bimetallic active phase of Rh-Pd nanoparticles supported on ceria.

2.4.1 Objectives of Part I

The specific objectives of the present Part are:

1. To synthesize RhPd/CeO_2 catalysts suitable for the ethanol steam reforming to produce H_2.
2. To characterize powdered and structured catalysts synthesized to assure a successful synthesis method.
3. To evaluate the catalytic performance of the developed RhPd/CeO_2 catalysts for the ethanol steam reforming reaction under realistic operational conditions.
4. To investigate the stability under practical ethanol steam reforming conditions of the RhPd/CeO_2 catalysts that attain the best ESR performance.
5. To study the interaction between the RhPd active phase and the CeO_2 support.
6. To study the reorganization of RhPd nanoparticles and the CeO_2 support driven by the exposure to different reactive environments.
7. To investigate the performance of RhPd/CeO_2 catalysts coupled to a metallic membrane to generate pure-hydrogen streams.
8. To investigate the miniaturization of the H_2 generation scale for small-scale applications using silicon microreactors.

3 Synthesis of $RhPd/CeO_2$ catalysts

In this Thesis, structured catalysts have been used to study the catalysts reaction performance due to the advantages that they offer over pellets or powdered catalysts, as already explained in the Introduction (section **1.5**).

The monolithic structures used are cordierite ($2MgO{\cdot}5SiO_2{\cdot}2Al_2O_3$) honeycombs of 1.8 cm in diameter and length with a channels density of 400 cells per square inch (cpsi). They were obtained by cutting larger commercial pieces from Corning Celcor©. The channels' walls were functionalized in two steps: first ca. 250 mg of cerium dioxide were used to develop a thin layer coating the channels' walls (following the so-called washcoating method) where Rh-Pd nanoparticles were subsequently anchored or grown.

3.1 Ceria support

Ceria was prepared from an aqueous solution of $CeCl_3{\cdot}7H_2O$ (99%, Alfa Aesar) by adding ammonia (28% NH_3, Alfa Aesar) dropwise to adjust the pH to 10. The precipitate was then filtered and washed with deionized water 5 times (each time using the same volume as for the aqueous solution) and dried for 2 hours at 383 K followed by calcination at 873 K (2 K/min) for 4 hours. In parallel, a binder solution of polyvinyl alcohol (PVA) was prepared following the procedure reported elsewhere [112]: 1.25 g of PVA (5 wt.%) (99+% hydrolyzed, Sigma-Aldrich) were added to 25 g of deionized water under continuous stirring and mild heating. 1 wt.% of acetic acid (99-100%, Riedel-deHaën) was added after 5 minutes under stirring and the mixture was aged overnight. The CeO_2 powder was then added to the PVA solution and was left overnight under stirring. Finally, the cordierite honeycombs were immersed in the CeO_2-containing solution and dried under axial rotation for 2 hours at 353 K and at 383 K. The process ended with a calcination at 873 K (2 K/min) for 4 hours. The monoliths coated with CeO_2 are referred to as **CeO_2//Mon**. This process is schematized in figure **3.1**.

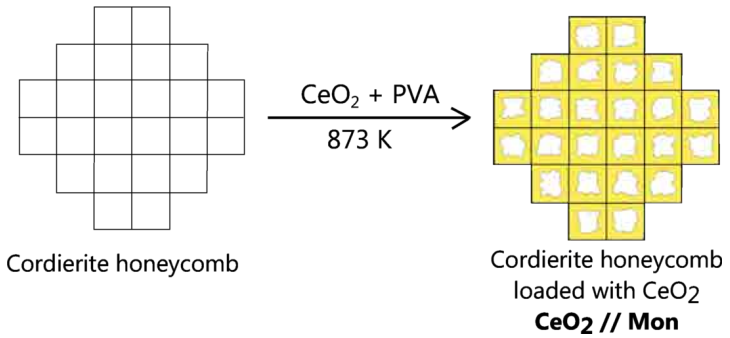

Figure 3.1: Schematic representation of the CeO_2 layer development over the cordierite channels.

3.2 RhPd nanoparticles

Three types of RhPd nanoparticles (NPs) were investigated:

1. Grown from $RhCl_3$ and $PdCl_2$ (99.9% Sigma-Aldrich, salt precursors).
2. Preformed RhPd nanoparticles encapsulated in dodecanethiol ligands.
3. Preformed Pd nanoparticles with Rh-functionalized ligands.

RhPd-based catalysts for the ethanol steam reforming reaction were first reported in a work by Idriss et al. [63]. In this work the authors tested RhPd/CeO_2 catalysts with several Rh:Pd ratios. Rhodium concentration was fixed at 0.5 wt.% and different Pd concentrations were tested: 0, 0.5, 1 and 2 wt.%. The authors obtained an optimum performance in terms of hydrogen yield at x=0.5 wt.% Pd, i.e, at Rh:Pd=1. They found that hydrogen selectivity steadily increased as Pd concentration increased, but the activity decreased considerably when Pd was present in excess. This gave direct evidence that H-H recombination reaction became more efficient in the presence of increasing amounts of Pd, but then ethanol conversion dropped. As a consequence, based on these previous results in this Thesis, the Rh:Pd ratio was fixed at 1 for all the synthesized catalysts, except for catalysts containing preformed Pd NPs with Rh-functionalized ligands, where the Rh:Pd ratio was predetermined to Rh:Pd=1.3/75 by the synthesis method.

Both types of preformed NPs were synthesized at the Dendrimers & Molecular Polygons Group (Department of Inorganic Chemistry of the Universitat de Barcelona). The RhPd NPs protected with dodecanethiol ligands were synthesized using a variation of a previously reported procedure [113] followed by an extraction process with dodecanethiol in toluene [114]. Synthesis details are reported elsewhere [115]. This method led to a bimetallic RhPd core (Rh:Pd=1:1) surrounded by dodecanethiol ligands, as schematically represented in figure 3.2a. The final

result of this synthesis process is a toluene solution with dispersed preformed RhPd NPs. These NPs are referred to as **RhPd@D**. On the other hand, the preparation procedure of Pd cores encapsulated in Rh-terminating ligands, which are are identified as **Pd@Rh**, is reported in [116]. In short, metallic Pd cores were encapsulated in hexanethiols functionalized with phosphine ligands, where metallic Rh was subsequently anchored. The resulting Pd@Rh NPs are schematically represented in figure 3.2b. The weight ratio between Rh and Pd of Pd@Rh NPs was Pd:Rh=75/1.3. These NPs were also suspended in toluene.

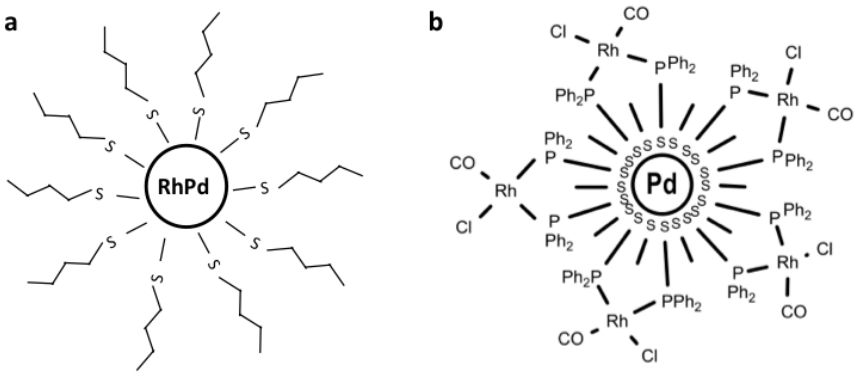

Figure 3.2: Scheme of preformed RhPd nanoparticles: a) encapsulated in dodecanethiol ligands: RhPd@D NPs; b) encapsulated in Rh-functionalized ligands: Pd@Rh NPs.

3.3 RhPd/CeO_2 catalysts

Preformed RhPd NPs were deposited on the ceria-coated monoliths by incipient wetness impregnation from the toluene solutions containing either RhPd@D or Pd@Rh NPs. The NPs synthesized from salt precursors ($RhCl_3$ and $PdCl_2$) were deposited on CeO_2 by incipient wetness impregnation of a $PdCl_2$ and $RhCl_3$ 0.012 M in acetone+water solution (Rh:Pd=1).

Once the noble metals were impregnated over the CeO_2 layer, the functionalized monoliths were dried under axial rotation at 353 K for 2 hours and subsequently calcined at 573 K (2 K/min) for 6 hours. The purpose of this final thermal treatment was: (i) to eliminate the organic ligands that surrounded the metallic cores (case of preformed RhPd@D or Pd@Rh NPs), leaving the noble metals exposed to reactants and (ii) to form the metal-support interaction, as depicted in figure 3.3.

The noble metals deposition on the CeO_2 layer, which is the final step of monoliths functionalization, is schematically represented in figure 3.4. The nomenclature of the resulting samples is given.

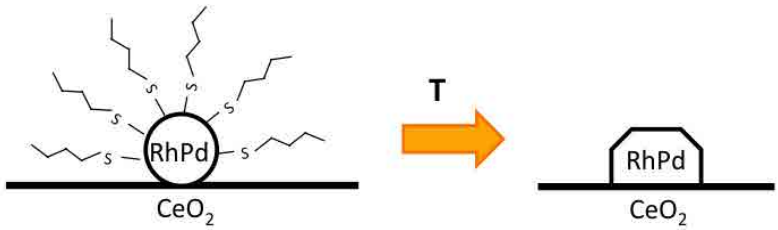

Figure 3.3: Schematic representation of the thermal treatment performed on preformed RhPd@D and Pd@Rh NPs.

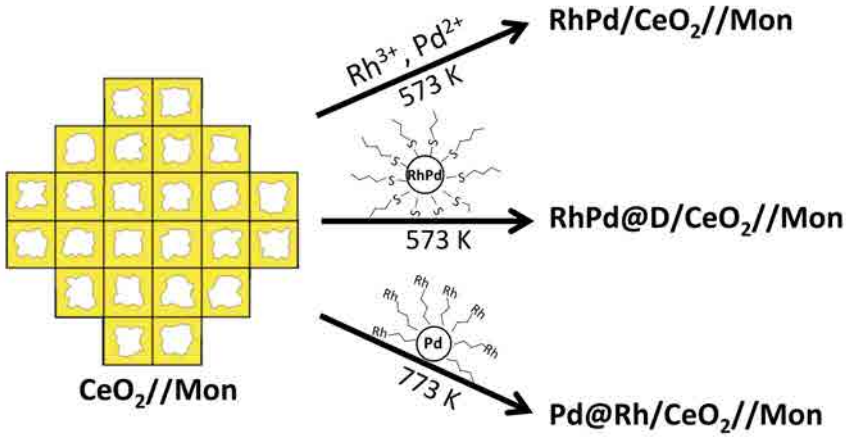

Figure 3.4: Scheme of RhPd loading into ceria-coated monoliths as prepared in this work and nomenclature of the resulting RhPd/CeO_2 catalysts.

The result of the cordierite monoliths coating process can be seen in figure **3.5**; the monolith on the left is a fresh cordierite monolith and the monolith on the right is coated with RhPd/CeO_2 catalyst. The washcoating method led to the formation of a very homogeneous catalytic layer successfully deposited over the monoliths' walls.

In order to be able to characterize in great detail the synthesized catalysts, the unsupported counterparts of these samples were also synthesized in powder form. Exactly the same catalysts were prepared without the cordierite honeycomb substrate. For these samples, once the CeO_2 powder was synthesized, the noble metals were directly anchored to it by using the incipient wetness method described above.

Several noble metals loadings were studied, which are indicated by the number preceding the element symbol of the active phase. For instance, the nomenclature of a ceria-catalyst containing 0.5 wt.% Rh + 0.5 wt.% Pd is: 1RhPd/CeO_2.

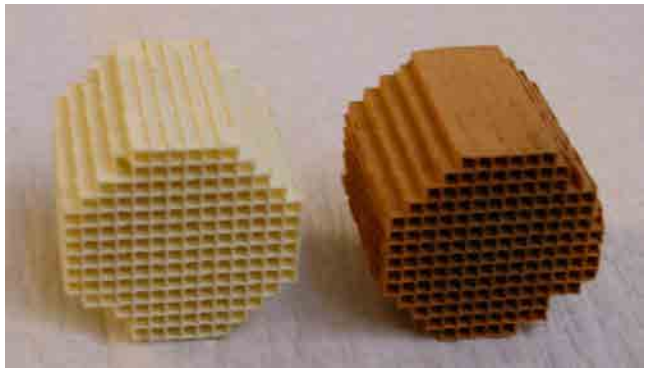

Figure 3.5: Left: Picture of a fresh cordierite monolith. Right: Cordierite monolith coated with RhPd/CeO_2 (sample: RhPd/CeO_2//Mon). The diameter of the monoliths is 1.8 cm.

In addition, the performance of the RhPd/CeO_2 system was also evaluated in a Si-based microreactor. Details concerning the Si micromonolith functionalization, characterization and catalytic performance are described in Chapter 8. The substrate used in this case was a silicon micromonolith and thus this sample is referred to as **RhPd/CeO_2//Si**.

Table 3.1 lists the nomenclature of the different RhPd/CeO_2 catalysts used throughout this Thesis.

Table 3.1: List of synthesized RhPd/CeO_2 catalysts.

Sample ID	Noble metal precursor	Substrate
RhPd/CeO_2//Mon	$RhCl_3$, $PdCl_2$	CM*
RhPd@D/CeO_2//Mon	Preformed RhPd@D NPs	CM
Pd@Rh/CeO_2//Mon	Preformed Pd@Rh NPs	CM
CeO_2//Mon	-	CM
RhPd/CeO_2	$RhCl_3$, $PdCl_2$	-
RhPd@D/CeO_2	Preformed RhPd@D NPs	-
Pd@Rh/CeO_2	Preformed Pd@Rh NPs	-
RhPd/CeO_2//Si	$RhCl_3$, $PdCl_2$	SiM**

*CM: Cordierite monolith. **SiM: Silicon micromonolith.

4 Characterization before reaction of $RhPd/CeO_2$ catalysts

Prior to the catalytic activity evaluation of the synthesized catalysts, a detailed characterization study of the samples was performed to analyze their morphology, crystalline structure, particle size distribution, noble metals dispersion and oxidation state, as these properties are key factors for catalytic activity. The catalysts' properties were investigated by using different techniques, namely X-ray diffraction, scanning and transmission electron microscopies (also on high resolution mode) and X-ray photoelectron spectroscopy. The surface area and pores distribution was also measured.

4.1 Ceria support

4.1.1 Crystalline structure

X-ray diffraction allows for the identification of crystalline phases and determination of crystallite size, which depends on the width of the diffraction peaks. In this Thesis, X-ray diffraction (XRD) was only used to identify the crystalline structure of the synthesized powders, since the mean particle size was accurately obtained from electron microscopy analyses.

Ceria has a fluorite-type (CaF_2) structure, which belongs to the $Fm\bar{3}m$ symmetry group. In the face-centered cubic (fcc) structure of CeO_2, Ce^{4+} ions occupy the fcc sites (forming a cubic close packing arrangement), while tetrahedral sites are occupied by the oxide ions, as depicted in figure 4.1 [79].

The XRD pattern of our synthesized CeO_2 powder was acquired at beamline X7B of the National Synchrotron Light Source (Brookhaven National Laboratory, BNL), during a PhD stay. The enormous brightness of synchrotron light allowed for acquiring the diffractogram in only 8 seconds with very high resolution as seen in figure 4.2, where sharp and well-defined peaks can be distinguished. By using

Bragg's law (equation **4.1**), the corresponding interplanar distance d_{hkl} of each peak was calculated. The d-spacings obtained were 3.12 Å, 2.71 Å, 1.91 Å and 1.63 Å, which were indexed to (111), (200), (220) and (311) planes of the ceria fcc structured, thus confirming the synthesis of ceria fluorite.

$$2d_{hkl}sin\theta = n\lambda \tag{4.1}$$

where d_{hkl} is the interplanar spacing, θ corresponds to the peak position and λ is the wavelength used to obtained the diffractogram; in this case, λ=0.3196 Å.

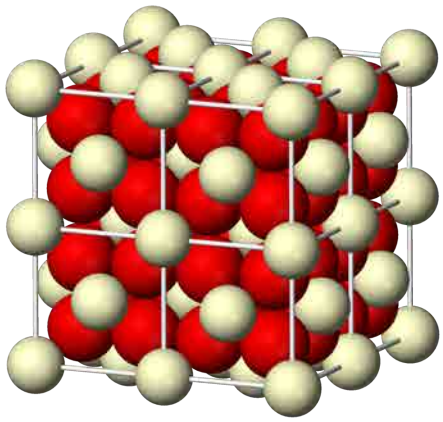

Figure 4.1: Ceria fluorite structure.

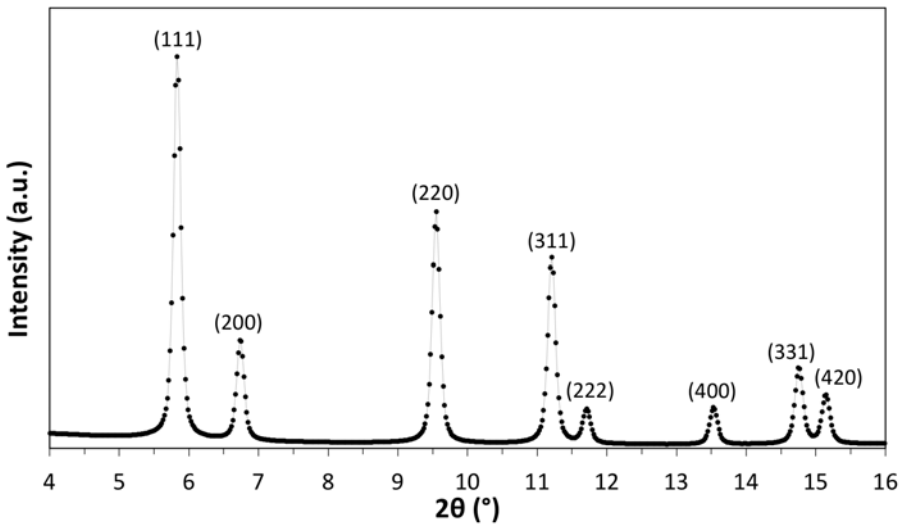

Figure 4.2: Ceria X-ray diffraction pattern acquired with λ=0.3196 Å. The corresponding indexes of the planes are shown.

4.1.2 Porosity

Nitrogen adsorption/desorption isotherms of the CeO_2 powder were measured to obtain quantitative data on surface area and mean pore diameter following BET (Brunauer, Emmett and Teller) [117] and BJH (Barrett, Joyner and Halenda) [118] models, respectively. The measurements were carried out at the Laboratory of Supercritical Fluids sited at MATGAS (Cerdanyola del Vallès). The BET surface area obtained was 36 ± 1 m^2/g and the average pore diameter was 8.7 nm.

4.2 Preformed RhPd nanoparticles

This section describes the characterization of preformed RhPd NPs, i.e., RhPd@D and Pd@Rh synthesized at the University of Barcelona. It is not possible to study unsupported RhPd NPs synthesized from $RhCl_3$ and $PdCl_2$, therefore these NPs are only described when they are supported on CeO_2 (section **4.3.1**).

4.2.1 RhPd@D: RhPd cores protected with dodecanethiols

Transmission electron microscopy (TEM) allows for particle size and morphology determination from direct observation of the samples. The TEM particle size is the diameter of the particles directly measured in the TEM images. Around 100 particles have to be analyzed to perform a statistical analysis and obtain the mean particle size and its distribution. In addition, in high resolution transmission electron microscopy (HRTEM), the electrons diffracted by the sample are used to form the image and, consequently, the crystalline structure of the samples can be studied measuring the distance between the lattice fringes formed in the image, which correspond to the interplanar distances d_{hkl}. As a result, the crystallographic structures (if any) of the samples can also be investigated.

Figure **4.3** shows representative HRTEM images of preformed RhPd@D NPs. The mean particle size of RhPd@D NPs, which was determined by statistical analysis, is 4 ± 1 nm.

A detailed HRTEM study of single RhPd@D NPs allowed to conclude that Rh and Pd coexisted in the NPs constituting and alloy. Single RhPd@D NPs, as the ones shown in figures **4.4**a and **4.4**c, were studied. Their corresponding Fourier transform (FT) images (figures **4.4**b and **4.4**d, respectively) exhibited spots which could be common to both Rh and Pd fcc at 2.23 Å and 1.93 Å. The interplanar distances of Rh and Pd fcc are very close: Rh fcc shows spots at 2.20 and 1.90 Å and Pd fcc at 2.24 and 1.95 Å. Therefore, it was not possible to unambiguously ascribe each reflection to one metal or the other. However, interestingly in the FT image shown in figure **4.4**d the forbidden reflections of Rh and Pd fcc $(0\bar{1}1)$ and $(2\bar{1}1)$

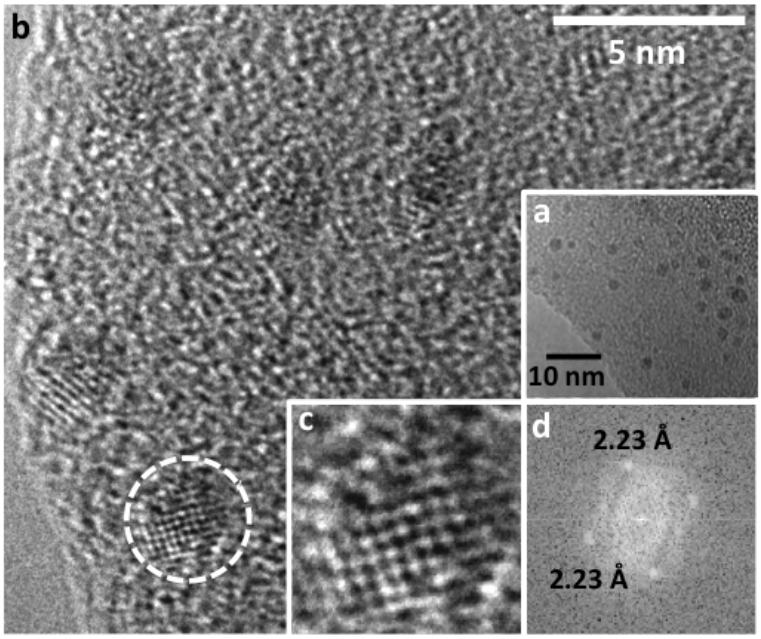

Figure 4.3: Representative HRTEM images of preformed RhPd@D NPs. a) and b) low-magnification images of RhPd@D NPs. c) Detail of the encircled NP in b). d) Corresponding Fourier transform image of the NP shown in c), showing spots at 2.23 Å.

were also visible. In figure 4.4d, forbidden reflections are marked with squares. This result indicated that the fcc lattice contained two different atomic species (Rh and Pd), which led to a symmetry disruption and, thus, forbidden reflections were made visible. Figures 4.4f and 4.4g show the reconstructed images obtained from the FT shown in figure 4.4d: figure 4.4f was reconstructed considering the spots of the fcc structure (marked with circles) and figure 4.4g was reconstructed taking into account also the extra spots (marked with squares). From the results of the reconstructed images, it is possible to conclude that the forbidden reflections must be considered in order to reproduce the raw image shown in figure 4.4e. In addition to these analyses, it has been recently reported that reflections at 1.93 and 2.23 Å of RhPd NPs can be indexed to the (200) and (111) planes of a RhPd alloy [119]. Therefore, the synthesis route used led to bimetallic alloyed NPs of Rh and Pd of 4 ± 1 nm in diameter.

Preformed RhPd@D NPs were used to model RhPd NPs, because RhPd@D NPs synthesis route led to NPs with well-defined and reproducible properties. These properties offered advantages over RhPd NPs synthesized from salt precursors for characterization purposes since:

1. RhPd@D NPs have controlled size and are monodisperse due to their synthesis method.

2. RhPd@D NPs are larger than NPs synthesized from salt precursors.

3. RhPd@D NPs synthesis route always led to NPs composed of both Rh and Pd atoms.

Therefore, these RhPd@D NPs model RhPd NPs systems and are referred to as *model* RhPd NPs.

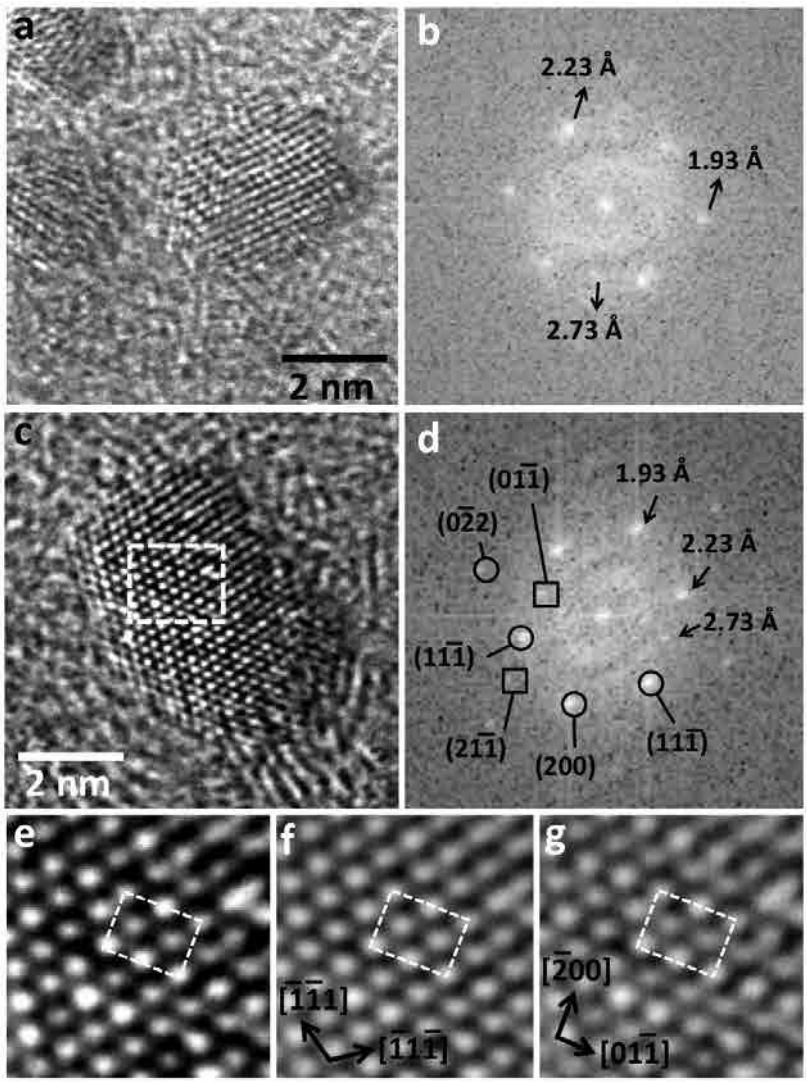

Figure 4.4: a) and c) HRTEM images of representative preformed RhPd@D NPs. b) and d) FT images of the NP shown in a) and c), respectively. In d) the spots marked with circles correspond to fcc reflections; spots marked with squares correspond to forbidden fcc reflections. e) Detail of the region of the NP enclosed in c). f) and g) reconstructed images of d) taking into account fcc reflections and forbidden reflections, respectively.

4.2.2 Pd@Rh nanoparticles

The Dendrimers & Molecular Polygons Group (UB) characterized the preformed Pd@Rh NPs by using nuclear magnetic resonance and thermogravimetric analyses (TGA) to corroborate a successful synthesis, as described in [116]. TGA analyses revealed an initial 10% mass loss at 483 K and at temperatures higher than 773 K the NPs did not experience any further removal of the organic shell. Additionally to this characterization, TEM analyses were performed in order to study particle size uniformity and particles dispersion and composition. The average diameter of Pd@Rh NPs determined by TEM analyses was 2.5 ± 0.5 nm. Figure 4.5a shows a low-magnification TEM image were uniform and approximately spherical Pd@Rh NPs can be distinguished. Figure 4.5b shows a higher magnification HRTEM image were some Pd@Rh NPs exhibited lattice fringes at 2.25 Å. The particle shown in the inset (figure 4.5c), exhibited crystallographic planes at 2.25 Å, which corresponded to (111) planes of the fcc crystallographic structure of the metallic Pd core. Pd@Rh NPs were also used to model RhPd NPs, but with a different Rh:Pd weight ratio (Rh:Pd=1.3/75), determined by the synthesis route (see section 3.2).

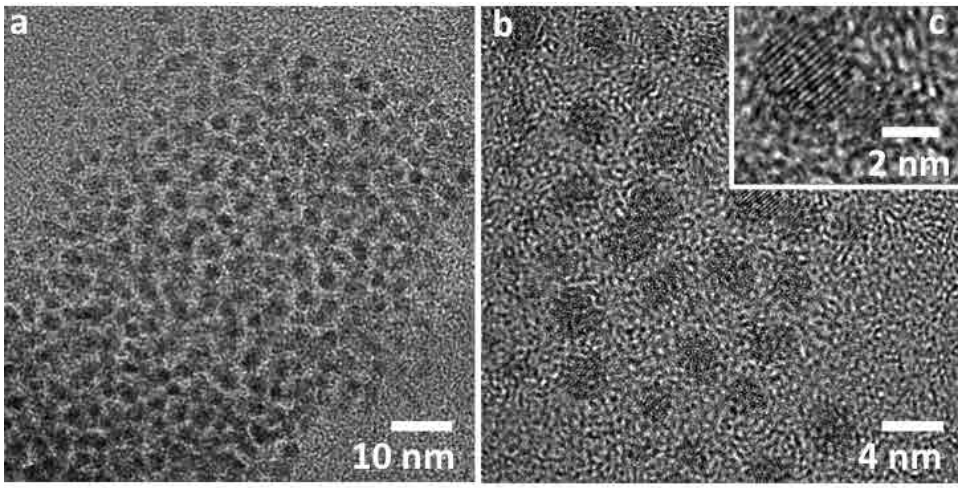

Figure 4.5: Representative TEM images of preformed Pd@Rh NPs. a) Low-magnification image. b) Higher magnification HRTEM image showing Pd@Rh NPs. c) Detail of a Pd@Rh NP exhibiting Pd (111) planes at 2.25 Å.

4.3 Powdered catalysts

Following the characterization of the ceria support and the RhPd NPs separately, the noble metals supported on ceria, constituting real catalysts, were subsequently characterized. These characterization results are discussed in this section.

4.3.1 Working RhPd/CeO_2 catalysts

Initially, the microstructure of a 1RhPd/CeO_2 catalyst (synthesized from $RhCl_3$ and $PdCl_2$) was analyzed by transmission electron microscopy after 10% H_2 reduction at 550 K[1]. Ceria-based catalysts with NPs synthesized from $RhCl_3$ and $PdCl_2$ are referred to as *working catalysts*, in contrast to catalysts composed of *model* NPs, since the ESR reaction performance of the RhPd-CeO_2 system was deeply examined using RhPd/CeO_2 catalysts.

TEM samples of powdered catalysts were prepared by suspending the catalytic powder in ethanol for about 1 minute under ultrasonic treatment. Once the suspension was settled, one drop of it was deposited on a holey carbon-coated grid.

Figure 4.6 shows representative HRTEM images of 1RhPd/CeO_2. HRTEM micrographs showed well-defined ceria crystallites of 10-20 nm with exposed crystallographic planes at 3.12 Å, 2.71 Å, 1.91 Å and 1.63 Å, which were indexed to (111), (200), (220) and (311) planes of the ceria fcc structure, respectively, which was in accordance with the XRD results. Interestingly, Rh and/or Pd NPs were not conclusively identified over the CeO_2 support and it appeared to lack NPs (see images in figure 4.6).

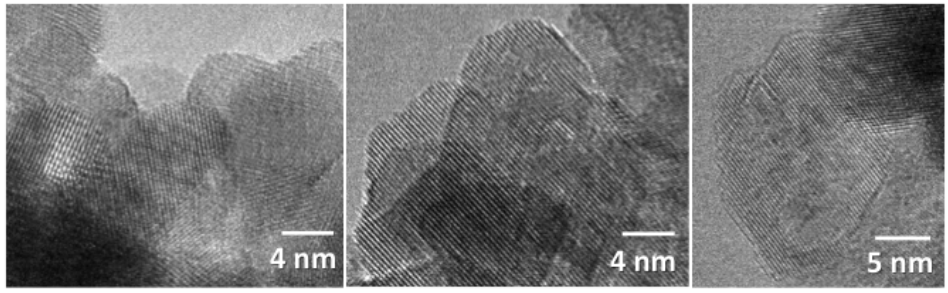

Figure 4.6: HRTEM of different regions of the 1RhPd/CeO_2 catalyst showing CeO_2 crystallites.

Nevertheless, in some areas small dots (of less than 0.5 nm) darker than CeO_2 were found, as seen in figure 4.7a (the dots are marked with arrows). The higher electron contrast exhibited by these dots with respect to ceria led to tentatively ascribe these regions to Rh/Pd metal clusters. Also in profile view these clusters were poorly defined (see figure 4.7b), but remarkably they were concentrated on high Miller index planes ({311} in the image), whereas the more stable {111} planes family did not exhibited these features. This is consistent with the higher energy of {311} planes family of CeO_2 compared with {111}, which are much less reactive [120].

[1]Unless noted otherwise, all the samples, prior to catalytic testing, were activated under 10% H_2 + 90% N_2 stream at 550 K for 1 hour.

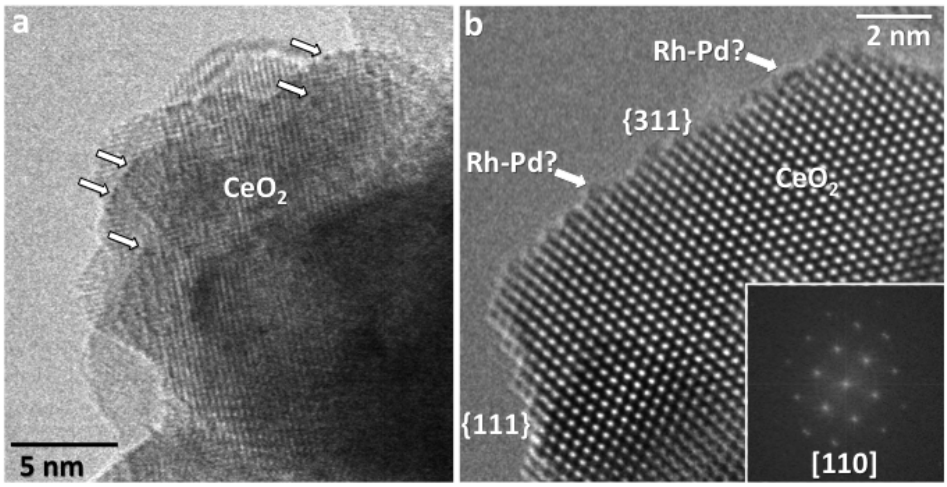

Figure 4.7: HRTEM of different regions of the $1RhPd/CeO_2$ catalyst showing CeO_2 crystallites and, probably, RhPd metal clusters.

The as-synthesized $1RhPd/CeO_2$ catalyst (after the calcination synthesis at 573 K) was studied by means of X-ray photoelectron spectroscopy (XPS). XPS allows for relative concentration determination of surface species as well as for determination of their oxidation states and chemical environment. This analysis was performed to control Rh and Pd surface concentrations. Rhodium 3d, Pd 3d and Ce 3d spectra were acquired and they were calibrated for energy using as a reference the adventitious C signal at binding energy 284.8 eV. Spectra fitting was performed with CasaXPS© software. Rhodium 3d and palladium 3d spectra were deconvoluted constraining the known distance and the areas ratio between $3d_{5/2}$ and $3d_{3/2}$ components of the spin-orbit doublet. Cerium 3d spectrum was deconvoluted using six peaks for Ce^{4+} (V, V", V"', U, U" and U"'), corresponding to three pairs of spin-orbit doublets, and four peaks for Ce^{3+} (V^0, V', U^0 and U'), which correspond to two doublets, based on the peak positions reported by Mullins et al. [121]. U and V refer to the $3d_{3/2}$ and $3d_{5/2}$ spin-orbit components, respectively. This deconvolution allows for the calculation of the Ce^{4+} and Ce^{3+} content; the as-synthesized $1RhPd/CeO_2$ catalyst contained 82% Ce^{4+}. Theoretical Rh 3d, Pd 3d and Ce 3d spectral features and binding energies were extracted from the *Handbook of X-ray photoelectron spectroscopy* [122]. The relative atomic concentration of the detected elements obtained from the spectra fitting are reported in table 4.1.

The mass concentration can also be calculated and these new values are listed in table 4.2. Rh/Ce and Pd/Ce mass ratios showed that both metals were well dispersed over the CeO_2 surface, as these values exceed the theoretical bulk values (0.5 wt.% Rh and 0.5 wt.% Pd). The larger values obtained for Pd than for Rh may indicate that Pd was dispersed forming smaller atomic aggregates than Rh.

Table 4.1: XPS results for the as-synthesized 1RhPd/CeO_2 catalyst.

Relative atomic concentration (%)					Atomic ratio		
Rh	Pd	Ce	C	O	Rh/Ce	Pd/Ce	C/Ce
0.4	1.0	36.0	3.7	58.8	0.01	0.03	0.01

Table 4.2: XPS results for the as-synthesized 1RhPd/CeO_2 catalyst.

Weight relative concentration (%)					Mass ratio		
Rh	Pd	Ce	C	O	Rh/Ce	Pd/Ce	C/Ce
0.8	1.7	81.3	0.7	15.5	0.01	0.02	0.01

A new RhPd/CeO_2 catalyst was synthesized doubling the noble metal loading, i.e., 1 wt.% Rh + 1 wt.% Pd, to facilitate TEM observation. The new sample, 2RhPd/CeO_2, was analyzed by scanning transmission electron microscopy (STEM). STEM (as TEM) also allows for particle size and particle morphology determination from direct observation of the samples. Nevertheless, the high angle annular dark field (HAADF) STEM imaging mode also provides information on elemental composition and electronic structure at the atomic level, as the images are formed by high-angle scattered electrons, thus directly relating the image contrast with the atomic number, Z, of the analyzed area (Z-contrast imaging).

2RhPd/CeO_2 was analyzed by STEM-HAADF at the Center for Functional Nanomaterials (CFN, at BNL) during a PhD stay. The microscope available at the CFN was an HITACHI HD2700C (aberration corrected) STEM-dedicated, which was equipped with an electron energy loss spectroscopy (EELS) detector. This technique did allow for unambiguous NPs detection. RhPd NPs can be identified as the bright dots dispersed on the ceria surface, as clearly seen in figures 4.8a and 4.8b, where well-dispersed RhPd NPs over the ceria support were identified. Ceria crystallites measured 21 ± 4 nm. Figure 4.8c shows the detail of a well-faceted ceria crystallite of 13 x 17 nm oriented along the [110] crystallographic direction.

This technique allowed for NP detection, so the chemical composition of individual RhPd NPs was analyzed by EELS. In EELS the electron energy losses produced by the interaction between incident electrons and the sample are measured, therefore information about chemical composition and oxidation states is obtained. Figure 4.9 shows STEM micrographs of the identified RhPd NPs. The size of RhPd NPs ranged 1-2 nm and most of them did not show an ordered atomic structure. It was also possible to identify few NPs where the atoms arranged in planes (see figure

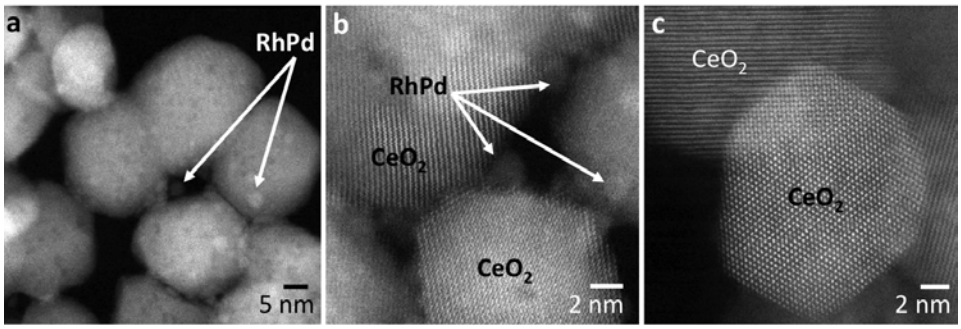

Figure 4.8: STEM images of the 2RhPd/CeO_2 catalyst showing the detail of ceria crystallites decorated with Rh and/or Pd NPs.

4.9e), but in the vast majority of identified NPs, the noble metals were dispersed over CeO_2 forming small aggregates of few atoms without preferred structure.

This is likely one of the reasons why NPs were not detected by HRTEM. The synthesized RhPd NPs did not exhibit crystalline structure and thus no diffraction pattern was formed on the HRTEM imaging mode. On the other hand, the size of the NPs was on the detection limit of the TEM microscope on the bright field imaging mode. The better resolution of the STEM microscope (aberration corrected) and the STEM-HAADF imaging mode made possible to identify NPs deposited over ceria planes with different orientations, not only on high Miller index planes, as initially suggested from the TEM analyses. EELS analyses suggested the bimetallic nature of the NPs, as all the sampled NPs showed Rh and Pd signals, demonstrating that they contained both noble metals.

4.3.2 Model RhPd@D/CeO_2 catalysts

Preformed RhPd@D NPs were anchored to CeO_2 by impregnating 1 g of CeO_2 powder with 2.39 cm^3 of RhPd@D toluene solution ($40 \cdot 10^{-3}$ M), constituting the 1RhPd@D/CeO_2 catalyst. RhPd@D/CeO_2 catalysts (synthesized using preformed or *model* RhPd@D NPs) are identified as *model catalysts*, because they were synthesized using model RhPd@D NPs and constituted a model of working catalysts. Besides, RhPd@D/CeO_2 model catalysts were used for extensive characterization of the RhPd bimetallic system.

1RhPd@D/CeO_2 catalyst was analyzed by HAADF-STEM at the CFN (BNL) using the same HITACHI microscope. In the 1RhPd@D/CeO_2 catalyst only few RhPd@D NPs could be identified. By comparing the images of 1RhPd@D/CeO_2 with the images of 2RhPd/CeO_2 (both samples were analyzed with the same microscope) much less NPs were identified in 1RhPd@D/CeO_2 (see figures 4.10a and 4.10b) than in 2RhPd/CeO_2 (see figures 4.8a and 4.8b), even though the pre-

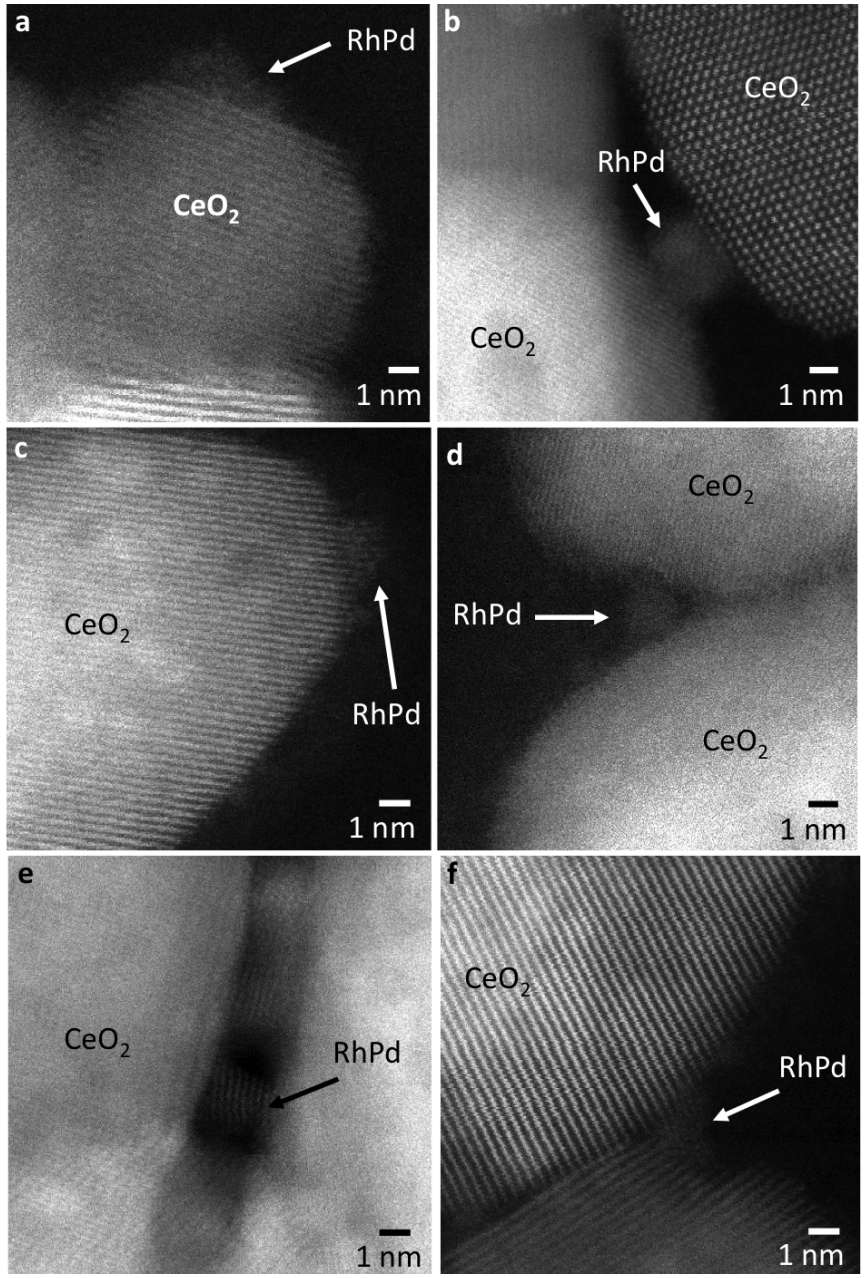

Figure 4.9: STEM images of the 2RhPd/CeO_2 catalyst showing the detail of Rh and/or Pd NPs deposited on ceria crystallites.

formed RhPd@D NPs are larger than the NPs synthesized from $RhCl_3$ and $PdCl_2$ salt precursors. The higher RhPd loading used in 2RhPd/CeO_2 probably helped to identify RhPd NPs. Nevertheless, some RhPd@D NPs could be identified, as seen in figures 4.10c and 4.10d. These figures show two RhPd@D NPs in close contact

with the ceria support. The NP shown in figure 4.10d exhibited planes only at 2.2 Å, which could correspond either to fcc (111) planes of Rh or Pd, thus making it impossible to confirm its bimetallic nature.

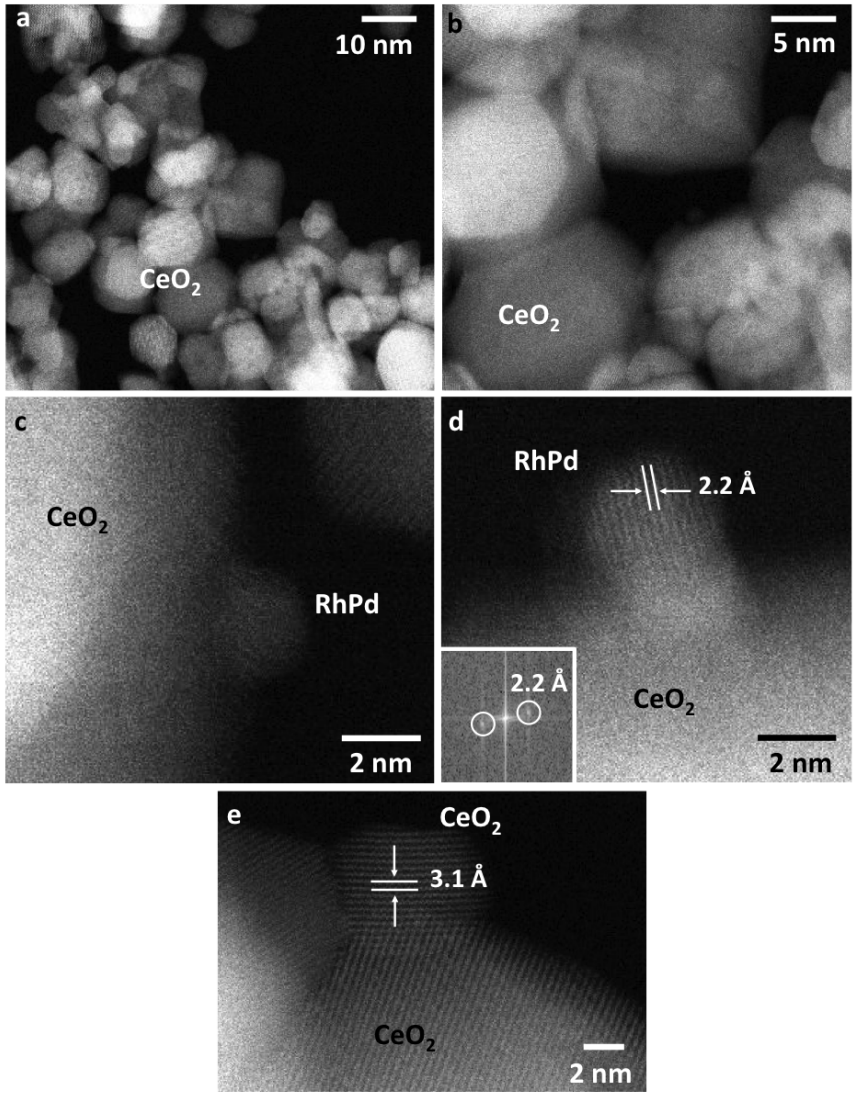

Figure 4.10: STEM images of the 1RhPd@D/CeO_2 catalyst.

In order to confirm that RhPd@D NPs were still bimetallic once they were supported on CeO_2, a new catalyst with higher noble metal loading (1.5% wt. Rh + 1.5% wt. Pd) was synthesized. The new 3RhPd@D/CeO_2 was analyzed by STEM at the Institut Català de Nanociència i Nanotecnologia with a FEI TECNAI F20 S/TEM microscope, equipped with an energy dispersive X-ray (EDX) detector. Figure 4.11a shows a low-magnification STEM image of the new 3RhPd@D/CeO_2

catalyst. The STEM microscope allowed to identify some RhPd@D NPs (see figure 4.11b) and EDX analyses were performed on the individual NPs identified. EDX analyses allowed to confirm the bimetallic nature of the metal particles, as all the sampled NPs showed Rh and Pd signals (see the representative spectrum acquired over a NP shown in figure 4.11c). Therefore, it was possible to conclude that the synthesis route preserved the RhPd alloy that constituted RhPd@D NPs and that NPs maintained their size after deposition on ceria.

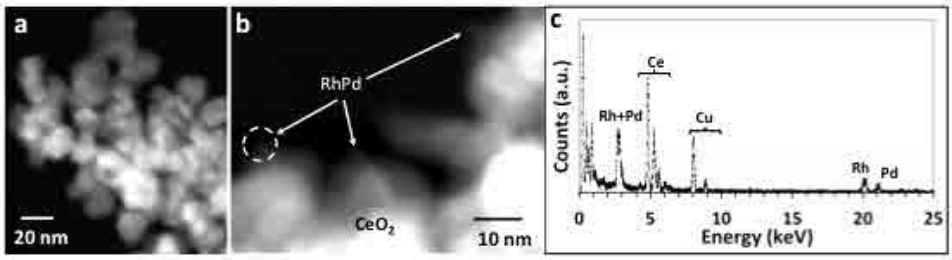

Figure 4.11: STEM images of the 3RhPd@D/CeO_2 catalyst. a) Low-magnification micrograph. b) Three RhPd@D NPs identified. c) EDX analysis performed on the RhPd@D NP encircled in b). The Cu signal seen in the spectrum is due to the Cu TEM grid.

4.4 Functionalized monoliths

The characterization process finished examining by scanning electron microscopy (SEM) the catalytic coatings developed over the cordierite honeycombs' walls following the preparation method described in Chapter 3.

SEM allows for surface topography and composition determination. SEM samples were prepared longitudinally cutting the functionalized monolith such that several inner channels were exposed, as seen in figure 4.12. The insulating monolith was covered with a carbon coating in order to be able to obtain SEM images.

Figure 4.13 shows SEM images of the channels coated with 1RhPd/CeO_2 catalyst. Figure 4.13a shows the detail of a coated channel were a homogeneous and well-developed ceria layer that completely covered the cordierite walls can be seen. Cordierite pores were still visible, thus indicating that the ceria layer deposited was thin enough to maintain cordierite porosity. The higher magnification image shown in figure 4.13b reveals uniform and well-dispersed ceria crystallites of 26 $\pm$ 5 nm. Ceria crystallites covered the whole cordierite surface forming a uniform layer. No cordierite parts without 1RhPd/CeO_2 coating were detected. As expected, RhPd NPs were not identified over the ceria coating, thus confirming the absence of large metal agglomerates.

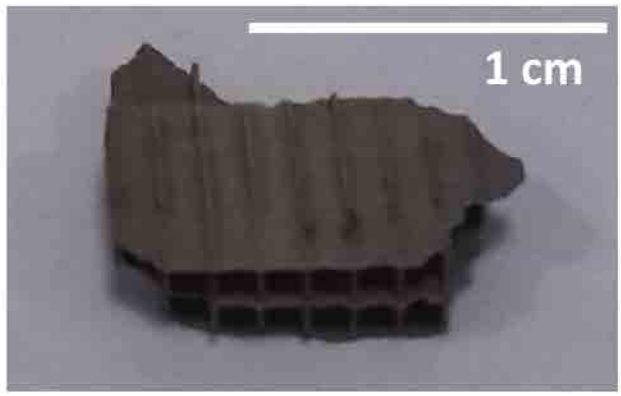

Figure 4.12: Picture of the longitudinal cut performed on a functionalized cordierite monolith.

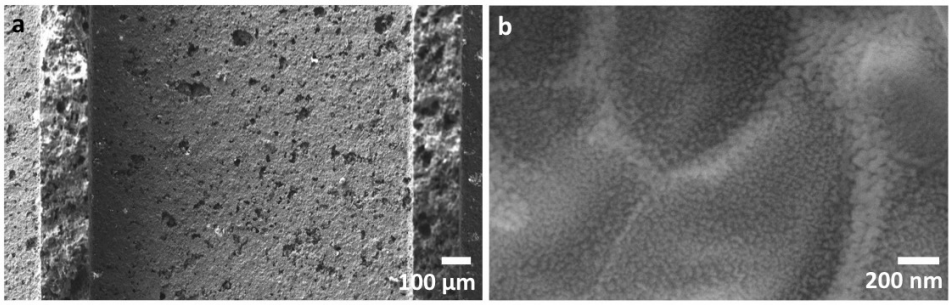

Figure 4.13: SEM images of the inner channels of a monolith coated with $1RhPd/CeO_2$.

After the characterization of the support, the active phases and the functionalized monolith, their catalytic activity was analyzed. Next Chapter (Chapter 5) focuses on the investigation of the catalytic activity of the systems examined along this Chapter.

5 Ethanol steam reforming catalytic tests

5.1 Reaction setup

The ethanol steam reforming reaction performance of functionalized monoliths was evaluated in the lab-scale setup represented in figure 5.1. For catalytic testing, one of the monoliths described in Chapter 3 was fitted in a tubular stainless steel reactor (21 mm internal diameter). The reactor was then placed inside a tubular electric furnace (Carbolite) governed with a PID electronic controller (Fuji PXR4). The liquid ethanol/water mixtures were provided by a HPLC pump (Knauer Smartline) directly from a storage tank. All the tests were carried out under undiluted conditions, i.e., no inert gas was added to the inlet mixture, thus representing practical operational conditions. Upstream the reactor, a three-way valve was installed to switch the inlet mixture to reducing/oxidizing/inert gaseous streams. Heating tapes were used to evaporate the liquid reactants and heat the sections before the furnace. Downstream the reactor, a back-pressure regulator (Swagelok) was placed to set the desired operational pressure. The condensable products of the reformate stream (acetaldehyde, acetone and unreacted water and ethanol) were trapped and the total volumetric flux and the composition of the gaseous outlet stream were subsequently measured.

A gas micro-chromatograph (µGC, Agilent 3000A) equipped with MS 5Å, Plot U and Stabilwax capillary columns and TCD detectors was used to measure online the concentration of the gaseous outlet stream every 5 minutes. The volumetric flux was measured with a bubble soap meter. The outlet molar fluxes of non-condensable components (H_2, CH_4, CO_2, CO) were calculated from the measured composition (by the µGC) and the total volumetric flux of the gaseous outlet stream, whereas the outlet fluxes of ethanol and water were evaluated by closing element balances.

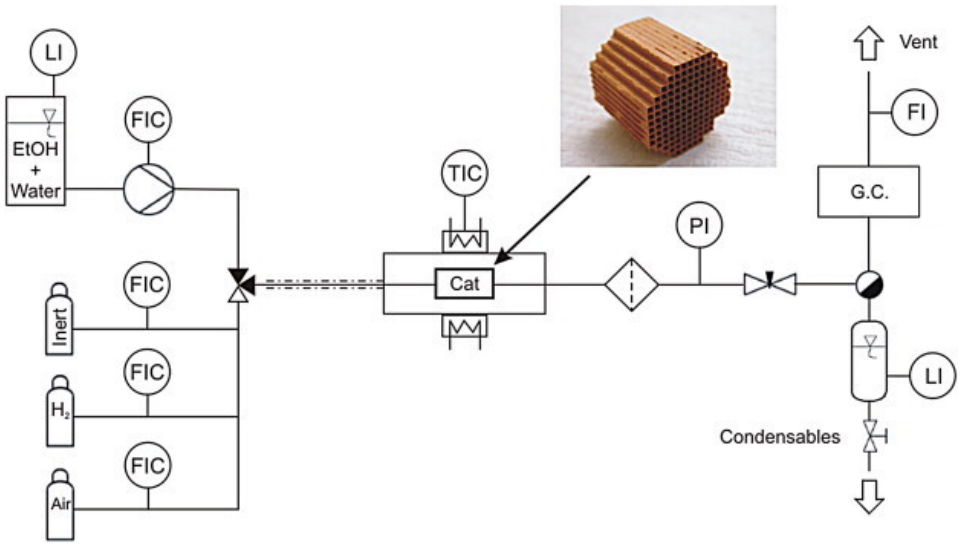

Figure 5.1: Schematic representation of the experimental setup.

5.2 Catalytic activity screening of working $RhPd/CeO_2$ catalysts

The catalytic activity of the RhPd-ceria system was first investigated for *working* $RhPd/CeO_2$ catalysts.

The influence of several reaction parameters on the ESR reaction performance such as reaction temperature, pressure, ethanol/water ratio and residence time were evaluated under steady state conditions. Realistic operational conditions were chosen for reaction evaluation and, once the steady state was achieved, 2-6 measurements were acquired to assure adequate reproducibility. Table **5.1** summarizes the experimental conditions tested.

Table 5.1: Experimental conditions tested.

Temperature (K)	500 - 950
Absolute pressure (bar)	1.5 - 6
Feed load ($\mu L_{liquid}/(mg_{catalyst} min)$	0.21 - 1.08
Feed concentration ($mol_{Ethanol}/mol_{H_2O}$)	1/4 - 1/8
Synthetic ethanol (99.8%, Panreac)	
Commercial bioethanol (*Bioetanol de La Mancha*)	

The review of ESR reaction catalytic pathways (section 2.2) and of the ESR reaction mechanisms proposed over RhPd/CeO_2 catalysts (section 2.3.1.b) allowed to compile the main reactions that may take place on RhPd/CeO_2 catalytic systems. The reaction scheme suggested is presented in the following equations (equations 5.1 - 5.6).

Ethanol decomposition: $C_2H_5OH \longrightarrow H_2 + CO + CH_4$ (5.1)

Ethanol dehydrogenation: $C_2H_5OH \longrightarrow H_2 + CH_3CHO$ (5.2)

Acetaldehyde decomposition: $CH_3CHO \longrightarrow CH_4 + CO$ (5.3)

Water gas shift (WGS) reaction: $CO + H_2O \leftrightharpoons H_2 + CO_2$ (5.4)

Methane SR: $CH_4 + H_2O \leftrightharpoons 3H_2 + CO$ (5.5)

Ethanol dehydration: $C_2H_5OH \longrightarrow C_2H_4 + H_2O$ (5.6)

The ethanol steam reforming performance is discussed in terms of ethanol conversion (χ_{Ethanol}, equation 5.7), hydrogen yield ($\mathrm{Y_{H_2}}$, equation 5.8), products selectivity on dry basis ($\mathrm{S_i}$, equation 5.9), gaseous fluxes ($\mathrm{F_i}$, equation 5.10) and residence time (τ, equation 5.11) or feed load (equation 5.12), as defined in the following equations. The hydrogen yield definition, $\mathrm{Y_{H_2}}$, is normalized by the maximum theoretical moles of $\mathrm{H_2}$ per mole of ethanol fed that can be produced through the ESR reaction (which is 6), so that $\mathrm{Y_{H_2}}$ is defined between 0-1.

$$\chi_{Ethanol} = \frac{\dot{n}_{Ethanol,in} - \dot{n}_{Ethanol,out}}{\dot{n}_{Ethanol,in}} \cdot 100, \quad \text{where } [\dot{n}] = \frac{mol}{s} \tag{5.7}$$

$$Y_{H_2} = \frac{\dot{n}_{H_2}}{6\,\dot{n}_{Ethanol,in}} \tag{5.8}$$

$$S_i = \frac{\dot{n}_i}{\sum_i \dot{n}_i} 100, \quad i = H_2, CH_4, CO_2, CO, ... \tag{5.9}$$

$$F_i = y_i \cdot F_{Total} \tag{5.10}$$

$$\tau = \frac{Reactor\,Volume}{F_{Ethanol,in_{gas}} + F_{H_2O,in_{gas}}} \tag{5.11}$$

$$v_{space} = \frac{F_{inlet\,mixture_{\,liquid}}}{g_{catalyst}} \tag{5.12}$$

5.2.1 Reaction temperature and pressure effect

A 1RhPd/CeO_2//Mon was synthesized to investigate the temperature and pressure effect on the ESR reaction performance at constant feed load and mixture concentration. A cordierite monolith was loaded with 0.245 g of 1RhPd/CeO_2 catalyst, following the methodology described in Chapter 3, which represented a catalyst

loading of 2.4 $mg_{catalyst}/cm^2$. Prior to each screening test, a catalyst activation treatment was performed with 10% H_2 balanced in N_2 at 550 K for 1 hour. Then, the working pressure was fixed and temperature screened from 500 K to 950 K. After that, a new reduction treatment was performed, a new value of pressure was set and temperature was varied again.

The first tests were carried out with ethanol/water mixtures of steam-to-ethanol ratio S/E=6 (molar), which doubles the stoichiometric ratio, and feed load or space velocity v_{space}=0.22 $\mu L_{liquid}/(mg_{cat}min)$, corresponding to 5.8 s residence time. Figure 5.2 shows the influence of the temperature (T) and pressure (P) on ethanol conversion and hydrogen yield.

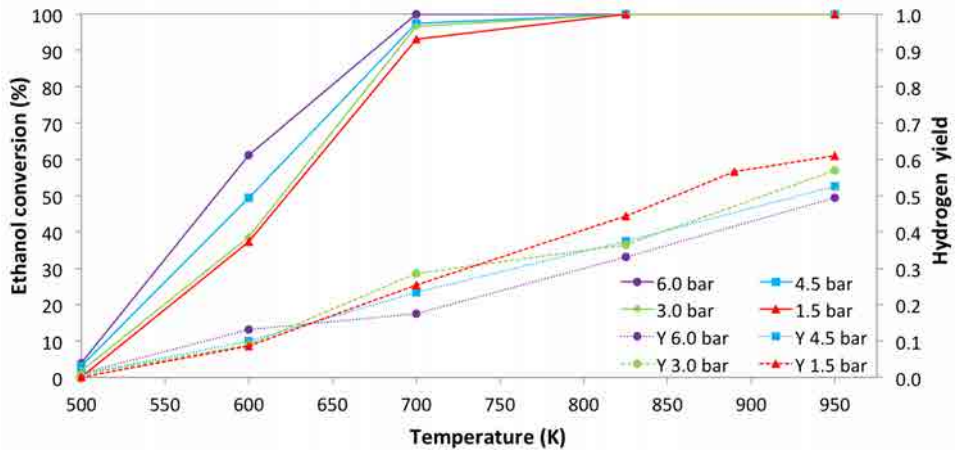

Figure 5.2: Influence of the temperature and pressure on ethanol conversion (solid lines) and hydrogen yield (dashed lines). Experimental conditions: S/E=6 and v_{space}=0.22 $\mu L_{liquid}/(mg_{cat}min)$.

As observed in figure 5.2, for the reaction conditions tested, $\chi_{Ethanol}$ increased as temperature increased and full ethanol conversion ($\chi_{Ethanol}$=100%) was achieved for T≥700 K. At 500 K, almost no ethanol conversion took place, indicating that this temperature was too low to operate ESR. For T=600 K, $\chi_{Ethanol}$ increased as pressure increased and the same trend was observed for the hydrogen yield: higher P rendered higher Y_{H_2}. On the contrary, for reaction temperatures T≥700 K, higher pressures rendered lower Y_{H_2}. This is consistent with two reactions regimes: one at low temperatures (T<700 K), where the reaction was controlled by the kinetics of the reactions, and the other one at T≥700 K, where the thermodynamic equilibrium was reached (for the reaction conditions tested). In the kinetic-controlled zone (pre-equilibrium conditions zone), higher P led to higher $\chi_{Ethanol}$, which is consistent with positive reaction orders of the reaction and thus the reaction rates (r) were $r \propto P^n$, $n \geq 0$. In the equilibrium zone (T≥700 K), where Le Châtelier's principle can be applied, higher pressures prevented higher

methane steam reforming promotion (MSR, equation 5.5) and, as a consequence, lower Y_{H_2} were achieved. The region of ∼700 K is a transition zone between the kinetic control regime and the thermodynamic equilibrium. Figure 5.3 shows the molar fluxes of H_2, CH_4, CO_2 and CO measured for these experiments.

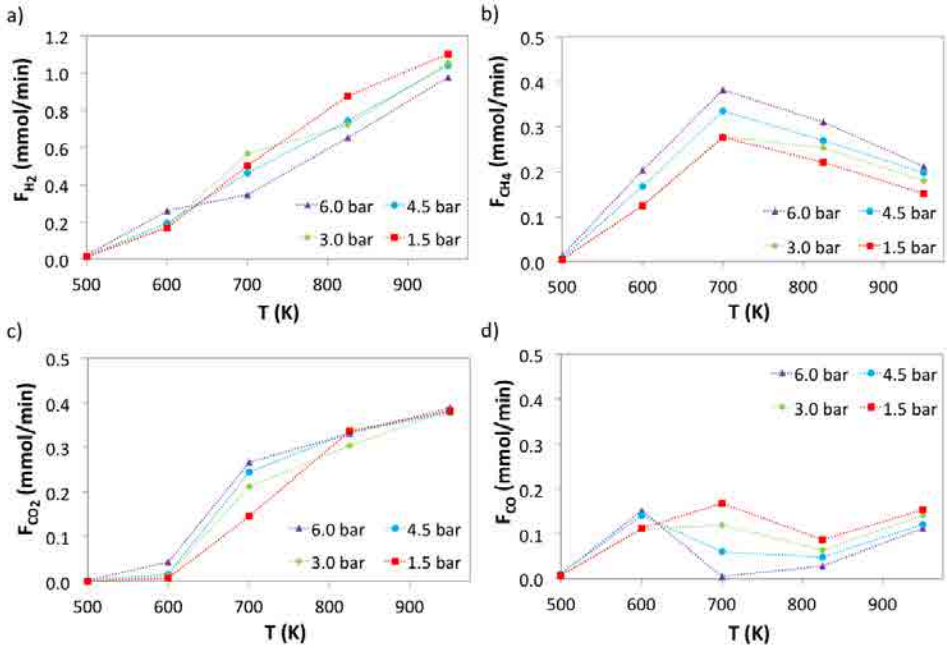

Figure 5.3: Influence of the temperature and pressure on the molar fluxes of the main species produced. Experimental conditions: S/E=6 and feed load v_{space}=0.22 $\mu L_{liquid}/(mg_{cat}min)$.

At temperatures of the order of 600 K, the product distribution showed similar amounts of H_2, CH_4 and CO, indicating that ethanol decomposition (equation 5.1) was the only reaction reaching a significant extent. At 700 K, the product fluxes rose as a consequence of the $\chi_{Ethanol}$ increase. Also, at higher temperatures, in addition to the occurrence of ethanol decomposition, the water gas shift reaction (WGS, equation 5.4) started to take place. This resulted in the appearance of CO_2 in detriment of CO (F_{CO}∼0 at 4.5 and 6.0 bar) and, accordingly, H_2 concentration increased. Interestingly, at 6.0 bar, H_2 concentration was lower than CH_4 concentration together with high CO_2 concentration (indicating that WGS reaction did take place), which probably reflected that at high P the reverse reaction of methane steam reforming, the so-called methanation reaction (see equation 5.13), took place consuming hydrogen and thus resulting in lower hydrogen yields than at lower pressures (P=1.5, 3.0, 4.5 bar).

$$\text{Methanation: } 3H_2 + CO \leftrightharpoons CH_4 + H_2O \tag{5.13}$$

Due to the high temperatures required for MSR [123], only at the highest temperatures tested (823 and 950 K), CH_4 formed from ethanol decomposition could further react and undergo steam reforming. MSR renders the highest H_2 production as 3 mol_{H_2} can be produced per each mol_{CH_4} reacted, as seen in equation 5.5. As a result, the highest hydrogen production at each pressure was achieved at 950 K, because MSR took place on its highest extent, which was confirmed by the consequent largest CH_4 consumption. Besides, at 950 K a non desired CO increase was measured for all pressures, due to the equilibrium nature of the exothermic WGS, indicating that at high temperature the reverse WGS (rWGS) was promoted. However, in spite of rWGS promotion at high temperatures, at 950 K the highest hydrogen productions were recorded, as already mentioned, because the effect of MSR promotion counterbalanced the hydrogen consumption via rWGS. On the other hand, for a given temperature within the 823-950 K temperature range, the effect of P can be clearly seen again in figures 5.2 and 5.3. The highest hydrogen production and hydrogen yield were achieved for the lowest pressure (P=1.5 bar), denoting that high pressures prevented MSR and methanation was favored. Only traces (<1%) of acetaldehyde were noticed and no other byproducts, such as ethylene or acetone, were detected during these experiments.

After these tests, a temperature programmed oxidation (TPO) was performed from room temperature to 773 K (5 K/min) and the gaseous outlet stream concentration was analyzed by a mass spectrometer (MKS Cirrus). The purpose of the TPO was to elucidate if carbon deposits were formed during the reaction performance (in this case, a CO_2 peak should be detected). The TPO analysis revealed $1.7 \cdot 10^{-3}$ $mg_{carbon}/mg_{catalyst}$. After the TPO, the catalytic monolith was tested again under several conditions without activation treatment (reduction with H_2 flux) and, in all cases, the same catalytic results were obtained (not shown here). This is a meaningful result and means that no activation is required for this catalytic system, which simplifies remarkably its implementation in a real application.

5.2.2 Feed load effect

The effect of the liquid feed load or space velocity of the reactants was evaluated over a new 1RhPd/CeO_2//Mon catalytic system loaded with 0.149 g of catalyst (1.5 $mg_{catalyst}/cm^2$). The catalytic activity was directly evaluated without performing the activation treatment with hydrogen. Five increasing liquid feed loads were chosen for activity evaluation at T=773 K, P=4.5 bar and S/E=6. The space velocities examined were v_{space}= 0.37, 0.55, 0.73, 0.91 and 1.08 $\mu L_{liquid}/(mg_{cat}min)$, which corresponded to residence times of 5.3, 3.6, 2.7, 2.2 and 1.8 s, respectively.

Figure 5.4 shows the ethanol conversion and hydrogen yield for the increasing liquid feed loads per unit mass of catalyst tested. Complementary, figure 5.5 shows

the corresponding selectivities to the main reaction products (H_2, CO, CO_2 and CH_4; the selectivity to acetaldehyde was kept under 0.7% in all cases).

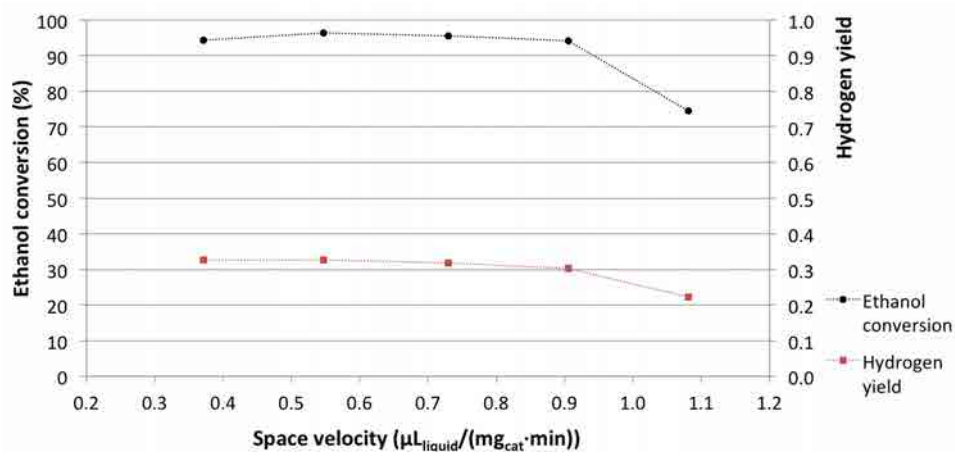

Figure 5.4: Influence of the space velocity on ethanol conversion and hydrogen yield. Experimental conditions: P=4.5 bar, T=773 K and S/E=6.

As observed in figure 5.4, ethanol conversion was nearly constant for the four first space velocities tested, whereas for the highest v_{space} examined a diminution of ethanol conversion was detected (from $\chi_{Ethanol}$~95% to $\chi_{Ethanol}$=75%), due to the reduced residence time at hand. Hydrogen yields experienced the same trend as $\chi_{Ethanol}$ (it decreased from Y_{H_2}~0.3 to Y_{H_2}~0.2), because H_2 was not only produced from ethanol decomposition, but also from the consecutive MSR and WGS reactions, which at the highest feed load took place to a minor degree. Nevertheless, higher feed loads led to higher net hydrogen productions in the feed load range where MSR and WGS maintained their extent, because there was more fuel (ethanol) available, as seen in table 5.2.

Table 5.2: Hydrogen molar fluxes produced for each feed load tested.

Space velocity ($\mu L_{liquid}/(mg_{cat}min)$)	F_{H_2} produced (hydrogen flux) (mmol/min)
0.37	0.6
0.55	1.0
0.73	1.2
0.91	1.5
1.08	1.3

For the highest load tested (v_{space}=1.08 $\mu L_{liquid}/(mg_{cat}min)$) two effects balance the net hydrogen production: higher amounts of available ethanol led to higher

hydrogen production, but shorter residence times prevented to some extent WGS and MSR reactions.

The remarkable influence of the residence time on the extent of the WGS reaction can be clearly seen in figure 5.5, where the selectivity to CO_2 (S_{CO_2}) dropped sharply in accordance with a S_{CO} increase as the feed load increased. The corresponding selectivities to CO ranged from S_{CO}∼3% for reduced loads to S_{CO}∼20% (which was higher than that of CO_2) for the highest inlet flux. In this last scenario (S_{CO}∼20%), a WGS reactor of considerable dimensions (or two shift reactors: high and low temperature WGS reactors) should be installed after the reformer to meet the recommended maximum inlet CO concentrations of ca. 2% for usual CO preferential oxidation reactors [124]. Conversely to CO and CO_2 trends, methane selectivity remained almost constant for the chosen range of feed loads. However, values in the order of S_{CH_4}∼20% represented a hydrogen loss. This was reflected on the highest hydrogen yields achieved, which were close to 0.33, as reported in figure 5.4, and corresponded to only 2 $mol_{H_2}/mol_{Ethanol,in}$. Therefore, operation at higher temperatures than in these experiments would be desirable to promote higher rates of MSR that would lead to higher H_2 production.

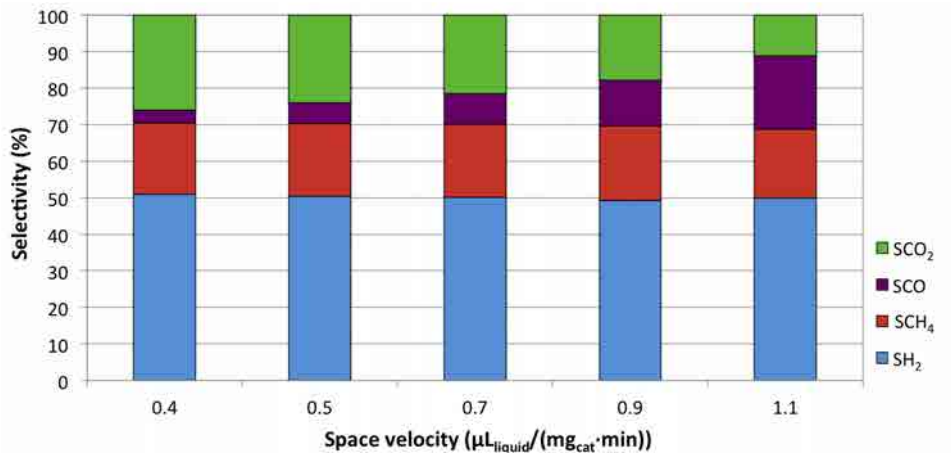

Figure 5.5: Influence of the feed load on the selectivity to the main species produced. Experimental conditions: P=4.5 bar, T=773 K and S/E=6.

5.2.3 Feed composition effect: steam-to-carbon variation

Usually higher steam-to-ethanol ratios than the stoichiometric (the stoichiometric ratio is S/E=3) (see equation 5.14) are chosen for operation in order to avoid carbon deposition and increase catalysts lifetime [39, 125, 126], as already described in the ESR overview (section 2.1.1). In addition, steam-to-ethanol ratios higher than 3

shift the thermodynamic equilibrium, rendering higher hydrogen yields.

$$\text{ESR: } C_2H_5OH_{(g)} + 3\,H_2O_{(g)} \longrightarrow 6\,H_{2(g)} + 2\,CO_{2(g)} \tag{5.14}$$

Commonly, the feed composition is defined using the steam-to-carbon ratio (S/C) rather than the steam-to-ethanol ratio. The S/C ratio is defined as the molar ratio of steam flux to the flux of the fuel $C_xH_yO_z$ multiplied by the number of carbon atoms in the fuel, x, as describes equation 5.15 [32]. In the case of ESR, the fuel, ethanol, contains 2 C atoms and therefore, ESR stoichiometry dictates S/C=1.5.

$$\text{Steam-to-carbon ratio: } \; S/C = \frac{\dot{n}_{H_2O}}{x\;\dot{n}_{C_xH_yO_z}} \tag{5.15}$$

A new 1RhPd/CeO_2//Mon synthesized using 0.254 g of 1RhPd/CeO_2 catalyst (2.5 $mg_{catalyst}/cm^2$) was prepared to investigate the influence of different feed compositions on the ESR performance. The effect on the ESR reaction was tested for S/C=2.0, 2.5, 3.0, 3.5 and 4.0 at different temperatures (T= 700, 825 and 950 K) and constant liquid feed load (v_{space}=0.22 $\mu L_{liquid}/(mg_{cat}min)$) and pressure (P=4.5 bar). Keeping constant the liquid feed load (at the HPLC pump) brings along a variation on the moles of ethanol supplied when the S/C is varied, as demonstrated in table 5.3.

Table 5.3: Ethanol molar fluxes supplied for the S/C variation experiments at constant feed load (v_{space}=0.22 $\mu L_{liquid}/(mg_{cat}min)$).

Steam-to-carbon	$F_{Ethanol,\ in}$ (µmol/min)
4.0	272
3.5	298
3.0	330
2.5	371
2.0	422

Figure 5.6 shows the ethanol conversion and hydrogen yield obtained along the different experiments performed and figure 5.7 shows the molar fluxes of CH_4, CO_2 and CO produced per mole of ethanol supplied and the total H_2 molar flux produced. Finally, figure 5.8 shows the corresponding selectivities to H_2, CH_4, CO_2 and CO. Selectivity to acetaldehyde, acetone and C_2 species (C_2H_4 + C_2H_6) was kept below 1.5% for all the experiments.

As seen in figure 5.6, at low temperature (700 K), higher S/C ratios led to higher $\chi_{Ethanol}$ and higher Y_{H_2}. The observed increment of ethanol conversion as the S/C increased was probably caused by the gradual diminution of the $mol_{Ethanol}$/min

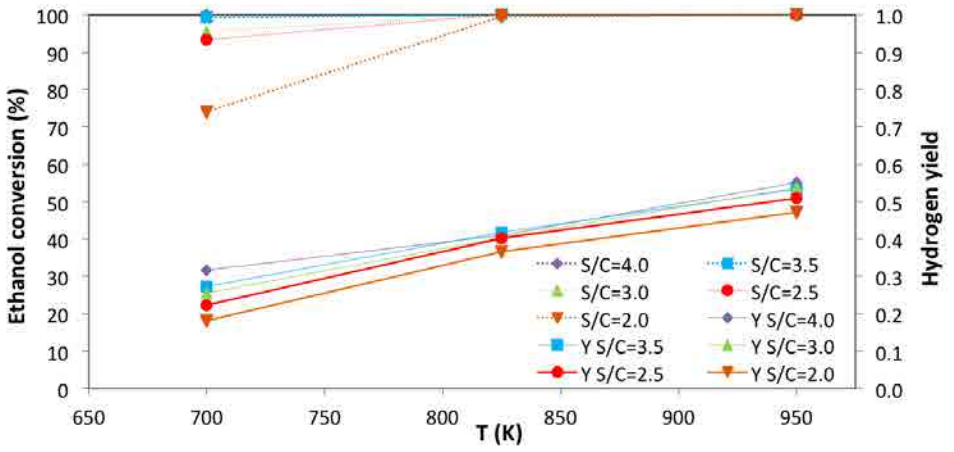

Figure 5.6: Influence of the S/C ratio on ethanol conversion (dashed line) and hydrogen yield (solid line). Experimental conditions: P=4.5 bar and v_{space}=0.22 $\mu L_{liquid}/(mg_{cat} min)$.

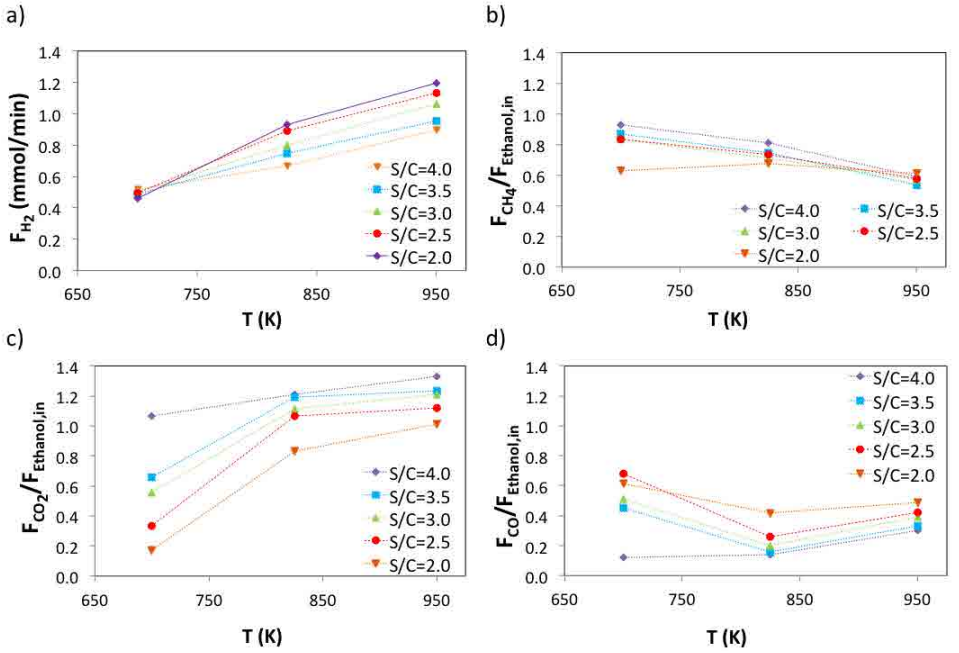

Figure 5.7: Influence of the S/C ratio on the hydrogen flux produced and molar fluxes of the main species produced per mole of ethanol supplied. Experimental conditions: P=4.5 bar and v_{space}=0.22 $\mu L_{liquid}/(mg_{cat} min)$.

fed. Nevertheless, despite the diminution of moles of fuel injected, the highest water contents (i.e. highest S/C) resulted in the highest H_2 production and highest H_2 yield (see figures 5.7a and 5.6, respectively) due to increasing shift on the WGS equilibrium. This effect is clearly seen in figures 5.7c and 5.7d, where the CO_2

molar flux increased at expenses of CO. As seen in figure 5.8, this also resulted in an increased selectivity to CO_2 at expenses of S_{CO} as the S/C increased. In addition, at 700 K MSR is not favored, as confirmed by the high S_{CH_4} values. Therefore, higher water contents prevented methanation, rendering lower S_{CH_4}, and, as a consequence, more hydrogen than lower S/C. At 825 K, full ethanol conversion was achieved for all the S/C tested except for S/C=2.0, indicating that for the highest ethanol load, T≥825 K were required to convert all the ethanol fed.

In the highest temperature range tested (825 K and 950 K), MSR was promoted yielding higher S_{H_2} (and lower S_{CH_4}, as a result) at higher temperatures; thus, the highest hydrogen productions were achieved again for the highest temperatures (T=950 K). Also, in this temperature range, for a given S/C, a temperature increase resulted in a S_{CO} increase, with the consequent diminution of the S_{CO_2} and hydrogen loss, as the rWGS was favored at high temperatures. Despite this fact, operation at high temperature was favorable, because the hydrogen diminution caused by rWGS was clearly counterbalanced by the higher occurrence of MSR. For instance, for S/C=3.0 at 825 K: S_{CO}=4.5%, S_{CO_2}=25.1%, S_{CH_4}=15.9% and S_{H_2}=54.5%, whereas at 950 K: S_{CO}=7.3%, S_{CO_2}=22.4% and S_{CH_4}=10.6%; in spite of the S_{CO_2} diminution, hydrogen selectivity increased to S_{H_2}=59.7%, because methane was reformed, which caused its selectivity diminution by ca. 5%.

The largest selectivities to CO for each S/C were recorded at the lowest temperature studied (700 K) (S_{CO} up to 25%, S/C=2). This trend may denote that this temperature was too low to promote the whole ESR reaction pathway, and after ethanol decomposition the consecutive WGS was not able to take place on a great extent.

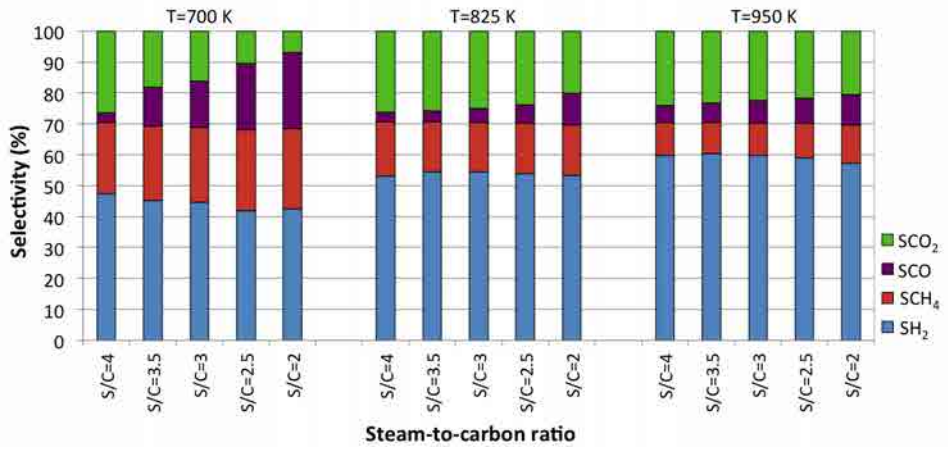

Figure 5.8: Influence of the feed composition on the selectivity to the main species produced. Experimental conditions: P=4.5 bar and v_{space}=0.22 $\mu L_{liquid}/(mg_{cat}min)$.

A common trend observed for all temperatures was that the higher the S/C (higher water content), the higher the hydrogen yield, due to larger promotion of the WGS reaction. Despite this fact, at 950 K (where hydrogen production was maximum) S/C≥3 had small influence on hydrogen yield ($Y_{H_2,\ S/C=4.0}$=0.55 versus $Y_{H_2,\ S/C=3.0}$=0.54). Thus, the economic cost related to evaporation and overheating of the excess water should be considered when choosing the reaction conditions.

In terms of net hydrogen production ($mmol_{H_2}$/min produced, see figure 5.7a), at 825 K and 950 K the dilution effect of the steam/ethanol mixtures clearly prevailed over the equilibrium shift effects and the highest net hydrogen production was achieved for the highest ethanol loads (i.e. low S/C and less diluted feeds). Nevertheless, when the results were normalized per $mol_{Ethanol}$ supplied and hydrogen yield was considered, higher S/C revealed a superior performance for the whole temperature range under study.

The collected catalytic data were used in a collaborative project with Planta Piloto de Ingeniería Química (Centro tecnológico CONICET, Bahía Blanca, Argentina) to derive the kinetic parameters of the 1RhPd/CeO_2 catalyst for reactor modeling purposes. The catalytic screening and the kinetic adjust obtained were published in *E. López, N. J. Divins, A. Anzola, S. Schbib, D. Borio, and J. Llorca, "Ethanol steam reforming for hydrogen generation over structured catalysts", International Journal of Hydrogen Energy, 38 (2013), pp. 4418* [127] and this is one of the papers of this Thesis.

5.2.4 Stability tests: long-term runs

Long-term experiments were finally performed to investigate catalyst's stability at intermediate operational conditions.

5.2.4.a Synthetic ethanol stability test

A new 1RhPd/CeO_2//Mon loaded with 0.140 g of catalyst was synthesized for this stability test. The test was conducted for >100 h on stream uninterruptedly at 773 K, 4.5 bar, S/C=3 and v_{space}=0.47 $\mu L_{liquid}/(mg_{cat}min)$ using synthetic ethanol. Figure 5.9 shows the ethanol conversion, hydrogen yield and the volumetric hydrogen production achieved during the stability test. After a short activation period, full ethanol conversion was achieved and the catalytic performance remained constant for ca. 80 hours of operation. In this period, a mean hydrogen yield of 0.34, which represents 2.1 $mol_{H_2}/mol_{Ethanol}$, was reached and the H_2 flux measured was 20 mL/min on average. The corresponding molar fluxes of the detected species are plotted in figure 5.10. During the period of constant activity, a gradual increase of the hydrogen molar flux was noticed, which took place along with a reduction of the methane molar flux, indicating that MSR was gradually promoted. For

the first 80 hours of operation, the mean selectivities to the main ESR products were S_{H_2}=49.9%, S_{CH_4}=21.3%, S_{CO_2}=27.1% and S_{CO}=2.3%. C_2 species (C_2H_4 + C_2H_6) appeared after 20 hours of operation and its concentration gradually rose up to ca. 0.01 mmol/min, where it stabilized[1].

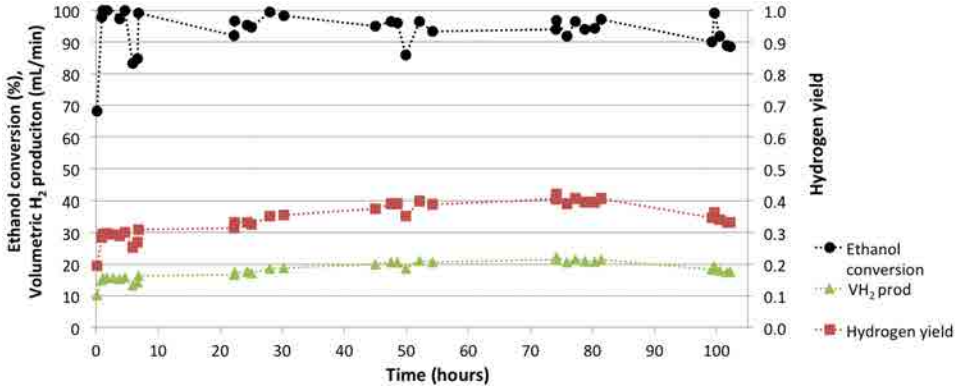

Figure 5.9: Ethanol conversion, hydrogen yield and volumetric H_2 production recorded for the stability test performed with synthetic ethanol. Experimental conditions: T=773 K, P=4.5 bar, S/C=3 and feed load v_{space}=0.47 $\mu L_{liquid}/(mg_{cat}min)$.

From 80 hours onwards of operation, the total gaseous production started to decrease, caused by the reduction on ethanol conversion. As seen in figure **5.10**, also the selectivity to H_2, CH_4, CO_2 and CO started to deteriorate and a noticeable increase of acetone and also acetaldehyde downstream the reactor was recorded, which might be responsible for the activity loss.

After 100 hours on stream, ethanol conversion decreased to $\chi_{Ethanol}$~89% and acetone was the main byproduct present on the reformate stream. A TPO analysis was then performed and it revealed only $0.047 \cdot 10^{-3}$ $mg_{carbon}/mg_{catalyst}$.

5.2.4.b Commercial bioethanol stability test

A new long-term test was carried out using commercial bioethanol in order to investigate the influence of real bioethanol on the catalyst operation. The impurities that commercial bioethanols contain can affect catalysts activity and easily deactivate them, as previously described in section **2.3.1.d**. For the new long-term run, a new 1RhPd/CeO_2//Mon loaded with 0.250 g of catalyst was synthesized and the reaction parameters evaluated in the previous stability test were chosen again, i.e: T=773 K, P=4.5 bar, S/C=3 and feed load v_{space}=0.47 $\mu L_{liquid}/(mg_{cat}min)$. The

[1]The concentration of condensable products, i.e. C_2H_4 species, acetone and acetaldehyde, could not be accurately measured as these products were trapped prior to the introduction of the gaseous outlet stream into the microchromatograph. Nevertheless, the concentration trends recorded were reliable since the outlet gaseous stream contained the vapor pressure of condensable products.

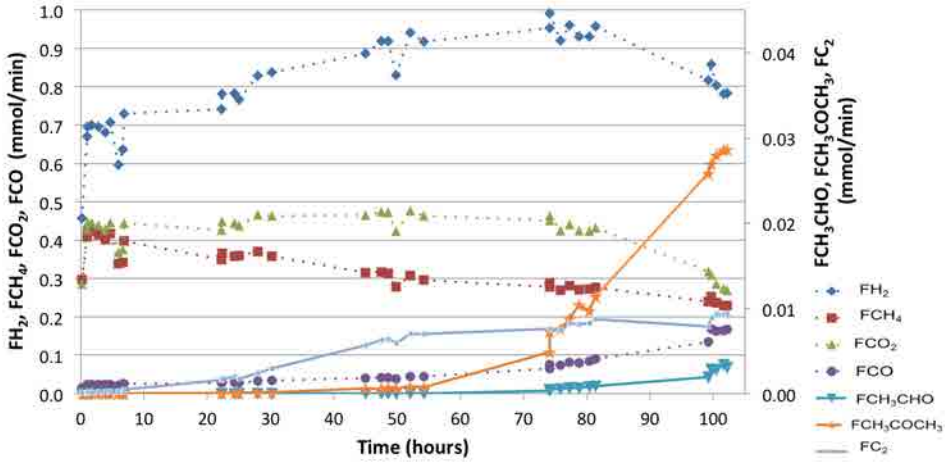

Figure 5.10: Molar fluxes of the species detected during the stability test performed with synthetic ethanol. Experimental conditions: T=773 K, P=4.5 bar, S/C=3 and v_{space}=0.47 $\mu L_{liquid}/(mg_{cat}min)$.

commercial bioethanol used was *Bioetanol de La Mancha* and its composition is presented in table 5.4.

Table 5.4: Composition of *Bioetanol de La Mancha*.

Detected species	Concentration
Ethanol	99.94 v/v %
Water	0.036 v/v %
Phosphorus	$<$ 0.4 ppm
Chlorine	$<$ 1 ppm
Sulfur	$<$ 5 ppm
Acetaldehyde	73.6 ppm
Acetone	0
Acetal	239.8 ppm
Methanol	3383.5 ppm
2-butanol	247.9 ppm
1-propanol	603.0 ppm
2-methyl-1-propanol	482.6 ppm
1-butanol	41.2 ppm
Amyl alcohol	1651.6 ppm

Figure 5.11 shows the ethanol conversion, the hydrogen yield and the hydrogen flux recorded during the bioethanol stability test. The molar fluxes of the species detected during the test are plotted in figure 5.12.

For the first 30 hours of operation, full ethanol conversion was achieved and the hydrogen yield values recorded were close to the ones obtained during the synthetic ethanol stability test. However, after ca. 40 hours on stream the catalyst's activity started to decrease and after ca. 52 hours on stream χ_{Ethanol}=70%. The catalytic activity was then quickly lost and after 67 hours of operation, the total gaseous outlet flux was only 2 mL/min, which clearly indicated that the catalyst was deactivated and the test was stopped. The activity loss was much more pronounced and fast in the bioethanol long-term test than in the test carried out with synthetic ethanol and, in addition, χ_{Ethanol} dropped to zero in 67 hours, whereas for the previous test χ_{Ethanol} gradually diminished to 89% after 102 hours of operation.

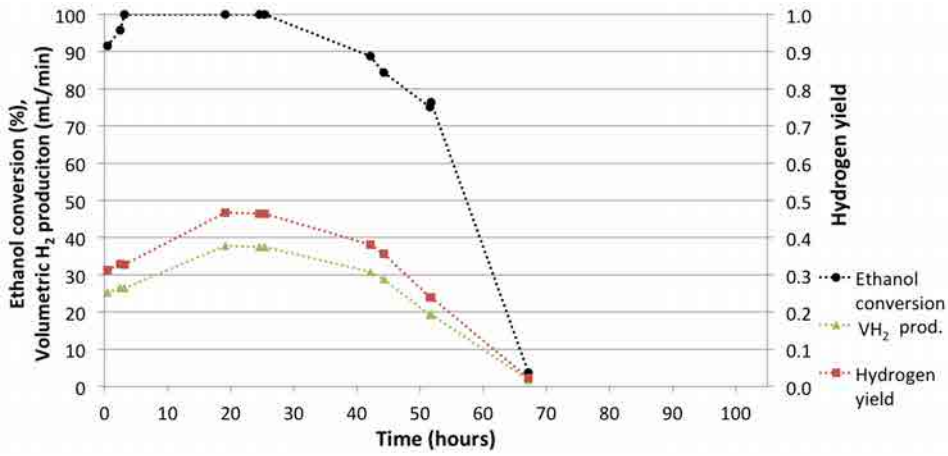

Figure 5.11: Ethanol conversion, hydrogen yield and volumetric hydrogen production for the bioethanol stability test. Experimental conditions: T=773 K, P=4.5 bar, S/C=3 and v_{space}=0.47 $\mu L_{liquid}/(mg_{cat}min)$.

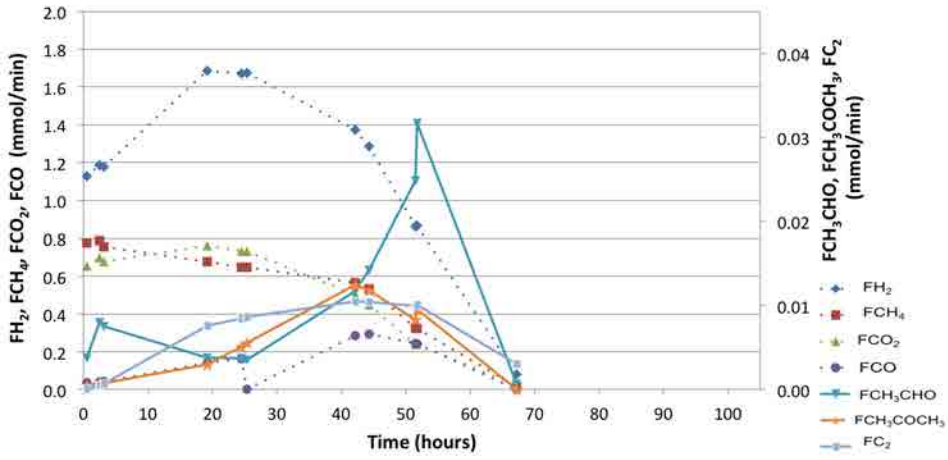

Figure 5.12: Reaction products molar fluxes for the bioethanol stability test. Experimental conditions: T=773 K, P=4.5 bar, S/C=3 and v_{space}=0.47 $\mu L_{liquid}/(mg_{cat}min)$.

The effect of raw bioethanol impurities has been the object of several studies, as for instance [66,94,96]. Duprez's group, in [94,96], studied the role of the main impurities of crude bioethanol such as methanol, 1-propanol, 1-butanol, 1-pentanol, isopropanol, 2-methyl-1-propanol and 3-methyl-1-butanol and also of aldehydes, amines, acids and esters. Duprez's group found that longer alcohols strongly decreased catalysts stability and they showed that the deactivation increased as the amount of carbon atoms in the molecule increased. In addition, this effect was more pronounced in the presence of branched alcohols compared to the linear ones. The deactivation process was mainly explained in terms of coke deposition, which was favored by the presence of principally higher alcohols, esters and acids. On the other hand, the presence of other impurities, such as sulfur, has also been investigated. In [66], Simson et al. found that the presence of only 5 ppm of S on the inlet mixture resulted in a rapid catalyst deactivation and demonstrated that large carbon deposits had formed on the catalyst surface, indicating that S had promoted carbon formation. Therefore, in the literature it has been demonstrated that the presence of different types of impurities leads to catalysts deactivation as coke formation is promoted. As a result, the presence of these higher alcohols as well as S in bioethanol *Bioetanol de La Mancha* could cause the deactivation of our 1RhPd/CeO_2//Mon catalyst due to carbon deposits formation. In consequence, following this long-term test, a regeneration test was performed in order to eliminate the carbon deposits and try to recover the catalyst's activity.

5.2.4.c Catalytic activity regeneration tests

As seen in figure 5.11, the catalytic activity was completely lost after 67 hours of operation with commercial bioethanol and the long-term test had to be stopped. Then, a regeneration treatment was performed to study the feasibility of catalytic activity recovery and hence the steam/ethanol mixture was switched to 21% O_2 stream (balanced in N_2). The oxidation was performed for 1 hour, keeping T at the reaction temperature (T=773 K) and P was reduced to atmospheric pressure. A large CO_2 peak was detected in the outlet stream by the µGC during this oxidation. After the regeneration treatment, the inlet flux was switched to the feed mixture (S/C=3) and the same operational parameters were evaluated. The usual catalytic performance was completely recovered. Therefore, most probably the catalytic activity was lost due to the formation of carbonaceous deposits that blocked the catalyst's active sites; these could be recovered after the regeneration treatment, because the deposited coke was calcined. The regeneration process was repeated several times.

Figure 5.13 shows the ethanol conversion and the hydrogen yield for the first 67 hours of operation already reported and the catalytic activity parameters recorded after several regeneration treatments. The orange vertical lines mark the oxidation treatments performed along with their duration. The trends after the first orange

line correspond to the catalyst's performance after the first regeneration treatment and so on and so forth.

As already mentioned, after the first oxidation, the usual catalytic performance was recovered as full ethanol conversion was achieved again and the hydrogen yield almost recovered the value achieved during the previous stationary performance. Nevertheless, after only 23 hours on stream the catalytic activity dropped again and the catalyst was deactivated. Thus, the inlet mixture was switched again to the oxygen stream (21% O_2/N_2) and the outlet gases were analyzed with the µGC to follow the CO_2 peak. This time, the catalyst was oxidized only for 30 minutes and after that the operational parameters were recovered.

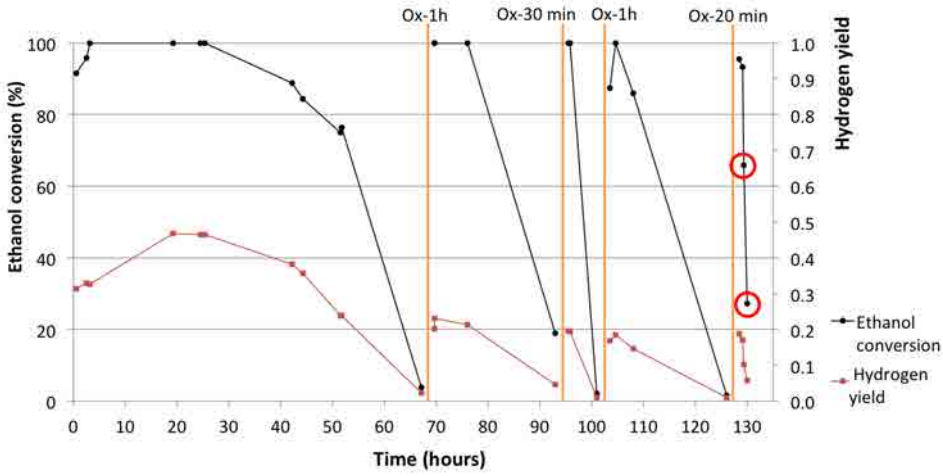

Figure 5.13: Ethanol conversion and hydrogen yield of the regeneration treatments. Experimental conditions: T=773 K, P=4.5 bar, S/C=3 and v_{space}=0.47 $\mu L_{liquid}/(mg_{cat}min)$. Orange vertical lines mark the oxidations performed and their duration.

As seen in figure **5.13**, initially, the catalyst recovered its usual activity but after only 6 hours of operation no gaseous outlet stream was produced, indicating that the catalytic active sites were blocked again. The inlet mixture was switched again to the oxidizing atmosphere and this time it was kept for 1 hour. Then, the O_2 inlet was switched to the ethanol/water mixture. After the third calcination, the catalytic activity was not immediately recovered and after 2 hours on stream the catalyst started to show again deactivation signs, although it completely lost its activity after 22 hours on stream. The final regeneration treatment was performed for only 20 minutes and the catalyst could not recovered its initial activity. The two encircled points in figure **5.13** correspond to experimental data obtained increasing the space velocity nearly three times, v_{space}=1.28 $\mu L_{liquid}/(mg_{cat}min)$. As seen on the ethanol conversion and hydrogen yield trends, the feed load incre-

ment had a dramatic effect on the catalyst's activity and after only 40 minutes on stream, ethanol conversion had already dropped to 27%. The regeneration study was then finished and the catalyst was kept on its deactivated state. The deactivated 1RhPd/CeO_2//Mon was removed from the reactor and it was longitudinally cut into two pieces. One of the two pieces obtained was studied by means of X-ray photoelectron spectroscopy and an *in situ* study regarding the regeneration treatments was performed. These results are presented in Chapter 6 (section 6.2.1.b).

The regeneration study showed that the catalyst's activity could be recovered by directly switching the feed mixture to an oxygen mixture and then again to the ethanol/water mixture without any activation treatment. After the oxidations, the catalyst recovered its activity but the period of maximum activity was shorter than when the catalyst was fresh, indicating that in spite of the catalytic activity recovery some amount of permanent damaged had occurred on the catalyst's surface, as already reported by Simson et al. [66]. Also, depending on the duration of the oxidation treatments, the catalytic activity was maintained for different periods of time, the periods being larger after longer oxidations.

After these catalytic activity screening tests, it was possible to conclude that the reaction parameters that led to improved catalytic activity were high temperatures ($T \geq 950$ K), low pressures (as low as the design of the reformer allows for) and $S/C \geq 3$. On the other hand, the catalyst did not require any activation treatment and could be easily regenerated by calcination.

After these tests, the catalyst was reformulated and a new ceria modified support for Rh and Pd was synthesized. Also, the RhPd concentration was optimized. Figure 5.14 shows 100 h of a stability test performed with commercial bioethanol. The new formulation led to improved stability of the catalysts and long-term runs of several hundred hours were performed without noticing any sign of catalyst deactivation. Up to 90 mL/min of hydrogen were produced under the operational conditions tested with a catalyst loading of 735 mg. The reformulated catalyst was registered in the Patents Office and there exists a non disclosure agreement with an industrial partner.

5.3 Catalytic activity screening of model $RhPd/CeO_2$ catalysts

The catalytic activity of model catalysts synthesized with preformed RhPd@D and Pd@Rh NPs was evaluated on structured catalysts as well. This section discusses the main catalytic results obtained on catalysts based on preformed NPs.

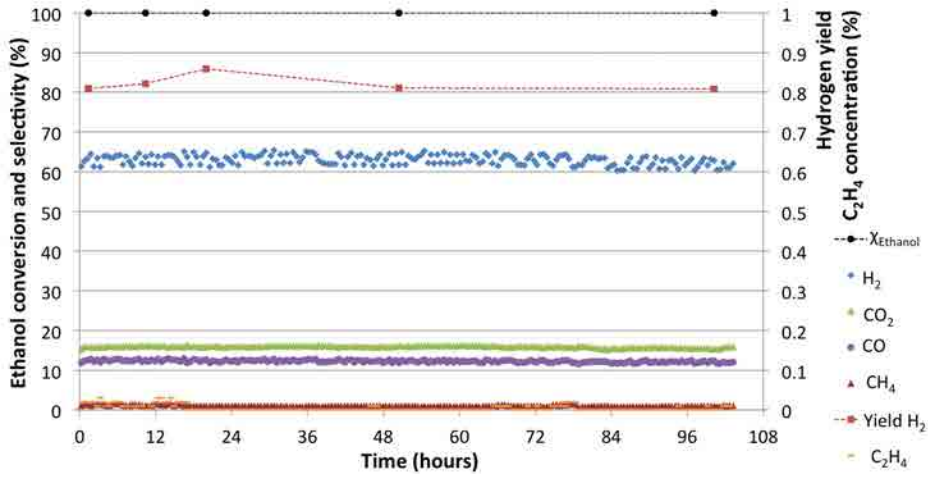

Figure 5.14: Ethanol conversion, hydrogen yield and concentration of the main species detected for 100 hours of a bioethanol stability test. Experimental conditions: T=1050 K, P=4.5 bar, S/C=3 and v_{space}=0.22 $\mu L_{liquid}/(mg_{cat} min)$ (residence time τ=1.9 s).

One of the conclusions arisen from the tests performed on working catalysts was that higher temperatures led to higher catalytic activity and thus in the catalytic tests of model catalysts reaction temperatures up to 1050 K were examined.

5.3.1 Pd@Rh/CeO_2 catalysts

The reaction performance of the Pd@Rh/CeO_2 system was evaluated over a cordierite monolith coated with 0.101 g of CeO_2, where Pd@Rh NPs were subsequently anchored. Then, the functionalized Pd@Rh/CeO_2//Mon was calcined at 773 K (2 K/min) for 2 hours, in accordance with the results of the TGA analysis. Prior to catalytic testing, a reduction treatment was performed for 1 hour at 550 K with 10% H_2 (balanced N_2).

For these tests, the noble metal loading chosen was 1.5 wt.% Pd, because model catalysts containing 1.5 wt.% Pd + 1.5 wt.% Rh allowed for their characterization before reaction (as described in section **4.3.2** and also under reaction conditions, which is reported in Chapter **6**, section **6.3.2**). Therefore, in order to keep Pd concentration constant in all the samples, for the catalytic activity screening tests of Pd@Rh/CeO_2 catalysts, Pd concentration was fixed at 1.5 wt.%. Taking into account that the Pd:Rh ratio in Pd@Rh NPs was Pd:Rh=75:1.3, the corresponding Rh content of the Pd@Rh/CeO_2//Mon was 0.03 wt.% Rh.

5.3.1.a Reaction temperature effect

The influence of temperature on the ESR reaction performance was investigated for temperatures ranging from 825 K to 1050 K at fixed pressure, space velocity

and S/C ratio. The operational parameters chosen for these tests were the same evaluated for working catalysts: P=4.5 bar, v_{space}=0.22 $\mu L_{liquid}/(mg_{cat}min)$ (residence time 12.2 s) and S/C=3. In figure **5.15**, the ethanol conversion, hydrogen yield and the volumetric H_2 production are plotted.

At 825 K, the Pd@Rh/CeO_2//Mon catalyst converted almost all the ethanol fed, $\chi_{Ethanol}$=95%, and the hydrogen yield was Y_{H_2}=0.3. Nevertheless, at the same temperature, working catalysts already converted all the ethanol fed and its hydrogen yield was close to 0.6, as seen in figure **5.2**, in spite of the shorter residence time of reactants evaluated over the working catalyst (5.8 s versus 12.2 s). In contrast to the previously observed trends, higher temperatures resulted in lower ethanol conversion and a further temperature increase (up to 950 K) resulted in further activity reduction. At 950 K, ethanol conversion was reduced to $\chi_{Ethanol}$=75%, indicating that the catalyst was deactivating. However, the temperature was increased again and the downward trend changed. Nearly full ethanol conversion ($\chi_{Ethanol}$=97%) was attained at 975 K and the hydrogen yield also increased. At T≥1000 K, $\chi_{Ethanol}$=100% and Y_{H_2} continuously increased up to 0.75 at 1050 K. Thus, the deactivation signs detected at T∼950 K disappeared at high temperatures. Even though, the outlet gaseous stream measured throughout these experiments was irregular and experienced large fluctuations.

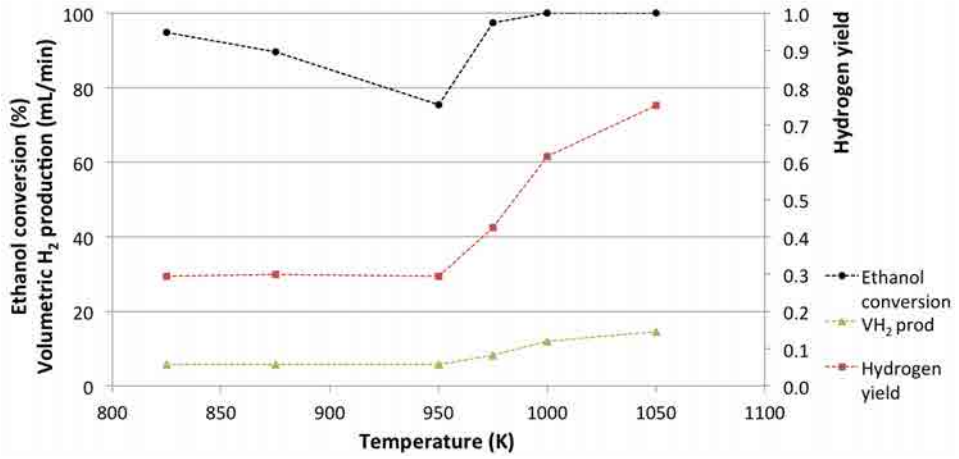

Figure 5.15: Influence of the temperature on ethanol conversion, hydrogen yield and volumetric hydrogen production of 1.5Pd@Rh/CeO_2//Mon catalyst. Experimental conditions: P=4.5 bar, S/C=3 and v_{space}=0.22 $\mu L_{liquid}/(mg_{cat}min)$.

Regarding the products distribution of these experiments, figure **5.16** shows the selectivity to the reaction products detected. The main species detected were H_2, CH_4, CO_2 and CO, but also traces of acetaldehyde and acetone (<0.5%) and less than 1% of ethane and ethylene (C_2 species) were present on the reformate stream.

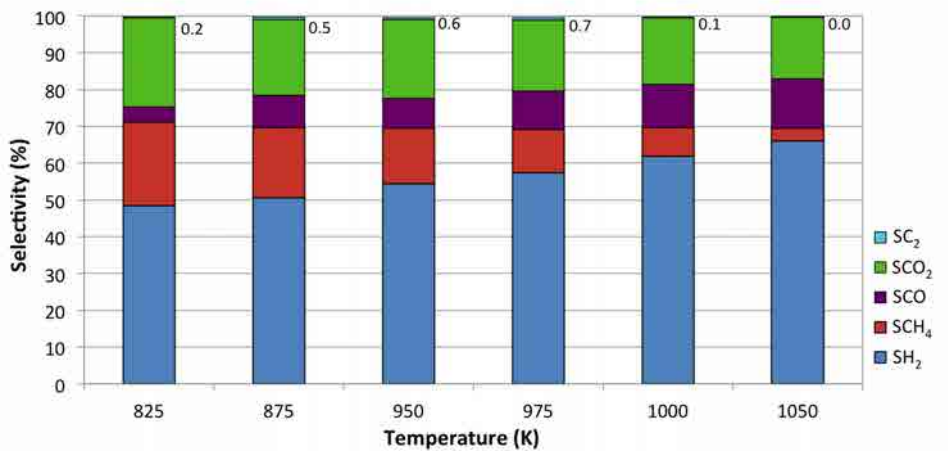

Figure 5.16: Influence of the temperature on the selectivity to the main species produced by 1.5Pd@Rh/CeO_2//Mon. Experimental conditions: P=4.5 bar, S/C=3 and v_{space}=0.22 $\mu L_{liquid}/(mg_{cat}min)$. The numbers show the selectivities to C_2 species.

At low temperatures, basically ethanol decomposition and WGS reactions took place. As the reaction temperature increased, MSR took place to a greater degree and at 1050 K methane selectivity was only S_{CH_4}=4%, resulting in a high H_2 production. Interestingly, no byproducts such as ethylene were detected in large amounts, whose presence could have caused the catalytic activity reduction recorded.

After this initial test, a new temperature screening test was performed at lower pressure (P=1 bar), maintaining S/C=3 and v_{space}=0.22 $\mu L_{liquid}/(mg_{cat}min)$. In figures 5.17 and 5.18 the new results obtained at 1 bar are represented.

These experiments revealed a completely different behavior. At low temperatures (T≤900 K), the catalyst exhibited poor catalytic activity as the ethanol conversion ranged 35-55% and the hydrogen yield was ca. 0.1. In contrast to working catalysts' performance, at low temperatures model catalysts produced considerable amounts of C_2 species[2], which may account for the low catalytic activity exhibited. Reaction temperatures between 925 K and 950 K clearly resulted in lower C_2 species selectivity, however they had minor influence on the selectivity to the main ESR reaction products, despite full ethanol conversion was achieved at 950 K. Finally, at T≥1000 K, ethane and ethylene vanished and MSR took place to a greater degree than at lower temperatures, bringing along larger H_2 production, which resulted in the hydrogen yield increment recorded. For instance, at 1050 K, S_{CH_4}=3% and S_{H_2}=67% and Y_{H_2}=0.7.

[2]As already mentioned, the concentration of condensable products could not be accurately measured, because these products were trapped prior to the introduction of the gaseous outlet stream into the microchromatograph. The condenser was emptied after each condition tested.

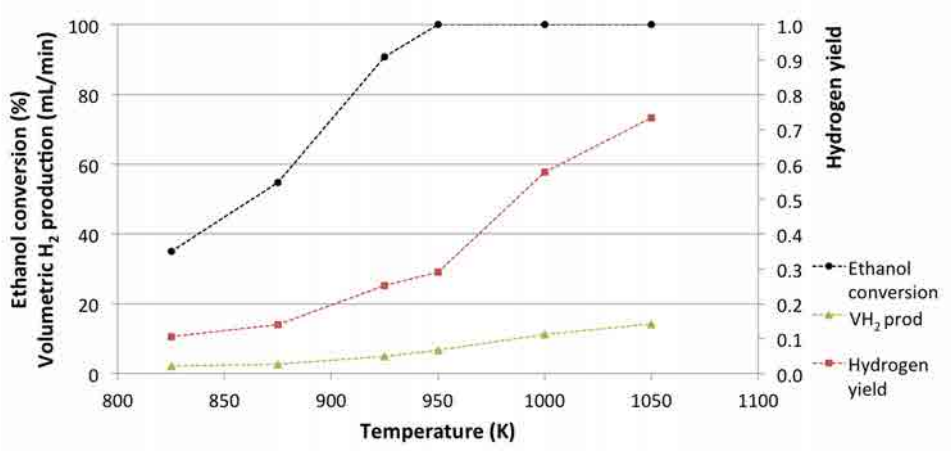

Figure 5.17: Influence of the temperature on the ethanol conversion, hydrogen yield and volumetric hydrogen production of 1.5Pd@Rh/CeO_2//Mon catalyst. Experimental conditions: P=1.0 bar, S/C=3 and v_{space}=0.22 $\mu L_{liquid}/(mg_{cat}min)$.

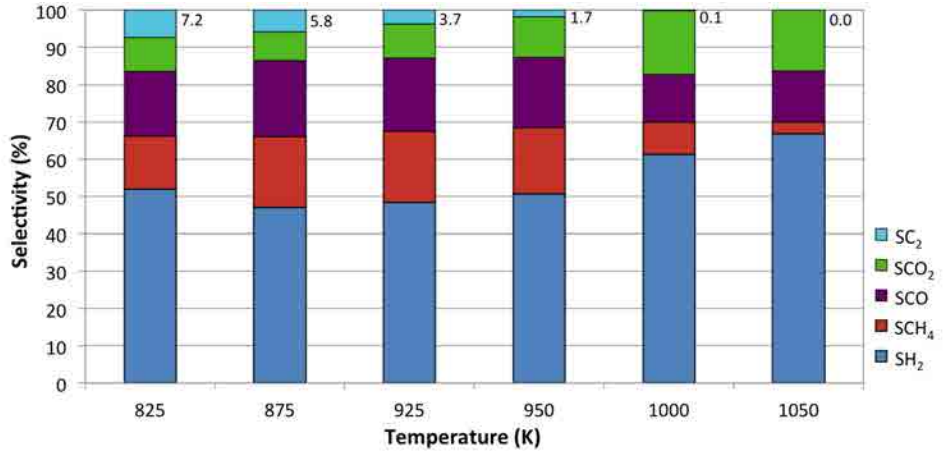

Figure 5.18: Influence of the temperature on the selectivity to the main species produced by 1.5Pd@Rh/CeO_2//Mon. Experimental conditions: P=1.0 bar, S/C=3 and v_{space}=0.22 $\mu L_{liquid}/(mg_{cat}min)$. The numbers show the selectivities to C_2 species.

5.3.1.b Feed load effect

The effect of the space velocity was subsequently evaluated at the highest temperature tested (T=1050 K). This temperature avoided the regime of decreasing ethanol conversion, which could lead to total catalyst deactivation and also avoided the formation of ethylene, a well-known coke precursor. Atmospheric pressure and S/C=3 were chosen for these analyses. The ethanol conversion and hydrogen yield obtained for the space velocities tested are shown in figure 5.19 and the corresponding products selectivities are plotted in figure 5.20. The corresponding residence times of these experiments are from low to high feed load, respectively: τ=4.9, 4.0,

3.5, 2.7, 1.8, 1.6, 1.3 and 1.1 s.

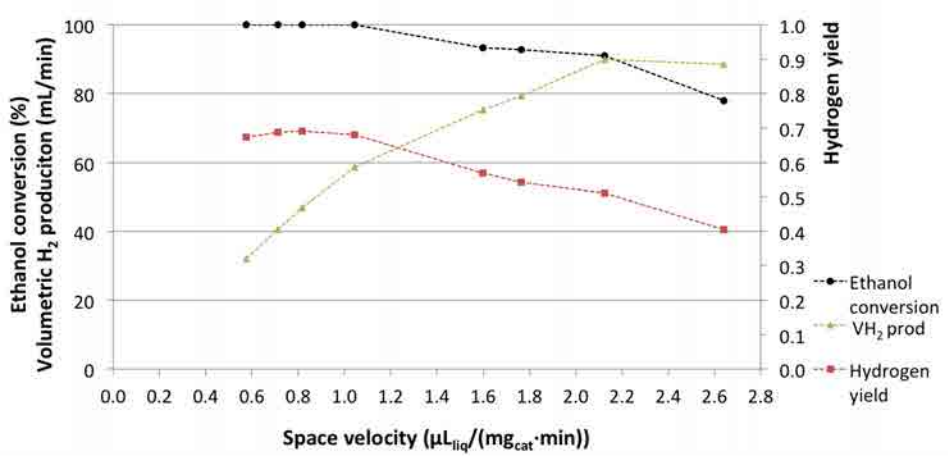

Figure 5.19: Influence of the space velocity on the ethanol conversion, hydrogen yield and volumetric hydrogen production of 1.5Pd@Rh/CeO_2//Mon catalyst. Experimental conditions: T=1050 K, P=1.0 bar and S/C=3.

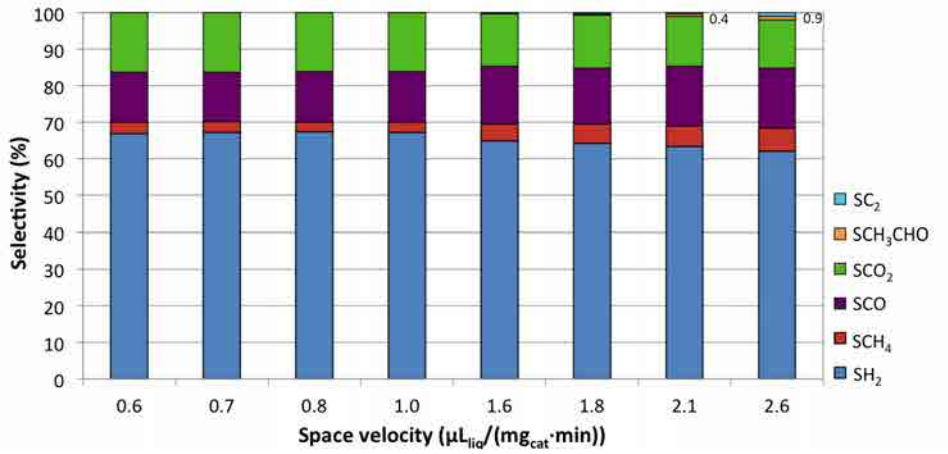

Figure 5.20: Influence of the space velocity on the selectivity to reaction products of 1.5Pd@Rh/CeO_2//Mon catalyst. Experimental conditions: T=1050 K, P=1.0 bar and S/C=3. The numbers show the selectivity to C_2 species.

Full ethanol conversion was recorded at feed loads per unit mass of catalyst between 0.6 and 1.0 $\mu L_{liquid}/(mg_{cat}min)$. Once v_{space}=1.6 $\mu L_{liquid}/(mg_{cat}min)$, ethanol conversion decreased to 90%. However, reaction performance was also evaluated for larger feed loads, because both ethanol conversion and hydrogen yield experienced a smooth variation for the consecutive space velocities v_{space}=1.6, 1.8 and 2.1 $\mu L_{liquid}/(mg_{cat}min)$. Their corresponding ethanol conversion and hydrogen yield were $\chi_{Ethanol}$=93, 93 and 91% and Y_{H_2}=0.55, 0.54 and 0.51, respectively.

Finally, for v_{space}=2.6 $\mu L_{liquid}/(mg_{cat}min)$ (τ=1.1 s), ethanol conversion experienced a larger reduction and decreased to 78%. For the working catalyst (see figures 5.4 and 5.5), the ethanol conversion diminution was obtained for v_{space}=1.1 $\mu L_{liquid}/(mg_{cat}min)$ (τ=1.8 s) where $\chi_{Ethanol}$=75%. Probably, this was due to the higher reaction temperature chosen for these analyses than for working catalysts (the feed load test of the RhPd/CeO_2//Mon was performed at T=773 K, compare with figure 5.4). The selectivity to detected species showed that larger feed loads led to larger CH_4 and CO selectivities, denoting again that the consecutive MSR and WGS reactions took place to a lesser extent at shorter residence times. For the highest feed load per unit mass of catalyst tested, v_{space}=2.6 $\mu L_{liquid}/(mg_{cat}min)$, 1% of acetaldehyde as well as 1% of ethane and ethylene were formed.

After these tests, the 1.5Pd@Rh/CeO_2//Mon had turned completely black and weighted 0.50 g more than fresh (5 times the catalyst mass loaded), denoting that large C deposits had formed on its surface. Despite the high catalytic activity achieved in the above-mentioned screenings at T≥1000 K, the large amount of carbon formed throughout these tests could easily compromise the catalyst's stability.

5.3.2 RhPd@D/CeO_2 catalysts

The activity screening of RhPd@D/CeO_2 catalysts was carried out with a catalyst containing 3 wt.% noble metal loading, i.e., with a 3RhPd@D/CeO_2 catalyst. For these analyses, higher noble metal concentration than for working catalysts was chosen, as this concentration allowed for RhPd@D/CeO_2 catalysts characterization before reaction (section 4.3.2) and, as described in Chapter 6, also allowed for characterization under reaction conditions (section 6.3.2). Therefore, in order to have a complete study of RhPd@D/CeO_2 catalysts comprising characterization and catalytic activity investigation, 3 wt.% RhPd was also chosen for catalytic activity testing.

A fresh 3RhPd@D/CeO_2//Mon was prepared using 0.250 g of ceria impregnated with 1.166 mL of RhPd@D NPs toluene solution ($64 \cdot 10^{-3}$ M), following the synthesis procedure described in section 3.3. The functionalized 3RhPd@D/CeO_2//Mon was calcined at 573 K (2 K/min) for 2 hours and then it was fitted inside a tubular stainless steel reactor. The reaction setup described in figure 5.1 was used to examine the catalytic activity and the hydrogen activation treatment was performed for 1 hour at 550 K with 10% H_2 (balanced N_2) prior to tests performance.

5.3.2.a Reaction temperature effect

The effect of reaction temperature on the ESR reaction performance was investigated for temperatures ranging from 825 K to 1050 K at fixed pressure (P=4.5 bar), feed load (v_{space}=0.22 $\mu L_{liquid}/(mg_{cat}min)$, τ=1.9 s) and S/C ratio (S/C=3).

The ethanol conversion and hydrogen yield obtained are plotted in figure 5.21 and the selectivities to reaction products are shown in figure 5.22. At 825 K, $\chi_{Ethanol}$ only reached ~70% and Y_{H_2}~0.2. These values are lower than the ones recorded at the same temperature for the working catalyst (compare with figure 5.2), for which full ethanol conversion was achieved at T≥825 K, and also lower than the ones obtained with the $Pd@Rh/CeO_2//Mon$ catalyst (see figure 5.15).

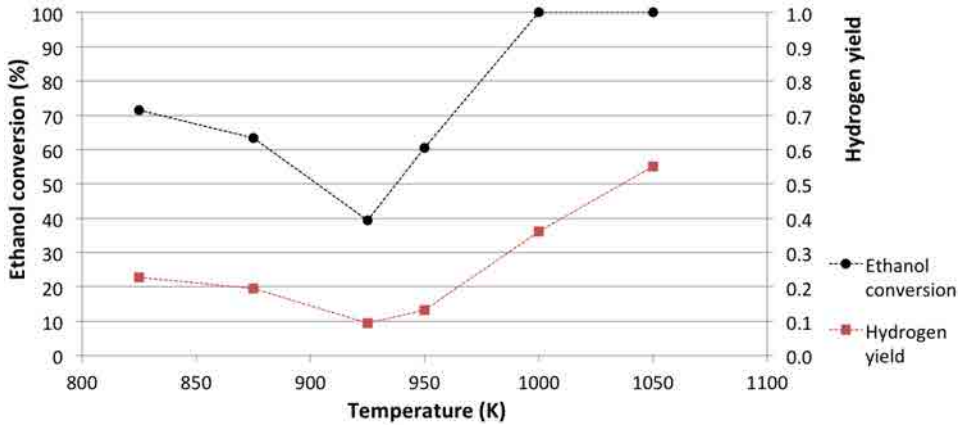

Figure 5.21: Influence of the temperature on ethanol conversion and hydrogen yield of $3RhPd@D/CeO_2//Mon$ catalyst. Experimental conditions: P=4.5 bar, S/C=3 and v_{space}=0.22 $\mu L_{liquid}/(mg_{cat}min)$.

Interestingly, the $3RhPd@D/CeO_2//Mon$ exhibited the same trend previously observed for the $1.5Pd@Rh/CeO_2//Mon$ and the next increasing temperatures (875 K, 925 K and 950 K) led to lower ethanol conversion and hydrogen yield, denoting again that the reaction temperature evaluated was too low for these catalysts. Together with the ethanol conversion diminution, the $3RhPd@D/CeO_2//Mon$ produced large amounts of acetone and C_2 species (C_2H_4 and C_2H_6), as seen in figure 5.22. This is in contrast with the behavior observed for the $1.5Pd@Rh/CeO_2//Mon$, which did not produce any byproduct during the activity depletion (see figure 5.16). At 825 K and 875 K, acetone was the main byproduct produced by the $3RhPd@D/CeO_2//Mon$, as well as, C_2 species. But once the temperature was T≥925 K, acetone vanished and ethane and ethylene were the most important byproducts (its concentration reached 10%) along with some acetaldehyde. It is well-known that ethylene is a coke precursor that leads to catalyst deactivation, therefore the high C_2 species concentration detected may be responsible for the activity loss noticed. In such a case, the operational regimes where they are produced should be avoided, as it is demonstrated in the following section 5.3.2.c. Remarkably, the working $1RhPd/CeO_2//Mon$ did not produce acetone neither C_2, and only traces of acetaldehyde were detected, even though the temperatures investigated ranged from 500 K to 950 K (section 5.2.1).

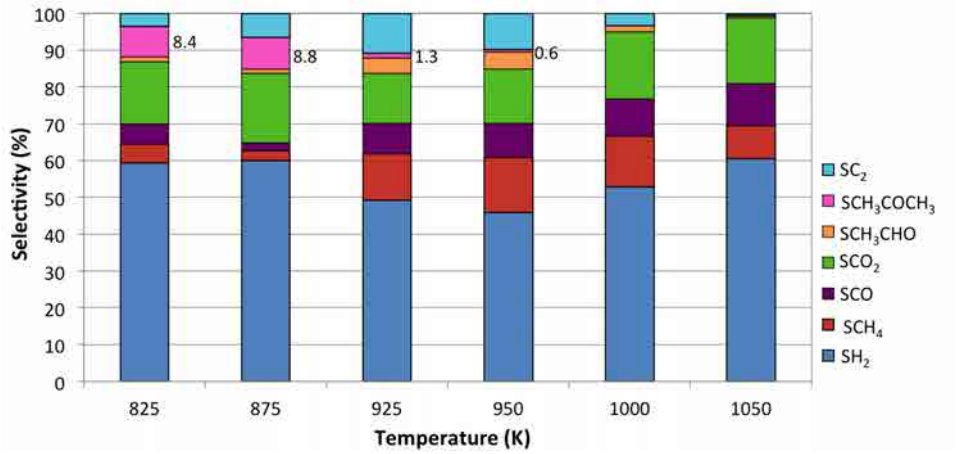

Figure 5.22: Influence of the temperature on the selectivity to the main species produced by 3RhPd@D/CeO_2//Mon catalyst. Experimental conditions: P=4.5 bar, S/C=3 and v_{space}=0.22 $\mu L_{liquid}/(mg_{cat}min)$. The numbers show the selectivity to acetone.

The downward trend was again reverted increasing the reaction temperature and, for this catalyst, at T≥950 K ethanol conversion and hydrogen yield increased once again. The 3RhPd@D/CeO_2//Mon catalyst achieved full ethanol conversion at T≥1000 K and all the byproducts were significantly reduced in this temperature range, indicating that ethanol decomposition, MSR and WGS reactions were the main processes that took place and other side reactions were avoided. Finally, at the highest temperature tested (1050 K), the total concentration of all the byproducts was < 1% and Y_{H_2}=0.55. This value was close to the highest hydrogen yield achieved with the working catalyst, although it was recorded at 950 K, and it is ∼25% smaller than the one obtained for the 1.5Pd@Rh/CeO_2//Mon. The longer residence time of the 1.5Pd@Rh/CeO_2//Mon experiments might allow MSR to take place to a greater degree, as deduced from the lower S_{CH_4} attained (S_{CH_4}=4%, figure 5.16, versus S_{CH_4}=9% for the 3RhPd@D/CeO_2//Mon), thus rendering larger Y_{H_2}.

These experiments showed that model 3RhPd@D/CeO_2 catalysts required higher operational temperatures than working catalysts to achieve the same catalytic activity and to avoid byproducts that led to catalyst deactivation.

Interestingly, both model catalysts exhibited a catalytic activity depletion in the low temperature regime (from 825 K to 950 K) during their first reaction tests, which was not observed for the working catalyst. However, both systems recovered the catalytic activity at T∼975 K and the usual catalytic performance was obtained for T≥1000 K. This temperature was higher than the one needed for full operation of working catalysts, possibly indicating that model catalysts needed more energy

to organize and accommodate the metal nanoparticles to the reactive environment, as they were composed of larger NPs.

5.3.2.b Feed load effect

The effect of the feed load (or space velocity) was evaluated at constant temperature and pressure (T=1050 K and P=4.5 bar) and S/C=3. The residence time of these experiments are from low to high feed loads per mass of catalyst: 11.7, 5.2, 0.8, 0.6, 0.5 and 0.4 s, respectively. Figure **5.23** shows the ethanol conversion and hydrogen yield recorded for this test. The corresponding H_2, CH_4, CO and CO_2 selectivities are plotted in figure **5.24**. In these experiments, as temperature was high enough to prevent side reactions, acetone and C_2 species concentrations were kept below 0.2% and only some acetaldehyde was detected. Therefore, in this case, only acetaldehyde was considered for the selectivities calculation.

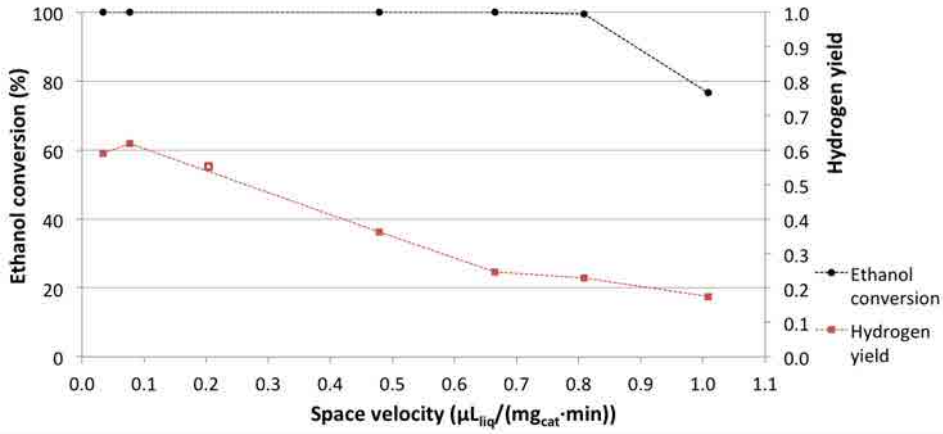

Figure 5.23: Influence of the space velocity on ethanol conversion and hydrogen yield of 3RhPd@D/CeO_2//Mon catalyst. Experimental conditions: T=1050 K, P=4.5 bar, S/C=3. The empty square shows the hydrogen yield recorded during the temperature screening (see figure **5.21**), v_{space}=0.22 $\mu L_{liquid}/(mg_{cat}min)$.

As seen in figure **5.23**, at 1050 K, full ethanol conversion was achieved for space velocities ranging from 0.03 to 0.67 $\mu L_{liquid}/(mg_{cat}min)$. For the next feed load (v_{space}=0.81 $\mu L_{liquid}/(mg_{cat}min)$), ethanol conversion slightly decreased, whereas for the highest feed load evaluated, v_{space}=1.01 $\mu L_{liquid}/(mg_{cat}min)$ (τ=0.4 s), the conversion diminished to 77%. As observed in figure **5.23**, the hydrogen yield diminished faster than ethanol conversion as the space velocity increased. The working catalyst also exhibited a faster diminution of the hydrogen yield than of ethanol conversion (see figures **5.4** and **5.5**), which indicated that, at the space velocities tested, both catalytic systems were able to decompose ethanol but the consecutive MSR and WGS reactions took place to a lesser extent at each increasing space velocity, due to the reduction of the residence time. This is corroborated by the products

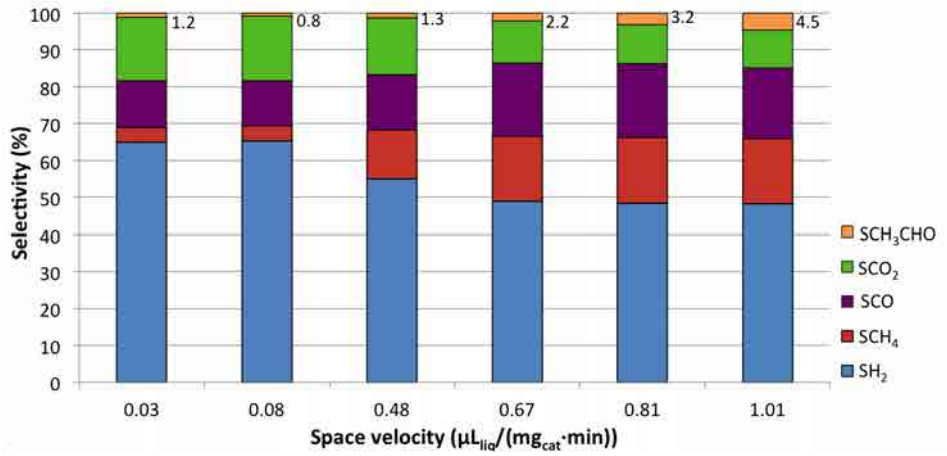

Figure 5.24: Influence of the space velocity on the selectivity to the main species produced by 3RhPd@D/CeO_2//Mon catalyst. Experimental conditions: T=1050 K, P=4.5 bar, S/C=3.

distribution (figure 5.24), in which higher feed loads per unit mass of catalyst led to larger CH_4 and CO concentrations and, as a result, to lower H_2 production. In addition, $\chi_{Ethanol}$ and Y_{H_2} values recorded for the highest loads were very similar in both catalytic systems, despite the difference in temperature between both tests (277 K difference), denoting that the model 3RhPd@D/CeO_2//Mon catalyst was much less active than the 1RhPd/CeO_2//Mon.

Comparing the results of the feed load tests of both model catalysts (both performed at 1050 K), 1.5Pd@Rh/CeO_2 catalysts showed an initial reduction of the ethanol conversion to 90% at v_{space}=1.6 $\mu L_{liquid}/(mg_{cat}min)$ (see figure 5.19). However, the ethanol conversion did not underwent a larger reduction until v_{space}=2.6 $\mu L_{liquid}/(mg_{cat}min)$, when it was reduced to $\chi_{Ethanol}$=78% and Y_{H_2}=0.4. On the other hand, the model 3RhPd@D/CeO_2 registered 77% ethanol conversion at half the space velocity (v_{space}=1.01 $\mu L_{liquid}/(mg_{cat}min)$), where Y_{H_2}=0.2 (see figure 5.23). However, if the corresponding residence times are compared, the 3RhPd@D/CeO_2 model catalyst showed the same ethanol conversion at a residence time of only 0.4 s versus the 1.1 s of the 1.5Pd@Rh/CeO_2. Therefore, the 3RhPd@D/CeO_2 catalyst was active enough to convert all the ethanol fed; the differences detected on the hydrogen yield arose again from the consecutive MSR and WGS reactions. These reactions occurred to a smaller degree on 3RhPd@D/CeO_2, as confirmed by the selectivities (compare figures 5.20 and 5.24), and thus the hydrogen yield recorded was lower (0.2).

Despite the larger amounts of C_2 species detected during these experiments than during 1.5Pd@Rh/CeO_2//Mon experiments, the 3RhPd@D/CeO_2//Mon gained only 0.110 g (44% of its initial mass) after the whole set of reactions.

At the beginning of the temperature tests of the 3RhPd@D/CeO_2 catalyst (section 5.3.2.a), high concentration of byproducts was recorded, which might be responsible for catalytic activity depletion. Therefore, the reaction temperature tests were repeated with a fresh 3RhPd@D/CeO_2//Mon catalyst, avoiding the low temperatures regime, where acetone and C_2 species were produced.

5.3.2.c Reaction temperature effect at 1 bar

For this test, a new 3RhPd@D/CeO_2//Mon catalyst was synthesized with 0.250 g of catalyst. The new temperature screening tests were carried out at 1 bar (instead of the 4.5 bar of the previous tests) and the temperature was varied between 923 K and 1050 K. Figure 5.25 shows the ethanol conversion, the hydrogen yield and the hydrogen flux obtained for these experiments. Prior to catalytic testing, the activation treatment with 10% H_2 (balanced N_2) was performed for 1 hour.

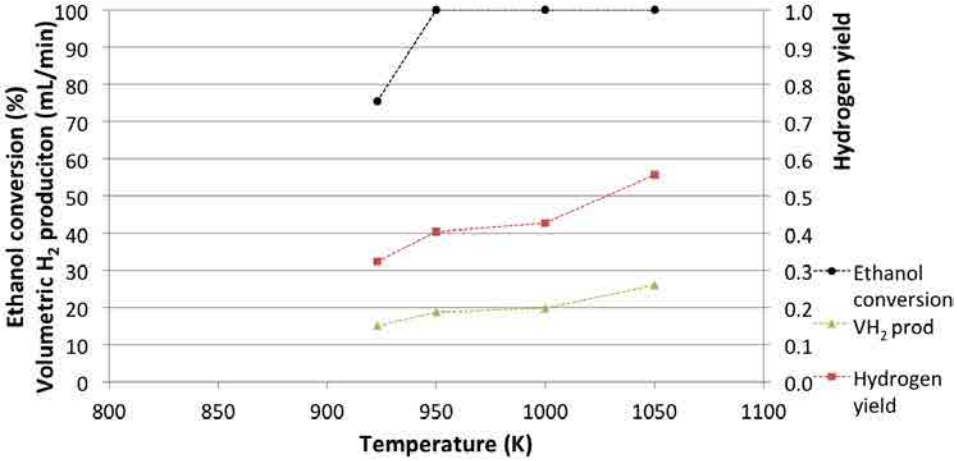

Figure 5.25: Influence of the temperature on ethanol conversion, hydrogen yield and volumetric H_2 production of 3RhPd@D/CeO_2//Mon catalyst. Experimental conditions: P=1 bar, S/C=3 and v_{space}=0.22 $\mu L_{liquid}/(mg_{cat} min)$.

As seen in figure 5.25, avoidance of the lowest temperatures led to improved catalytic activity and full ethanol conversion was achieved at 950 K, whereas in the previous test it was achieved at 1000 K (compare with figure 5.21). Moreover, at the lowest temperature tested now (923 K), $\chi_{Ethanol}$ was 75%, whereas before it reached its minimum at this temperature and $\chi_{Ethanol}$=40%. Despite this catalytic activity improvement, higher temperature than for the working catalyst was needed to achieve full ethanol conversion. Also, the hydrogen yield obtained at 923 K, 950 K and 1000 K was higher than in the previous tests, but the same maximum was achieved, 0.55, at 1050 K. This improved catalytic activity may be due to the suppression of acetone and C_2 species formation. During these experiments, acetaldehyde concentration was $< 0.3\%$, acetone concentration was kept below 0.5% and

ethane and ethylene concentrations were considerably reduced. As seen in figure 5.26, the highest selectivity to C_2 species recorded was 2.7%, which was recorded at the lowest temperature, and their selectivity gradually diminished as temperature increased. These experiments confirmed that avoidance of catalytic pathways that produce ethylene, ethane and acetone led to improved catalytic activity and prevented its depletion.

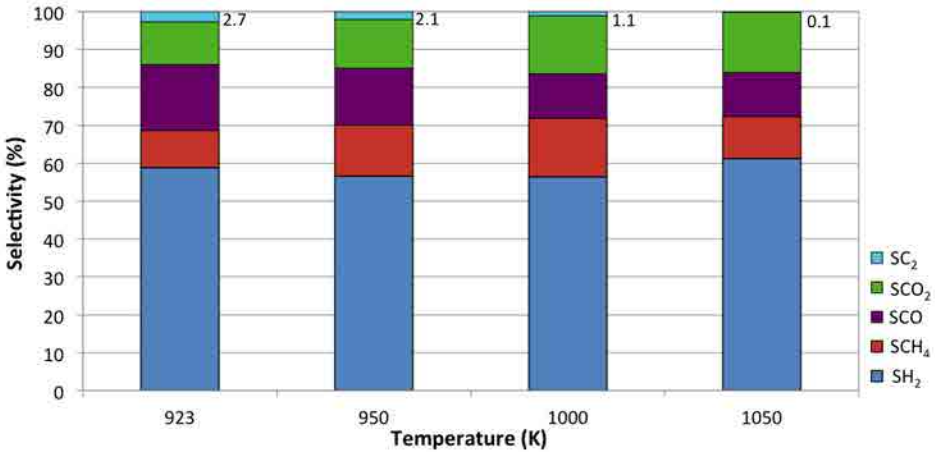

Figure 5.26: Influence of the temperature on the selectivity to reaction products of 3RhPd@D/CeO_2//Mon catalyst. Experimental conditions: P=1 bar, S/C=3 and v_{space}=0.22 $\mu L_{liquid}/(mg_{cat}min)$. The numbers show the selectivities to C_2 species.

5.3.3 Unsupported RhPd@D nanoparticles

The catalytic activity of unsupported RhPd@D NPs was subsequently studied in order to elucidate the activity differences between unsupported and supported NPs. To do so, a cordierite monolith was impregnated with exactly the same amount of RhPd@D NPs solution as in the tests of 3RhPd@D/CeO_2//Mon catalysts (1.166 mL) and then the impregnated RhPd@D//Mon was calcined at 573 K (2 K/min) for 2 hours.

Only a temperature screening was carried out with unsupported RhPd@D NPs and the operational parameters chosen were the ones that led to the best catalytic activity of the 3RhPd@D/CeO_2//Mon. Therefore, the reaction parameters evaluated were: 923 K$\leq$T$\leq$1050 K, P=1 bar, S/C=3 and v_{space}=0.22 $\mu L_{liquid}/(mg_{cat}min)$. The ethanol conversion, hydrogen yield and the volumetric hydrogen production obtained are plotted in figure 5.27, whereas figure 5.28 shows the corresponding selectivities.

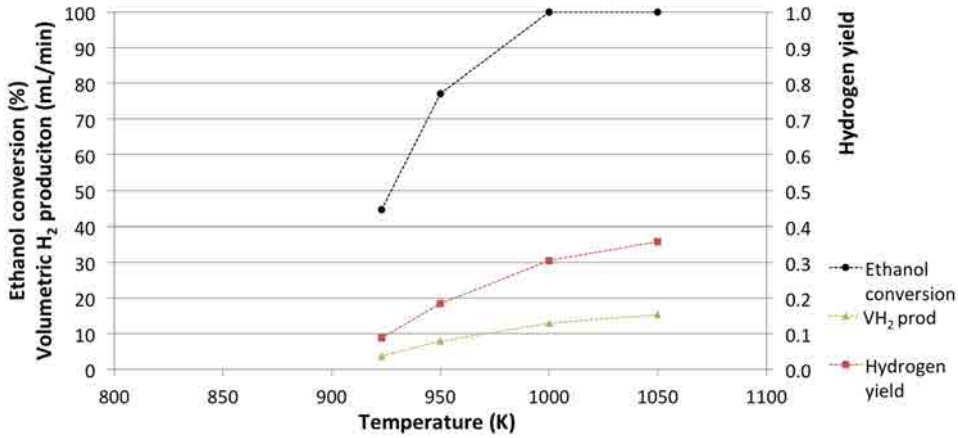

Figure 5.27: Influence of the temperature on ethanol conversion, hydrogen yield and volumetric H_2 production of unsupported RhPd@D NPs. Experimental conditions: P=1 bar, S/C=3 and v_{space}=0.22 $\mu L_{liquid}/(mg_{cat}min)$.

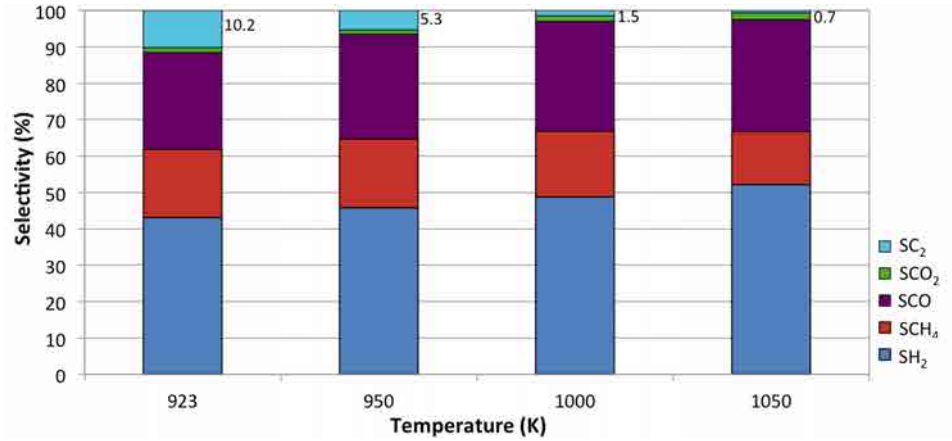

Figure 5.28: Influence of the temperature on the selectivity to reaction products of unsupported RhPd@D NPs. Experimental conditions: P=1 bar, S/C=3 and v_{space}=0.22 $\mu L_{liquid}/(mg_{cat}min)$. The numbers show the selectivities to C_2 species.

As seen in figure 5.27, the unsupported RhPd@D NPs were less active towards ethanol decomposition and full ethanol conversion was attained at T≥1000 K, whereas the same amount of supported NPs exhibited full ethanol conversion at T≥950 K (see figure 5.25). The hydrogen yield also showed differences with the previous experiments and the registered values were lower again for all the temperatures tested. Also the hydrogen flux produced was significantly lower than over the supported NPs. For instance, at 1050 K, the amount of hydrogen produced by the 3RhPd@D/CeO_2//Mon catalyst almost doubled that achieved by the RhPd@D NPs (28 versus 15 mL_{H_2}/min). In addition, the product distribution obtained was notably different in both systems, as arises from the comparison

between figures 5.26 and 5.28. The much higher CO_2 concentration attained by the 3RhPd@D/CeO_2//Mon than that obtained by the unsupported NPs (15.9% versus 1.8%, at 1050 K) shows promotion of the WGS reaction by CeO_2, as already reported [128]. In the case of the unsupported NPs, the lack of WGS promotion was also confirmed by the presence of large quantities of CO in the reformate stream (31.1% versus 12.3% for 3RhPd@D/CeO_2 catalyst at the same temperature). For all the temperatures tested, S_{CO_2} was kept below 2%, clearly indicating that WGS almost did not take place on the unsupported NPs and as a result S_{CO} was close to 30% for all the tests. Additionally, methane concentration was lower in the case of the real catalyst (11.0% for the 3RhPd@D/CeO_2//Mon versus 14.7% for the unsupported NPs, at 1050 K) indicating that MSR also took place to a greater degree in the presence of the CeO_2 support. These two effects led to higher hydrogen production for the 3RhPd@D/CeO_2 system than for the unsupported NPs, thus demonstrating the essential role of the ceria support for ESR. Another important difference between both systems was that for the unsupported RhPd@D NPs again large quantities of C_2 species were produced. The highest C_2 species concentration was again recorded for the lowest temperature, when the $S_{C_2}\sim10\%$ for the RhPd@D//Mon whereas with the 3RhPd@D/CeO_2//Mon its selectivity was $<3\%$, highlighting again the important role of the ceria support for ESR.

5.4 Catalytic screening of the CeO_2 support

A cordierite monolith was coated with 0.839 g of CeO_2 powder and then the functionalized CeO_2//Mon was calcined for 6 hours at 873 K (2 K/min). A temperature screening was carried out to investigate the ESR reaction performance of the bare ceria support. The operational parameters chosen were the previously tested for the unsupported RhPd@D NPs and again only the effect of one P and one S/C was evaluated. The operational conditions tested were: 825 K$\leq$T$\leq$1050 K, P=4.5 bar, S/C=3 and the space velocity of reactants was adjusted to the previously studied value v_{space}=0.22 $\mu L_{liquid}/(mg_{cat}min)$. This space velocity represented a residence time of 1.71 s. The ethanol conversion, hydrogen yield and volumetric hydrogen production are presented in figure 5.29. The selectivities to detected species are plotted in figure 5.30.

The bare CeO_2 support, in the absence of the active phase, converted 70% of the ethanol fed at 825 K, however the main species produced were H_2, CO_2 and C_2, as well as, ca. 5% of acetone. At T$\geq$875 K full ethanol conversion was attained and still high amounts of ethylene were present in the reformate stream. Even at 1050 K, $\sim$8% of C_2 species was produced. Methane concentration gradually increased as the temperature increased and the same trend was observed for CO, although the CO increment was smaller.

These tendencies indicated that principally ethanol decomposition, ethanol dehydration and WGS reactions were the reactions taking place. As a consequence, the hydrogen yield obtained during these experiments was low and nearly constant at 0.2, i.e, only 1.2 moles of H_2 were produced per mole of ethanol fed. After these tests, the CeO_2//Mon had turned black.

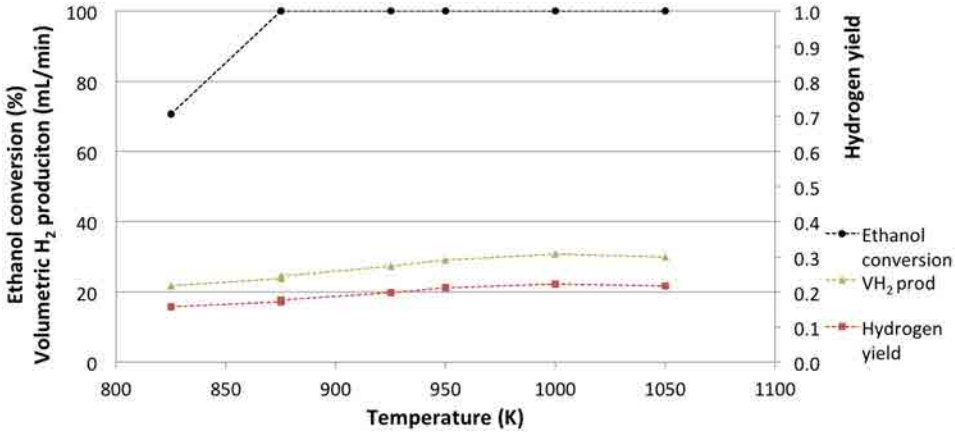

Figure 5.29: Influence of the temperature on ethanol conversion, hydrogen yield and volumetric H_2 production of CeO_2 support. Experimental conditions: P=4.5 bar, S/C=3 and v_{space}=0.22 $\mu L_{liquid}/(mg_{cat}min)$.

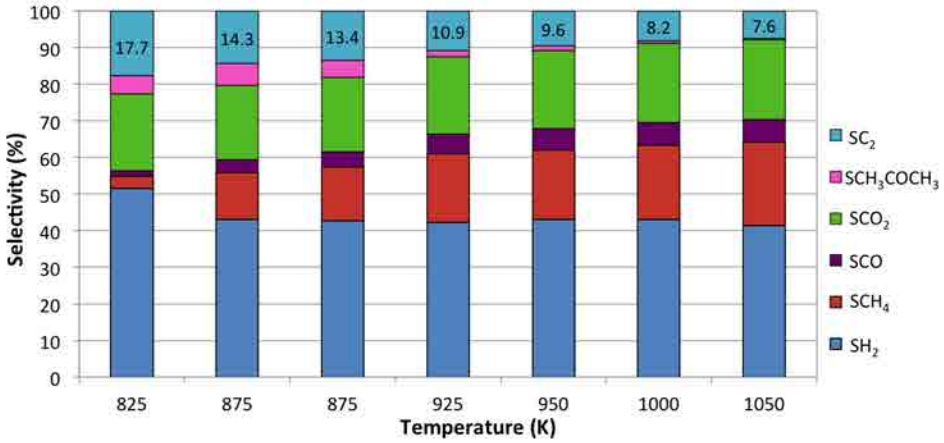

Figure 5.30: Influence of the temperature on the selectivity to reaction products of CeO_2 support. Experimental conditions: P=4.5 bar, S/C=3 and v_{space}=0.22 $\mu L_{liquid}/(mg_{cat}min)$. The numbers show the selectivities to C_2 species.

The reaction tests of the bare ceria support and of the unsupported RhPd@D NPs showed that the reaction performance of the $RhPd/CeO_2$ system was not the addition of the performance of its phases separately; a synergic effect existed between

the noble metals and the ceria support that led to better catalytic performance than the sum of the one attained by both systems separately.

5.5 Blank tests

The catalytic screening tests finished with the reaction evaluation of a blank stainless steel reactor in order to obtain the activity background of our reactors, as ESR reaction performance was evaluated at very high temperatures.

The reaction performance of the stainless steel reactors used as the housing of the functionalized monoliths was examined using the same operational parameters previously tested. To perform these experiments, an empty stainless steel reactor was placed inside the tubular furnace and the ethanol/water mixture was injected at the same rate as the one used for the CeO_2 support tests ($\dot{V}_{pump}$=0.171 mL/min), which corresponded to a residence time of 1.71 s. Initially, the reaction tests were intended to be performed at 4.5 bar. Nevertheless, due to the low catalytic activity of the blank reactor, pressure could not be risen and the tests had to be carried out at atmospheric pressure. At 1050 K, the reaction pressure could be fixed at 4.5 bar and the same catalytic results obtained at 1 bar were obtained at 4.5 bar. Figures 5.31 and 5.32 show the results obtained for these tests.

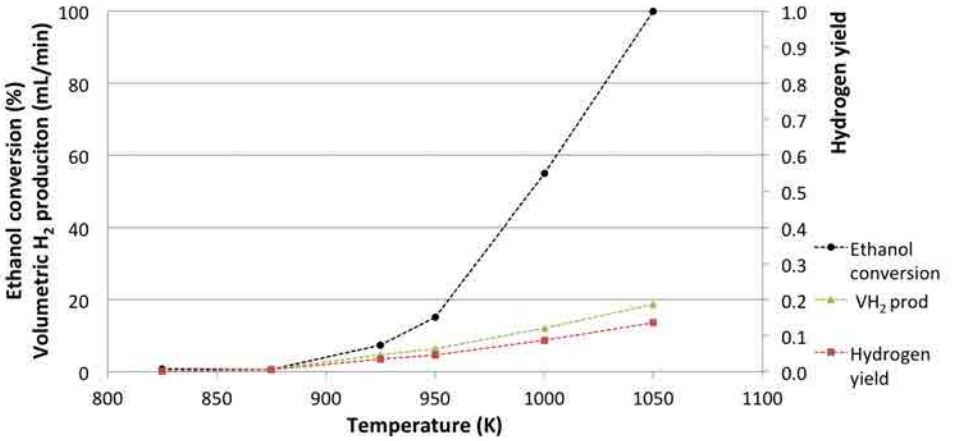

Figure 5.31: Influence of the temperature on ethanol conversion, hydrogen yield and volumetric H_2 production of the blank reactor. Experimental conditions: P=1 bar, S/C=3 and τ=1.71 s.

The blank reactor exhibited poor ESR activity performance and only for T≥1000 K ethanol conversion was significative. At 1050 K, full ethanol conversion was attained but the selectivity to reaction products showed that only ethanol decomposition took place along with some ethanol dehydration leading to the formation of C_2 species. Therefore, the ESR reaction performance observed for our catalysts

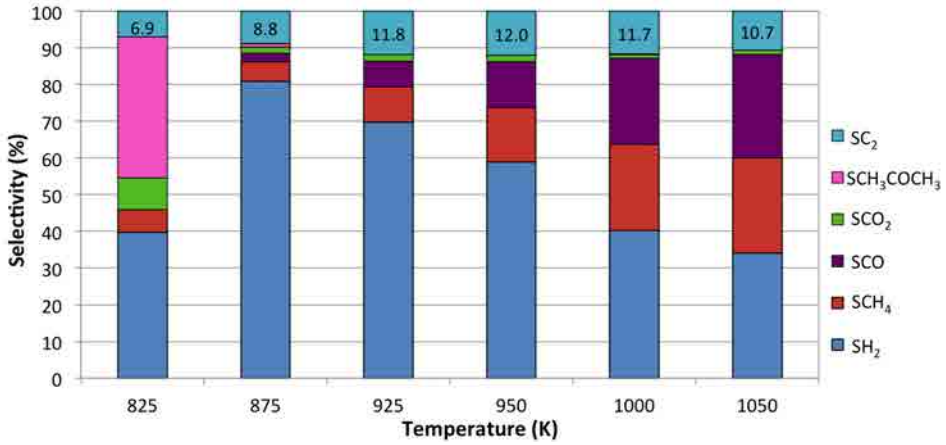

Figure 5.32: Influence of the temperature on the selectivity to reaction products of the blank reactor. Experimental conditions: P=1 bar, S/C=3 and residence time τ=1.71 s. The numbers show the selectivities to C_2 species.

during the screening tests was not significantly affected by the high temperatures tested themselves nor the presence of the stainless steel from which the reactors were made of.

5.6 Catalysts performance comparison

This section aims at comparing the catalytic performance of all the systems that have been described throughout this Chapter. To do so, the yield of the reaction products, as defined in equation **5.16**, has been considered, as it provides information about the ethanol conversion and the products distribution simultaneously.

$$Y_i(\%) = \frac{\chi_{Ethanol} \cdot S_i}{100}, \quad i = H_2, CH_4, CO_2, CO, ... \tag{5.16}$$

Figure **5.33** shows the comparison of the activity performance for all the catalytic systems investigated. The operational conditions chosen for the comparison are: T=950 K, S/C=3, v_{space}=0.22 $\mu L_{liquid}/(mg_{cat}min)$ and 1 bar. The results of the working catalyst were acquired at 1.5 bar (figure **5.3**), as no data was recorded at 1 bar. However, as already explained, figure **5.2** shows that lower P led to higher Y_{H_2}, thus even higher Y_{H_2} would be recorded at 1 bar. CeO_2 results shown correspond to the experiments performed at 4.5 bar.

As seen in figure **5.33**, only the catalytic systems composed of noble metals + support, i.e., 1RhPd/CeO_2, 1.5Pd@Rh/CeO_2 and 3RhPd@D/CeO_2, and the bare CeO_2 support were able to convert all the ethanol fed at 950 K and, among them, the one rendering the highest H_2 yield was the working catalyst 1RhPd/CeO_2. In

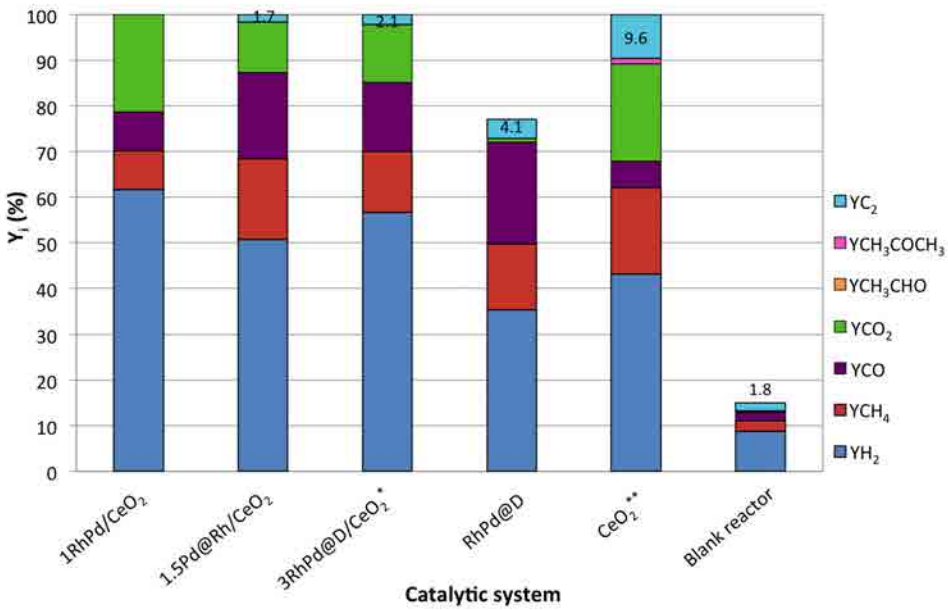

* Results of the second 3RhPd@D/CeO_2 catalyst tested (section **5.3.2.c**, figure **5.25**).

** Results obtained at 4.5 bar.

Figure 5.33: Reaction performance comparison between the different catalytic systems investigated. Experimental conditions: T=950 K, S/C=3 and v_{space}=0.22 $\mu L_{liquid}/(mg_{cat} min)$. The numbers show the selectivities to C_2 species.

addition, at the experimental conditions tested, only the 1RhPd/CeO_2 catalyst did not produce C_2 species and their avoidance is of major importance as it is a well-known route of catalysts deactivation. Regarding the hydrogen yield, the presence of the metal nanoparticles on the CeO_2 support clearly resulted in enhanced hydrogen production with respect to the bare CeO_2 support, as expected. Finally, with respect to the noble metals ratio, Pd@Rh/CeO_2 catalysts, where the Pd:Rh ratio was greater than the unity (Pd:Rh=75:1.3), favored hydrogen selectivity, however in terms of hydrogen yield, catalysts with Pd:Rh=1 performed better, as previously reported by Idriss et al. [63] and, in addition, produced less coke.

Throughout the temperature and feed load screening tests and also in the summarizing figure **5.33**, it has been shown that model catalysts were less active and selective than working catalysts, as model catalysts required higher operational temperatures to obtain the same catalytic activity as well as to avoid the formation of byproducts such as acetone, ethane and ethylene, which may cause catalyst deactivation. The catalytic activity differences exhibited by both catalytic systems (working catalysts -synthesized from salt precursors- or model catalysts -synthesized from preformed NPs-) may have their origin in the differences in particle size, as deduced from the transmission electron microscopy images (see section **4.3**). Large NPs have

less number of exposed metal atoms, but also small NPs may have electronic properties that make them specially reactive [129]. Should be taken into account here, that in the case of the 1.5Pd@Rh/CeO_2 catalyst, the differences in NPs composition may add to the differences caused by different particle size. In order to suppress the effect of different amount of metal exposed surface and confirm the hypothesis that larger NPs may be less reactive, the volumetric hydrogen production per mole of ethanol fed (i.e., $6{\cdot}Y_{H_2}$) was normalized per exposed surface of noble metals (NM) for the working and model catalysts tested. Spherical NPs were considered for calculations: of 4 nm in diameter for model 3RhPd@D/CeO_2 catalysts (see figure 4.3), of 2.5 nm in diameter for model 1.5Pd@Rh/CeO_2 catalysts (see figure 4.5) and of an average diameter of 2.0 nm for working catalysts' NPs (see figure 4.9). The same experiments chosen for comparison in figure 5.33 were compared here. Accordingly, the volumetric hydrogen production considered corresponded to the results obtained at T=950 K, S/C=3, v_{space}=0.22 $\mu L_{liquid}/(mg_{cat}min)$ and 1 bar for 1.5Pd@Rh/CeO_2//Mon and 3RhPd@D/CeO_2//Mon (figures 5.15 and 5.25, respectively) and 1.5 bar for the working catalyst (figure 5.3). Table 5.5 shows the parameters taken into account for the calculations and the results obtained are shown in table 5.6.

Table 5.5: Model and working catalysts properties.

Sample	Diameter (nm)	Metal loading (wt.%)	Catalyst mass (mg)
1. 1RhPd/CeO_2//Mon	2.0	1	245
2. 1.5Pd@Rh/CeO_2//Mon	2.5	1.5	101
3. 3RhPd@D/CeO_2//Mon	4.0	3	250

Table 5.6: Model and working catalysts activity normalized per exposed surface area of noble metals.

Sample	NM exposed surface (S, m^2)	$F_{H_2}/F_{Ethanol,in}$ $(\frac{mol_{H_2}}{mol_{Ethanol,in}})$	$F_{H_2}/(F_{Ethanol,in}{\cdot}S)$ $(\frac{mol_{H_2}}{mol_{Ethanol,in}{\cdot}m^2})$
1. 1RhPd-based	0.6	3.7	6.1
2. 1.5Pd@Rh-based	0.3	1.7	5.6
3. 3RhPd@D-based	0.9	2.4	2.6

The normalization of the hydrogen molar flux per mole of ethanol supplied and per unit of exposed surface of NM (the normalized production $F_{H_2}/(F_{Ethanol,\ in}{\cdot}S)$)

showed that the working 1RhPd/CeO_2//Mon catalyst was the most active catalyst tested. The normalized production of the 1RhPd/CeO_2//Mon catalyst more than doubled that achieved by the 3RhPd@D/CeO_2//Mon catalyst (6.1 versus 2.6 $mol_{H_2}/(mol_{Ethanol} \cdot m^2)$). Taking into account that these catalysts contained the same Rh:Pd ratio (Rh:Pd=1 for both catalytic systems), it was possible to conclude that smaller RhPd NPs were more reactive than the larger ones.

The normalized hydrogen production of the 1.5Pd@Rh/CeO_2//Mon catalyst was exceptionally good, even higher than that of 3RhPd@D/CeO_2//Mon. Nevertheless, the weight gained by 1.5Pd@Rh/CeO_2//Mon during its catalytic tests (5 times the catalyst mass), clearly denoted that large amounts of coke had deposited on its surface, resulting in an inadequate candidate for the ESR reaction. This could be related to the low amount of Rh in the catalyst, which is the responsible for the C-C bond scission.

6 Characterization after reaction and under reaction conditions

After the characterization of the as-synthesized catalysts and the study of their performance under several reaction conditions, this Chapter focuses on the study of catalysts while they are under reaction conditions and after being exposed to them. *In situ* and *operando* X-ray photoelectron spectroscopy allowed us to monitor the surface rearrangement of Rh and Pd, as well as of the ceria support while they were exposed to different surrounding environments. Also, the catalysts were characterized by transmission electron microscopy after being under reaction conditions in order to study morphology changes and carbon deposits formation driven by the exposure to reactants. Our first analyses started with the characterization of the catalysts after being under reaction conditions.

6.1 Characterization after reaction by electron microscopy

6.1.1 Powdered catalysts

The working catalyst 2RhPd/CeO_2 was analyzed by STEM and HRTEM after being under reaction conditions at 950 K for 2 hours and at 1050 K for 2 hours more at atmospheric pressure. The catalytic tests were carried out with S/C=3 and a rather high feed load (0.81 $\mu L_{liquid}/(mg_{cat}min)$) without dilution (see figure **5.4**). The noble metals concentration chosen for these analyses was 1 wt.% Rh + 1 wt.% Pd in order to compare NPs morphology and composition before (see section **4.3.1**) and after reaction.

The study of the 2RhPd/CeO_2 catalyst by HRTEM (Jeol2010F) after reaction allowed for the identification of Rh and/or Pd NPs dispersed over the ceria sup-

port, as shown in figure 6.1. The identified NPs allowed for mean particle size determination after reaction and the size distribution obtained was 3.1 ± 1.2 nm, whereas before reaction NPs ranged 1-2 nm (see figure 4.9). Under the reaction conditions tested, the NPs developed round shape and grew, although no noble metals aggregates were detected, denoting that massive sintering did not take place.

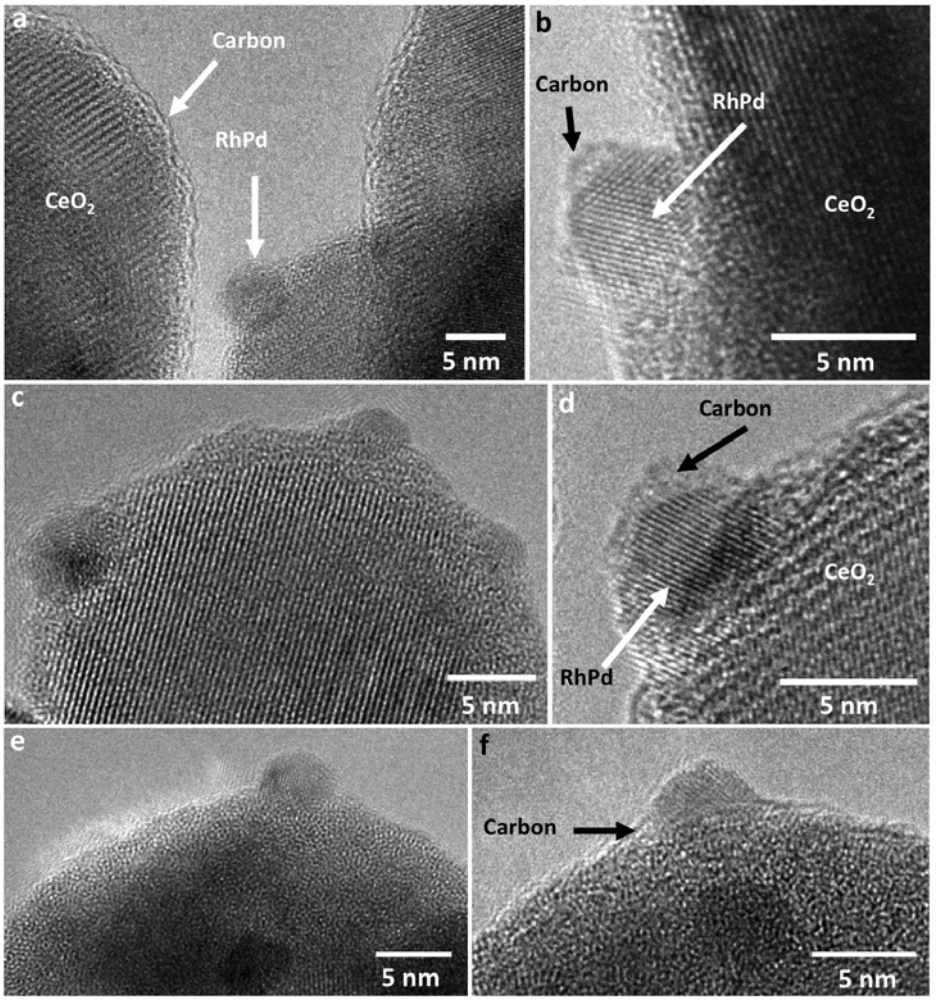

Figure 6.1: HRTEM images of the post-reacted 2RhPd/CeO_2 catalyst showing the detail of the NPs identified.

Interestingly, HRTEM micrographs revealed NPs with crystalline structure, indicating that NPs synthesized from $RhCl_3$ and $PdCl_2$ reorganized during the reaction conditions tested, in contrast to the as-prepared catalyst. The STEM images of the as-synthesized 2RhPd/CeO_2 catalyst showed NPs with no ordered atomic structure, as previously discussed in section 4.3.1 (see figure 4.9). However, as seen in the HRTEM images shown in figure 6.1, during the reaction conditions tested RhPd

NPs clearly developed atomic order. In figures 6.1b and 6.1d RhPd lattice fringes are the clearest. The NPs found exhibited mostly one family of crystallographic planes at 2.23 Å, which corresponded to the (111) reflection of the fcc lattice of either metallic Rh or Pd and consequently its bimetallic nature could not be assured. In some areas, it was possible to detect some carbon deposits surrounding the ceria support, as seen in figure 6.1a, or surrounding the NPs as seen in images 6.1b, 6.1d and 6.1f. Carbon deposits can be identified as the blurry material that surrounds NPs and the ceria support. No structured carbon was detected neither carbon formed separating the NPs from the support.

The reacted 2RhPd/CeO_2 catalyst was also analyzed by STEM (at the Institut Català de Nanociència i Nanotecnologia with a FEI TECNAI F20 S/TEM microscope) in order to elucidate the composition of the NPs detected, as it could not be unambiguously determined by HRTEM. Figure 6.2 shows representative STEM images of the post-reacted 2RhPd/CeO_2 catalyst. In these STEM images, RhPd NPs can be identified as the bright dots dispersed over the ceria surface. Energy dispersive X-ray (EDX) analyses were performed on individual NPs and all the sampled NPs exhibited Rh and Pd signals (see figure 6.2d), indicating that after reaction NPs maintained their alloyed composition. The STEM images also revealed the formation of voids on the ceria support, probably due to the reaction conditions tested, because they were not noticed in the fresh catalyst. These voids can be identified in figures 6.2a and 6.2b as the dark regions of the ceria support.

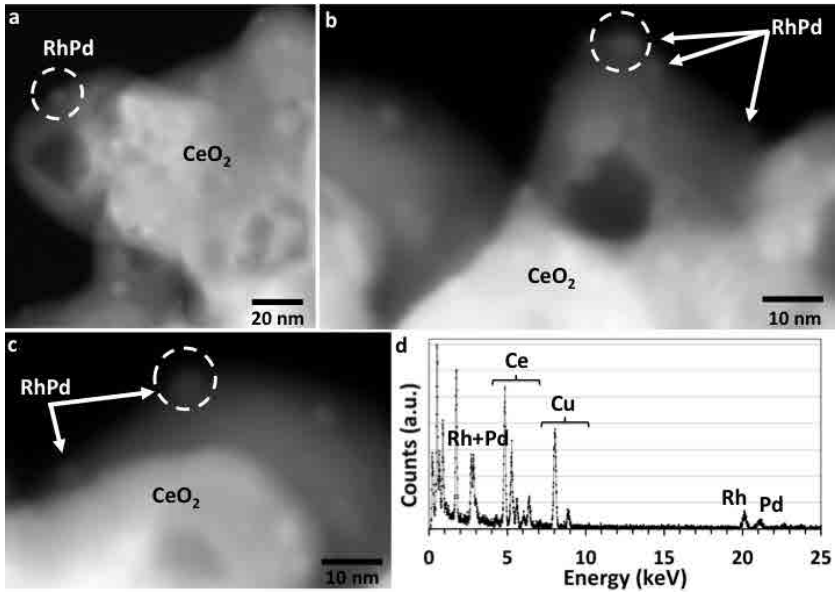

Figure 6.2: a to c) Representative STEM images of the post-reacted 2RhPd/CeO_2 catalyst. Circles mark the analyzed NPs. d) Representative EDX spectrum acquired in the NP encircled in c. The Cu signal originates on the Cu TEM grid.

The 2RhPd/CeO_2 morphology was also studied after a high temperature reduction: 2RhPd/CeO_2 powder was placed inside a stainless steel reactor and the catalyst was reduced with 4% H_2 (balanced in Ar) at the highest reaction temperature evaluated (1050 K, 13 K/min) for 1 hour. Then, the reduced 2RhPd/CeO_2 powder was analyzed by STEM in the high angle annular dark field imaging mode at the Center for Functional Nanomaterials (BNL, with an Hitachi HD2700C aberration corrected microscope). Figure **6.3** shows representative images of the identified RhPd NPs. After the reduction treatment, the NPs also developed round shape and agglomerated as their present mean size was 3.9 ± 2.4 nm. Electron energy loss spectroscopy (EELS) analyses revealed Rh and Pd signals on the NPs sampled. The exposure to a hydrogen atmosphere at 1050 K led to larger NPs than the exposure to ethanol steam reforming conditions at the same temperature. The STEM-HAADF imaging mode also allowed for RhPd clusters detection between two ceria crystallites (see figure **6.3**c), similar to the ones detected before reaction (see figure **4.9**e), and their bimetallic composition was confirmed by EELS.

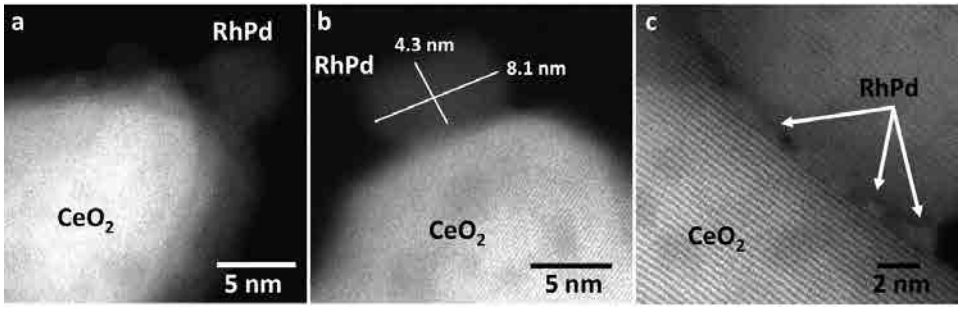

Figure 6.3: STEM images of the reduced 2RhPd/CeO_2 catalyst at 1050 K.

Additionally, a model catalyst was also studied after the same high temperature reduction (4% H_2 at 1050 K for 1 hour) to investigate the NP growth experienced by supported preformed RhPd@D NPs. Representative STEM images are shown in figure **6.4**.

For these analyses, the 3RhPd@D/CeO_2 model catalyst was chosen. This sample was chosen as the 3 wt.% noble metal content allowed for RhPd@D/CeO_2 catalysts characterization before reaction (section **4.3.2**), as well as under reaction conditions (these results are discussed in section **6.3.2**). As seen in figure **6.4**, after the hydrogen reduction at 1050 K, the RhPd@D NPs constituting the 3RhPd@D/CeO_2 catalyst exhibited a wide distribution of particle size and its distribution was 4.4 ± 2.0 nm. The growth experienced by the RhPd@D NPs was similar to that exhibited by the RhPd NPs.

In addition to powdered catalysts characterization after reaction, also the structured catalyst 1RhPd/CeO_2//Mon was analyzed by SEM after catalytic testing.

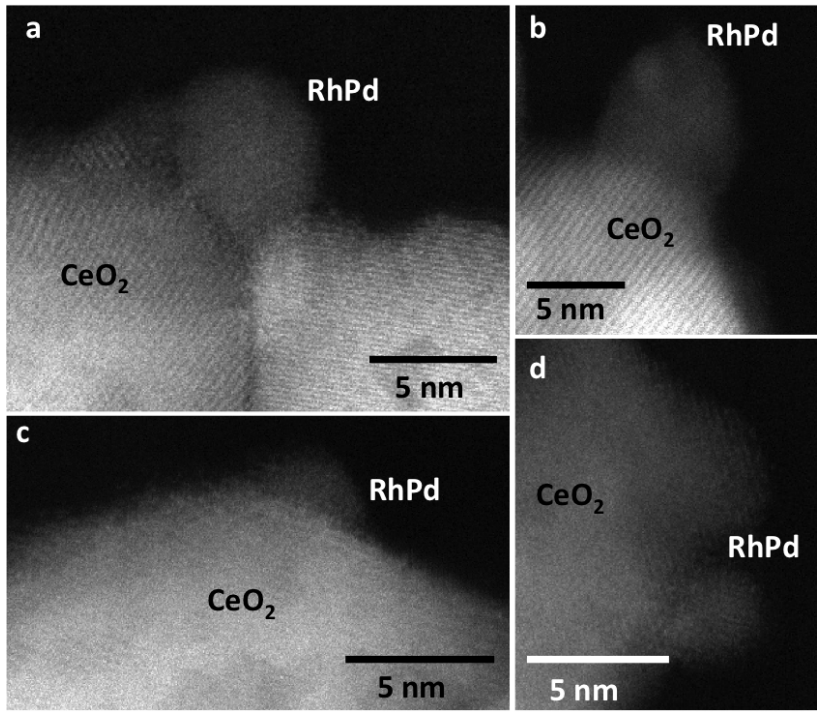

Figure 6.4: STEM images of the reduced 3RhPd@D/CeO_2 catalyst at 1050 K.

6.1.2 Functionalized monoliths

Morphological changes underwent after reaction by the ceria coating developed over cordierite monoliths were studied over a reacted 1RhPd/CeO_2//Mon by means of SEM, as the catalytic activity of RhPd/CeO_2 working catalysts was deeply examined in this Thesis. It is important to study the status of the ceria coating after reaction and investigate if it withstands the reaction conditions to which the ceria layer is subjected to.

The fresh 1RhPd/CeO_2//Mon studied by SEM in section 4.4 (see figure 4.13) is studied here after reaction. The fresh 1RhPd/CeO_2//Mon was longitudinally cut in two pieces as schematically represented in figure 6.5: one of the pieces was studied on its fresh form and was described in section 4.4, and the other piece was placed inside a stainless-steel reactor where the ethanol steam reforming (ESR) reaction at T=950 K, S/C=3 and 0.81 $\mu L_{liquid}/(mg_{cat}min)$ was performed for 2 hours in our laboratory. After this catalytic test, the reacted piece was examined by SEM.

Figure 6.6a shows three adjacent channels with a homogeneous ceria coating completely covering the cordierite channels and the subjacent cordierite macropores.

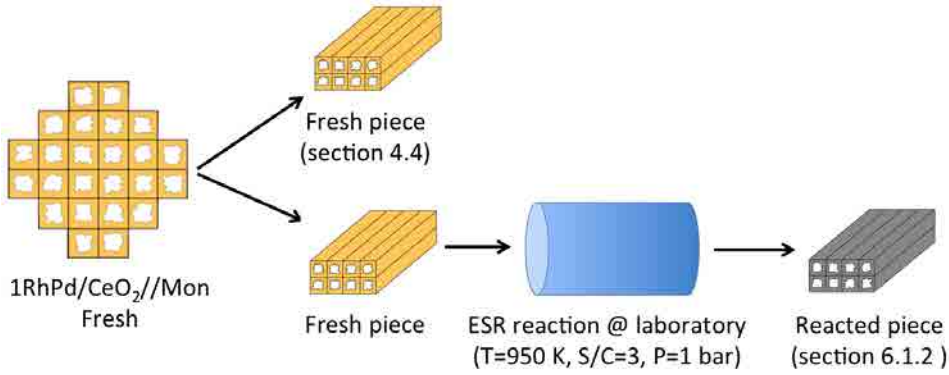

Figure 6.5: Scheme of the longitudinal cut performed on the fresh 1RhPd/CeO_2//Mon catalyst and the steps followed on each piece.

In the higher magnification SEM images **6.6**b and **6.6**c, well-dispersed and uniform CeO_2 particles can be seen once more. Practically no morphological differences with the fresh monolith were noticed (compare figures **6.6**b and **4.13**b), except for the scarce nanocracks detected on the reacted 1RhPd/CeO_2//Mon (figure **6.6**c) and no carbon deposits were detected neither. During the reaction conditions tested, ceria crystallites maintained their shape and only a slight size variation was detected as the mean crystallite size after reaction was 30 ± 7 nm, whereas before reaction ceria crystallites ranged 26 ± 5 nm, indicating that no strong sintering occurred during reaction. Probably this small increase in size of the ceria crystallites was responsible for the few nanocracks observed in some areas of the ceria coating. The SEM located at the Centre de Recerca en Nanoenginyeria (CRnE) (Universitat Politècnica de Catalunya, UPC) is equipped with a focused Ga^+ ion beam (FIB) that allows for groove performing so that deep layers get exposed and depth-profile studies can be carried out.

Figure **6.6**d shows the groove made with the FIB on one of the reacted channels. The black zone in figure **6.6**d (which is the deepest region of the FIB-cut) corresponds to the cordierite honeycomb. On top of the cordierite monolith, the catalytic layer that completely covered the cordierite surface and also filled one of its pores can be distinguished. On top of the RhPd/CeO_2 layer, the carbon coating deposited by sputtering to allow SEM analysis and a Pt strip can be differentiated. The Pt strip was deposited in order to perform a clean FIB-cut. Figure **6.6**e shows a higher magnification image of the area enclosed by white dots in figure **6.6**d, where a detailed view of the layers profile made with the FIB-cut is shown. As seen in figure **6.6**e, after reaction, the revealed CeO_2 layer was homogeneous, uniform, well-adhered and perfectly filled the cordierite pore of variable thickness between 100 and 200 nm. Therefore, the developed method to coat honeycombs led to successfully ceria coated cordierite monoliths with homogeneous layers that withstood reaction conditions.

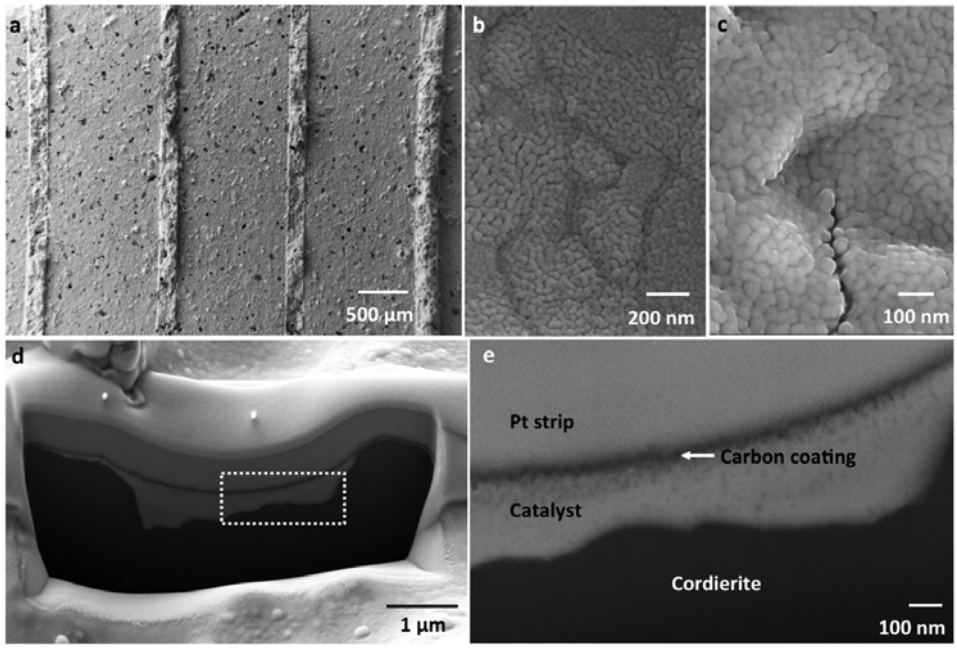

Figure 6.6: a to c) SEM images of the reacted 1RhPd/CeO_2//Mon inner channels. d) FIB-cut performed in one of the channels. e) Detail of the region enclosed in d) showing the FIB-cut and the profile view of the layers developed over the cordierite honeycomb.

6.2 *In situ* characterization by X-ray photoelectron spectroscopy

Powdered and structured catalysts were analyzed by X-ray photoelectron spectroscopy (XPS) in order to identify the species present on the catalyst surface and subsequently quantify the ratio between ceria and noble metals and ceria and reaction residues such as carbonaceous deposits. In addition, the XPS apparatus available at the CRnE (UPC) is coupled to a high pressure cell (reaction chamber) where gaseous reactions can be performed *in situ*, i.e. without removing the samples of the system and exposing them to the atmosphere. During reaction performance, the reaction chamber is isolated from the rest of the system and the desired reactants are introduced into it in gaseous form where pressures up to 20 bar can be reached. The available equipment also allows to increase the temperature up to ∼873 K, although the exact temperature reachable depends on the examined atmosphere. The reaction chamber is equipped with a mass spectrometer to analyze the gaseous products formed during the experiment and assure that the studied reactions take place. Sample transfer between the XPS analysis chamber and the high pressure cell (and vice versa) is carried out under ultra high vacuum (UHV) conditions and therefore, in principle, the state of the sample is preserved (or *quenched*) during

transfer. Figure 6.7 shows a picture of the XPS system. In summary, *in situ* XPS allows for catalysts exposure to different reaction environments, preserve the new induced state under UHV conditions, although some articles claim that UHV may alter the surface of the catalysts [130] (samples are kept under UHV during the whole process), and, subsequently, analyze them by XPS without manipulating the samples neither exposing them to the atmosphere.

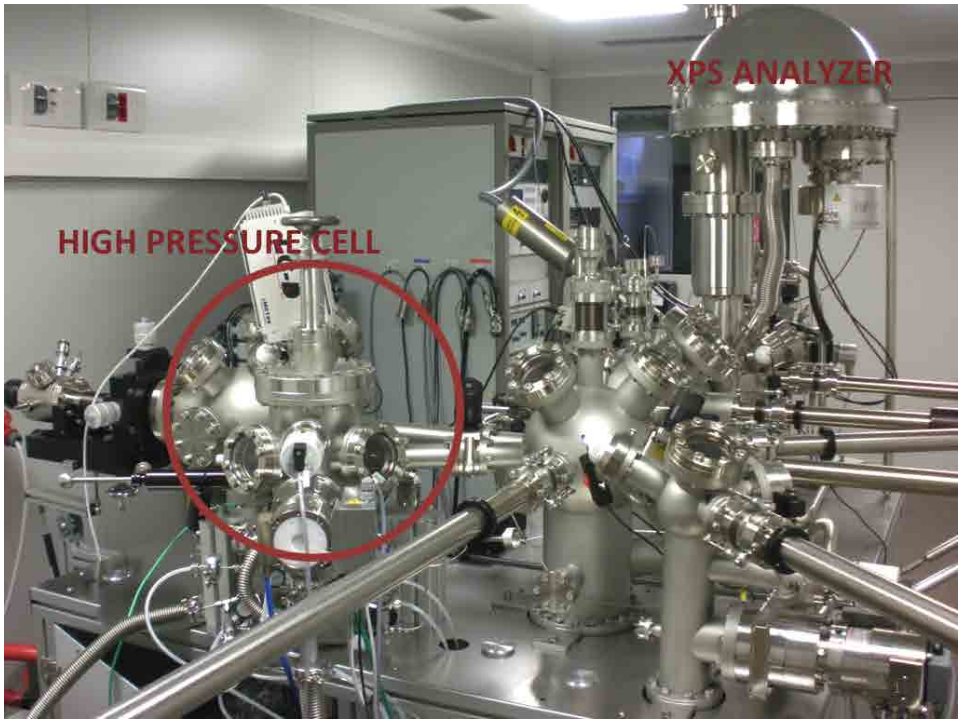

Figure 6.7: XPS equipment located at CRnE (UPC).

6.2.1 Functionalized monoliths

6.2.1.a *In situ* ESR reaction study

A fresh 1RhPd/CeO_2//Mon was synthesized in order to monitor the changes underwent after *in situ* ESR reaction performance. The sequence followed for this investigation was: 1) XP spectra acquisition of the as-synthesized 1RhPd/CeO_2//Mon, 2) ESR reaction performance at T=823 K, S/C=3 and atmospheric pressure inside the high pressure cell, 3) XP spectra acquisition of the reacted monolith. This sequence is schematically represented in figure 6.8, along with the nomenclature of the sample at each step.

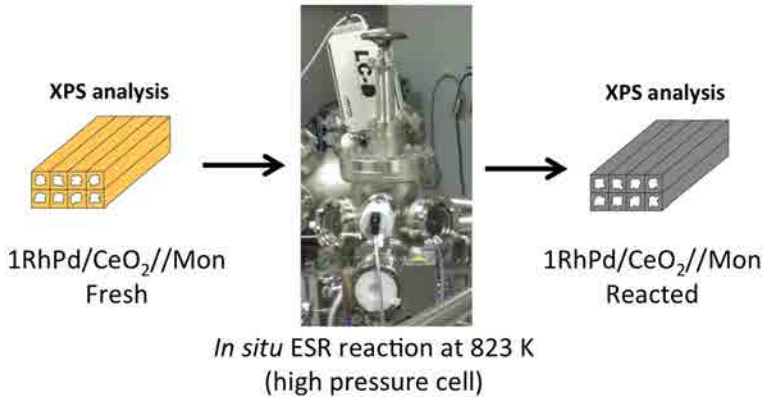

Figure 6.8: Sequence of XPS analyses performed on the fresh 1RhPd/CeO_2//Mon catalyst along with the nomenclature of the sample at each step.

The 1RhPd/CeO_2//Mon was first analyzed by XPS as synthesized. The flood gun was used in order to compensate the charge of the sample and its parameters (voltage and intensity) were adjusted till the position of the adventitious C 1s was at 284.8 eV. In all the experiments of the RhPd/CeO_2 system the parameters of the flood gun were adjusted in the same way. The first survey spectrum revealed high concentration of adventitious carbon due to sample manipulation and hence, in order to reduce it, the fresh monolith had to be cleaned in the analysis chamber with the Ar^+ ion gun. After the cleaning process, a survey spectrum and Rh 3d, Pd 3d, Ce 3d, C 1s spectral regions were acquired. The same procedure described in section **4.3** was followed here to deconvolute the acquired spectra by using CasaXPS© software: all spectra were referred to the adventitious C 1s signal at binding energy (BE) 284.8 eV. Rhodium 3d and Pd 3d spectra were deconvoluted constraining the known distance and the areas ratio between the $3d_{5/2}$ and $3d_{3/2}$ components of the spin-orbit doublet. Finally, cerium 3d spectrum was deconvoluted using six peaks for Ce^{4+} (V, V", V"', U, U" and U"') and four peaks for Ce^{3+} (V^0, V', U^0 and U'), where U and V refer to the $3d_{3/2}$ and $3d_{5/2}$ spin-orbit components, respectively [121], and the constraining in the $3d_{5/2}$ and $3d_{3/2}$ areas ratio was also taken into account. Subsequently to the XPS analysis of the fresh 1RhPd/CeO_2//Mon, the sample was transferred to the high pressure cell and ESR was performed at 823 K. The ethanol/water mixture was introduced into the reaction chamber using a bubbler where 20 mL/min N_2 were flown. According to Raoult's law, the concentration of the ethanol/water mixture in the bubbler was set to S/C=8 in order to obtain a saturated stream with S/C=3 at atmospheric pressure. Synthetic ethanol was used in this experiment and ESR reaction was performed for 20 minutes. After 20 minutes of reaction, the high pressure cell was opened and the gaseous effluent concentration was qualitative analyzed by the mass spectrometer. The mass spectrometer showed H_2, CO, CO_2, CH_4 and acetaldehyde signals, which confirmed that ESR did take place during our experiment inside the reaction chamber. Once

the reaction chamber gases were pumped down and high vacuum was recovered, the sample was transferred to the analysis chamber and a survey spectrum and C 1s, Rh 3d, Pd 3d and Ce 3d spectra were recorded once again.

First of all, survey spectra were examined in order to identify all the contributions present, as signals from the elements of our $RhPd/CeO_2$ coating and also from the cordierite[1] honeycomb were recorded. Figure 6.9 shows the survey spectra with all the XPS and Auger peaks identified on the fresh $1RhPd/CeO_2//Mon$ (figure 6.9a) and on the monolith after the *in situ* ESR reaction performance (figure 6.9b). Argon peaks from the ion gun cleaning were identified on both spectra. The results obtained from spectra deconvolution for the fresh and reacted status are reported in table 6.1. In this case, due to the high cordierite signals recorded, the noble metals could not be unambiguously deconvoluted and only the C/Ce atomic ratio and Ce oxidation state could be accurately calculated.

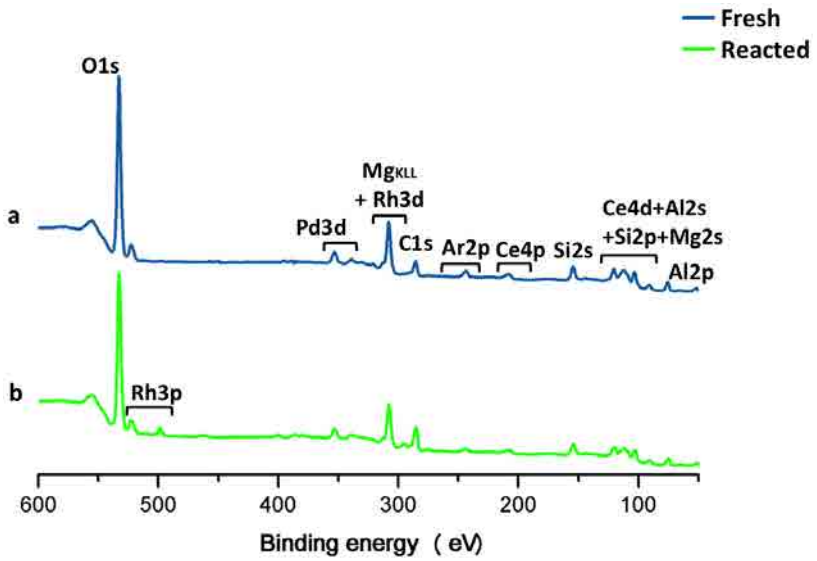

Figure 6.9: Survey XP spectra recorded for the: a) fresh $1RhPd/CeO_2//Mon$. b) *in situ* reacted $1RhPd/CeO_2//Mon$.

Table 6.1: XPS results of the fresh and *in situ* reacted $1RhPd/CeO_2//Mon$.

	Atomic ratio	
Status	C/Ce	$Ce^{4+}/(Ce^{4+}+Ce^{3+})$
Fresh	0.85	0.26
Reacted	2.28	0.28

[1]Cordierite is a magnesium iron aluminum silicate of general formula $(Mg, Fe)_2Al_4Si_5O_{18}$.

From the XPS results it was possible to conclude that, despite the initial sample cleaning with the Ar^+ ion gun, high amounts of C were still detected as indicated the high C/Ce atomic ratio (0.85) obtained on the fresh 1RhPd/CeO_2//Mon. In addition, as a consequence of the cleaning process ceria strongly reduced and only 26% of Ce was Ce^{4+} (should be reminded here that the last step of the synthesis process is a calcination at 573 K). Figure 6.10a shows the Ce 3d spectrum acquired on the fresh 1RhPd/CeO_2//Mon after the ion gun cleaning and figure 6.10b shows the Ce 3d spectrum of the 1RhPd/CeO_2//Mon after the *in situ* performance of the ESR reaction. Both spectra show the high contribution of the Ce^{3+} V^0, V', U^0 and U' components. The nomenclature of the Ce 3d peaks follows the Burroughs convention [121] and their order from low to high binding energy is V^0, V, V', V", V"', U^0, U, U', U" and U"'. After ESR reaction, the amount of C increased three times with respect to the fresh sample and cerium remained strongly reduced (only 28% was Ce^{4+}). Unfortunately, the evolution of the noble metals could not be elucidated due to the high contribution of the elements of the cordierite monolith.

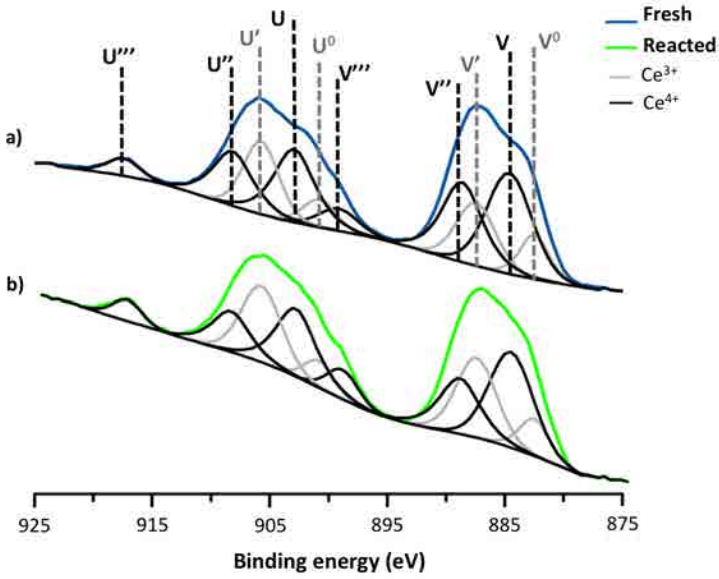

Figure 6.10: XP spectrum of Ce 3d recorded for the: a) fresh 1RhPd/CeO_2//Mon catalyst. b) *in situ* reacted 1RhPd/CeO_2//Mon.

Therefore, we decided to repeat these tests with powdered catalysts which facilitated the analyses as only features corresponding to the elements of our RhPd/CeO_2 catalyst were recorded. These results are discussed in section 6.2.2.

6.2.1.b *In situ* regeneration study

An additional XPS study of a functionalized cordierite monolith was performed prior to the analysis of powdered catalysts. The 1RhPd/CeO_2//Mon used on the

bioethanol stability test and the oxidative regeneration treatments described in sections 5.2.4.b and 5.2.4.c, respectively, was analyzed by XPS. After the last oxidation at 773 K followed by the catalytic test in the laboratory reactor described in section 5.2.4.c, the 1RhPd/CeO_2//Mon on its deactivated form was longitudinally cut and a piece was placed inside the XPS apparatus. Initially, a survey spectrum and Rh 3d, Pd 3d, Ce 3d and C 1s spectra were acquired and analyzed as previously reported. In this case, no ion gun cleaning was performed in order to preserve the elements state. After the acquisition of the 1RhPd/CeO_2//Mon spectra on its deactivated form, the sample was transferred to the high pressure cell where an *in situ* oxidation at 773 K with 40 mL/min of air was performed for 30 minutes at atmospheric pressure. The same conditions were chosen for the *in situ* oxidation as for the oxidations performed in the laboratory reactor in order to emulate in the XPS apparatus the previously tested conditions and investigate the changes that oxidations had induced on the catalyst surface. This process is schematized in figure 6.11, where also the nomenclature of the samples at each step is given.

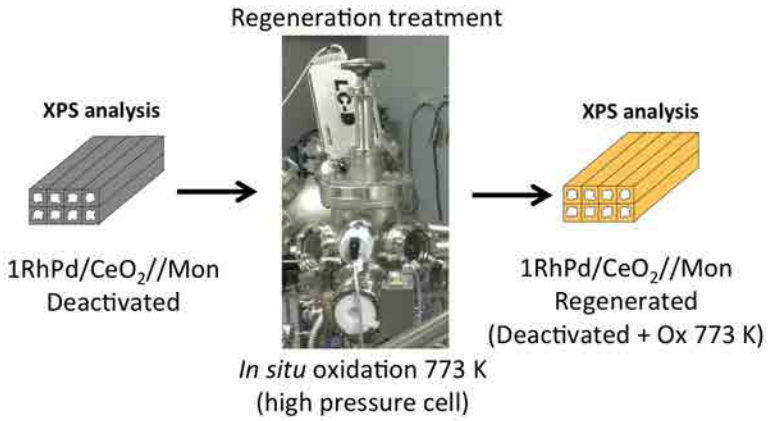

Figure 6.11: Sequence of XPS analyses performed on the deactivated 1RhPd/CeO_2//Mon after the bioethanol stability test along with the nomenclature of the sample on each step.

Once the 1RhPd/CeO_2//Mon was regenerated *in situ*, it was transferred back to the analysis chamber and the same parameters were chosen for XP spectra acquisition. Once more, the previously reported procedure was followed for XP spectra deconvolution and analysis.

Both survey spectra were initially examined in order to identify all the contributions present, as signals from our RhPd/CeO_2 coating, but also from the cordierite honeycomb were recorded. In this experiment, the survey spectra were also checked for impurities derived from bioethanol and only chlorine was detected on the deactivated sample (no sulfur traces were recorded). Tungsten signals from the sample

holder were also identified. Figure **6.12** shows the survey spectra with all the XPS and Auger peaks identified over the deactivated 1RhPd/CeO_2//Mon (figure **6.12**a) and over the regenerated (deactivated + Ox773 K) catalyst (figure **6.12**b), where Cl was nearly imperceptible. The Ce 3d XP spectra corresponding to these analyses are shown in figures **6.13**a and **6.13**b, respectively.

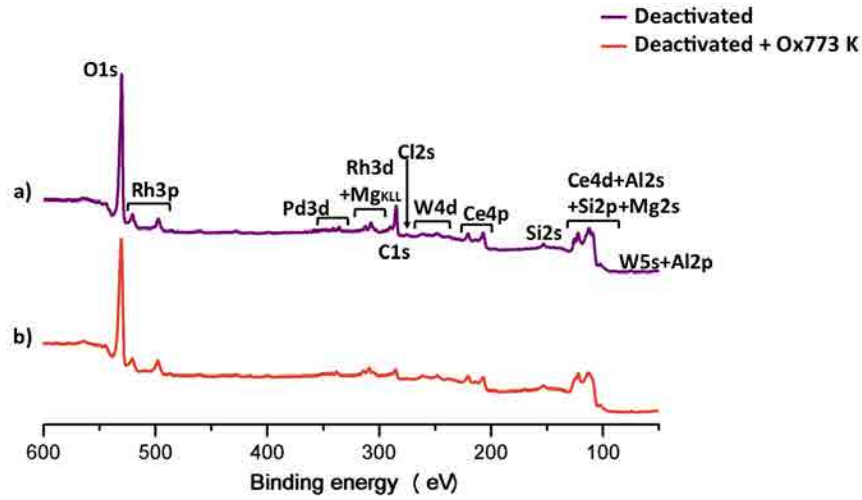

Figure 6.12: Survey XP spectrum recorded for: a) the deactivated 1RhPd/CeO_2//Mon after the bioethanol stability test. b) The *in situ* regenerated (deactivated + Ox773 K) 1RhPd/CeO_2//Mon.

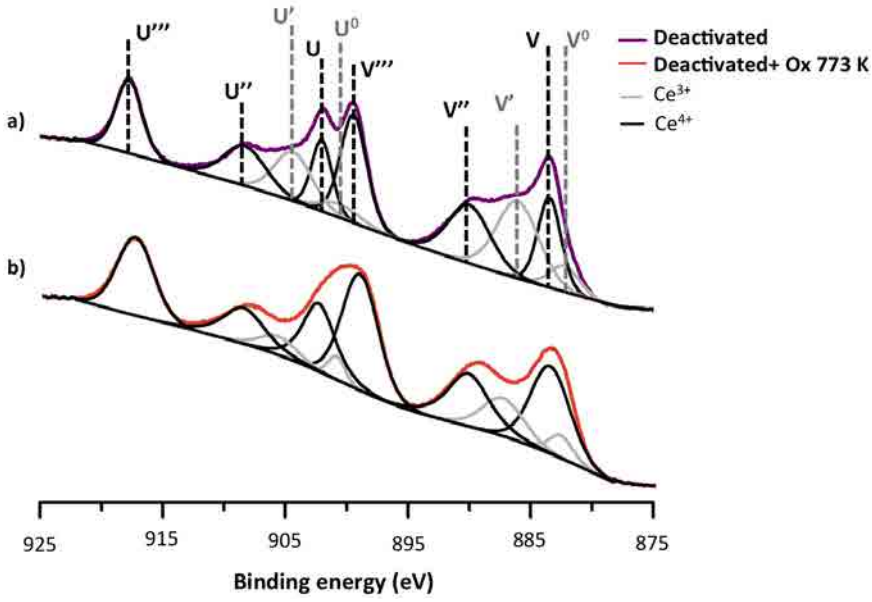

Figure 6.13: XP spectrum of Ce 3d recorded for: a) the deactivated 1RhPd/CeO_2//Mon. b) The regenerated (deactivated + Ox773 K) 1RhPd/CeO_2//Mon.

The results obtained from the XP spectra deconvolution are listed in table **6.2**.

Table 6.2: XPS results for the deactivated and *in situ* regenerated 1RhPd/CeO_2//Mon.

	Atomic ratio				
Status	Rh/Ce	Pd/Ce	C/Ce	Cl/Ce	Ce^{4+}/Ce
Deactivated	0.03	0.02	0.59	0.02	0.66
Regenerated	0.03	0.02	0.18	-	0.84

XPS results compiled in table **6.2** show for the deactivated catalyst that the surface carbon detected was ∼60% of that of surface cerium. Cerium was mainly oxidized as 66% Ce was found on the +4 oxidation state. As expected, after the oxidation at 773 K, C was considerably reduced. The C/Ce ratio was reduced one third, which represented a variation on nearly the same proportion as the one recorded for the *in situ* reacted monolith, where after ESR reaction the C/Ce ratio increased three times (table **6.1**). The formation of carbon deposits during ESR may be responsible for catalytic activity loss, as C formed superficially blocking ceria and NPs surface, as seen in HRTEM images of figure **6.1**. Interestingly, Rh/Ce and Pd/Ce ratios did not change after the oxidation at 773 K, indicating that further nanoparticle sintering did not take place during the oxidizing treatment[2]. This constituted an important result since NP sintering is also a well-known cause of catalyst deactivation and the oxidizing treatments allowed for catalytic activity recovery without leading to NP growth. These results may indicate, that once the NPs grew during the first exposure to the reactants (as seen in figure **6.1**), the successive treatments did not cause more NP sintering. As seen in figure **6.13**b, during the regeneration treatment, cerium oxidized and almost all (84%) was Ce^{4+}, as derived from the increase of the contribution of Ce^{4+} components after the *in situ* oxidation.

6.2.2 Powdered 1RhPd/CeO_2 catalyst

Unsupported 1RhPd/CeO_2 catalyst was characterized by *in situ* XPS in order to monitor the changes that each catalytic treatment provoked on the catalyst surface, which were performed during the synthesis and reaction processes, and avoid the spectral features of the cordierite monoliths.

Fresh 1RhPd/CeO_2 (noble metal loading 0.5 wt.% Rh + 0.5 wt.% Pd synthesized from $RhCl_3$ and $PdCl_2$) powder catalyst was synthesized and subsequently calcined at 573 K for 6 hours, following the synthesis process described in Chapter

[2]XPS is a surface sensitive technique and if NP sintering occurs the amount of exposed surface diminishes and consequently its XPS signal diminishes too.

3. Then the catalytic powder was pressed to form a self-consistent disk (pellet) that was placed over a stainless steel XPS sample holder and then introduced into the XPS system.

The sequence of *in situ* XPS analyses performed on the working 1RhPd/CeO_2 catalyst was: 1) catalyst as prepared, 2) oxidation at 573 K, 3) activation treatment (H_2 atmosphere at 573 K), 4) ESR performance at 823 K and 5) regeneration treatment at 773 K (oxidation at 773 K). An initial XPS analysis was performed in order to record the as deposited state of the sample (which corresponds to step 1) and then the mentioned catalytic treatments were carried out in the XPS reaction chamber at 1 bar. After each of these steps, the sample was transferred back to the analysis chamber, where a survey spectrum and Rh 3d, Pd 3d, Ce 3d, C 1s, O 1s regions were recorded. For this 1RhPd/CeO_2 catalyst, the sequence was extended and three treatments more were performed inside the high pressure cell, namely: 6) new activation with H_2 at 573 K, 7) ethanol oxidative steam reforming (OSR) at 823 K and 8) final reduction with H_2 at 773 K. These treatments were also carried out at 1 bar and the same spectral regions were acquired.

The ESR reaction test was performed following the procedure explained in section 6.2.1 and the ethanol/water mixture (S/C=3) was introduced into the high pressure cell by using the same bubbler. In the case of the OSR tests, the oxygen-to-ethanol ratio was fixed at O/E=1/2 and the steam-to-carbon at S/C=2. The required oxygen was supplied by adding 15 mL/min of air to 30 mL/min of N_2 and the total gaseous stream was flown through the bubbler.

Figure 6.14 shows the deconvolution of Rh 3d and Pd 3d regions for the whole sequence of *in situ* treatments. In this sample, Rh 3d and Pd 3d spectra were calibrated for energy taking into account the position of the reduced component of both noble metals (307.0 eV and 334.9 eV for Rh $3d_{5/2}$ and Pd $3d_{5/2}$, respectively), as the binding energy shifts underwent by Rh, Pd and Ce were different for each metal, probably due to differential charge effects and the nanoparticle size of the Rh-Pd system [131, 132]. On the other hand, the deconvolution of Ce 3d spectra for the whole sequence of experiments is shown in figure 6.15. From the spectra deconvolution, the relative atomic concentrations and the ratio between elements were calculated. Results obtained for the whole sequence are compiled in table 6.3.

Despite the low signal to noise ratio of Rh 3d and Pd 3d spectra, as a consequence of the low noble metal (NM) loading (0.5 wt.% Pd + 0.5 wt.% Rh), the analysis of the spectra allowed for the quantification of the total area of noble metals. Thus, the dispersion of both NM on the ceria surface and the formation and removal of carbon deposits after each catalytic treatment could be monitored.

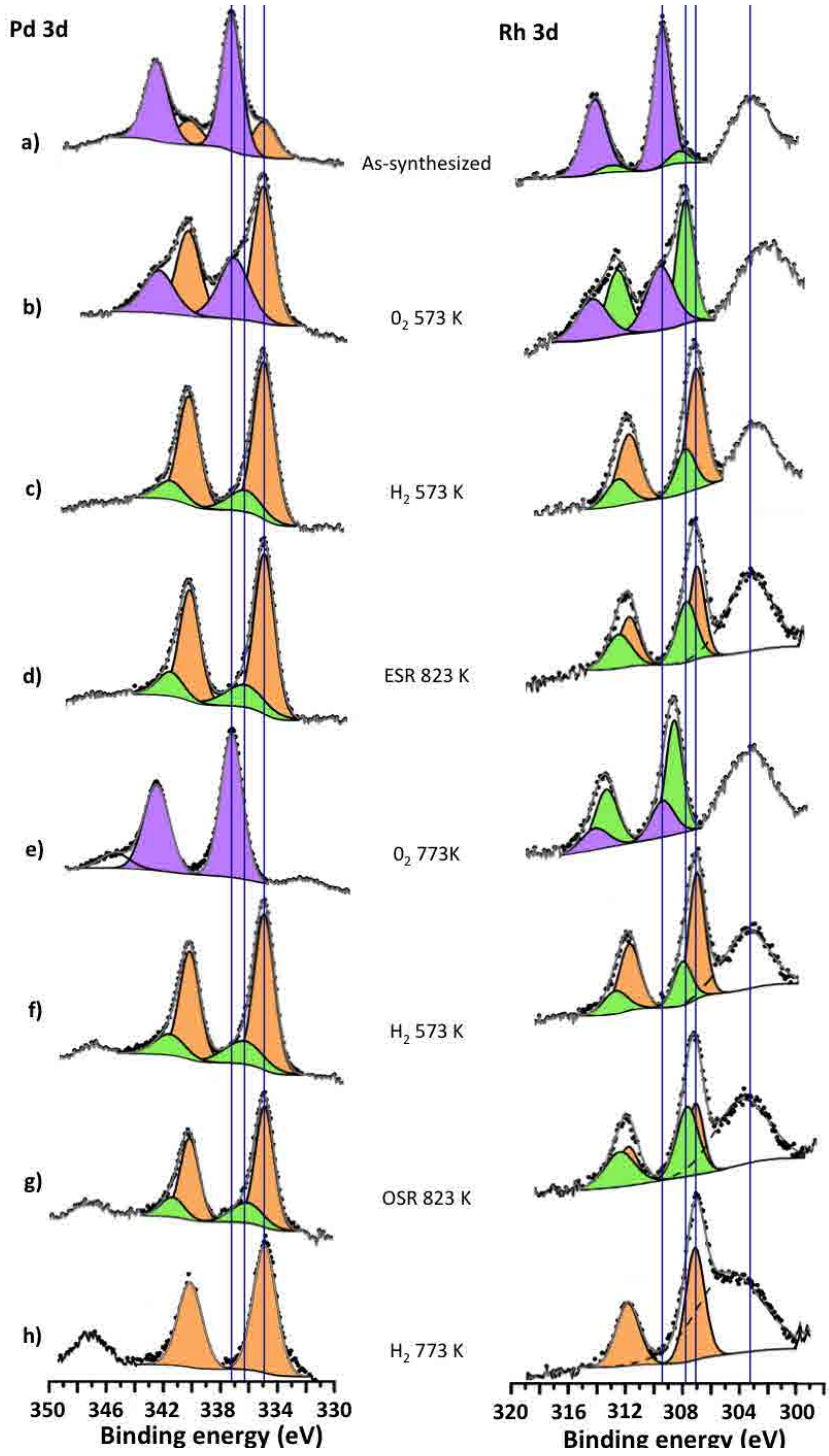

Figure 6.14: XP spectra of Rh 3d and Pd 3d recorded for the whole sequence of *in situ* treatments performed on 1RhPd/CeO_2 catalyst.

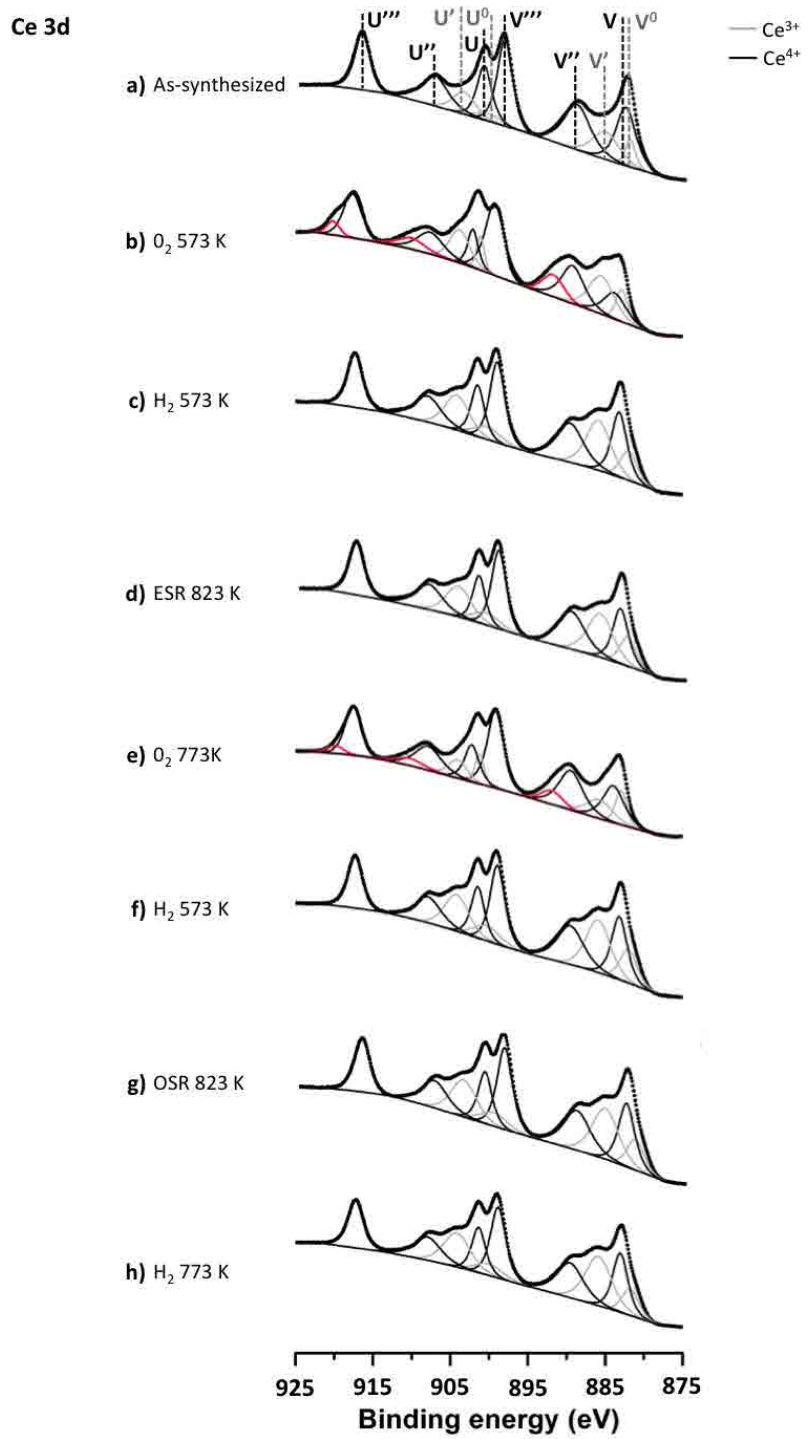

Figure 6.15: XP spectra of Ce 3d recorded for the whole sequence of *in situ* treatments performed on 1RhPd/CeO_2 catalyst.

Table 6.3: XPS results of the *in situ* treatments performed on the working 1RhPd/CeO_2 catalyst.

	Relative atomic concentration (%)				Atomic ratio		
Treatment	Rh	Pd	Ce	C	NM*/Ce	C/Ce	Rh/(Rh+Pd)
1. Fresh	1.3	2.7	90.7	5.3	0.04	0.06	0.32
2. O_2 573 K	1.4	3.1	92.8	2.7	0.05	0.03	0.31
3. H_2 573 K	1.2	2.4	94.7	1.7	0.04	0.02	0.33
4. ESR 823 K	0.8	2.0	84.5	12.7	0.03	0.15	0.28
5. O_2 773 K	1.1	3.2	94.4	1.3	0.05	0.01	0.26
6. H_2 573 K	1.1	2.8	95.2	0.9	0.04	0.01	0.28
7. OSR 823 K	1.0	1.3	95.6	2.1	0.02	0.02	0.42
8. H_2 773 K	0.8	1.3	96.6	1.4	0.02	0.01	0.3

*NM: Noble Metals, i.e, Rh + Pd

Also, the oxidation states of the NM and Ce were investigated. Regarding the deconvolution of Rh 3d spectra, a large component on its low binding energy region at ∼303.2 eV was detected for the whole sequence investigated, as clearly seen in figure 6.14. The origin of this band was carefully addressed. It was ruled out that it constituted a photoemission line because none of the elements of the catalyst neither the sample holder show photoemission lines at this binding energy and if it were a Rh 3d photoemission line it should have had its associated doublet, which was not present in the spectra. Also the broadening of the unknown component pointed to other spectral features rather than to a photoemission line. The existence of Auger peaks from the elements of the catalyst or the sample holder in this region was initially discarded using the reported spectra in handbooks [122, 133]. Nevertheless, in Gayen et al. [134], the authors also saw this peak at 303.3 eV and they ascribed it to Ce(M_3VV) Auger lines. Also, from data reported in the literature this peak could be tentatively ascribed to a shake-up excitation of Ce 4s ($BE_{Ce_{4s}}$=290 eV) as reported in Bagus et al. [135]. Therefore, this component could be ascribed to Ce and it was excluded from the deconvolution of Rh 3d spectra. This set of Rh 3d spectra was the only set where this Ce spectral feature was identified, because, due to the low Rh concentration studied, the intensity of this Ce peak was comparable to that of Rh 3d.

Initially, the as-synthesized 1RhPd/CeO_2 catalyst exhibited double Pd relative concentration than Rh, indicating again that, initially, Pd may be dispersed forming smaller aggregates than Rh. Also some adventitious surface carbon was detected on the as-synthesized catalyst, that diminished after the subsequent oxidation at

573 K. No chlorine species from Rh and Pd precursors were detected. The oxidation at 573 K and the consequent C removal, left more Ce and NM (both Rh and Pd) surface exposed, as indicated the increase on their relative atomic concentration. In addition, during this oxidation, no NP sintering occurred as the NM/Ce ratio increased, which is in accordance with the reported results for the 1RhPd/CeO_2//Mon regeneration treatment (section **6.1.2**) and, probably, NPs had already grown during the oxidation of the synthesis (performed at the same temperature). In contrast, hydrogen reduction at 573 K led to NP sintering as the relative atomic concentration of both Rh and Pd and the NM/Ce ratio decreased. After hydrogen reduction at 573 K, further C diminution was recorded.

After the ESR reaction performance at 823 K, surface C increased substantially and the C/Ce atomic ratio increased up to C/Ce=0.15, indicating that carbonaceous species accumulated on the catalyst surface during ESR performance. Carbon formation brought along the reduction of the amount of Rh, Pd and Ce relative atomic concentrations due to C coverage but also, in the case of Rh and Pd, to NP sintering as the NM/Ce ratio also diminished. This denoted that RhPd NPs agglomerated during ESR reaction, in accordance with the HRTEM analyses of the sample after reaction, which showed larger NPs with crystalline structure (see figure **6.1**).

After the regeneration treatment with air at 773 K (step 5), carbon was almost completely removed and the C/Ce (C/Ce=0.01) ratio was lower than before ESR reaction performance (C/Ce=0.02). Rh and Pd relative atomic concentrations increased as well as the NM/Ce ratio and almost the initial values were recovered, indicating that surface carbonaceous deposits were removed and also that RhPd NP reduced their size redispersing over the ceria surface. This oxidation at higher temperature (773 K instead of 573 K of step 2) allowed to reduce C concentration below its initial concentration without leading to NP sintering. These results confirmed the previous results obtained on the functionalized monolith (section **6.2.1**), implying that catalyst surface can be regenerated after ESR with oxidizing treatments at 773 K.

New experiments were carried out after this reaction and regeneration cycle in order to monitor the changes suffered by the surface after OSR, too. Therefore, once the surface was regenerated, a new activation treatment with hydrogen at 573 K was performed. After the new reduction at 573 K, the same trends were observed as in the reduction of step 3. Again, RhPd NPs sintered and C concentration was reduced even further than in the previous oxidation at 773 K. After the OSR reaction at 823 K, C concentration increased moderately and its concentration was much lower than after the ESR reaction, as expected, indicating that during OSR less carbon was deposited. The NM/Ce ratio (NM/Ce=0.02) dropped

sharply and was even lower than after ESR reaction (NM/Ce=0.03), indicating that RhPd NP sintered. Interestingly, after the OSR, Rh concentration diminished slightly and approximately maintained the same value as in the previous steps. On the contrary, after the OSR Pd relative concentration diminished 46%, which entailed a new change on the Rh/Pd atomic ratio. Both variations registered on the Rh/(Rh+Pd) atomic ratio were produced along with a substantial reduction of the relative atomic concentration of either Rh or Pd.

The sequence finished with a reduction at 773 K. The objective of this final reduction was to check the differences between exposing the catalyst to a hydrogen atmosphere at the reaction temperature and hydrogen generation *in situ*, as during ESR performance ca. 60% hydrogen is produced. However, with H_2 the temperature of the reaction chamber could not be risen up to 823 K and only 773 K could be reached. Therefore, the temperature of the final reduction had to be lowered to 773 K. Results showed that after hydrogen reduction at 773 K, the NM/Ce ratio slightly decreased again, probably due to NPs agglomeration. In addition, a new reduction on the relative atomic C concentration was recorded, revealing that reducing treatments also allowed for C reduction, but they had the associated negative effect of NP sintering.

Regarding the oxidation states of the NM, Rh 3d was deconvoluted using three spectral features: one at 307.0 eV, which corresponded to metallic Rh (Rh^0) [122], and two oxidized components at 307.8 eV and 309.3 eV, which corresponded to Rh^+ and Rh^{3+}, respectively [136, 137]. The energy difference between Rh $3d_{5/2}$ and Rh $3d_{3/2}$ was constrained at 4.75 eV and the ratio between their areas was also constrained. The Pd 3d region was fitted with three components at 334.9 eV, 336.1 eV and 337.2 eV, which can be assigned to the position of Pd $3d_{5/2}$ of metallic Pd, Pd^{2+} and $Pd^{\delta+}$ ($2<\delta<4$), respectively. The BE of $Pd^{\delta+}$ was significantly higher than that of PdO and lower than PdO_2, which suggested that $Pd^{\delta+}$ species were more cationic than PdO. In the literature, this effect has been ascribed to the strong metal-support interaction effect between Pd and CeO_2. That is, the Pd-O bonding does not belong to Pd-O-Pd, but rather to Pd-O-Ce in the Pd/CeO_2 interface [138]. Otto et al. demonstrated by XPS observations that two types of oxidized Pd can coexist on γ-alumina [139]. The characteristic binding energy of PdO was ascribed to relatively large particles, which could be readily transformed to Pd metal at room temperature in hydrogen. The second type of oxide, predominantly present at low palladium loadings ($\leq$0.5 wt%), was characterized by a binding energy shifted approximately 1.6 eV to higher BE than that for PdO, and was found to be resistant to reduction to Pd metal at room temperature in hydrogen [140]. Otto et al. associated this BE shift with a metal-support interaction at concentrations where Pd is highly dispersed, as identified in the case of our catalyst (see figure 4.7).

The energy difference between Pd $3d_{5/2}$ and Pd $3d_{3/2}$ was constrained at 5.25 eV and also the ratio between their areas was kept constant. The oxidized fraction of each metal was calculated as the corrected area of the oxidized component (or components) of the metal evaluated divided by its total corrected area. In the same way, the reduced fraction of Rh and Pd was calculated by dividing the corrected area of the peak ascribed to the metallic state by the total corrected area of the metal.

The as-synthesized catalyst exhibited highly oxidized Rh and Pd, as the previous treatment was a calcination at 573 K for 6 hours. After the performance of the same oxidation *in situ* (30 minutes long) as the one performed in the muffle, both NM exhibited more reduced components. Rhodium and palladium exhibited the high BE oxide component, but it was smaller than in step 1, whereas their metallic component was larger. This may indicate that the preservation of the sample under UHV affected the oxidation state of the metals as both underwent a reduction inside the XPS system. Interestingly, after this *in situ* oxidation, the Ce 3d spectrum exhibited new components in the U"', U" and V" peaks region, as clearly seen by the broken symmetry of these peaks (figure **6.15**b). As a result, extra components were needed to fit the experimental spectrum and they are marked with a red line. Probably these new components account for a new type of Ce^{4+} as deduced from their position. Nevertheless the resolution of the spectrum and CasaXPS software did not allow to properly fit the spectra with 12 components ascribed to Ce^{4+} (6 components per Ce^{4+}) plus 4 components of Ce^{3+}. Therefore, the spectrum was fitted following the same procedure described above: using 6 components for Ce^{4+} and 4 components for Ce^{3+}, and only the clearly distinguishable extra components (marked with red lines) that were needed to match the experimental spectrum were added. As a consequence the Ce^{4+}/Ce^{3+} ratio could not be calculated. This new type of Ce^{4+} may account for surface Ce in close contact with the oxygen atoms of the oxidized NM. However, to the best of our knowledge, this phenomenon has not been previously described in the literature. After the first reduction at 573 K, these extra Ce components disappeared and Ce^{3+}/Ce^{4+}=0.51. Both NM reduced, but still 18% Pd and and 28% Rh remained oxidized, indicating that the reduction at 573 K did not completely reduce the NM, as already observed in [141].

After ESR reaction, Pd and Ce underwent a minor variation on their oxidation states (22% oxidized Pd and Ce^{3+}/Ce^{4+}=0.51), but Rh oxidized and 46% of Rh was found on Rh^{+} state. The strong oxidation at 773 K completely oxidized both NM (figure **6.14**e) and the Ce extra components appeared again (figure **6.15**e), indicating that the appearance of these bands is a phenomenon related with the oxidations of the catalyst. After the second activation treatment (step 6), the NM exhibited nearly the same oxidation state as after the first activation treatment (step 3), and Ce extra components disappeared again. The Ce^{3+}/Ce^{4+} ratio was

0.56. After OSR, in spite of the presence of oxygen in the reformate stream, only Rh underwent a stronger oxidation than after ESR: 56% of Rh was Rh^{+}, whereas 77% Pd remained on its metallic state, which is nearly the same value found after ESR. When the catalyst was exposed to hydrogen atmosphere at 773 K (step 8), both Rh and Pd completely reduced (both NM exhibited only the reduced component), which pointed to that higher temperatures are required to fully reduce the NM nanoparticles of the $1RhPd/CeO_2$ catalyst. Also, their oxidation states differed from the ones after ESR conditions at 823 K, when only 54% of Rh and 78% of Pd were found on their metallic states, highlighting the different effect between dosing H_2 and its generation on the catalyst surface.

The analysis of the $1RhPd/CeO_2$ working catalyst allowed for monitoring the formation and removal of carbon deposits and also RhPd NPs sintering and redispersion processes after each of the treatments performed, which emulated the synthesis and reaction treatments of working catalysts. Also, these experiments allowed for the discussion of the oxidation state of the elements of the catalyst. Nevertheless, the reorganization of the bimetallic Rh-Pd system within the NPs could not be investigated. The X-ray source of the XPS apparatus is a dual Al/Mg anode that can produce K_α radiation lines at 1486.6 eV or 1253.6 eV, respectively [142]. In our research, all the XPS analyses were performed with Al_{K_α} radiation which produces Rh 3d and Pd 3d photoelectrons of kinetic energies around 1179 eV and 1151 eV, respectively, as calculated from equation **6.1**.

$$h\nu = E_B + E_K + \Phi \tag{6.1}$$

Where hν is the photons energy (hν=1486.6 eV in these analyses), E_B is the binding energy of the emitted photoelectrons and E_K is their corresponding kinetic energy. Φ represents the work function of the material.

Rhodium and palladium 3d photoelectrons with kinetic energies of 1179 eV and 1151 eV account for inelastic mean free paths[3] (IMFP) of 1.59 nm and 1.56 nm, respectively (these values were calculated using [143]). Or in other words, the detected Rh 3d and Pd 3d photoelectrons came from depths $\leq$1.6 nm with 68% probability. Therefore, taking into account that the as-synthesized $1RhPd/CeO_2$ catalysts are composed of RhPd NPs ranging 1-2 nm, the NPs were entirely or almost entirely sampled with the Al_{K_α} radiation and the reorganization of Rh and Pd within the NPs could not be elucidated. Figure **6.16** depicts the analyzed volume with Al_{K_α} radiation of a spherical NP of diameter 2 nm (figure **6.16**a) and

[3]The IMFP was defined by Committee E-42 on Surface Analysis of the American Society for Testing and Materials as the average of distances, measured along the trajectories, that particles with a given energy travel between inelastic collisions in a substance [143]. A practical definition of the IMFP is the distance travelled by an electron where the probability of escape has decayed to 1/e or 37%. [144]

compares it to the volume analyzed in NPs of 4 nm (figure 6.16b). In figure 6.16, the grey region of the spheres represents the volume demarcated by one IMFP ($IMFP_{1486.6\ eV}$=1.6 nm) from the exterior surface of the spheres, which is the assumed *sampled volume*, while the blue region of the NPs remains unanalyzed. As a result, we decided to perform an *in situ* XPS study with larger and size-controlled RhPd NPs in order to also investigate Rh and Pd rearrangement within the NPs.

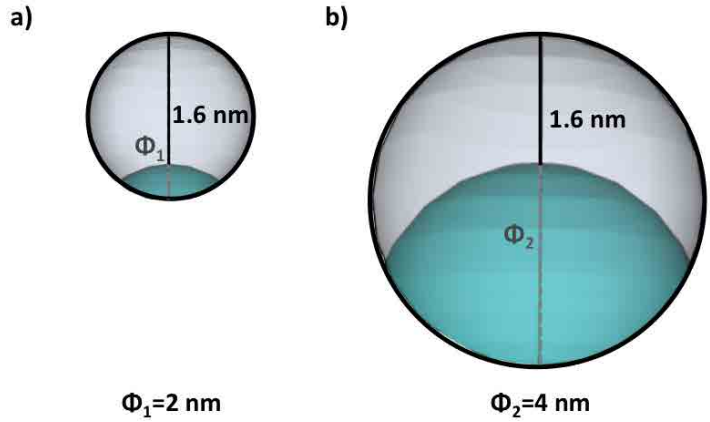

Figure 6.16: Schematic representation of the sampled volume using Al_{K_α} radiation for NPs of diameter: a) 2 nm. b) 4 nm.

6.2.3 Rhodium-palladium bimetallic system studies

Preformed RhPd@D NPs described in section 4.2.1 were used for the investigation of Rh and Pd rearrangement. Although catalysts based on preformed RhPd@D NPs exhibited inferior reaction performance than the ones based on RhPd NPs (synthesized form $RhCl_3$ and $PdCl_2$), for this investigation RhPd@D NPs offer advantages over RhPd NPs as:

1. RhPd@D NPs have controlled size due to their synthesis method.
2. RhPd@D NPs are larger than RhPd NPs.
3. RhPd@D NPs synthesis route led to NPs composed of both Rh and Pd atoms.

For these reasons, the working $RhPd/CeO_2$ catalyst was modeled with RhPd@D NPs dispersed over CeO_2 powder, constituting a model of a working $RhPd/CeO_2$ catalyst. The dimensions of RhPd@D NPs allowed for sampling only their upper portion, as depicted in figure 6.16b. Following this representation, for RhPd@D NPs of 4 nm in mean diameter, the volume enclosed within one IMFP from the exterior surface inside a sphere of diameter 4 nm using Al_{K_α} radiation (1.6 nm) represents approximately 57% of the NPs total volume.

The restructuring of bimetallic systems and, in particular, of RhPd and PtPd nanoparticles was first studied in 2008 by means of synchrotron-based ambient pressure X-ray photoelectron spectroscopy at the Advanced Light Source Synchrotron (Berkeley, USA) in a seminal work by Tao et al. [144]. These authors studied unsupported model NPs of about 15 nm in diameter while they were exposed to NO, O_2, H_2 and NO+CO environments, which are relevant reactions applied to pollution abatement. These spectra were recorded under *operando* conditions, i.e. while the gases surrounded the NPs. They found that RhPd NPs developed core-shell structures under the reducing and oxidizing environments tested. This constituted an important finding since it was shown for the first time that surface rearrangements in bimetallic systems occurred in response to reactive environments at nearly ambient pressures. However, only model NPs without support were analyzed in this article.

Consequently, as RhPd NPs restructuring had already been shown, our investigation focused on the study of smaller RhPd@D NPs restructuring (our preformed RhPd@D NPs measured 4 nm in diameter), which are closer to real catalysts, after being exposed to reducing, oxidizing and, most important, to ethanol steam reforming conditions, that had not been previously tested. Furthermore, we also investigated the restructuring of RhPd@D NPs supported on ceria and we differentiated the changes underwent by the unsupported RhPd@D NPs and the supported ones, which constituted a real RhPd@D/CeO_2 catalyst. The study of supported RhPd@D NPs is important since catalysts used for heterogeneous processes are generally composed of metal NPs dispersed over a high surface area support and the presence of the support may strongly affect both the physical and chemical properties of metal NPs, as is demonstrated in the following sections.

The *in situ* XPS studies of Rh and Pd restructuring were first carried out on the simplified system, the unsupported RhPd@D (section **6.2.3.a**), and afterwards the RhPd@D/CeO_2 catalyst was analyzed (section **6.2.3.b**).

6.2.3.a Unsupported model RhPd@D nanoparticles

The sample with model RhPd@D nanoparticles was prepared by drop casting the toluene solution of preformed NPs onto a stainless steel XPS sample holder which was subsequently dried for 10 minutes with an IR lamp. A survey spectrum of the stainless steel sample holder was acquired before NPs deposition to check it for contaminations and no residues were detected.

The sequence of XPS analyses and *in situ* treatments performed on the RhPd@D NPs were: 1) RhPd@D NPs as deposited on the sample holder, 2) oxidation with air at 473 K, 3) oxidation with air at 573 K, 4) oxidation with air at 673 K, 5) oxidation with air at 823 K, 6) reduction at 573 K, 7) ESR performance (S/C=3)

at 823 K and 8) final reduction with H_2 at 823 K. During these experiments, the temperature of the high pressure cell could be risen up to 823 K with 1 bar of H_2 and, therefore, the temperature tested in the final H_2 treatment was 823 K.

An initial XPS analysis of the as-deposited RhPd@D NPs was performed in order to record the as deposited state of the sample (step 1) and afterwards the mentioned catalytic treatments were carried out in the XPS reaction chamber at 1 bar. This sample was stepwise oxidized with 20 mL/min of air at different temperatures in order to monitor the C removal from the dodecanethiol protecting shell that surrounded the RhPd cores. After each of these steps, the sample was transferred back to the analysis chamber, where a survey spectrum and Rh 3d, Pd 3d, C 1s, S 2p spectra were recorded. All the spectra were deconvoluted and analyzed using exactly the same procedure described for the 1RhPd/CeO_2 catalyst (section 6.2.2). So, Rh 3d and Pd 3d spectra were calibrated for energy taking into account the position of the reduced component of both noble metals (307.0 eV and 334.9 eV for Rh $3d_{5/2}$ and Pd $3d_{5/2}$, respectively). In this sample, Rh 3d spectra were deconvoluted using 3 components: one corresponding to metallic Rh at 307.0 eV; and two oxide components: one of Rh^+ at 308.2 eV and one of Rh^{3+} at 309.3 eV. Three components were also used for Pd 3d deconvolution: one of metallic Pd at 334.9 eV and two for Pd oxides at 335.8 eV and 336.7 eV. The results obtained for the whole sequence are listed in table 6.4. The Fe signal recorded came from the sample holder. Ca. 1% sulfur was detected on the as-deposited RhPd@D NPs, but after the oxidation at 573 K, S was totally removed. Figure 6.17 shows Pd 3d and Rh 3d XP spectra deconvolution for the whole sequence of treatments.

Table 6.4: XPS results for the *in situ* treatments of the model RhPd@D nanoparticles.

	Relative atomic concentration (%)				Atomic ratio			
Treatment	Rh	Pd	C	Fe	NM/C	NM/Fe	Fe/C	Rh/NM
1. Fresh	0.0	0.3	99.7	0	0.00	-	0.00	-
2. O_2 473 K	0.3	1.2	98.5	0.0	0.02	-	0.00	0.18
3. O_2 573 K	0.8	3.4	95.8	0.0	0.04	-	0.00	0.19
4. O_2 673 K	1.1	4.3	91.7	2.9	0.06	1.89	0.03	0.21
5. O_2 823 K	7.6	18.8	56.2	17.4	0.47	1.52	0.31	0.29
6. H_2 573 K	9.5	15.6	52.1	22.9	0.48	1.01	0.44	0.38
7. ESR 823 K	4.7	6.6	56.2	32.5	0.20	0.35	0.58	0.42
8. H_2 823 K	5.0	7.1	57.6	30.3	0.21	0.40	0.53	0.41

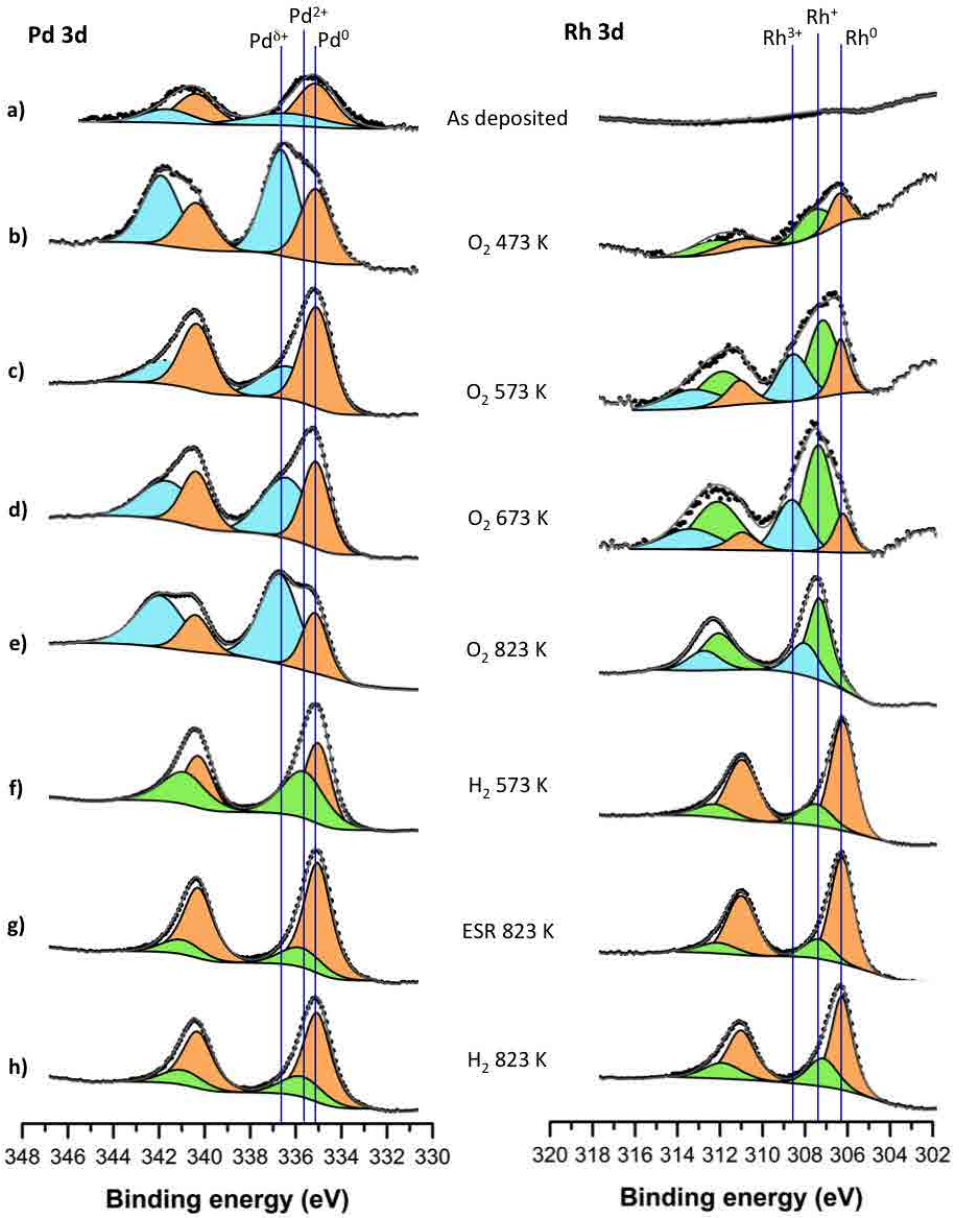

Figure 6.17: XP spectra of Pd 3d and Rh 3d recorded for the whole sequence of *in situ* treatments performed on RhPd@D NPs.

Initially, Rh and Pd were almost completely covered with C and the survey spectrum did not show Fe species from the sample holder. During the stepwise oxidations, the NM/C atomic ratio gradually increased. However, it was only after the oxidation at 823 K that the amount of C was significantly reduced and, consequently, the relative atomic concentration of both noble metals increased. The

ratio between Rh and Pd remained nearly constant after the oxidations at 473 K, 573 K and 673 K. After the oxidation at 823 K, when high carbon removal took place, Rh concentration increased on a higher extent than Pd concentration in the sampled volume causing a variation on their relative ratio. Despite the different oxidations performed, C was not completely removed and its relative atomic concentration still was 56%. This result, along with the Fe relative concentration increase, may indicate that during the oxidation at high temperature (823 K) almost all the adventitious C and dodecanethiols were removed (which is in accordance with the TGA results of the RhPd@D NPs) and, as a result, the C signal detected would originate from the stainless steel sample holder. Carbon 1s spectra corresponding to the oxidations exhibited only one component and thus this hypothesis could not be confirmed with the spectra deconvolution. After the subsequent hydrogen reduction at 573 K, carbon relative concentration was only reduced by 9% (along with Fe increase), whereas the previous reductions of the 1RhPd/CeO_2 led to 30-40% C diminution and allowed to remove nearly all C. This is in agreement with our hypothesis and most probably the C signal recorded would mainly originate from the sample holder and adventitious C and dodecanethiols would be almost completely removed after the oxidation at 823 K leaving exposed the RhPd core. After H_2 reduction, NM/Fe ratio diminished indicating that in addition to C removal RhPd@D NPs sintered, as previously reported for the 1RhPd/CeO_2 catalyst.

Results after ESR reaction performance showed that during ESR reaction carbonaceous deposits developed, which led to a reduction of the NM/C ratio, and a new component on the C 1s region appeared. Also, after ESR reaction high NPs sintering took place as the NM/Fe ratio diminished one third. The strong agglomeration of RhPd@D NPs also led to an increase of the Fe/C ratio as more sample holder area was left uncovered.

Results concerning the reorganization of Rh and Pd are shown in figure **6.18**, where the relative ratio between both noble metals for the whole sequence of treatments is plotted. The Rh and Pd ratios plotted were calculated as Rh/(Rh+Pd) and Pd/(Rh+Pd), respectively. Figure **6.18** also shows the oxidized and reduced fractions of each metal: the dashed regions of the bars correspond to the oxidized fraction of each metal.

The relative ratio of the as-deposited RhPd@D NPs could not be inferred as both Rh and Pd concentrations were too low. After the firsts oxidations (at 473 K, 573 K and 673 K) the sampled volume of the RhPd@D NPs was Pd-rich as the Pd relative ratio was ∼0.8. After these oxidations, ca. 65% Pd remained reduced, except for the oxidation at 473 K, after which Pd exhibited a large oxidized component and 62% was oxidized Pd (see figure **6.17**b). After the oxidations at 473 K and 573 K, ca. 50% Rh was found on its metallic state. As seen in figure **6.18**, only after

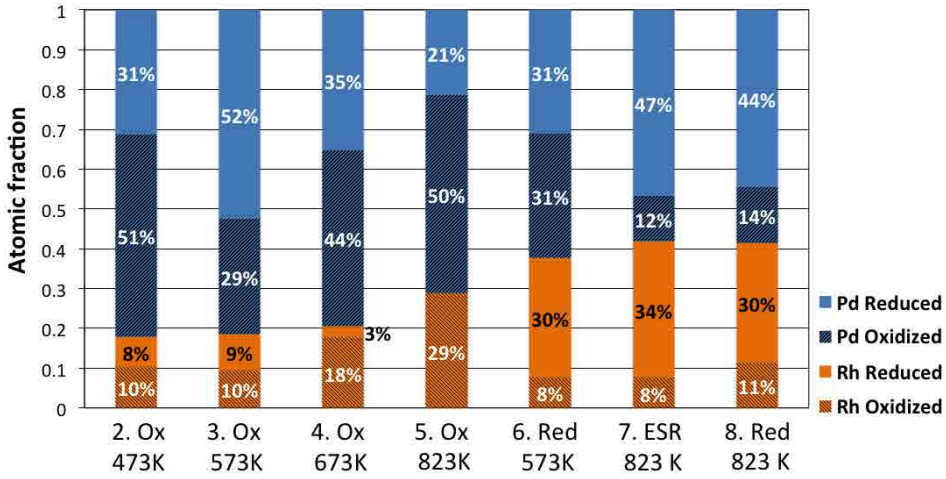

Figure 6.18: Rhodium and palladium atomic fractions and oxidation states for the whole sequence of treatments performed inside the XPS reaction chamber on RhPd@D NPs.

the oxidation at 673 K, Rh almost fully oxidized. Interestingly, only during these oxidations the Rh^{3+} component could be identified.

After the oxidation at high temperature (823 K, step 5), when C was almost completely removed, Rh migrated towards the surface as its relative concentration increased in the sampled volume and a Rh relative ratio of 0.3 was registered. Rhodium was completely oxidized, but the position of the Rh^{3+} component slightly shifted towards low BE. Palladium exhibited again the large oxidized component, achieving its highest oxidation state with 70% oxidized Pd. This is in contrast to the behavior observed for the $1RhPd/CeO_2$ catalyst where both NM completely oxidized after the oxidation at 773 K. The subsequent reduction at 573 K had the same effect on NM migration and a new Rh-enrichment was recorded on the external region of the NPs. Concerning the oxidation states of the NM, both underwent a reduction, although Rh got more reduced than Pd and nearly 80% Rh was found on its metallic state. Ca. 50% Pd was still oxidized, indicating again that H_2 reduction at 573 K did not completely reduce the NM NPs. After ESR reaction performance, Rh continued migrating towards the surface and its relative ratio increase up to 0.4. Interestingly, Pd underwent a stronger reduction than under H_2 atmosphere and Rh remained unchanged, so 82% Rh and 80% Pd were found on their metallic state. After the final reduction at high temperature (823 K), the ratio between the NM slightly changed and the oxidation states underwent a small variation. Surprisingly, both NM oxidized somewhat after H_2 reduction at 823 K (72% Rh and 76% Pd were reduced), indicating that during ESR reaction at 823 K both noble metals underwent a stronger reduction than during a reducing treatment at the same temperature. This is again in contrast to the previously

observed behavior for the 1RhPd/CeO_2 catalyst, where both NM were completely reduced after the H_2 reduction at 773 K (even though in that case the temperature was lower). To summarize, Rh and Pd constituting the unsupported RhPd@D NPs rearranged depending on the treatments performed and, along the experiments, the outermost region of the RhPd@D NPS underwent a Rh-enrichment. Also, some differences were already noticed between the 1RhPd/CeO_2 catalyst and unsupported RhPd@D NPs.

Once the analyses of the RhPd@D NPs sample were finished, the sample was removed from the XPS system and analyzed by SEM in order to observe the morphological changes underwent by the NPs after the whole sequence of treatments. The stainless steel sample holder with the treated RhPd@D NPs was directly studied by SEM and one of the representative images acquired is shown in figure **6.19**. The particle size distribution of the RhPd@D was 6 ± 1 nm, indicating that NPs agglomerated during the treatments performed in the XPS high pressure cell (their size before deposition was 4 ± 1 nm). In some areas of figure **6.19**, groups of individual RhPd@D can be distinguished forming islands of about 40 nm. SEM images showed larger NPs than as-synthesized, thus confirming the nanoparticle sintering inferred by XPS. Nevertheless, RhPd@D NPs maintained their nanoparticle entity and the formation of large Rh and Pd aggregates was discarded.

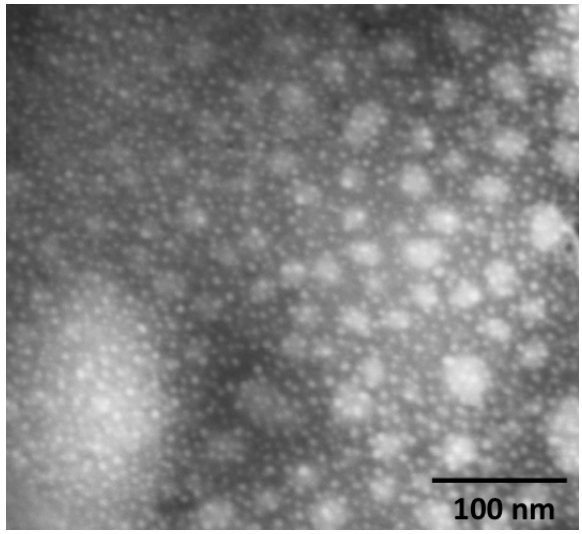

Figure 6.19: SEM image of the RhPd@D NPs after the XPS treatments sequence.

6.2.3.b Model RhPd@D/CeO_2 catalyst

As already mentioned, catalysts used for heterogeneous processes are usually composed of metal NPs dispersed over a high surface area support. The support can

play an important role in the catalytic process by providing new active sites and it may strongly affect both the physical and chemical properties of metal NPs. The synergic effect exerted by the support on the catalytic performance of metal particles has been extensively studied and immense effort has been made on elucidating the exact mechanisms involved in the metal-support interaction [145–150]. As already shown in Chapter 5, the presence of the ceria support had a strong effect on the ESR catalytic performance of RhPd@D NPs: the catalytic performance of RhPd@D/CeO_2 was clearly superior to that of unsupported RhPd@D NPs. For instance, the amount of hydrogen produced by 3RhPd@D/CeO_2 doubled that achieved by the model RhPd@D NPs (28 mL/min versus 15 mL/min). Therefore, we also studied by XPS RhPd@D NPs deposited on the ceria support in order to elucidate the rearrangement of NPs that constitute a real catalyst and investigate the differences exhibited by supported and unsupported NPs.

Initially, a 1RhPd@D/CeO_2 catalyst was synthesized and analyzed after RhPd@D NPs deposition on ceria by XPS. The signal to noise ratio of Rh 3d and Pd 3d spectra were too low and did not allow for a proper deconvolution of the different Rh and Pd components and only the whole area could be accurately obtained, as already happened with the 1RhPd/CeO_2 catalyst. Therefore the catalyst was re-synthesized with higher noble metal loading in order to be able to obtain an accurate deconvolution of both noble metals. A new catalyst was prepared by impregnating 20 mg of ceria powder with 0.6 cm^3 of RhPd@D NPs toluene solution ($40 \cdot 10^{-3}$ M), thus obtaining a 12RhPd@D/CeO_2 catalyst.

The sequence of treatments performed on the 12RhPd@D/CeO_2 model catalyst was the same as on the unsupported RhPd@D, i.e.: 1) RhPd@D NPs deposition on the ceria support, 2) oxidation with air at 473 K, 3) oxidation with air at 573 K, 4) oxidation with air at 673 K, 5) oxidation with air at 823 K, 6) reduction at 573 K, 7) ESR performance (S/C=3) at 823 K and 8) final reduction with H_2 at 823 K. An initial XPS analysis was performed in order to record the as deposited state of the sample (which corresponds to step 1) and it was confirmed that the new NM concentration allowed for Rh 3d and Pd 3d accurate deconvolution. After the first analysis, the subsequent catalytic treatments were carried out in the XPS high pressure cell at 1 bar. After each of these steps, the sample was transferred back to the analysis chamber where Rh 3d, Pd 3d, Ce 3d, C 1s, S 2p and a survey spectrum were recorded. All the spectra were deconvoluted and analyzed following the procedure described in previous sections. The deconvolution of Rh 3d and Pd 3d XP spectra for all the treatments is shown in figure 6.20, whereas figure 6.21 shows Ce 3d deconvolution. In these experiments, where the RhPd@D NPs were supported on CeO_2, the NM spectra showed new features that had not been seen on the spectra of unsupported RhPd@D NPs.

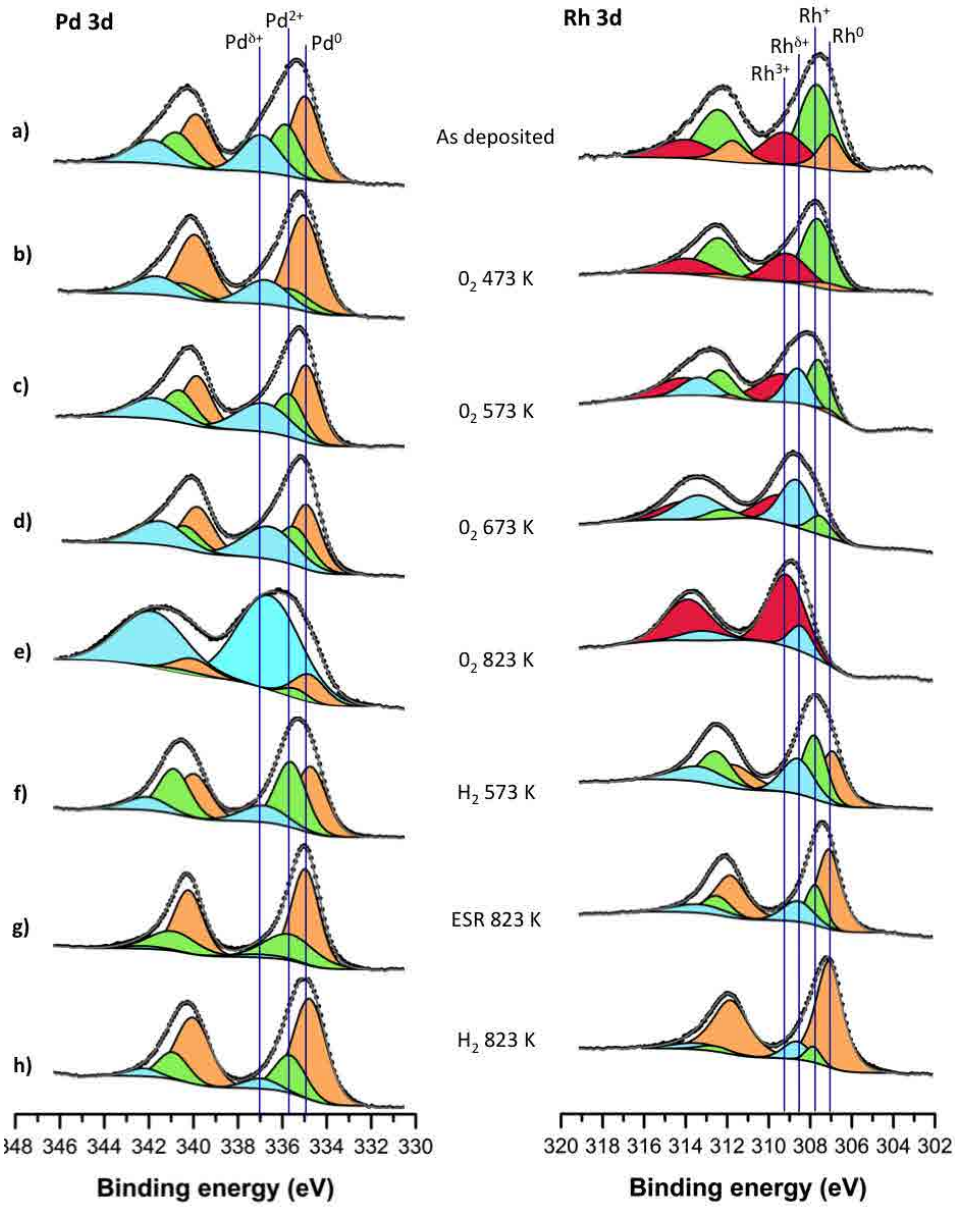

Figure 6.20: XP spectra of Pd 3d and Rh 3d recorded for the whole sequence of *in situ* treatments performed on 12RhPd@D/CeO_2 catalyst.

Remarkably, Pd 3d presented an additional component in all the cases in comparison with the unsupported NPs. Moreover, the binding energy of Pd^0 and Pd^{2+} coincided with their respective photoemission lines of the RhPd@D NPs (334.9 eV and 335.9 eV), but the position of the third component shifted towards high BE (337.0 eV versus 336.7 eV for the unsupported NPs), suggesting again that $Pd^{\delta+}$

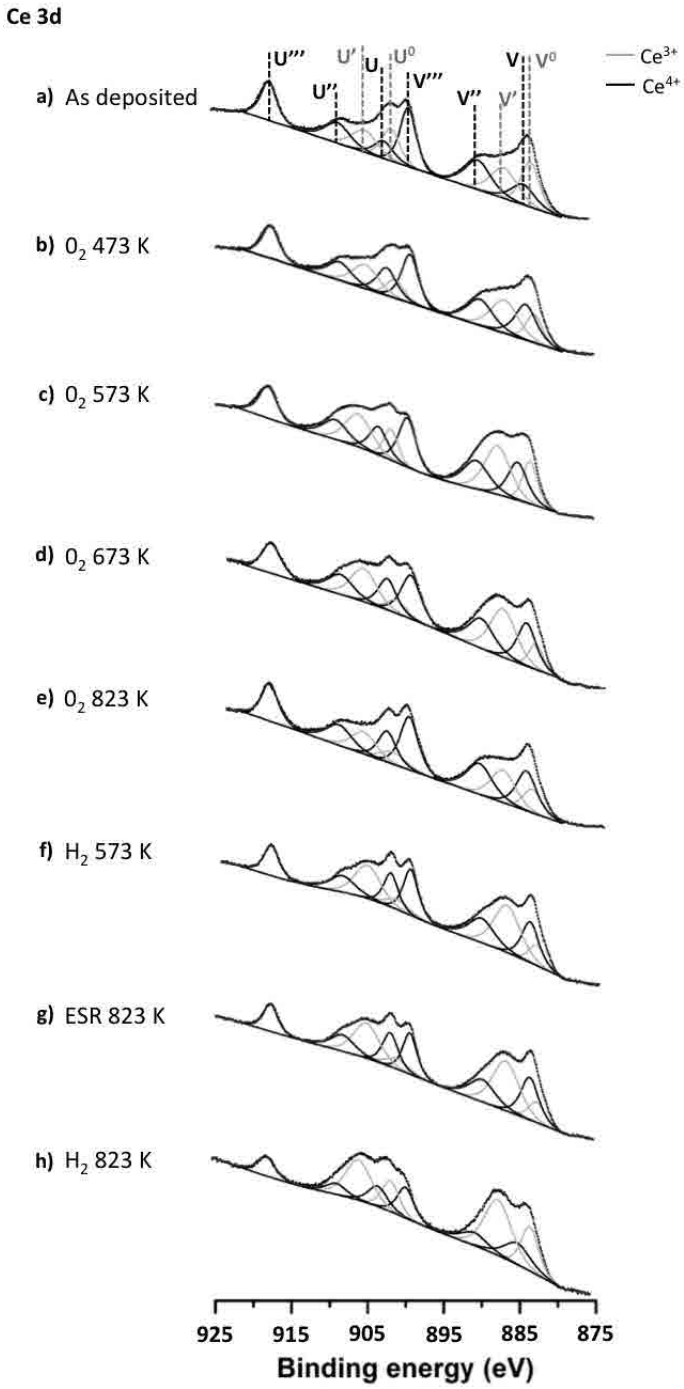

Figure 6.21: XP spectra of Ce 3d recorded for the whole sequence of *in situ* treatments performed on 12RhPd@D/CeO_2 catalyst.

species are more cationic than PdO. Palladium$^{\delta+}$ species were also present after the H_2 reductions at 573 K and 823 K (see figures **6.20**f and **6.20**h). In the literature this phenomenon has been ascribed to the strong metal-support interaction effect between Pd and CeO_2. That is, the Pd-O bonding does not belong to Pd-O-Pd, but rather to Pd-O-Ce in the Pd/CeO_2 interface [138]. In our experiments, the $Pd^{\delta+}$ BE (337.0 eV) was closer to the one registered for the 1RhPd/CeO_2 catalyst (337.2 eV) than for the unsupported NP (336.7 eV), which also points to the hypothesis of the strong metal-support interaction. For Rh deconvolution of the RhPd@D/CeO_2 catalyst, four spectral lines were needed, whereas only three were needed for the unsupported RhPd@D NPs (see figures **6.20** and **6.17**, respectively). In this case, Rh 3d was fitted with components at 307.0 eV, 307.8 eV, 308.6 eV (the additional component) and 309.3 eV. The need for an additional component is again indicative of the metal-support interaction. Another important remark is that Ce 3d for the 12RhPd@D/CeO_2 catalyst did not show the additional spectral features observed on the 1RhPd/CeO_2 catalyst (see figure **6.15**). The appearance of the Ce additional component in the 1RhPd/CeO_2 catalyst may originate from the size differences observed by STEM between NPs constituting RhPd@D/CeO_2 and RhPd/CeO_2 catalysts. The NPs of the latter are much smaller and did not show crystalline structure after its synthesis (see figures **4.10** and **4.9**, respectively).

Results obtained from the spectra deconvolution for the whole sequence are compiled in tables **6.5** and **6.6**.

Table 6.5: XPS relative atomic concentration for the *in situ* treatments of the model 12RhPd@D/CeO_2 catalyst.

	Relative atomic concentration (%)			
Treatment	Rh	Pd	Ce	C
1. Fresh	3.4	5.6	19.2	69.8
2. Oxidation 473 K	4.7	7.0	20.6	66.5
3. Oxidation 573 K	5.7	9.2	34.0	50.9
4. Oxidation 673 K	7.7	10.9	21.5	60.0
5. Oxidation 823 K	10.5	15.3	39.6	34.6
6. Reduction 573 K	15.8	19.6	36.3	28.3
7. ESR 823 K	9.9	9.0	32.7	47.4
8. Reduction 823 K	8.6	11.2	26.7	53.4

Table 6.6: Atomic ratio for the *in situ* treatments of the model 12RhPd@D/CeO_2 catalyst.

	Atomic ratio				
Treatment	NM/C	NM/Ce	C/Ce	Rh/(Rh+Pd)	Ce^{4+}/Ce
1. Fresh	0.13	0.47	3.64	0.38	0.58
2. Oxidation 473 K	0.18	0.57	3.23	0.40	0.63
3. Oxidation 573 K	0.29	0.44	1.50	0.38	0.57
4. Oxidation 673 K	0.31	0.87	2.79	0.41	0.61
5. Oxidation 823 K	0.75	0.65	0.87	0.41	0.68
6. Reduction 573 K	1.25	0.97	0.78	0.45	0.57
7. ESR 823 K	0.40	0.58	1.45	0.52	0.55
8. Reduction 823 K	0.37	0.74	2.00	0.44	0.39

The atomic fraction of Rh and Pd recorded along the different experiments is plotted in figure 6.22, where the corresponding oxidized and reduced fraction of each metal is also presented.

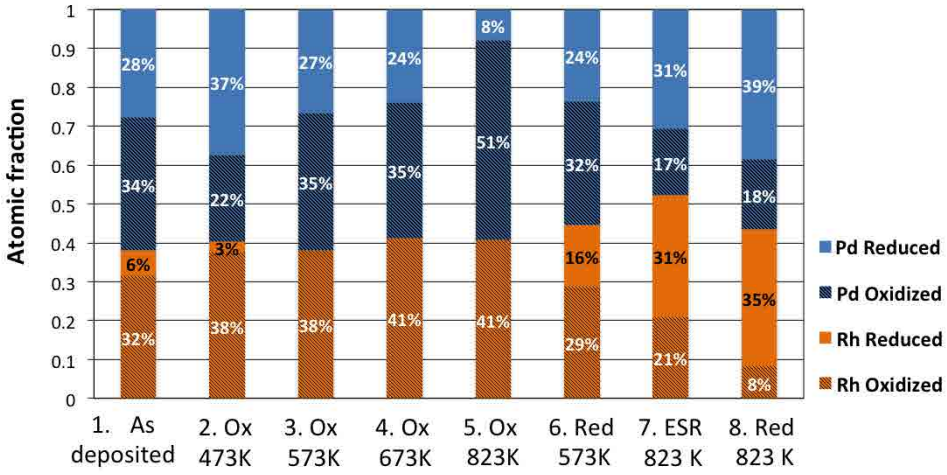

Figure 6.22: Rh and Pd atomic fractions and oxidation states for the whole sequence of treatments performed inside the XPS reaction chamber on the 12RhPd@D/CeO_2 catalyst.

As expected, the as deposited RhP@D/CeO_2 catalyst exhibited again high C concentration (69.8%), even so the relative atomic concentration of both noble metals could be calculated and Rh relative ratio was 0.38. Both Rh and Pd were mainly oxidized as well as Ce, which 58% was Ce^{4+}. After the oxidation at 473 K, the sampled volume of the RhPd@D NPs was again Pd-rich, although the Rh atomic

ratio was higher for the supported NPs than for the unsupported NPs (0.4 versus 0.2). After the successive oxidations with air (at 473 K, 573 K, 673 K and 823 K), C was gradually removed and, consequently, the NM/C ratio increased whereas the C/Ce ratio decreased. The NM/Ce ratio also gradually increased implying that no RhPd@D NPs sintering took place. After the oxidation at 823 K, C relative concentration was reduced by half and the relative ratio between NM remained nearly constant after all the oxidations. Concerning the oxidation states, Rh was totally oxidized after each calcination, but Pd always exhibited the Pd^0 component. It was only after the 823 K oxidation that Pd got substantially reduced and only a small amount (13%) of Pd was still metallic. In the case of Ce, the Ce^{4+} amount gradually increased after each oxidation (except after the oxidation at 473 K) and reached its maximum after the oxidation at 823 K where 68% of Ce corresponded to Ce^{4+}. The trend of oxidation states for the supported noble metals was similar to that observed for the unsupported RhPd@D NPs, although supported NPs were more oxidized than their unsupported counterparts after all the steps. Interestingly, only after the oxidation at 573 K Rh started to exhibit the component at 308.6 eV, which may be ascribed to metal-support or metal-metal interaction, whereas Pd exhibited the $Pd^{\delta+}$ from the beginning of the experiments.

Upon reduction at 573 K, both NM got reduced but to a lesser degree (35% Rh and 43% Pd were reduced) than unsupported RhPd@D NPs, denoting again that higher reduction temperatures are required to fully reduce Rh and Pd constituting the RhPd@D/CeO_2 catalyst. In addition also Ce reduced and 57% of Ce was Ce^{4+}. After ESR reaction performance, Rh migrated towards the surface and the relative ratio between Rh and Pd increased up to 0.52, whereas for the unsupported NPs the Rh ratio only increased up to 0.42. Interestingly, after ESR reaction performance Rh and Pd of both samples (unsupported RhPd@D and RhPd@D/CeO_2) underwent a reduction (60% Rh and 64% Pd in the case of the RhPd@D/CeO_2 catalyst and 82% Rh and 80% Pd for RhPd@D NPs), nevertheless the unsupported NPs underwent a stronger reduction than the supported NPs. Cerium also reduced after ESR reaction and the $Ce^{4+}/(Ce^{3+}+Ce^{4+})$=0.55. The final reduction at 823 K, led to a further reduction of all the metals and the Ce^{4+} relative ratio decreased to 0.39. In contrast to the behavior observed for the unsupported NPs, after the reduction at 823 K, the Rh relative ratio nearly recovered the value of the previous reduction at 573 K and both NM still exhibited oxide components. Nevertheless, the highest reduced state was recorded and 81% Rh and 68% Pd were metallic.

Once all the experiments were performed, the catalyst pellet was removed from the XPS system and a TEM sample was prepared with it. Figure **6.23** shows some of the NPs identified. After the explained experiments, HRTEM showed RhPd@D NPs of 6 ± 2 nm, confirming that RhPd@D NPs sintered during the environments tested, although not large RhPd aggregates were detected. In some areas, carbon

deposits were also identified surrounding both the NPs and the ceria support. The size of the post-reacted NPs of the 12RhPd@D/CeO_2 catalyst is very similar to the size found for the unsupported NPs after the XPS treatments (see figure 6.19).

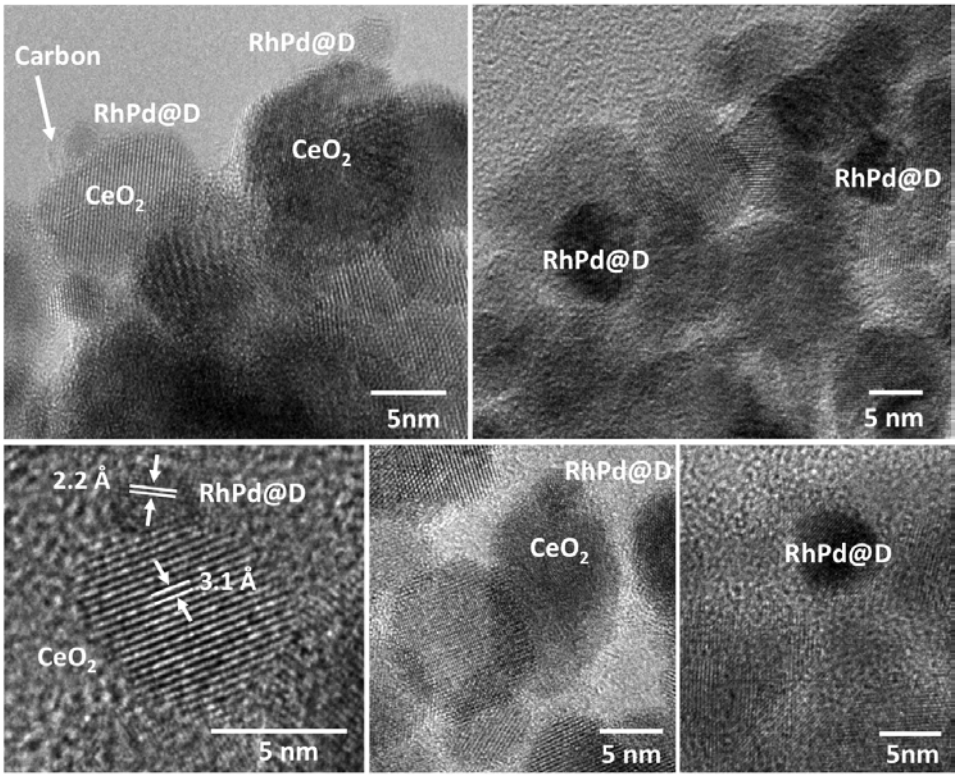

Figure 6.23: HRTEM images of the 12RhPd@D/CeO_2 catalyst after the XPS treatments.

By comparing the results obtained in both systems, the firsts differences were noticed in the rearrangement and oxidation states of both Rh and Pd constituting unsupported or supported NPs. Figure 6.24 shows the discussed atomic fractions of Rh and Pd for both systems together.

The reorganization of both noble metals followed the same global trend on supported and unsupported NPs after each treatment performed. However, their segregation was much higher on the unsupported NPs than on the supported ones. After the oxidizing treatments, the sampled volume was Pd-rich in both systems and Rh gradually moved towards the surface after the reduction at 573 K. The Rh atomic fraction reached its highest value after the ethanol steam reforming conditions, indicating that this metal migrated to the surface after reaction.

These results indicated that the ceria support played a role in the rearrangement

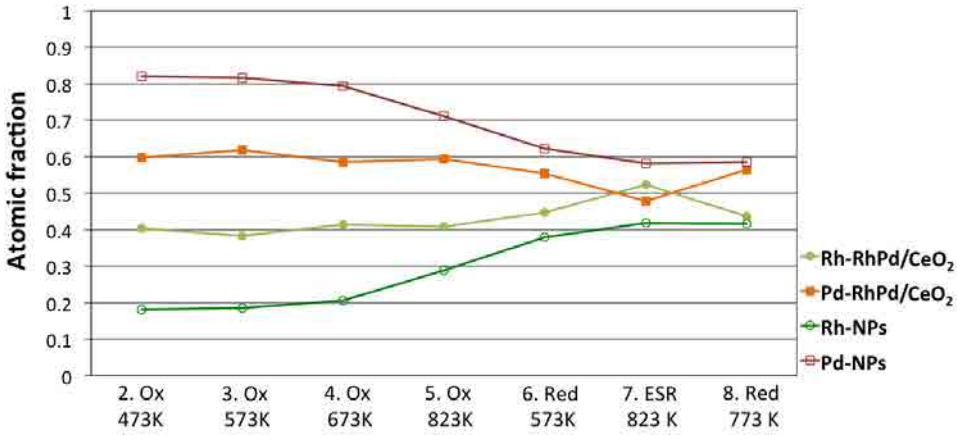

Figure 6.24: Rhodium and palladium relative ratio for the unsupported RhPd@D NPs and the 12RhPd@D/CeO_2 catalyst.

of the NM by limiting their segregation and also by strongly altering their oxidation states. Nevertheless, all these spectra were acquired under UHV, and UHV may alter the oxidation states of some metals. Moreover, another effect can play a major role in the results obtained, as the state of the catalyst surface was recorded under UHV. This may strongly differ from the state while the catalyst is under working conditions. Therefore, we complete our *in situ* X-ray photoelectron study of the bimetallic RhPd system studying both systems while they were exposed to reactants at the ALBA synchrotron (Cerdanyola del Vallès, Spain).

6.3 *Operando* characterization by X-ray photoelectron spectroscopy

The structure of heterogeneous catalysts is dynamic and depends on the composition of the surrounding environment. Thus, both their surface structure and composition may be modified when the gaseous conditions change in order to adapt their electronic properties and geometry to the new surrounding environment. These changes have been demonstrated in previous sections, where the surface of RhPd/CeO_2 catalysts changed after being exposed to different reactive environments. Nevertheless, some structures and active phases only exist under reaction conditions and can differ from those identified under ultra high vacuum (UHV) conditions [151, 152]. Consequently, the study of catalytic systems under real operating or *operando* conditions is essential to identify the active species at work, as the restructuring driven by the environment may induce strong changes in both the properties and behavior of catalysts [153, 154]. In this regard, the advent of several *operando* surface sensitive techniques has allowed the characterization of

surfaces under controlled atmospheres that can closely reproduce the real working conditions of these systems [155], thus overcoming the pressure gap effect. Nonetheless, given the complexity of these techniques and of real catalysts, most of the fundamental work has been conducted in model systems such as single crystals with specific orientations, thin films or well-defined isolated model NPs, as demonstrated in the thorough review of Starr et al. [153]. For instance, in the work by Tao et al. [144], the rearrangement of Rh and Pd was studied under *operando* conditions but only the behavior of unsupported model RhPd NPs (15 nm in diameter) was examined. However, the use of model systems may not truly represent the behavior of real catalysts (the so-called material gap effect) as these systems lack some important features found in real catalysts such as a high surface area, different types of defects, exposed planes and anchoring sites, the presence of reactive hydroxyl groups, the ability to activate certain reactants, etc., which all play an important role in the catalytic processes. In the preceding section, we overcame this problem by directly studying a pellet of a real RhPd/CeO_2 catalyst. As a result, the effect of the ceria support could be demonstrated as the rearrangement of unsupported and supported RhPd NPs differed in both systems after being exposed to the same environments. However, our analyses were conducted under UHV conditions and, as deduced from the literature, these results may differ from the results obtained under *operando* conditions.

In March 2014, we completed the investigation of the rearrangement of the RhPd bimetallic system by means of synchrotron-based ambient pressure X-ray photoelectron spectroscopy (AP-XPS). The AP-XPS experiments were carried out at the CIRCE beamline of the ALBA synchrotron light source [156], where the methodology used along the *in situ* studies was followed and both the surface restructuring and chemical state of both systems (unsupported model RhPd@D nanoparticles and RhPd@D nanoparticles supported on CeO_2 powder, which constitutes a model of a real catalyst) was monitored under operating conditions. In fact, this was the first AP-XPS experiment carried out at ALBA. Figure **6.25** shows a picture of the AP-XPS endstation of CIRCE beamline.

Synchrotron light allows for photoelectron spectra acquisition in the presence of a gaseous atmosphere thanks to the higher brilliance (photon flux) of the undulator (CIRCE's X-ray source) in comparison to a conventional X-ray tube and to the modified detector which is equipped with four differentially pumped stages connected by small apertures. In the detector, a set of electromagnetic lenses focuses the electrons through the apertures to maximize transmission [157]. Such a setup allows the detector to be kept under ultra high vacuum while the sample is at a maximum pressure of 20 mbar. In addition, at the CIRCE beamline the photons energy can be varied (in previous sections the photons energy hν=1486.6 eV was fixed) so that different depths of the samples can be analyzed and depth-profile

Figure 6.25: Picture of the AP-XPS endstation of CIRCE beamline, ALBA synchrotron.

studies can be performed. Initially, at ALBA synchrotron, some tests were carried out at 1486 eV photons energy, nevertheless the photons production efficiency dropped at this hν and nearly no photoelectrons reached the detector making it impossible to obtain spectra with good signal-to-noise ratio. Therefore, the experiments had to be performed with lower photon energies where the photons flux was higher. Finally, 670, 875 and 1150 eV photon energies were chosen. These three photons energies were accurately chosen as they generate Rh 3d and Pd 3d photoelectrons with average kinetic energies (KE) of 349, 554 and 829 eV, respectively, which account for inelastic mean free paths (IMFPs) of Rh 3d and Pd 3d photoelectrons of ca. 0.7, 0.9 and 1.2 nm, respectively (as described above, for hν=1486 eV the IMFP of Rh 3d and Pd 3d photoelectrons was 1.6 nm) [143]. As a consequence, during the *operando* studies more superficial layers were analyzed than by the *in situ* XPS studies. It should be noted that O 1s photoelectrons are emitted with lower kinetic energy (138, 343 and 618 eV for photon energies 670, 875 and 1150 eV, respectively). Therefore, for the same photon energy, O 1s photoelectrons have lower KE than Rh 3d and Pd 3d photoelectrons and do not exactly correspond to the same depth as for Rh and Pd. In the case of Ce, due to the high binding energy of Ce 3d electrons, they were excited only with 1150 eV photon energy and their respectively kinetic energy ranged from 234 to 267 eV.

The photon energy variation allowed us to perform a depth-profile study of the RhPd@D NPs and infer the environment-induced rearrangement and the development of a core-shell structure for each of the treatments performed. These IMFPs

define three different volumes in the NPs that were calculated as the volume enclosed within one IMFP from the exterior surface inside a sphere of diameter 4 nm, taking into account that photons only reach the particle from one side (the side exposed to photons). The sampled volumes or "illuminated" volumes with the three different photon energies are depicted in figure 6.26, where the whitish regions correspond to the volumes reached by the photons. The regions defined from these three depths account for 25, 34 and 44% of the total volume of the NPs for 670, 875 and 1150 eV photon energies, respectively, and each of these regions will be referred to as: outer shell, intermediate layers and core, respectively. It should be note that the analyzed volume in the region defined as *intermediate layers* contains the weighted contribution of the outer shell + intermediate layers and the region defined as *core* also contains the weighted contribution of the outer shell + intermediate layers + core.

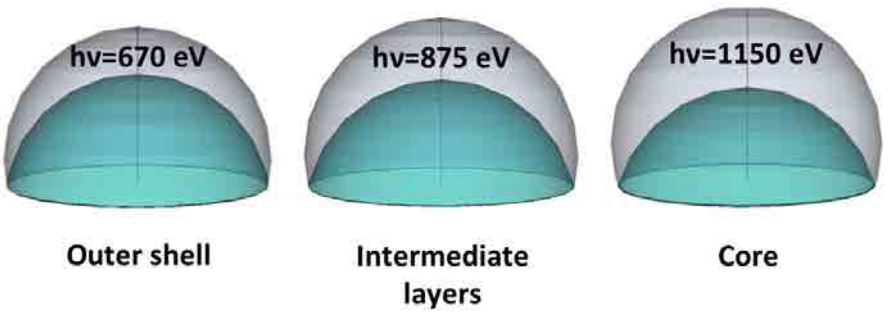

Figure 6.26: Schematic representation of the volumes defined by the different photon energies tested inside a sphere of 4 nm in diameter.

The sequence of the *operando* experiments performed for both systems is as follows: 1) O_2 at 573 K, 2) H_2 at 573 K, 3) ethanol steam reforming (S/C=3) at 823 K and 4) H_2 at 823 K. Samples pressure was kept at 0.05 mbar for all the treatments and the three different photon energies ($h\nu_1$=670 eV, $h\nu_2$=875 eV and $h\nu_3$=1150 eV) were used during each treatment to obtain XP spectra of Rh 3d, Pd 3d, O 1s, C 1s and Ce 3d (the latter excited only by $h\nu_3$=1150 eV). For the ethanol steam reforming tests, the ethanol-water mixture was placed again in the bubbler (the S/C ratio of the liquid mixture was set to S/C=8 in order to obtain a saturated stream with S/C=3.2) and was connected to the analysis chamber by a UHV leak valve. Two other leak valves were used to dose O_2 or H_2 to the analysis chamber. Sample temperature was increased by using an infrared laser (λ=808 nm) focused on a tungsten plate on top of which the samples were mounted. In this setup, 823 K could be reached under H_2 atmosphere and, thus this temperature was chosen for the analyses in order to test the effect of a hydrogen atmosphere at the reaction temperature. The laser heating system available at ALBA overcomes the typical problems from resistive button heaters and thus prevents potential leak

currents or interaction of the filament with the reactant gases, which can induce misinterpretations in data analysis. The temperature was monitored during all the experiments with a K-type thermocouple in direct contact with the samples. Due to short beamtime availability, the stepwise oxidations could not be performed and only one oxidizing treatment at mild conditions was carried out at 573 K, which is the oxidation performed after RhPd deposition over the ceria support.

6.3.1 Model RhPd@D nanoparticles

The sample with model RhPd@D nanoparticles was prepared by drop casting the toluene solution of preformed NPs onto a tungsten foil, that was placed onto the above-mentioned tungsten plate. Figure 6.27 shows a picture of the RhPd@D NPs sample inside the analysis chamber of the CIRCE beamline (ALBA).

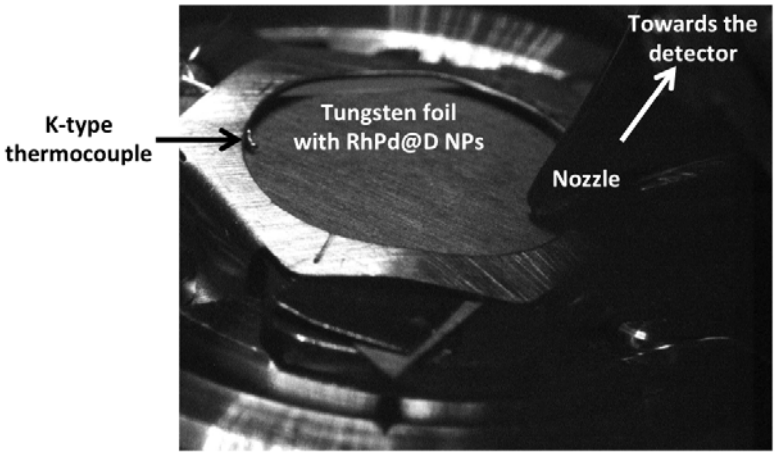

Figure 6.27: Picture of the RhPd@D NPs deposited on a tungsten foil inside the analysis chamber during H_2 reduction at 823 K.

For the *operando* studies, the results obtained from the spectra deconvolution are represented inside semicircles, which schematically symbolize RhPd@D NPs. In each figure, the three regions shown symbolize the results obtained for each sampling depth or photon energy, i.e: the outer semicircle shows the atomic ratio obtained with hν_1=670 eV, the intermediate semicircle the results obtained with hν_2=875 eV and finally the inner semicircle shows the weighted contribution of the core+intermediate layers+outer shell, which are the results obtained with hν_3=1150 eV (see figure 6.26 schematically representing the different sampled volumes).

Figure 6.28 shows the percentage atomic ratios between Rh and Pd together with their oxidation states calculated from the XP spectra recorded for the model RhPd@D NPs under the different gaseous environments tested and the three photon

energies monitored. During the first treatment (calcination at 573 K, O_2 atmosphere; figure 6.28a), the model NPs showed a Pd/Rh ratio close to unity and did not show substantial differences at the different depths studied. The Pd atomic fraction in the outer region (excited at hν=670 eV) was 0.52 ± 0.03, whereas for the inner region (excited at hν=1150 eV) it was 0.57 ± 0.03 (figure 6.28a). As regards the oxidation state of the metals, also represented in figure 6.28, Pd was highly reduced at all depths with concentrations of metallic Pd of 65-72%. Rh was also reduced in all the layers, but to a lesser extent (51-65%). For both metals, oxidation increased towards the NPs surface, which were in direct contact with the O_2 atmosphere. RhPd@D NPs spectra acquired during the different treatments performed are shown in next section (section 6.3.2, figures 6.33, 6.34 and 6.35) together with the spectra acquired for the RhPd@D/CeO_2 catalyst.

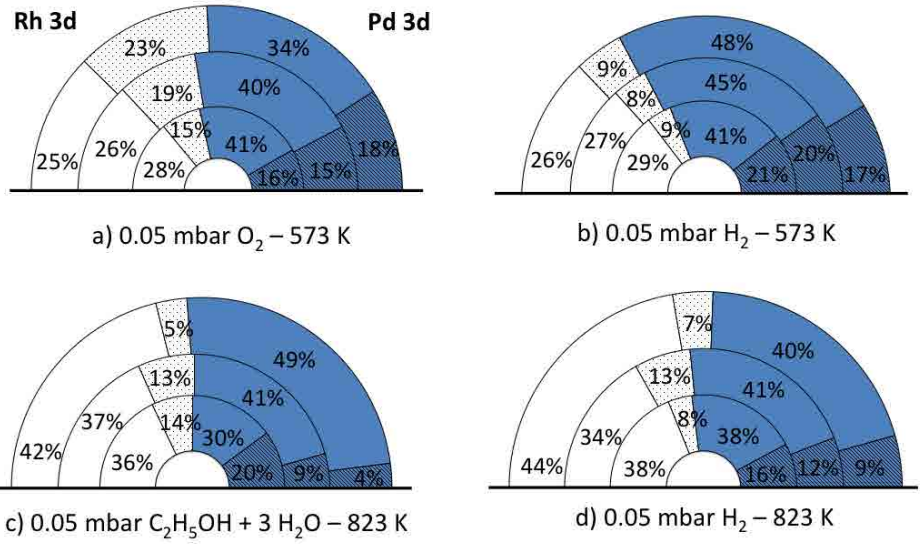

Figure 6.28: Atomic fractions of Pd and Rh calculated for the model RhPd@D NPs. Semicircles show the atomic fractions of Pd (depicted in blue) and Rh (depicted in white), where the dashed regions correspond to the oxidized fraction of each metal. The outer semicircle corresponds to the atomic fractions obtained with 670 eV photon energy (hν_1); the intermediate semicircle to hν_2=875 eV; and the inner semicircle to hν_3=1150 eV. a, b, c and d correspond to the different gaseous environments evaluated.

Upon reduction with H_2 at 573 K (for catalyst activation, figure 6.28b and figure 6.33), Pd segregation towards the surface was clearly observed, with a Pd atomic fraction of about 0.65 ± 0.03. This fully agrees with the work of Tao et al. [144], where a migration of Pd atoms towards the surface during H_2 exposure was also reported. At the same time, Rh experienced a strong reduction and ca. 75% of both metals were present in the metallic state. After H_2 activation of the sample, the ESR process was studied by dosing ethanol and water directly inside the analysis

chamber at 823 K. A survey spectrum of the analysis chamber was acquired while the ethanol/water mixture was entering the chamber in order to analyze the gas phase and check that both reactants were being introduced in the analysis chamber. Figure **6.29** shows the gas phase spectrum. Carbon and oxygen peaks were identified in the survey spectrum which correspond to ethanol and water, as well as, Ar peaks corresponding to the inert gas flown through the bubbler. Therefore, it was confirmed that ethanol and water were entering the analysis chamber.

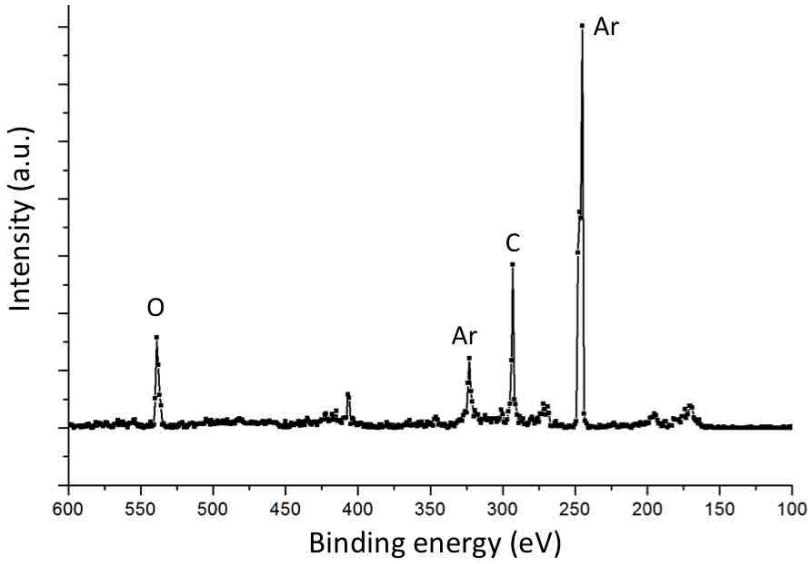

Figure 6.29: Survey spectrum of the gas phase during ESR reaction at 823 K.

Under ESR (figure **6.28**c), the NPs experienced a new restructuring as Rh atoms migrated towards the surface and again the atomic ratio of Rh and Pd was ca. 1:1. Furthermore, the outer region of the RhPd@D NPs further reduced and approximately 90% of Rh and Pd were found in their metallic state, which again was ascribed to the reducing effect of the hydrogen generated during the ESR reaction at 823 K. This effect was corroborated by studying the RhPd@D NPs under pure H_2 at the same temperature (figure **6.28**d and figure **6.35**). At this temperature the noble metals did not experience substantial changes compared with the previous ESR environment.

After the AP-XPS experiments, the analyzed RhPd@D NPs sample was removed from the AP-XPS system and was examined by SEM in order to investigate the changes experienced by the RhPd@D NPs after the sequence of AP-XPS treatments. To do the comparison, a fresh sample of RhPd@D NPs deposited on the same W foil was also examined by SEM. Figure **6.30**a shows the W foil with the as deposited RhPd@D NPs and figure **6.30**b after the whole set of *operando* experiments.

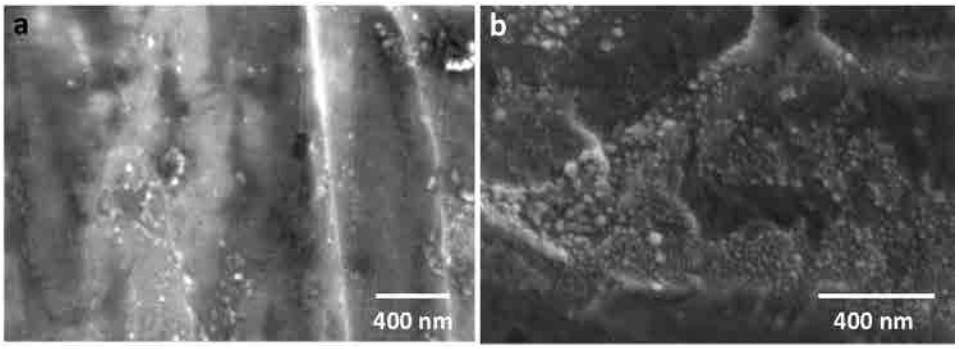

Figure 6.30: SEM images of RhPd@D NPs deposited on a W foil. a) Before AP-XPS experiments. b) After the AP-XPS treatments sequence.

The SEM images did not have high quality as the W foil had high surface roughness which made it difficult to obtain clear SEM images and only the larger NPs could be distinguished. In addition, the appropriate technique to investigate NPs size is TEM, but as the NPs were supported on the W foil its observation with the TEM microscope was not possible. Nevertheless, SEM allowed to survey the W foil to look for RhPd agglomerations and none of them were identified in the post-reacted sample. Despite the poor resolution of SEM images, larger RhPd@D NPs than as deposited were detected and the mean particle size of the post-reacted RhPd@D NPs was 20.1 ± 6.6 nm. The images of the sample before reaction showed more isolated RhPd@D NPs but the quality of the images was poorer than those of the post-reacted samples as also charging took place, probably due to the protecting organic shell. The mean particle size before reaction determined by SEM was 26.3 ± 8.2 nm, which is not consistent with the TEM observations of the as-synthesized RhPd@D NPs (section **4.2.1**) and confirmed the poor resolution of the pre-reaction SEM images. Therefore, probably also the mean particle size of the post-reacted NPs was overestimated. Nevertheless the SEM analyses allowed to discard large RhPd agglomerations after the *operando* experiments and to confirm that some RhPd@D NPs sintered.

6.3.2 Model RhPd@D/CeO_2 catalyst

The first analyses of the RhPd@D/CeO_2 catalyst were carried out with a catalyst with noble metal loading 0.5 wt.% Rh + 0.5 wt.% Pd, however nearly no signal of the noble metals was obtained when the gases were dosed to the analysis chamber. Therefore, a higher NM concentration had to be used for this investigation and a new RhPd@D/CeO_2 catalyst with higher NPs concentration was synthesized. The noble metal content was increased to 1.5 wt.% Rh + 1.5 wt.% Pd and a new 3RhPd@D/CeO_2, which was characterized before reaction in section **4.3.2**, was synthesized. Then, the AP-XPS sample was prepared by pressing ca. 20 mg of

the freshly prepared 3RhPd@D/CeO_2 powder to form a self-consistent disk (pellet) that was placed over the W plate of the CIRCE sample holder. Figure 6.31 shows a picture of the RhPd@D/CeO_2 catalyst inside the analysis chamber. A gold foil was also placed on the sample holder to use it as a binding energy reference.

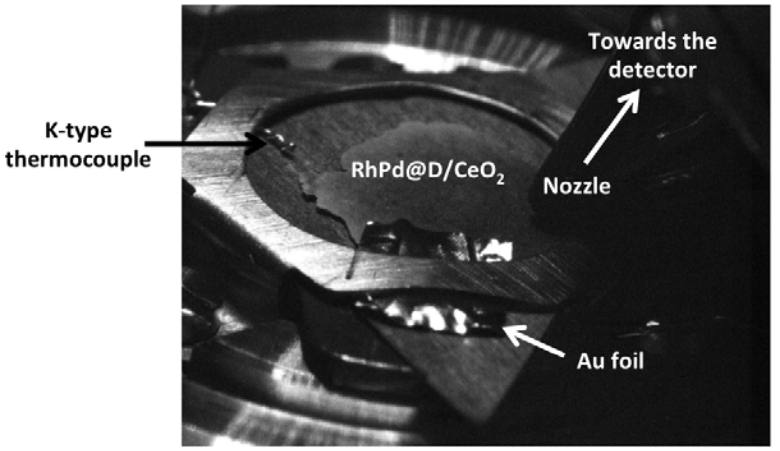

Figure 6.31: Picture of the 3RhPd@D/CeO_2 catalyst placed over the tungsten plate inside the analysis chamber during H_2 reduction at 573 K.

The analyses of the 3RhPd@D/CeO_2 catalyst started with the oxidation at 573 K, as for the unsupported NPs investigations, but this time no counts were recorded, probably due to the insulating nature of the 3RhPd@D/CeO_2 powder. It was only after dosing H_2 to the analysis chamber that photoelectrons generated could reach the detector. Therefore the initial oxidizing treatment could not be performed under *operando* conditions as no counts were recorded under O_2 atmosphere (step 1). For this reason, the experiments had to be restarted and a new 3RhPd@D/CeO_2 sample was prepared and calcined in a muffle at 573 K for 6 hours. This treatment was performed in order to emulate the first calcination treatment and leave the catalyst in the state prior to H_2 reduction, which was the first treatment performed over the 3RhPd@D/CeO_2 catalyst under *operando* conditions.

A different scenario resulted when the model RhPd@D NPs were supported on CeO_2. Figure 6.32 shows the percentage atomic ratios between Rh and Pd together with their oxidation states.

For the real 3RhPd@D/CeO_2 catalyst, the reduction treatment at 573 K resulted in a Pd-rich surface with Pd atomic fractions of about 0.65 (figure 6.32a and figure 6.33). This is fairly similar to the value found for the unsupported NPs under the same environment (figure 6.28b). The spectra acquired during hydrogen reduction at 573 K for the 3RhPd@D/CeO_2 and the unsupported RhPd@D NPs are shown in figure 6.33.

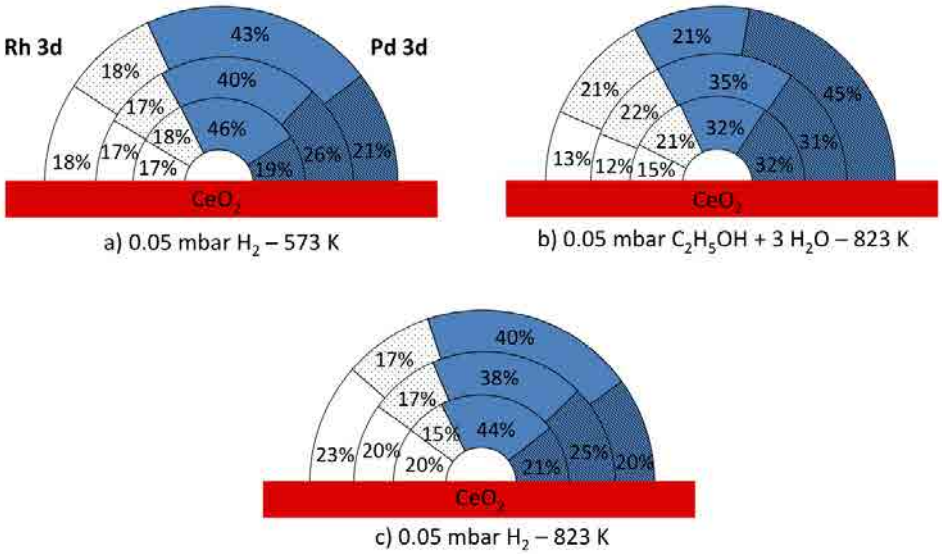

Figure 6.32: Atomic fractions of Pd and Rh calculated for the 3RhPd@D/CeO_2 catalyst. Semicircles show the atomic fractions of Pd (depicted in blue) and Rh (depicted in white), where the dashed regions correspond to the oxidized fraction of each metal. The outer semicircle corresponds to the atomic fractions obtained with 670 eV photon energy (hν); the intermediate semicircle to hν_2=875 eV; and the inner semicircle to hν_3=1150 eV. a, b and c correspond to the different gaseous environments evaluated.

However, under ESR conditions at 823 K, there was no migration of Rh or Pd at all. The atomic fraction of both NM remained approximately constant at the same values as in the previous reducing treatment for all depths. This was in contrast to the behavior observed for the unsupported NPs, where surface Pd enrichment experienced during catalyst activation was reversed during the ESR reaction. Most importantly, the oxidation state of both metals experienced an important variation and both became more oxidized (figure **6.32**b), once again in clear contrast to the behavior observed for unsupported NPs, where the NM were predominantly reduced (figure **6.28**c). Furthermore, Pd developed a core-shell structure of oxidation states, as seen in figure **6.34**, where a large oxidized Pd component can be identified in the outer shell of the 3RhPd@D/CeO_2 catalyst (figure **6.34**d). It is likely that the activation of water by CeO_2, as deduced from the catalytic results (explained in section **5.3.2**), created hydroxyl groups (-OH) at the catalyst surface, thus leading to the oxidation of the outermost layer of the NPs.

This remarkable difference with the unsupported model NPs indicated that the strong interaction of the metal NPs with the ceria support plays a key role in the catalytic behavior of the RhPd alloy NPs by limiting the reorganization of the metals under reaction conditions (*quenching effect*) and by providing active oxygen atoms to the metals at the surface of the NPs. Figure **6.34** shows Rh 3d,

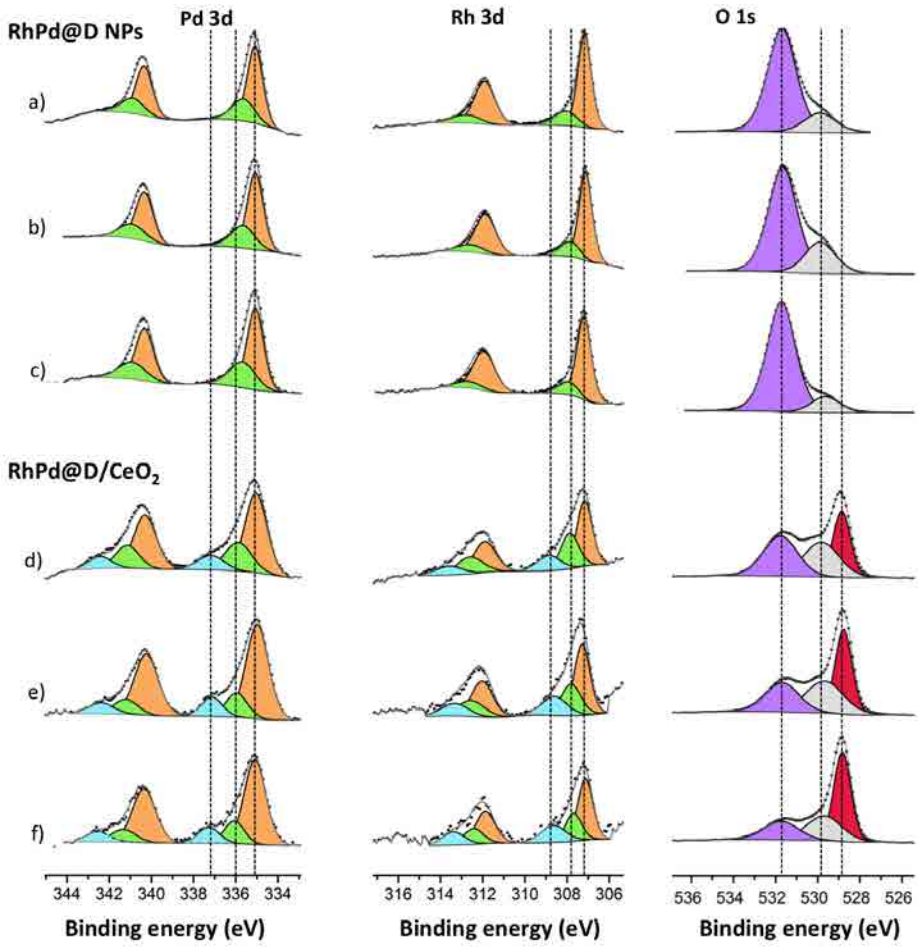

Figure 6.33: Ambient pressure X-ray photoelectron spectra of Pd 3d, Rh 3d and O 1s recorded for both the model RhPd@D nanoparticles (a to c) and the 3RhPd@D/CeO_2 catalyst (d to f) under H_2 at 573 K. The photon energies used were 670 eV (a and d), 875 eV (b and e) and 1150 eV (c and f). The O 1s regions in b), c), e), and f) correspond in kinetic energy scale to the metal regions in a), b), d), and e), respectively. The sample pressure was 0.05 mbar.

Pd 3d and O 1s XP spectra recorded for both the model RhPd@D NPs and the 3RhPd@D/CeO_2 catalyst under ESR conditions at 823 K.

Remarkably, the photoemission lines of the noble metals of the real catalyst contain, in all cases, an additional component with respect to the unsupported NPs at ca. 308.7 and 337.8 eV for $Rh_{3d5/2}$ and $Pd_{3d5/2}$, respectively, which was ascribed to the metal-support interaction discussed above [158]. The O 1s spectra of the RhPd@D/CeO_2 showed three spectral features: the component at low binding energy (529.1 eV) was ascribed to O-Ce, the component at 530 eV to O-metals

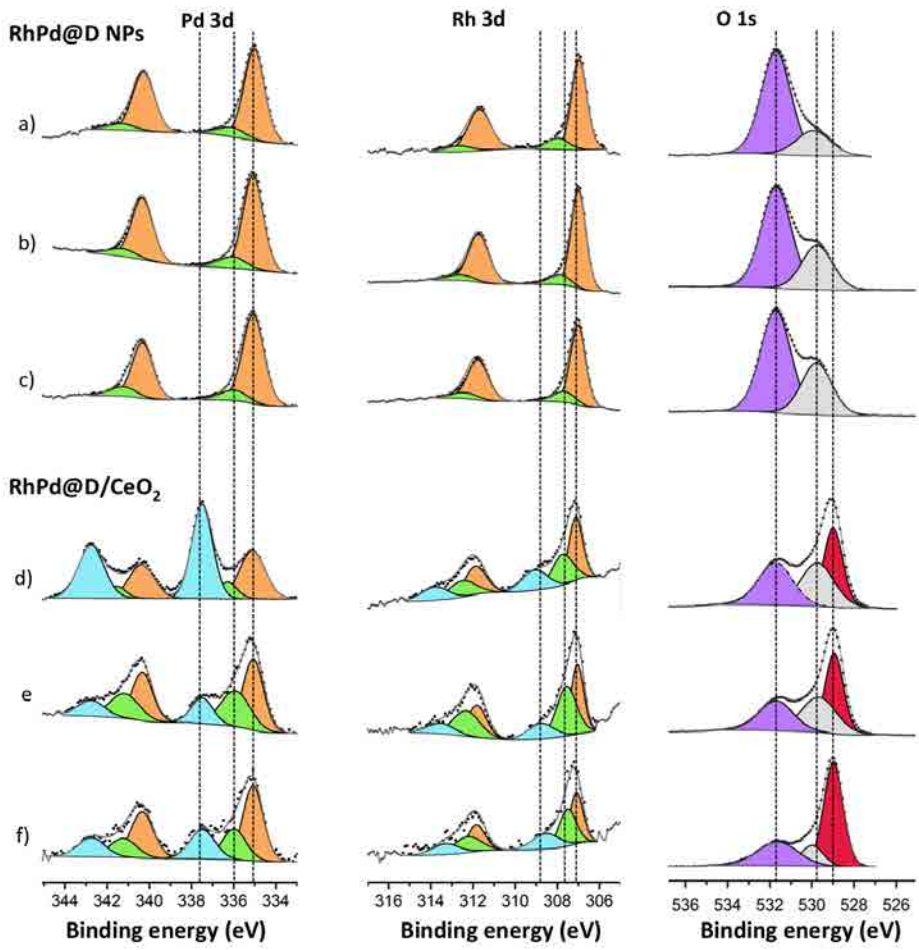

Figure 6.34: Ambient pressure X-ray photoelectron spectra of Pd 3d, Rh 3d and O 1s recorded for both the model RhPd@D nanoparticles (a to c) and the 3RhPd@D/CeO_2 catalyst (d to f) under ESR conditions at 823 K. The photon energies used were 670 eV (a and d), 875 eV (b and e) and 1150 eV (c and f). The O 1s regions in b), c), e), and f) correspond in kinetic energy scale to the metal regions in a), b), d), and e), respectively. The sample pressure was 0.05 mbar.

(Rh and/or Pd) and the component at 531.8 eV to -OH present on the surface of the catalyst (figure **6.34** O 1s d to f) [159, 160]. Interestingly, the ratio between the area of the O-Ce peak and the -OH peak increased as the photon energy increased, i.e., as the sampling depth increased, which highlights the sensitivity to different depths of the chosen photon energies and the presence of the -OH groups on the surface of the 3RhPd@D/CeO_2 catalyst. The same trend was observed for the unsupported NPs, where the ratio between the O-metal peak and the -OH peak also increased when the photon energy was increased (figure **6.34** O 1s a to c).

Finally, the oxidation state of both metals in the 3RhPd@D/CeO_2 catalyst very nearly recovered the values of the first reducing treatment at lower temperature (figure 6.32a) during the reduction with pure H_2 at the reaction temperature (823 K, figure 6.32c and figure 6.35), unlike the model NPs. Once again this pointed to the stabilizing effect of the ceria support.

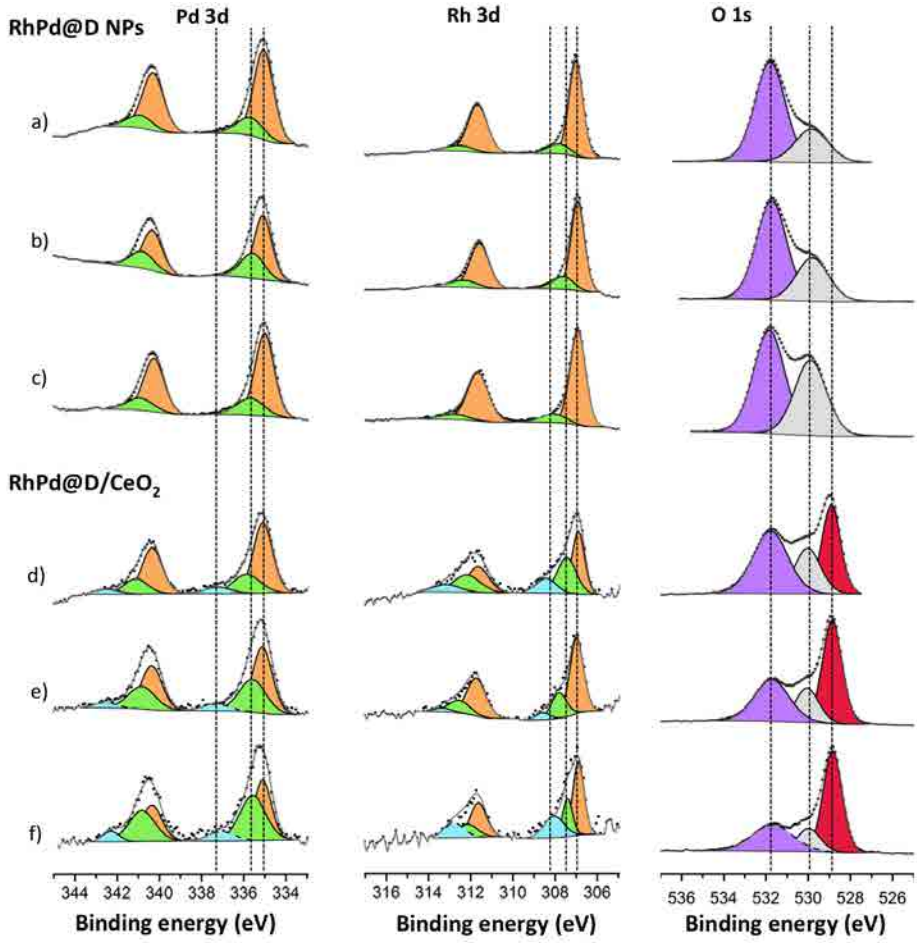

Figure 6.35: Ambient pressure X-ray photoelectron spectra of Pd 3d, Rh 3d and O 1s recorded for both the model RhPd@D nanoparticles (a to c) and the 3RhPd@D/CeO_2 catalyst (d to f) under H_2 at 823 K. The photon energies used were 670 eV (a and d), 875 eV (b and e) and 1150 eV (c and f). The O 1s regions in b), c), e), and f) correspond in kinetic energy scale to the metal regions in a), b), d), and e), respectively. The sample pressure was 0.05 mbar.

Figure 6.36 shows Ce 3d AP-XP spectra acquired during all the treatments performed. Analysis of the oxidation state of cerium (performed only with hν=1150 eV) revealed variations depending on the gaseous environment and temperature.

Under H_2 and 573 K, the Ce^{4+}/Ce^{3+} atomic ratio was 1.59. The ratio increased to 1.72 during the ESR reaction at 823 K, after oxidation experienced by the catalyst, and it strongly decreased to 1.20 under H_2 at 823 K.

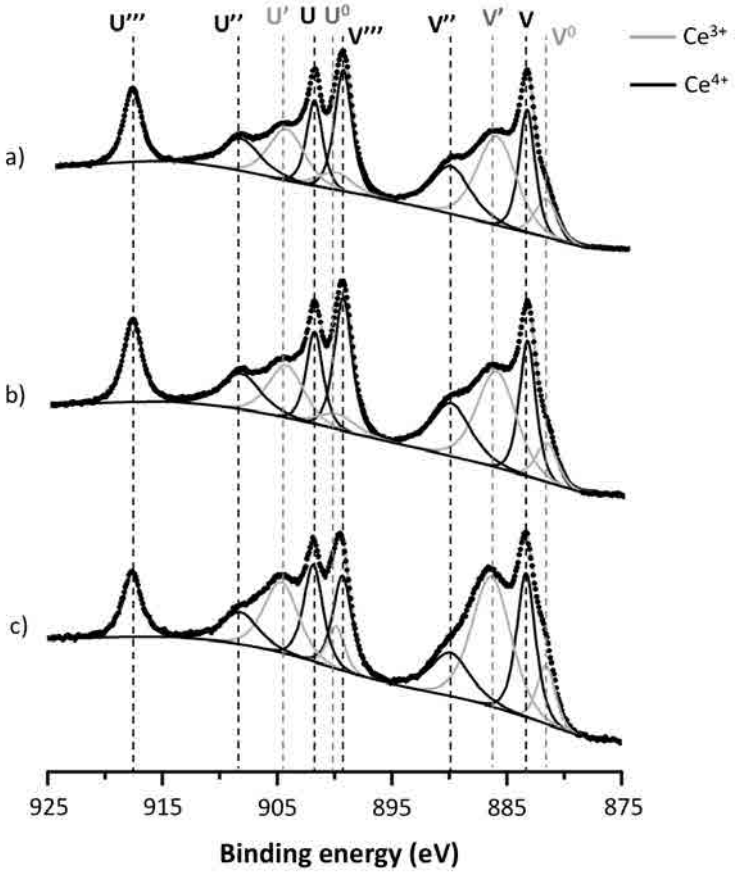

Figure 6.36: Ambient pressure X-ray photoelectron spectra of Ce 3d recorded for the 3RhPd@D/CeO_2 catalyst: a) under H_2 at 573 K; b) under ESR at 823 K and c) under H_2 at 823 K. The sample pressure was 0.05 mbar.

In summary, the unsupported RhPd@D NPs under ESR conditions suffered a strong reduction and the outermost layer was mainly metallic (∼90%), whereas the same NPs supported on ceria experienced the opposite: they became oxidized and Pd exhibited a different ratio of oxidation states at different depths. During the performance of the ESR reaction, the Pd_{red}/Pd_{ox} ratio increased at a greater depth within the NPs, i.e., Pd presented a core-shell structure of oxidation states. Under the same environment (ESR at 823 K), CeO_2 also experienced oxidation. In the absence of a support, the model NPs experienced stronger reduction for all the environments tested and the reduction temperature affected the amount of metallic

phase found in Rh and Pd. Compared with the unsupported NPs, the capability of CeO_2 as a support to activate water and to donate oxygen atoms clearly determined the oxidation states of the noble metals under the same reaction conditions. In addition, the interaction between the ceria support and the metal NPs prevented the reorganization of the Rh and Pd atoms.

Throughout this Chapter, the pivotal role of the metal-support interaction in the reorganization of metal atoms in supported bimetallic catalysts under *operando* and *in situ* conditions has been shown. The strong influence that the metal-support interaction had on the catalytic performance was evidenced in the preceding Chapter 5. *In situ* and *operando* XPS studies of the same systems have shown different results, highlighting the importance of the presence of the reactants while the measurements are being performed, as some species only exist under the presence of the reactive atmosphere.

Another conclusion of the *operando* experiments is that AP-XPS (and other *operando*) studies carried out on unsupported model systems may not provide reliable information on supported real catalysts. For this reason, it is very important to also take into account the influence of the support, in spite of the experimental difficulties often encountered.

Results regarding the study under operating conditions were published in *Núria J. Divins, Inma Angurell, Carlos Escudero, Virginia Pérez-Dieste and Jordi Llorca, "Influence of the support on surface rearrangements of bimetallic nanoparticles in real catalysts", Science 346 (2014), pp. 620* [115] and this is one of the papers of this Thesis.

7 Hydrogen production in a membrane reactor

In this Chapter, a pure hydrogen generation device is presented based on the coupling of the RhPd/CeO_2//Mon catalyst to a membrane reactor provided with Pd-Ag membranes. Parametric sensitivity analyses regarding temperature, pressure, feed composition and load were performed in order to obtain the optimal operating windows.

7.1 Introduction

Palladium-alloy membranes have been used in membrane reactors mainly for water-gas shift (WGS) and steam reforming (SR) reactions of methane and methanol, but their use in the ESR is relatively new [161]. In the literature, mainly the role of the membrane has been evaluated [39], by analyzing the performances of the reaction system in terms of ethanol conversion, hydrogen yield and hydrogen recovery, which indicates the amount of hydrogen collected in the permeate side versus the total hydrogen produced during the reaction. Also, different coupling degrees of hydrogen production and membrane purification have been reported.

A large piece of work on ESR with Pd-Ag membranes (wall thickness ∼50 µm) using sweep-gas has been carried out at the University of Calabria (Italy). Gallucci et al. [162] studied both methanol and ethanol steam reforming over Ru/Al_2O_3 catalysts in three different Pd-Ag membrane reactors. For ESR, the highest conversion attained at 723 K was about 50% and it was significantly higher in the catalytic membrane reactor (CMR), where the catalyst was placed inside the membrane tube, than that attained in a traditional reactor. However, in the CMR coke deposition took place to a large extent with the consequent deactivation of the catalyst. Basile et al. [163] and Tosti et al. [164] used the same catalyst formulation for performing ESR; the former in a dense Pd-Ag membrane reactor where hydrogen recoveries (defined as the percentage ratio between permeate H_2 and the total H_2 produced, R_{H_2}) up to 22% and hydrogen yields (defined as the percentage ratio between the hydrogen permeated and the maximum theoretical H_2 production, η_{H_2}) ∼56% were reported and the latter in a dense thin-wall (50-60 µm) Pd-Ag

tube were η_{H_2} increased up to 80% at 723 K and 2 bar. In both cases, a significant improvement over the performance obtained with conventional catalytic reactors was reported because reaction conversion beyond the thermodynamic equilibrium, which is an upper limit to be considered in a traditional reactor, was attained due to the continuous removal of one of the reaction products (shift effect). The same Ru/Al_2O_3 catalyst was also studied for OSR in a CMR by flowing sweep gas into the permeate side of the reactor [165]. A maximum R_{H_2}∼30% was attained at an oxygen-to-carbon ratio O/C=1.2. The dense thin-wall Pd-Ag tube (50-60 µm, reported in [164]) was used to test the performance of Pt- and Ni-based catalysts. Platinum- and Ni-based catalysts showed a poor performance in terms of hydrogen yield with respect to the Ru-based catalyst (Ru > Ni > Pt at low feed, while for higher feed fluxes, the sequence was Ru > Ni = Pt) [164]. In [166], Tosti et al. obtained kinetic expressions and modeled the CMR operation based on the results obtained for Ru-, Ni- and Pt-based catalysts in order to optimize the membrane reformer by assessing the ratio between the reaction and permeation kinetics. Pd-Ag tubes with thicker walls (150 µm thickness) were used to study the influence of pressure in the range from 1 to 8 bar. At 723 K and 4 bar, Tosti et al. [167] obtained R_{H_2}∼100%. In [168], a traditional fixed bed reformer loaded with a Rh-based catalyst supported on alumina was used to perform ESR at 963-1163 K and was coupled to a multi-tube Pd-Ag membrane reactor where both the water-gas shift reaction and the separation of pure hydrogen took place. They evaluated the effect of temperature, pressure and membrane sweeping mode. Tosti et al. achieved up to 3.5 LN_{H_2}/min of pure hydrogen by using the ∼1800 cm^2 membrane separation unit. Ethanol OSR was also studied by Santucci et al. [169] over a Pt/Al_2O_3 catalyst in a membrane module with a finger-like configuration. At 723 K and 2 bar, a maximum of 4.1 moles of permeated hydrogen per mole of ethanol fed were attained by using a water/ethanol/oxygen feed molar ratio of 10/1/0.5. The comparison with ESR results performed under the same experimental conditions showed that the addition of O_2 had a positive effect on the hydrogen yield. Iulianelli and Basile [170] and Iulianelli et al. [171] studied the ESR performance over Co/Al_2O_3 catalysts by varying several operating parameters such as temperature, pressure, sweep-gas flow and load. At 673 K, 3 bar and gas hourly space velocity GHSV=0.2/h, the unit exhibited a hydrogen recovery R_{H_2}=95% and η_{H_2}=60%. Basile et al. [172] tested the same catalyst at 673 K in a porous stainless steel (PSS)-supported Pd membrane reactor to investigate the membrane properties and pressure (from 3 to 8 bar) influence on the ESR reaction performance. Under full ethanol conversion, R_{H_2}∼50% was reached. The performance of Co/Al_2O_3 and Ni/ZrO_2 catalysts for bioESR (modeled with a water/ethanol/acetic acid/glycerol mixture of molar ratio 1/13/0.18/0.04) was tested by using a PSS membrane reactor at 673 K and 9-12 bar. About 94% of bioethanol conversion was obtained at 12 bar and GHSV=800/h over the Co/Al_2O_3 catalyst, with 40% hydrogen yield and 40% hydrogen recovery [173].

Lin et al. from Chienkuo Technology University (Taiwan) studied the ethanol OSR performance of a $CuZn/Al_2O_3$ catalyst loaded on a Pd-Ag/PSS membrane reactor (membrane thickness 20 µm) [174]. The catalyst was placed inside the annular space defined by two concentric tubes, being the Pd-Ag membrane the inner tube. The OSR performance was tested at temperatures ranging from 593 K to 723 K and pressures from 3 to 10 bar. The maximum hydrogen yield reported was ∼45% at 9 bar, 723 K and ethanol/water/oxygen molar ratio 1/1/0.2. The addition of oxygen to the feed stream also resulted in higher ethanol conversions, as previously reported. The same study was conducted over a Ni-Pd-Ag ternary alloy membrane reactor with similar results [175].

High-pressure ESR to produce the hydrogen needed to refuel the high-pressure tanks of PEMFC vehicles was investigated by Papadias et al. [176] at Argonne National Laboratory (USA). The experiments were conducted at pressures ranging from 7 to 70 bar, temperatures from 873 K to 1023 K, S/C=3-12 and GHSV=$8{\cdot}10^3$-$8{\cdot}10^5$ h^{-1} in a Pd-Ag (30 µm) CMR loaded with Rh/La_2O_3-Al_2O_3 catalyst. As expected from thermodynamics, low hydrogen yields were achieved as higher pressures inhibited hydrogen formation in favor of methane production.

At Universitat Politècnica de Catalunya (Spain), Domínguez et al. studied the ESR reaction over a CMR loaded with a cobalt talc catalyst at temperatures ranging from 598 K to 673 K and pressures from 5 bar to 15 bar [177]. The hydrogen yield attained in the CMR was improved with respect to a traditional reactor and also showed rapid response to changes in the feed. A cobalt hydrotalcite-derived catalyst doped with potassium was bed packed around a Pd-Ag membrane (30 µm) in a work by Espinal et al. [178]. In this work, stable operation of the CMR for 650 hours was achieved with hydrogen recoveries up to 80% at 873 K and 12 bar. The hydrogen production (3.7 $L_{H_2}/(mL_{\text{liquid ethanol, in}}{\cdot}g_{cat})$ at 12 bar and 873 K) of the CMR was three times higher than the one obtained with a staged reactor. The experiments of Papadias et al. [176], Domínguez et al. [177] and Espinal et al. [178] were performed without sweep gas, therefore, pure hydrogen was obtained in the permeate side of the membrane, ready to feed a PEMFC.

Although most of the ESR work in catalytic membrane reactors has been done with Pd-Ag selective membranes, there are also some examples elsewhere [179,180] of ESR in different types of membrane reactors aimed at reducing their cost, such as Pt-impregnated Knudsen membranes, Pt/TiO_2-based CMR or Pd-Cu membranes.

7.2 Catalyst synthesis

Five cordierite monoliths were functionalized with $1RhPd/CeO_2$ catalyst following a variation of the procedure described in Chapter **3**. In this case, the CeO_2 layer

was deposited by repetitively immersing the cordierite monoliths in an aqueous solution of $Ce(NO_3)_2{\cdot}6H_2O$ (Fluka) followed by 2 hours drying at 353 K under continuous rotation (60 rpm) and calcination at 773 K. The expected fcc CeO_2 phase was formed. Then, 0.5 wt.% Rh + 0.5 wt.% Pd were added in a single step by incipient wetness impregnation, following the regular procedure. This procedure was repeated for five cordierite monoliths being the total amount of $1RhPd/CeO_2$ catalyst incorporated 1.3 g and the total volume of the monolithic structures 24 cm^3. In figure 7.1 the five functionalized $1RhPd/CeO_2//Mon$ are shown. As seen in figure 7.1, the functionalized monoliths were sandwiched between two short inert cordierite monoliths (white) for assembly reasons.

Figure 7.1: $1RhPd/CeO_2//Mon$ implemented in the membrane reactor. The scale is shown in cm.

7.3 Experimental device

Hydrogen generation via ESR and hydrogen purification using selective Pd-Ag membranes were conducted in a single module in order to obtain a simplified setup. The five functionalized monoliths were implemented into a stainless steel membrane reactor, which included the feed evaporation and outlet conduits for both permeate and retentate streams (Reb Research & Consulting). Figure 7.2 shows on the left a schematic representation of the staged reactor developed, where the different elements that constituted it are represented. On top, the hydrogen generation zone can be seen, which was comprised by the five $1RhPd/CeO_2//Mon$ in series, and where ESR took place. Therefore, in this zone mainly H_2 was produced along with CO, CH_4 and CO_2. Right after was placed the separation chamber, which was comprised by four Pd-Ag membranes dead-end tubes 3" tall and diameter 1/8". Finally, the lower head, which allowed the exit of the separated streams (permeate and retentate streams), was placed. As operation without sweep gas was chosen, pure hydrogen (H_2 purity $>$ 99.999%) was obtained on the permeate stream. Figure 7.2 shows on the right a picture of the final implementation of the reaction-separation tube. The ethanol/water mixtures were introduced into the reactor through a coil

surrounding it in order to profit the heat supplied to the reactor and evaporate the feed mixtures. A nut on top of the reactor allowed for catalyst loading and replacement. The dimensions of the reactor were 25.4 cm (10") tall and 2.54 cm (1") external diameter.

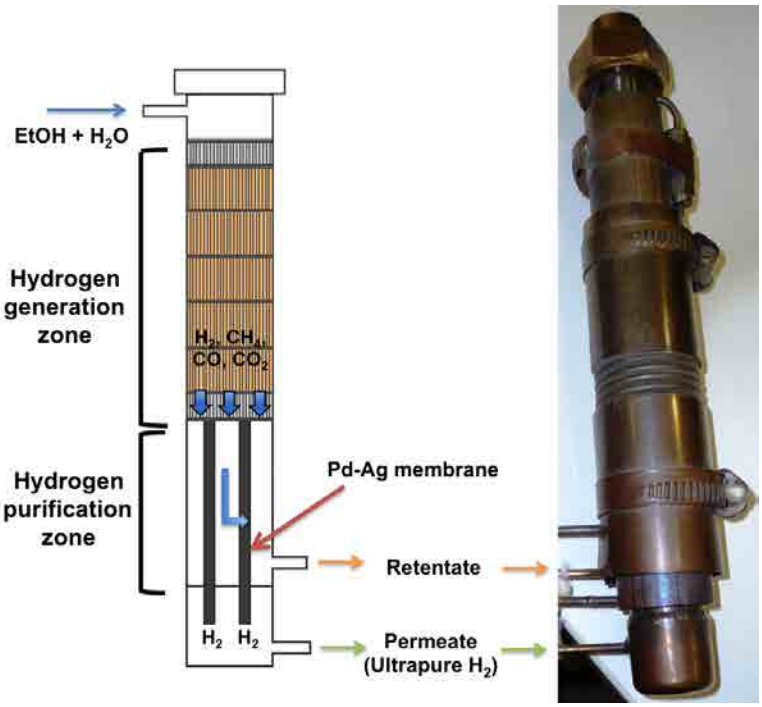

Figure 7.2: Schematic representation of the stage reactor designed.

The total active area of the four Pd-Ag membranes used amounted 30.4 cm^2. The Pd-Ag active layer was 30 µm thick and was supported over PSS.

The reaction-separation module was implemented into the proper periphery which included a liquid reservoir (ethanol+water tank), a liquid injection HPLC pump directly connected to the reservoir, a temperature controller, thermal insulating elements, a pressure transducer and a liquid condenser. Figure 7.3 shows a schematic representation of the experimental setup.

For the sake of simplicity, a single electrical heater was implemented to operate the reactor at the desired temperature, providing the heat of reaction and also the heat for feed evaporation. Therefore, both reaction and separation processes operated at the same temperature. The maximum temperature reachable with the installed heater was 923 K. An electronic PID controller (Fuji PXR4) connected to a K-type thermocouple in contact with the reactor wall governed the heating device. The membrane reactor was thermally insulated by ceramic elements. The retentate

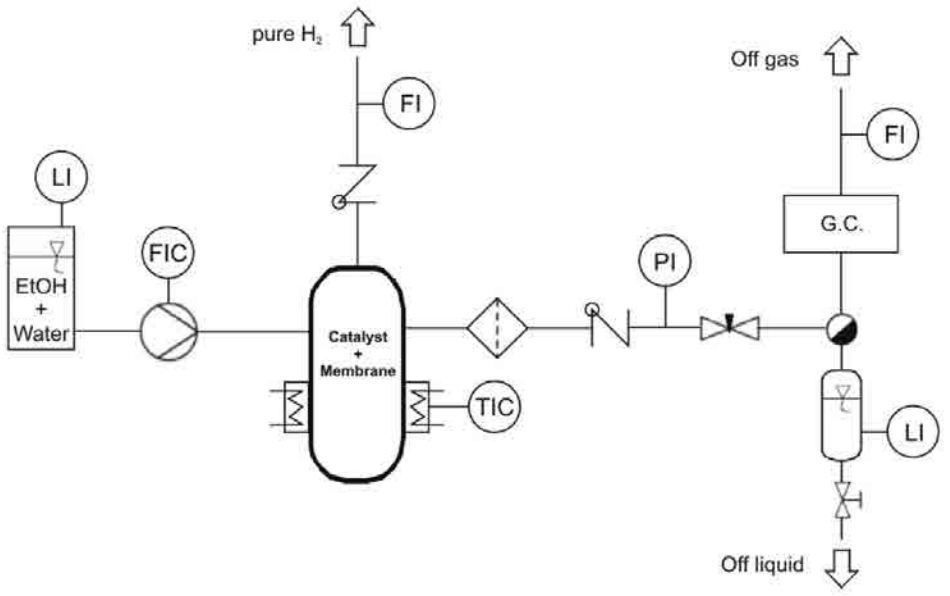

Figure 7.3: Schematic representation of the experimental setup designed.

pressure was adjusted and controlled by a manually-operated back-pressure regulator (Swagelok), which was identical to the device used in Chapter 5. No pressure regulation was implemented on the permeate side, thus the pure hydrogen stream was obtained at atmospheric pressure. Condensable components in the retentate stream, such as acetaldehyde, or unreacted water and ethanol, leaving the reactor were condensed and stored in a tank with liquid level indication. The whole system was arranged to build up a portable compact unit. The dimensions of the designed prototype were 35 x 60 x 40 cm. Two pictures of the final H_2 production-purification unit developed are seen in figure 7.4: on the left-hand side, the frontal view of the prototype is given, where the controls that governed the unit are seen. On the right side, a lateral view is shown. The pure-hydrogen generation unit was built as a demonstrator in the framework of a VALTEC technology transfer project (Generalitat de Catalunya).

The gaseous composition of the retentate stream was analyzed online by the micro-chromatograph (Agilent 3000A, see section 5.1) every five minutes. The permeate stream was also analyzed to verify the selectivity of the membrane towards hydrogen and H_2 purities $> 99.999\%$ were recorded. Additionally, total volumetric fluxes of both permeate ($V_{H_2,p}$)[1] and dry retentate streams (V_r) were measured by a bubble soap meter. Molar fluxes of H_2, CO, CO_2 and CH_4 in the reactor effluent were calculated using the chromatographic analyses and the total volumetric flux data acquired.

[1] r stands for retentate and p for permeate.

Figure 7.4: Pictures of the pure-hydrogen generation unit designed.

7.4 Catalytic activity screening

Several experiments were conducted to study the steady-state performance of the hydrogen generation unit. The conditions tested are reported in table 7.1.

Table 7.1: Experimental conditions tested.

Temperature (K)	723 - 923
Absolute retentate pressure (P_r) (bar)	1 - 11
Absolute permeate pressure (P_p) (bar)	1
Feed load ($\mu L_{liquid}/(mg_{catalyst} min)$)	0.09 - 0.32
Feed concentration ($mol_{Ethanol}/mol_{H_2O}$)	1/2 - 1/6 (S/C=1 - 3)

The performance of the reaction-purification prototype was evaluated using the same parameters discussed in other Chapters (see sections 5.2 and 8.3), such as ethanol conversion (equation 7.1), hydrogen yield (equation 7.2), volumetric hydrogen production ($V_{H_2,p+r}$) and selectivities (equation 7.3) as well as new parameters that had to be defined in order to asses the performance of the whole hydrogen generation unit, such as the hydrogen recovery of the unit (R_{H_2}, equation 7.4) and the overall efficiency (η_{H_2}, equation 7.5).

$$\chi_{Ethanol} = \frac{\dot{n}_{Ethanol,in} - \dot{n}_{Ethanol,out}}{\dot{n}_{Ethanol,in}} \cdot 100, \text{where } [\dot{n}] = \frac{mol}{s} \tag{7.1}$$

$$\theta_{H_2} = \frac{\dot{V}_{H_2,p+r}}{\dot{V}_{Ethanol,in}} = 6 \cdot Y_{H_2} \tag{7.2}$$

$$S_i = \frac{\dot{n}_i}{\sum_i \dot{n}_i} \cdot 100, \quad i = H_2, CH_4, CO_2, CO, ... \tag{7.3}$$

$$R_{H_2} = \frac{\dot{V}_{H_2,p}}{\dot{V}_{H_2,r+p}} \cdot 100 \tag{7.4}$$

$$\eta_{H_2} = \frac{\dot{V}_{H_2,p}}{6\dot{V}_{Ethanol,in}} \tag{7.5}$$

7.4.1 Reaction temperature effect

Initially, the effect of the reaction temperature was evaluated. The reaction temperature was varied between 723 K and 923 K, whereas the other reaction parameters were kept constant at: S/C=1.5, feed load or space velocity v_{space}=0.22 $\mu L_{liquid}/(mg_{catalyst}min)$ and retentate pressure P= 9 bar. Prior to this screening test, the catalyst was activated with a reducing treatment (10% H_2 balanced in N_2) at 550 K for 1 hour. Figure 7.5 shows the influence of temperature on the unit performance. At 723 K ethanol conversion reached only 20% and the selectivity for acetaldehyde 4% (results not shown), as a consequence, no more experiments were performed at 723 K, because this T was too low to perform ESR, as previously identified in Chapter 5.

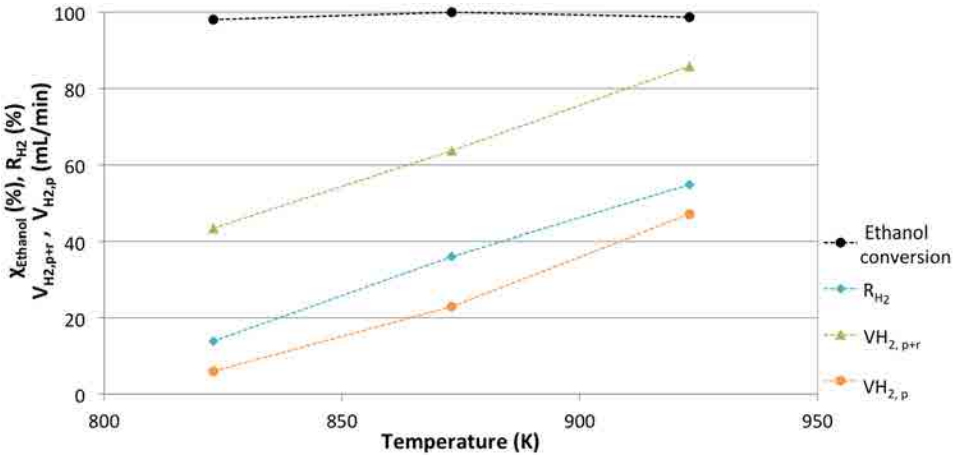

Figure 7.5: Influence of temperature on ethanol conversion, hydrogen recovery (R_{H_2}), volumetric hydrogen production ($V_{H_2,p+r}$) and permeation ($V_{H_2,p}$). Experimental conditions: P=9 bar, S/C=1.5 and v_{space}=0.22 $\mu L_{liquid}/(mg_{catalyst}min)$.

As seen in figure 7.5, as temperature increased from 823 K to 923 K, both the hydrogen production rate ($V_{H_2,p+r}$) and the hydrogen flux permeated ($V_{H_2,p}$) through the membrane increased. At complete ethanol conversion, higher temperatures caused higher methane conversions due to MSR promotion (S_{CH4}=47% at 823 K versus S_{CH4}=31% at 923 K) and, consequently, higher hydrogen yields were achieved. In fact, the $V_{H_2,p+r}$ almost doubled for the 100-K temperature variation shown in figure 7.5. At the highest temperature tested (923 K) with complete ethanol conversion, a hydrogen yield Y_{H_2}=0.3 was achieved, with a H_2/CO_2 ratio of 2.1. Higher temperatures could not be essayed with the developed equipment.

Hydrogen permeated through a Pd-Ag membrane can be described by Sievert's law (equation 7.6), assuming a hydrogen permeation mechanism of solution-diffusion-type [181].

$$F_{H_2,permeate} \propto \frac{e^{(-E_a/RT)}}{d}\left(\sqrt{P_{H_2,retentate}} - \sqrt{P_{H_2,permeate}}\right), \quad [40]$$
$$P_{H_2} = P \cdot y_{H_2} \tag{7.6}$$

$P_{H_2,retentate}$ and $P_{H_2,permeate}$ are the hydrogen partial pressures at each side of the membrane and d denotes the membrane thickness. Hydrogen transport through a Pd membrane is a temperature-activated process, with an Arrhenius-like dependence on temperature. The noticeable increase of the H_2 flux permeated ($V_{H_2,p}$) as T increased reported in figure 7.5 was not only caused by the temperature influence in the exponential term of equation 7.6, but also due to the hydrogen partial pressure increase in the retentate side ($y_{H_2,r}$), as more methane was reformed yielding more hydrogen. As a result, the hydrogen recovery (R_{H_2}) also increased with T, reaching values in this case of 55%.

7.4.2 Reaction pressure effect

The retentate pressure of the experimental setup could be varied between atmospheric pressure and 11 bar. As the pressure in the permeated side of the membrane was not governed in this device and the membrane selectivity for hydrogen was 100%, the hydrogen partial pressure on the permeate side was always 1 bar. As shown in equation 7.6, the difference of the square roots of hydrogen partial pressures on both sides of the membrane is the driving force for the hydrogen permeation through the membrane. Consequently, it could seem straightforward that the higher the retentate total pressure, the better in terms of hydrogen permeated. Nevertheless, when the system was operated under experimental conditions leading to full ethanol conversion (for these experiments T>823 K), hydrogen production over RhPd/CeO_2-based catalysts responded to methane steam reforming (MSR) and this reaction is favored at low operation pressures (Le Châtelier's principle), as already observed and discussed in section 5.2.1. Therefore, the effect in the unit performance of increasing operating pressures was not so obvious.

Figure 7.6 reports the volumetric hydrogen fluxes generated and permeated as well as hydrogen recoveries and overall efficiencies for retentate total pressures ranging from 1 to 11 bar at 923 K and S/C=2.

As expected, higher pressures rendered lower hydrogen production ($V_{H_2,p+r}$), because MSR was further prevented at each increasing P. Nevertheless, from 1 to 9

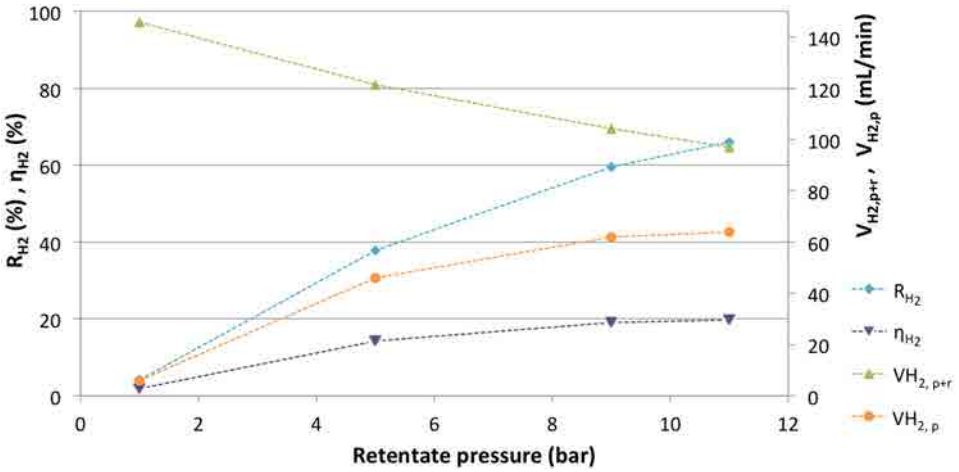

Figure 7.6: Influence of the pressure on ethanol conversion, hydrogen recovery (R_{H_2}), volumetric hydrogen production ($V_{H_2,p+r}$) and permeation ($V_{H_2,p}$). Experimental conditions: T=923 K, S/C=1.5 and v_{space}=0.22 $\mu L_{liquid}/(mg_{catalyst}min)$.

bar the effect of high total pressures weighted more in the driving force expression than the H_2 partial pressure, and the amount of hydrogen permeated ($V_{H_2,p}$) increased with P. At P>10 bar, hydrogen permeation reached a plateau as the hydrogen partial pressure diminution, due to less H_2 production, counterbalanced the retentate pressure increase. R_{H_2} increased in the whole range of pressures tested (maximum value of 66%), but its slope gradually diminished. The overall efficiency of the unit (η_{H_2}) for these experiments qualitatively followed the same trend as the permeated hydrogen flux, because the inlet flux and composition were constant for all the experiments shown in figure 7.6; maximum values of η_{H_2}=0.2 were achieved here.

7.4.3 Feed composition effect: S/C variation

Three different feed mixtures were chosen to test the performance of the membrane reactor. Along with the stoichiometric mixture (i.e. S/C=1.5), we chose a sub-stoichiometric mixture (S/C=1) and an over-stoichiometric mixture (S/C=2). Mixtures with higher water contents (S/C=3) were not considered to avoid high dilution effects by the excess of water. Total inlet fluxes were kept constant to operate with similar residence times. Figure 7.7 shows the volumetric flux of permeated hydrogen, the hydrogen recovery and the hydrogen yield (in this plot θ_{H_2}=6·Y_{H_2} is given, denoting mol_{H_2} produced per $mol_{Ethanol}$ fed) for the different inlet mixtures, as an indicator of the reaction performance. Additionally, hydrogen and water molar fractions (y_{H_2} and y_w, respectively) at the membrane entrance (monoliths outlet) are also represented. The latter were calculated from mass balances, combining retentate and permeate fluxes and products distribution.

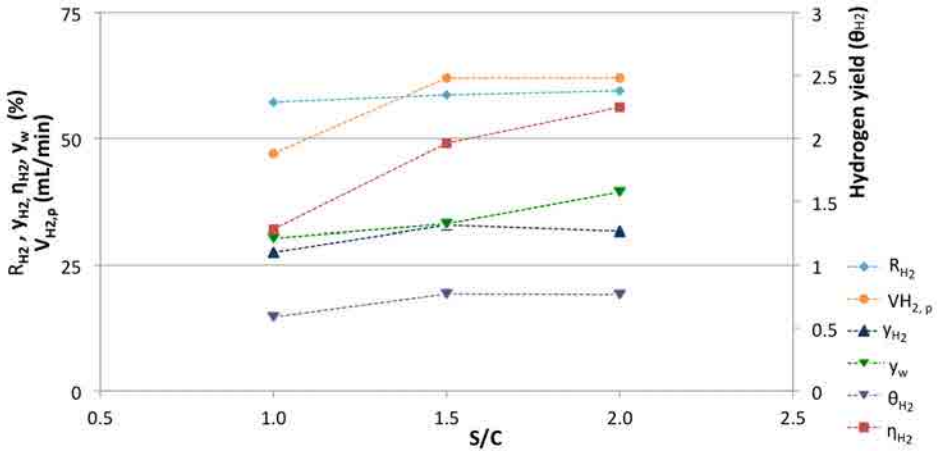

Figure 7.7: Influence of the feed composition on the volumetric hydrogen permeated ($V_{H_2,p}$), the hydrogen recovery (R_{H_2}) and hydrogen yield (θ_{H_2}). Molar fluxes of hydrogen and water at the membrane inlet are also shown. Experimental conditions: T=923 K, P=9 bar and v_{space}=0.22 $\mu L_{liquid}/(mg_{catalyst}min)$.

As expected, higher water contents shifted methane steam reforming and water-gas shift reactions towards reaction products, both rendering higher specific (normalized per mol of ethanol fed) hydrogen outputs, as also evidenced in section 5.2.3, where the effect of the feed composition was evaluated for $1RhPd/CeO_2//Mon$ and the same results obtained in Chapter 5 apply here. In addition, at constant total inlet flux, higher S/C resulted in lower ethanol fluxes supplied (see table 5.3). As seen in figure 7.7, the clear improvements achieved for the reaction performance as S/C increased did not result in improved R_{H_2}. In fact, the improvement in the hydrogen yield was balanced by the diminution of the hydrogen molar fraction (y_{H_2}) due to water dilution (y_w increment) when S/C increased. For the inlet mixtures tested, $V_{H_2,p}$ only increased from S/C=1 to S/C=1.5, then it remained constant; however R_{H_2} and θ_{H_2} remained almost constant for all the S/C tested. Nevertheless, as referenced elsewhere [39, 125, 126] and previously reported in sections 2.1.1 and 5.2.3, sub-stoichiometric inlet mixtures (S/C<1.5) are not recommended in order to avoid coke formation and increase catalysts' lifetime. A few experiments were performed with S/C=3 at the reactor entrance achieving very poor permeation fluxes due to high dilution of the hydrogen produced. Therefore, water contents in feed slightly over-stoichiometric (S/C∼1.6-1.7) appeared to be the most appropriate ones to balance the ethanol steam reforming enhancement and H_2 dilution by excess water, without compromising the catalyst's stability.

7.4.4 Feed load effect

Finally, a series of experiments varying the load of the liquid fed to the reactor was performed to study its influence on the reforming+separation performance. Figure

7.8 shows the volumetric fluxes of hydrogen produced and permeated, R_{H_2} and η_{H_2} obtained for the experiments performed at a retentate pressure of 11 bar, T=923 K and S/C=1.5. Despite the residence time diminution as a result of the feed load increase from 0.09 to 0.33 $\mu L_{liquid}/(mg_{catalyst}min)$ (the corresponding residence time at standard temperature and pressure, τ, varied form $\tau \sim 3$ s to $\tau \sim 0.8$ s, respectively), total ethanol conversion was attained for all the experiments reported in figure 7.8. In this scenario, as the inlet flux increased the volumetric hydrogen production rate also increased. However, the total amount of hydrogen permeated depended on the total area of the membrane implemented in the device and the H_2 partial pressure on the retentate side (note that F_{H_2} of equation 7.6 is defined per membrane thickness). As seen in figure 7.8, at increasing feed loads, the permeated H_2 flux ($V_{H_2,p}$) could not follow the H_2 flux produced by ESR reaction and finally reached a plateau at the highest inlet loads. Therefore, once $V_{H_2,p}$ reached the plateau, hydrogen recovery markedly dropped, as also did the overall efficiency. In this situation, the permeation was limited by the membrane area, with a specific permeation flux of 2.4 $mL_{H_2}/(min \cdot cm^2_{membrane})$, which corresponded to $V_{H_2,p}$=73 mL_{H_2}/min.

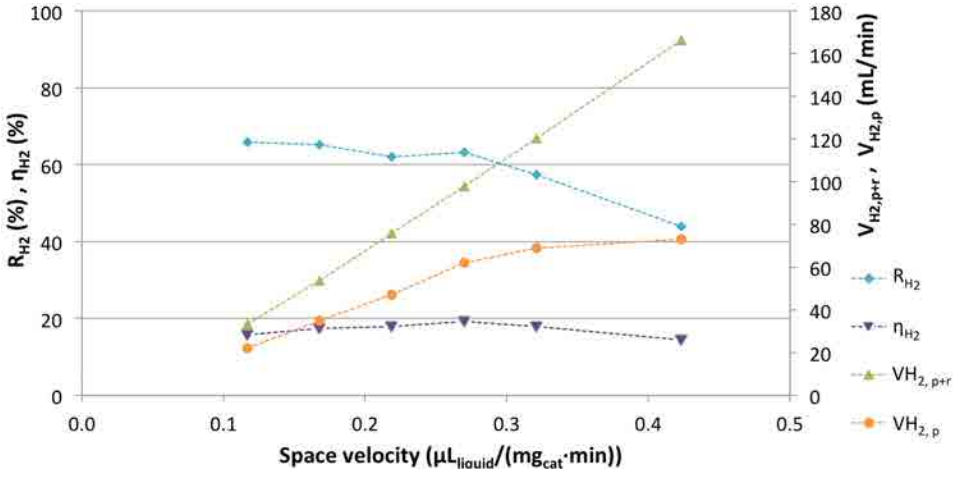

Figure 7.8: Influence of the feed load on the hydrogen recovery (R_{H_2}), volumetric hydrogen production ($V_{H_2,p+r}$) and permeation ($V_{H_2,p}$) and on the overall efficiency. Experimental conditions: T=923 K, P=11 bar and S/C=1.5.

Another set of experiments was performed with feed mixtures of S/C=1 at the maximum temperature and pressure tested (i.e., 923 K and 11 bar). Results obtained are represented in figure 7.9. For S/C=1, the previously obtained trends for S/C=1.5 were also observed here. However as the feed mixture was less diluted, higher H_2 partial pressures were attained in the retentate side resulting in higher H_2 permeated fluxes than for the experiments of S/C=1.5 and hence hydrogen recovery was improved. Nevertheless, the $V_{H_2,p}$ plateau was also reached, but at slightly higher space velocities and R_{H_2} also diminished at increasing feed loads,

following the previously observed trend. In this case, a maximum specific permeation flux of 3.65 $mL_{H_2}/(min{\cdot}cm^2{}_{membrane})$ was achieved, which corresponded to $V_{H_2,p}$=111 mL_{H_2}/min. However, as described in the preceding section (section **7.4.3**), over-stoichiometric S/C ratios are more convenient to preserve catalysts's life.

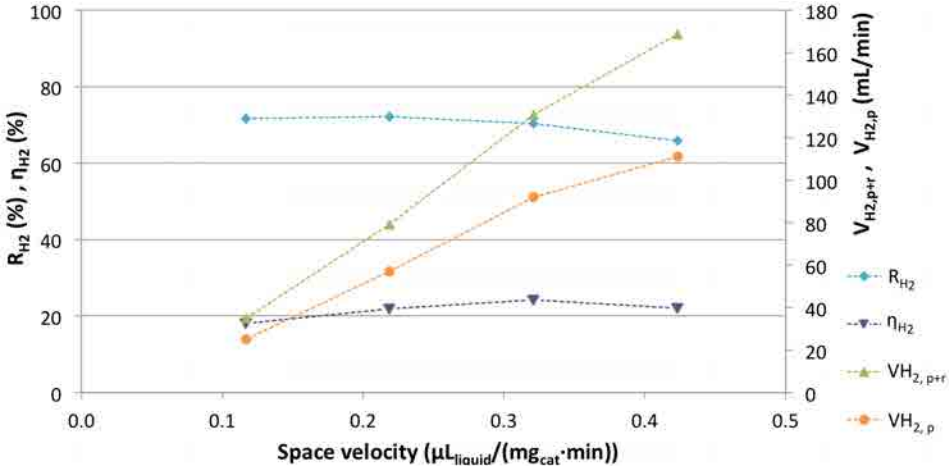

Figure 7.9: Influence of the feed load on the hydrogen recovery (R_{H_2}), volumetric hydrogen production ($V_{H_2,p+r}$) and permeation ($V_{H_2,p}$) and on the overall efficiency. Experimental conditions: T=923 K, P=11 bar and S/C=1.

7.4.5 Performance comparison with data reported in the literature

Although a direct comparison with the data reported in the literature is hardly attainable, in general the performance of the pure-hydrogen generation unit that we developed compared adequately with the reported data in terms of specific hydrogen production rate and hydrogen recovery.

For hydrogen generation units operating at almost complete fuel conversion, the 3.65 $mL_{H_2}/(min{\cdot}cm^2{}_{membrane})$ achieved here lay in between the values reported in the literature: ∼2 $mL_{H_2}/(min{\cdot}cm^2{}_{membrane})$ were attained by Tosti et al. [168] for ethanol steam reforming as well; whereas 9.1 $mL_{H_2}/(min{\cdot}cm^2{}_{membrane})$ were reported by Buxbaum and Lei [182] for methanol steam reforming and Chang et al. [183] reported 12.5 $mL_{H_2}/(min{\cdot}cm^2{}_{membrane})$ for autothermal methane reforming. In our device, hydrogen recoveries up to 70% were attained, which were comparable values with those reported in the literature for Pd or Pd-Ag-based membranes: 30-95% for ethanol steam reforming [170, 171], 22-78% for methane steam reforming [184] and up to 77% for methane dry reforming [185].

7.4.6 Hydrogen-rich gas generation

The unit was also operated as a H_2-rich gas generator without membrane separation, by blocking the permeate-side outlet. Here, the operating conditions were chosen in order to maximize the hydrogen flux generated, thus low pressure (P_r=1 bar) and excess water in the inlet mixture (S/C=2) to achieve higher MSR and WGS rates were chosen. Total outlet fluxes, V_r, up to 300 mL/min of composition 60% H_2, 12.1% CH_4 and 8.5% CO, 19.4% CO_2 were measured.

Also, experiments at S/C=1 and 1, 5, 7, 9 and 11 bar were performed blocking the membrane. A comparison of the volumetric fluxes of the main reaction products generated for two experiments performed under the same operating conditions with membrane (staged reactor) and without membrane (hydrogen-rich gas generation unit) separation are presented in figure 7.10. Figure 7.10a shows the experiments performed at T=923 K, S/C=1 and P=11 bar and figure 7.10b results of experiments performed at T=923 K, S/C=1 and P=1 bar.

As deduced from the results presented in figure 7.10, when the prototype was operated with membrane separation (reaction+purification unit), ESR occurred in-series with hydrogen separation, i.e., the presence of the membrane did not affect the ESR reaction performance by shifting the equilibria of MSR, WGS nor ethanol decomposition reactions and the unit exhibited the same performance as the one obtained without membrane, as expected. This occurred because the unit was designed following a staged-reactor scheme. However, high-purity H_2 streams (without dilution) were obtained readily to feed PEMFC.

After more than 250 hours of operation of the pure-hydrogen generation unit, results showed a remarkable uniformity on the selectivities and pure-hydrogen permeation rates, indicating that both the catalyst and the membrane maintained their activity and did not deactivate.

This work was published in *Eduardo López, Núria J. Divins and Jordi Llorca, "Hydrogen production from ethanol over Pd-Rh/CeO_2 with a metallic membrane reactor", Catalysis Today, 193 (2012), pp. 145* [38].

The investigation of the catalytic behavior of the pure-hydrogen generation based on RhPd/CeO_2 catalysts continued in our group and included the characterization of the dynamic behavior of the unit, its integration with a PEM-fuel cell and the design and implementation of a control system aimed at governing the combined unit [186]; an exergy study has also been performed [187]. A new reactor configuration where ESR reaction and hydrogen separation take place in the same chamber is currently being investigated.

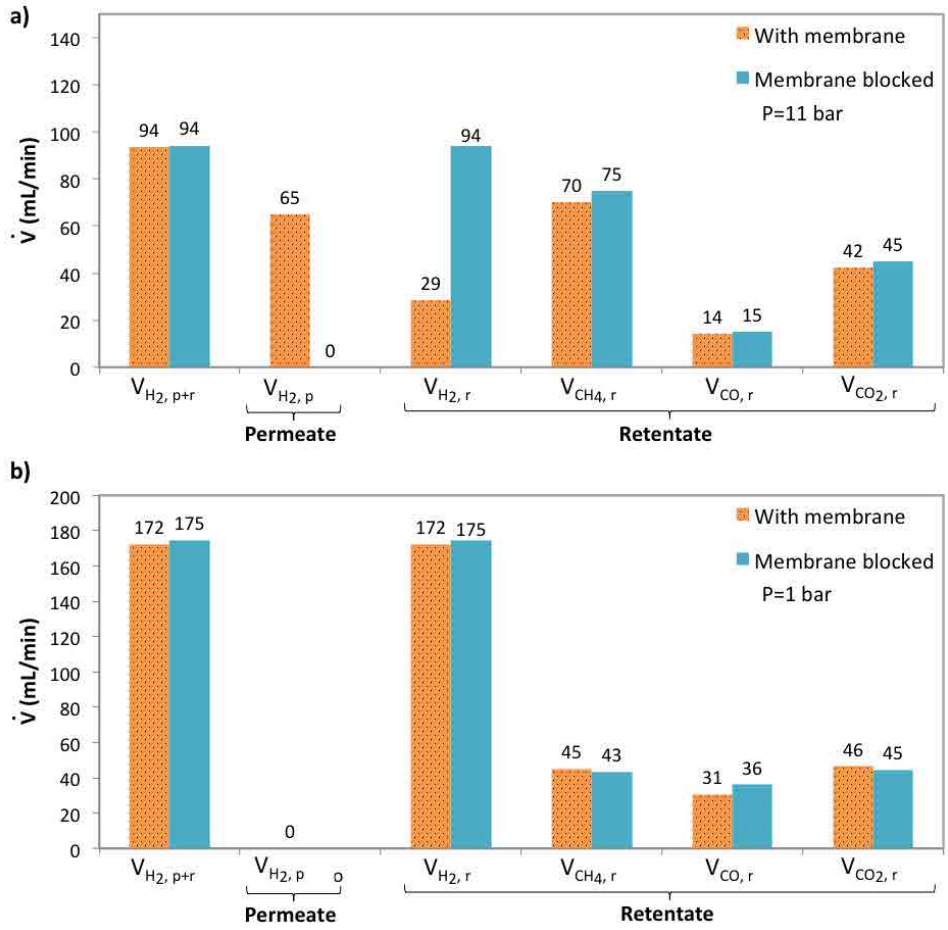

Figure 7.10: Performance comparison in terms of reaction products volumetric fluxes for operation with membrane (orange bars) and without membrane (blue bars). Experimental conditions: T=923 K, S/C=1, v_{space}=0.22 $\mu L_{liquid}/(mg_{catalyst} min)$; a) P=11 bar, b) P= 1 bar.

8 Ethanol steam reforming in silicon microchannels

The evaluation of the ethanol steam reforming reaction performance of $RhPd/CeO_2$-based catalysts over cordierite monoliths described in Chapter 5 showed that working $RhPd/CeO_2$ catalysts have appealing properties for hydrogen production such as high hydrogen yields and long stability (see figure 5.14). Therefore, as microreactors have improved heat transfer properties, which are particularly relevant for endothermic reactions, such as ESR, the reaction performance of $RhPd/CeO_2$ catalysts was tested over microreactors intended to feed microfuel cells for portable devices.

8.1 Introduction

Numerous micro-devices for hydrogen production from methanol steam reforming at 533-723 K have been reported [188], but the high temperatures required for ethanol steam reforming (ESR) has prevented extensive work in this field [189]. Men et al. from the Mainz Institute of Microtechnology (IMM, Germany) tested several catalyst formulations based on Ni, Rh, Co, and Ni-Rh for ESR in a microchannel reactor (channels 500 µm width and 250 µm depth) [112]. The best results were obtained over $Ni\text{-}Rh/CeO_2$, which showed no deactivation during a 100 h catalytic test at 923 K. Casanovas et al. from the Universitat Politècnica de Catalunya (UPC, Spain) developed a microreactor for hydrogen generation from ethanol under an autothermal regime [190]. A two-sided platelet microreactor was designed for transferring the heat released during total catalytic oxidation of ethanol over a $CuMnO_x$ catalyst in one side of the microreactor to the other side, where ESR occurred over a CoO_x-ZnO catalyst. Görke et al. from the Institute for Micro Process Engineering (Karlsruhe, Germany) used a microchannel reactor (channels 200 µm width and depth) to produce hydrogen by ESR over a Rh/CeO_2 catalyst [191]. For temperatures above 898 K, a space time yield four times higher than that obtained in conventional reactors was reached. Cai et al. from the University of Lyon (Centre National de la Recherche Scientifique, CNRS, France) used a microreactor

with channels 500 µm width and depth, loaded with an Ir/CeO_2 catalyst. The hydrogen production was found significantly higher than in conventional fixed-bed reactors, essentially due to better heat and mass transfers [192]. These are pioneering examples reported in the open literature concerning the generation of hydrogen from ethanol by using microreaction technologies.

In 2008, also in a pioneering work, Llorca et al. from UPC used the novel Si micromonoliths described in the Introduction (section **1.5.1.a**) as a structural support for a Co_3O_4-ZnO catalyst devoted to ESR [46]. High and stable selectivity to H_2 (>73 vol% H_2) and CO_2 was attained at 773 K and S/C=3 at contact times <5 milliseconds per channel (GHSV=$2{\cdot}10^6$ h^{-1}). Under these reaction conditions, a constant H_2 flow of 20 µL/s (0.054 mmol/min) was generated.

More recently, Peela et al. from the Indian Institute of Technology (IIT) performed steam reforming and oxidative steam reforming of ethanol over $Rh/CeO_2/Al_2O_3$ in a microreactor with channels 500 µm-wide and 400 µm-deep and showed that microchannels produced hydrogen without diffusional effects in the catalyst layer with respect to a packed bed reactor [85, 193, 194]. Domínguez et al. from UPC coated a plate microreactor with cobalt talc, $Co_3[Si_2O_5]_2(OH)_2$, and performed ESR at low temperature (648 K) with trace CO formation [195]. Rahman et al. from the Imperial College (London) used a catalytic hollow fiber microreactor loaded with a $Ni/MgO\text{-}CeO_2$ to carry out ESR, with a flow rate of hydrogen three fold higher than that obtained in a fixed-bed reactor [196, 197]. Finally, Kolb et al. from IMM in collaboration with Rosetti Marino company tested Rh-Ni and $Rh\text{-}Co/Al_2O_3$-based catalysts and designed the concept of a microstructured 50 kW ethanol fuel processor [198].

In this Chapter, we use the novel Si micromonolith designed at UPC (section **1.5.1.a**) as a substrate for the developed $RhPd/CeO_2$ catalyst in order to reduce the hydrogen generation scale studied in this Thesis.

8.2 Micromonolith functionalization: catalyst coating

As already indicated in the Introduction (section **1.5.1.a**), a new coating method had to be specifically developed in order to homogeneously coat 3.3 µm channels with working $RhPd/CeO_2$ catalyst and without blocking them. Moreover, the catalyst coating developed had to be well-adhered to the microchannels walls and withstand reaction conditions. Figure 8.1 shows SEM images of a bare Si micromonolith that had to be functionalized. Figures 8.1a and 8.1b show the detail of the Si microstructure, while figure 8.1d shows the microchannels over which the

CeO_2 layer had to be developed and RhPd nanoparticles subsequently anchored. Figure 8.1c shows a schematic representation of the channels arrangement shown in figure 8.1d.

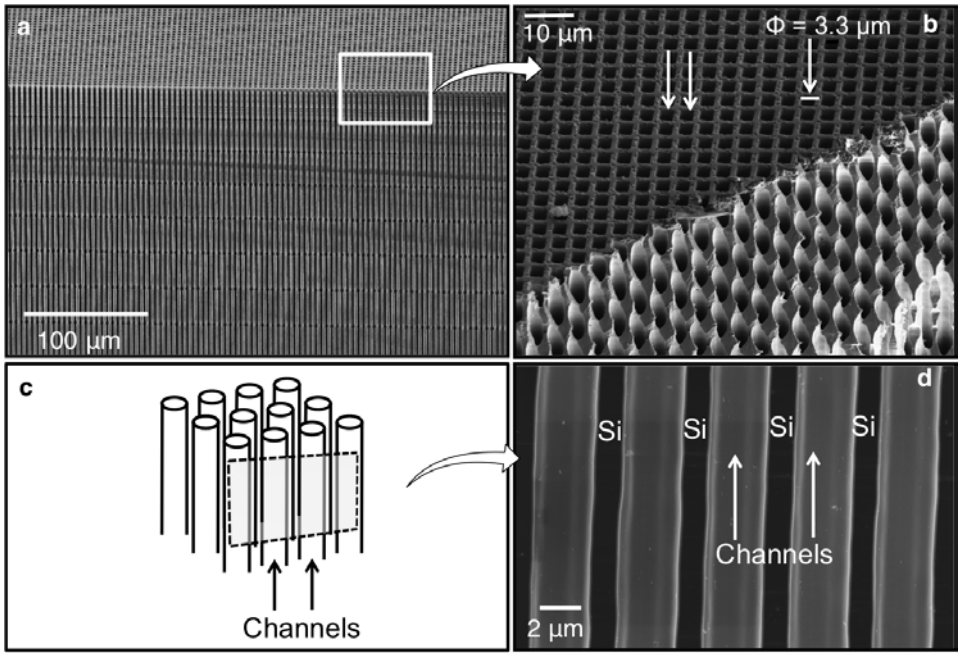

Figure 8.1: Representative SEM images of the Si micromonolith structure. a) and b) General view of the Si micromonolith structure. c) Schematic representation of the channels arrangement shown in d. d) Inner walls of 5 consecutive microchannels. Black areas correspond to the Si matrix.

Taking into consideration the small dimensions of the microchannels and its high depth/diameter ratio, the conventional and easiest way to deposit catalytic coatings over catalytic walls, the so-called washcoating method, proved to be inadequate. For that reason, a new method had to be specifically designed to coat the microchannels' walls. The developed method started with a thermal treatment at 1373 K under a dry O_2 atmosphere for 30 minutes to develop a SiO_2 layer over the walls of the Si microchannels that facilitated the adherence of our catalyst. The terminal hydroxyl groups of the SiO_2 layer were then exchanged at room temperature with cerium methoxyethoxide (Alfa Aesar), which was forced to pass through the microchannels by applying a pressure gradient of 75 kPa between both sides of the microreactor. The hydroxyl groups attached to the surface of the silicon oxide layer acted as anchoring sites which interacted with the cerium alkoxyde precursor ($Ce(O\text{-}CH_2\text{-}CH_2\text{-}O\text{-}CH_3)_4$), leading to the formation of a homogeneous CeO_2 layer upon calcination at 773 K for 6 hours (5 K/min), due to thermal decomposition of cerium methoxyethoxide. The ceria layer synthesis was studied by X-ray diffraction (XRD) with a conventional XRD apparatus. The acquired diffractogram (collected

from 10 to 80°, at step size 0.02° and step time 1 s), shown in figure 8.2, revealed peaks at 28.6°, 33.1°, 47.5° and 56.3°, corresponding to the interplanar distances (d_{hkl}) of the CeO_2 fcc structure 3.1 Å, 2.7 Å, 1.9 Å and 1.6 Å, respectively. Thus the expected fluorite CeO_2 phase was formed.

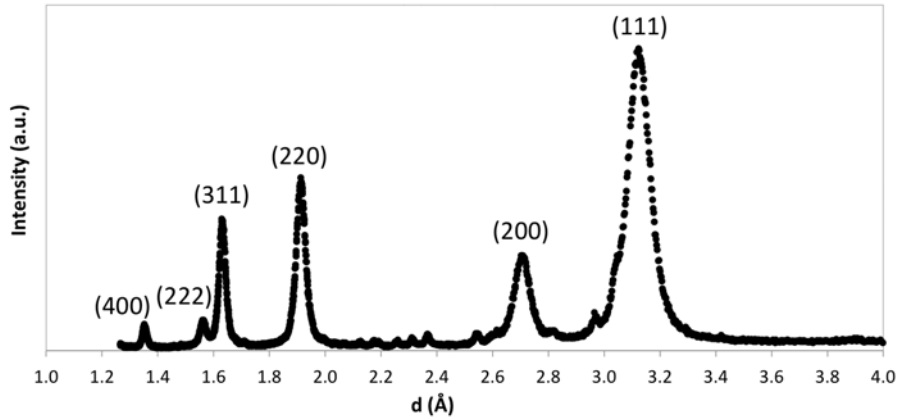

Figure 8.2: Ceria X-ray diffraction pattern of the CeO_2 layer developed over the Si microchannels acquired with λ=1.5406 Å. The planes indexes are shown.

Finally, the noble metals (0.5 wt.% Rh + 0.5 wt.% Pd) were grafted onto the CeO_2 support by free impregnation of a $PdCl_2/RhCl_3$ (99.9%, Sigma-Aldrich) water/acetone 0.012 M solution, which also was forced to pass through the silicon microchannels coated with CeO_2. The resulting catalytic silicon micromonolith was dried at 393 K and calcined in air at 573 K for 6 h (2 K/min). This sample is referred to as $1RhPd/CeO_2//Si$. In order to study the functionalized microchannels by SEM, the Si micromonolith had to be broken and therefore it was analyzed after reaction tests. In the following section, the catalytic activity tests performed are described, nevertheless the SEM images obtained are shown here in order to have the complete characterization study of the Si micromonolith. SEM images shown in figure 8.3 were directly obtained over the functionalized and post-reacted Si micromonolith. A general profile view of adjacent microchannels after cutting the micromonolith is shown in figure 8.3a and detailed images at higher magnification corresponding to the areas enclosed by black squares in figure 8.3a are shown in figures 8.3b and 8.3c.

In figure 8.3b a detail of the different layers is seen: the grey area on the right corresponds to the silicon matrix, which was covered by a compact, homogeneous, and well-defined SiO_2 layer of about 100 nm thickness (black). On top of the SiO_2 layer, a homogeneous and very uniform layer of CeO_2 was perfectly anchored (light grey), which was also about 100 nm thick. Very well-dispersed noble metal nanoparticles appeared as bright dots over the CeO_2 support (figures 8.3a and 8.3c), most of them measuring <5 nm in size (figure 8.3c).

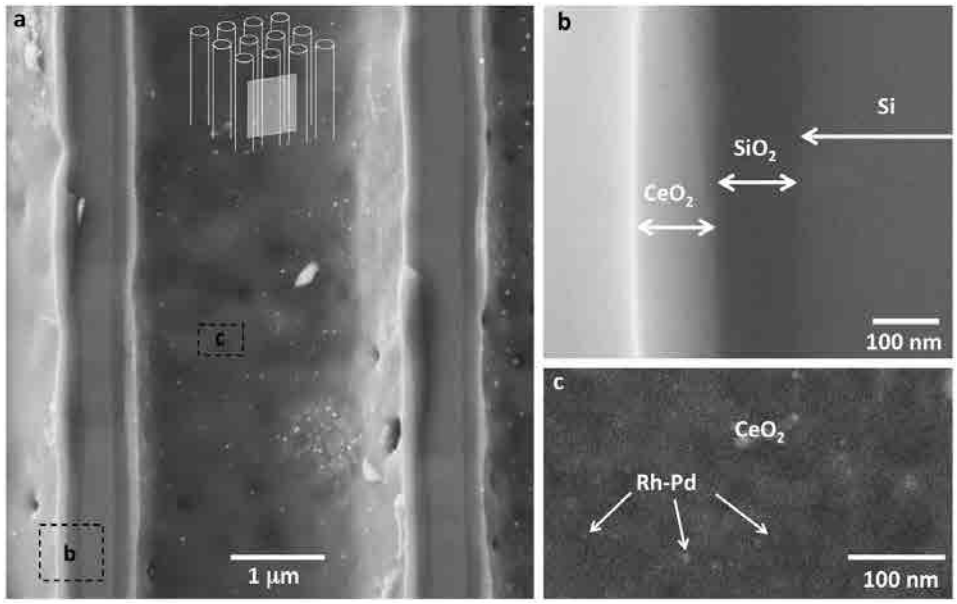

Figure 8.3: Representative SEM images of RhPd/CeO_2//Si. a) RhPd/CeO_2 layer developed over one oxidized Si microchannel. In these images, Si microchannels are arranged as depicted in the drawing. b) High magnification image of the area enclosed by black dots in a. Detail of a microchannel wall showing the SiO_2 and CeO_2 layers developed over the Si substrate. c) High magnification image of the area enclosed by black dots in a. Detail of the developed RhPd/CeO_2 layer.

Therefore, we established a method to successfully coat the Si microchannels with the working RhPd/CeO_2 catalyst that withstood the reaction conditions tested. Neither channels without catalyst nor blocked channels were detected by SEM. The CeO_2 layer thickness inferred by SEM analyses allowed to estimate the amount of catalyst deposited on the microchannels. Taking into account that the developed CeO_2 layers were ∼0.1 µm thick and that $1.5{\cdot}10^6$ channels were exposed to the reactants, the calculated catalyst mass incorporated into the *working* microchannels (microchannels exposed to the reactants) was only ca. 3 mg.

8.3 Catalytic activity screening

In order to evaluate the reaction performance of the functionalized silicon micromonolith, the 1RhPd/CeO_2//Si was cut with a laser device and the resulting disk of 8 mm in diameter was glued with epoxy onto a stainless steel washer (external diameter 19 mm, internal diameter 7 mm), which was subsequently sealed in a stainless steel reactor. The experimental setup described in Chapter 5 (figure 5.1) used for functionalized cordierite monoliths catalytic testing was used for catalytic testing of the Si micromonoliths too. Similarly, the reactor was placed inside a tubular furnace (Carbolite), the ethanol/water mixtures were delivered by a HPLC

pump (Knauer) and the mixtures were preheated before reaching the microreactor. For these experiments, non-diluted conditions were again tested and several reaction experiments were performed under ESR conditions as well as under oxidative ethanol steam reforming (OSR) conditions. For the OSR experiments, different concentrations of O_2 were dosed by an independent mass flow controller (M + W Instruments). Reaction products were analyzed online continuously with the same gas micro-chromatograph (Agilent 3000A). The molar fluxes of reaction products, H_2, CO, CO_2, CH_4 and CH_3CHO, in the reactor effluent were calculated using the chromatographic analyses and total volumetric flux data. During the ethanol and bioethanol SR analyses, only negligible amounts of acetone, ethane and ethylene were detected ($< 1\%$).

The experimental conditions tested for the micromonolith performance evaluation are presented in table 8.1.

Table 8.1: Experimental conditions tested.

Temperature (K)	773 - 973
Absolute pressure (bar)	1
Feed concentration ($mol_{H_2O}/mol_{Ethanol}$)	2 - 6
Oxygen concentration ($mol_{O_2}/mol_{Ethanol}$)	0 (ESR) - 1
Residence time (τ, s)	0.04 - 0.002
Gas hourly space velocity (GHSV, h^{-1})	10^5 - $2{\cdot}10^6$
Ethanol	Synthetic (99.8%, Panreac) Bioethanol *La Mancha**

*See table 5.4 for bioethanol composition details.

As already explained in the ESR introduction (section 2.1), the main drawback of ESR is its high endothermicity, $\Delta H^0_{298\ K}$=173.3 kJ/mol. However the ESR reaction energy balance can be improved by introducing O_2 into the reaction mixture and running a combination of pure ESR and partial oxidation, the so-called ethanol oxidative steam reforming (OSR), which may approach and autothermal regime (ATR, $\Delta H^0_{298\ K} \sim 0$), at expenses of hydrogen yield, as seen in equation 8.1.

$$C_2H_5OH_{(g)} + (3-2x)\,H_2O_{(g)} + x\,O_{2(g)} \longrightarrow (6-2x)\,H_{2(g)} + 2\,CO_{2(g)}, \qquad (8.1)$$

$$\Delta H^0_{298K} = (173.3 - 483x)\ \text{kJmol}^{-1}$$

Although hydrogen production diminishes when O_2 is present in the reactor feed, the energy balance is highly improved and the overall balance is positive provided that the O_2/ethanol ratio is properly adjusted. As reported in [76, 199], oxy-

gen/ethanol ratios between 0.3 and 0.6 appear the most appropriate in order to obtain conveniently high hydrogen yields and slightly exothermic operating conditions. For larger oxygen/ethanol values, the reaction becomes intensely exothermic at the expense of excessive hydrogen losses, rendering its usage economically unfeasible.

The reaction performance of the Si microreactor was evaluated using the same parameters discussed throughout Chapter 5, and thus ethanol conversion (χ_{Ethanol}, equation 8.2), hydrogen yield ($\mathrm{Y_{H_2}}$, equation 8.3), volumetric hydrogen production rate ($\dot{\mathrm{V}}_{\mathrm{H_2}}$, equation 8.4) and selectivity to main species ($\mathrm{S_i}$, equation 8.5) were also evaluated for the Si micromonolith experiments.

$$\chi_{Ethanol} = \frac{\dot{n}_{Ethanol,in} - \dot{n}_{Ethanol,out}}{\dot{n}_{Ethanol,in}} \cdot 100, \quad \text{where } [\dot{n}] = \frac{mol}{s} \tag{8.2}$$

$$Y_{H_2} = \frac{\dot{n}_{H_2}}{6\ \dot{n}_{Ethanol,in}} \tag{8.3}$$

$$\dot{V}_{H_2} = F_{Total} \cdot S_{H_2} \tag{8.4}$$

$$S_i = \frac{\dot{n}_i}{\sum_i \dot{n}_i} 100, \quad i = H_2, CH_4, CO_2, CO, CH_3CHO \tag{8.5}$$

Regarding equation 8.3, the factor 6 in the denominator was applied only in the cases where equal or higher amounts of water than stoichiometric were fed. Hence, the factor 6 was used in all ESR experiments and also in all the OSR experiments operated at S/C=2. For the OSR tests ran with S/C=1, the referred factor 6 should be replaced by a factor 5, as deduced from equation 8.1. In addition, for these experiments the space velocity parameter used in Chapter 5 was not calculated, as the amount of catalyst finally deposited over the microchannels could only be estimated. Therefore, the reaction performance was evaluated in terms of the residence time, τ, and the space velocity, which is expressed in terms of the gas hourly space velocity ($1/\tau$); in both parameters only the total volume of the microchannels is taken into account for their calculation. The reactants flux was calculated at standard temperature and pressure.

8.3.1 Ethanol steam reforming tests

Steam reforming of synthetic ethanol was performed for ethanol/water mixtures of S/C=3 at temperatures ranging between 773 and 973 K. For a constant feed load corresponding to τ=8.5 ms (GHSV=$4.2{\cdot}10^5$ $\mathrm{h^{-1}}$), full ethanol conversion was attained for T>873 K, which indicated the absence of by-passes and channels lacking catalyst.

8.3.1.a Feed load effect

The influence of increasing feed loads resulting in increasing space velocities was studied at 873 K and S/C=3 (P=1 bar for all the experiments). The residence times (τ) tested for these experiments were: 17.1, 8.5, 5.7, 4.3, 3.4 and 2.8 milliseconds which corresponded to space velocities GHSV=(2.1, 4.2, 6.3, 8.4, 10.5, 12.6)·10^5 h^{-1}, respectively. Ethanol conversion, hydrogen yield and volumetric hydrogen production are reported in figure 8.4. The corresponding selectivities are plotted in figure 8.5, where also the expected selectivities at the thermodynamic equilibrium (marked as *EQUILIBRIUM*) calculated for the experimental conditions tested [200] are represented.

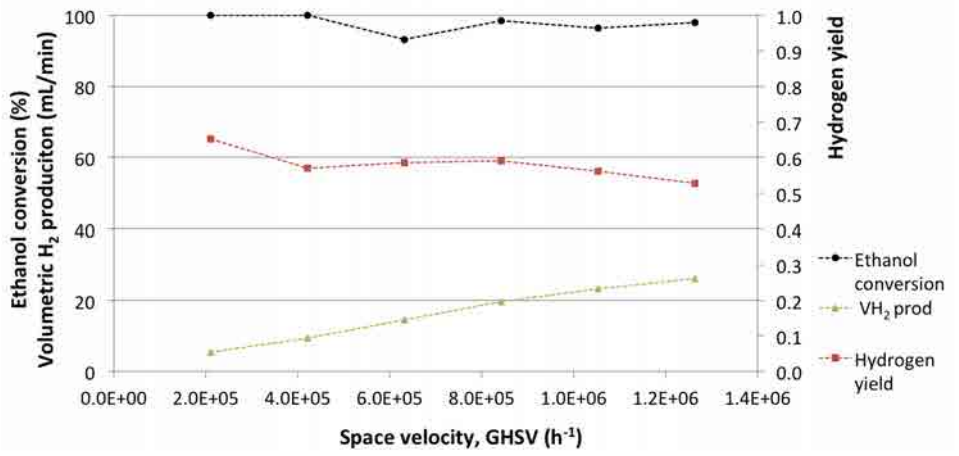

Figure 8.4: Space velocity effect on the ethanol conversion and hydrogen yield of the 1RhPd/CeO_2//Si catalyst. Experimental conditions: T=873 K, P=1 bar, S/C=3.

As seen in figure 8.4, ethanol conversion was almost complete for all the contact times tested. However the hydrogen yield decreased from 0.65 to 0.53 at high space velocities, due to the appearance of acetaldehyde at low contact times, as seen in figure 8.5. This indicated that ethanol dehydrogenation ($C_2H_5OH \longrightarrow CH_3CHO + H_2$) took place, which resulted in lower hydrogen yields. As seen in figure 8.5, the selectivity values were close to equilibrium, except for the presence of acetaldehyde. Besides and most importantly, large volumetric hydrogen productions were recorded for these experiments, as up to 25 mL/min of H_2 were produced with the Si micromonolith at the highest feed load tested.

8.3.1.b Bioethanol tests

ESR tests were also carried out with bioethanol/water mixtures of S/C=2. This S/C ratio is closer to the stoichiometric value and represented severer reaction conditions. Nevertheless, 97% bioethanol conversion and 0.66 hydrogen yield were achieved at 873 K and 19 milliseconds residence time. The products distribution at-

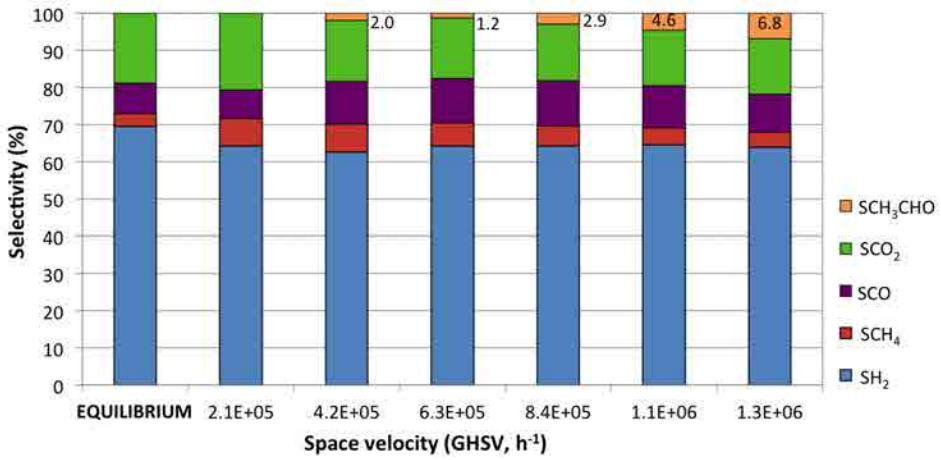

Figure 8.5: Influence of the space velocity on the selectivity to the main species produced by the 1RhPd/CeO_2//Si catalyst. Experimental conditions: T=873 K, P=1 bar, S/C=3. The numbers show the selectivities for acetaldehyde.

tained at this temperature was S_{H_2}=65.0%, S_{CH_4}=6.9%, S_{CO_2}=19.0%, S_{CO}=9.1%. Therefore, the values reached were very similar to those obtained with synthetic ethanol and also close to the equilibrium.

8.3.2 Ethanol oxidative steam reforming tests

8.3.2.a Oxygen concentration effect

The influence of different O_2 concentrations in the feed mixture was evaluated at 873 K and S/C=2. The liquid mixture was fixed at S/C=2 and the O_2 amount was gradually increased and thus the space velocity also increased. Figure 8.6 shows the ethanol conversion, hydrogen yield and the volumetric hydrogen production recorded for these tests; the corresponding selectivities are represented in figure 8.7. Additionally, the reaction enthalpy calculated for each experimental condition tested is also plotted in figure 8.7.

As seen in figure 8.6, the hydrogen yield diminished when the O_2 concentration increased, decreasing from 0.68 for ESR conditions (O_2:ethanol=0) to 0.56 for O_2:Ethanol=0.85. This was a consequence of smaller H_2 production together with smaller CH_4 and CO production and increasing amounts of CO_2, when higher amounts of oxygen were dosed (at constant liquid feed), as expected because more ethanol was oxidized. These trends are shown in figure 8.7. No acetaldehyde was detected during these tests. Nevertheless, the energy balance was highly improved when oxygen was present in the reactor feed, as deduced from the enthalpy results shown in figure 8.7. The autothermal (ATR) regime could be achieved for

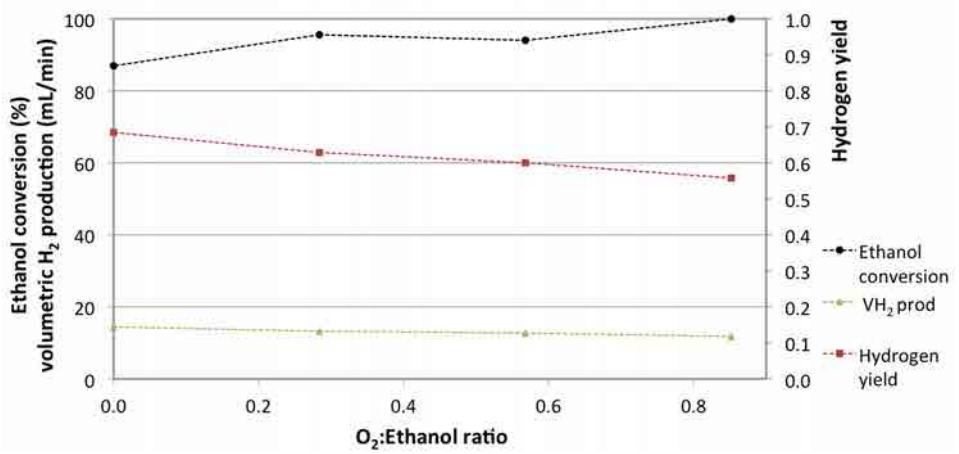

Figure 8.6: Influence of the O_2:ethanol ratio on the ethanol conversion, hydrogen yield and volumetric hydrogen production of the 1RhPd/CeO_2//Si catalyst. Experimental conditions: T=873 K, P=1 bar, S/C=2, GHSV=$3.8{\cdot}10^5$ h^{-1} - $4.5{\cdot}10^5$ h^{-1}.

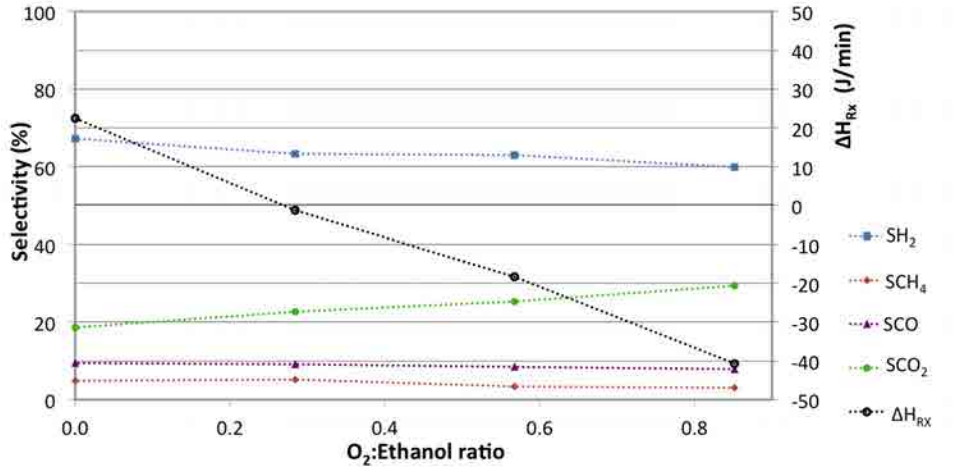

Figure 8.7: Influence of the O_2:ethanol ratio on the reaction enthalpy and the selectivity to the main species produced by the 1RhPd/CeO_2//Si catalyst. Experimental conditions: T=873 K, P=1 bar, S/C=2, GHSV=$3.8{\cdot}10^5$ h^{-1} - $4.5{\cdot}10^5$ h^{-1}.

O_2:Ethanol=0.28. Therefore, slightly higher O_2:Ethanol>0.28 appeared the most convenient in order to balance hydrogen production and energy supply, as mentioned above.

8.3.2.b Feed load effect

The effect of the feed load was tested at S/C=1 maintaining the O_2:Ethanol ratio constant at 0.56 and temperatures ranging from 773 K to 923 K. The space

velocities tested in these experiments were: GHSV=$3.8{\cdot}10^5$, $7.5{\cdot}10^5$ and $11.2{\cdot}10^5$ h^{-1}, which corresponded to residence times τ=9.5, 4.8 and 3.2 milliseconds, respectively. Figure 8.8 shows the yield for reaction species at 873 K, as defined in equation 8.6 (the yield for reaction species was previously used in section 5.6) and the volumetric hydrogen production.

$$Y_i(\%) = \frac{\chi_{Ethanol} \cdot S_i}{100}, \quad i = H_2, CH_4, CO_2, CO, CH_3CHO \tag{8.6}$$

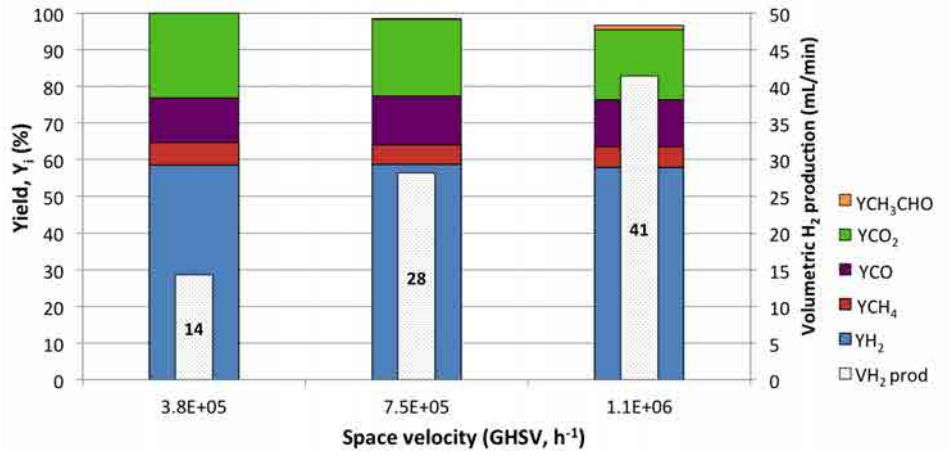

Figure 8.8: Influence of the space velocity on the yield for the main species produced by the 1RhPd/CeO_2//Si catalyst. Experimental conditions: T=873 K, P=1 bar, S/C=1, O_2:ethanol=0.56. The numbers show the volumetric hydrogen production in mL/min.

As seen in figure 8.8, the hydrogen selectivities decreased 2% on average when compared to experiments with S/C=2. Also a slight diminution in the moles of hydrogen generated per mol of ethanol fed was measured, indicating poorer reforming conditions, because, as previously described in section 5.2.3, higher amounts of water in the inlet mixture shift the equilibria of MSR and WGS reactions, promoting its extension and thus yielding higher H_2 amounts. Nevertheless, mixtures with lower S/C, for the same amount of liquid fed, have more ethanol available and thus higher volumetric hydrogen production rates were measured for S/C=1 than for S/C=2 (figure 8.6), at the same temperature. For these experiments, the Si microreactor attained H_2 productions up to 41 mL/min. Also, the presence of O_2 in the inlet mixture prevented the formation of acetaldehyde and only ∼1% acetaldehyde was formed at the highest feed load tested, whereas in the pure ESR experiments (see figure 8.5), even at S/C=3, ∼5% acetaldehyde was produced at the same GHSV.

8.3.2.c Bioethanol effect

The effect of bioethanol impurities on the OSR performance was evaluated as well. A temperature screening test was performed at temperatures ranging from 773 K to 873 K at fixed S/C=2, O_2:Ethanol=0.5 and GHSV=$2.1{\cdot}10^5$ h^{-1}. Results showed that higher temperatures led to higher ethanol conversion and H_2 yield, as previously observed in Chapter 5, and $\chi_{Ethanol}$=100% was attained at 873 K. At this temperature, the product distribution was S_{H_2}=60.4%, S_{CH_4}=4.9%, S_{CO_2}=25.3%, S_{CO}=9.3%; these values were very close to the ones registered for synthetic ethanol under the same operating conditions (see figure 8.7; O_2:Ethanol=0.56).

The whole set of experiments performed represented ∼80 hours of operation and no deactivation signs were noticed.

8.4 Performance comparison with cordierite monoliths

When a comparison of the performance between the Si micromonolith and the conventional cordierite monolithic catalysts (400 cpsi) was intended, the inclusion of some kind of intensive measurement appeared appropriate to equalize the obvious use of non similar operating conditions given the ca. 3 orders of magnitude differences in the dimensions of both systems. In these terms, a specific hydrogen production rate ($V_{H_2}^{sp}$) was defined as the volumetric hydrogen production rate normalized by the reactor volume and the ethanol injection load, as established in equation 8.7.

$$V_{H_2}^{sp}\left[\frac{NmL_{H_2(g)}}{mL_{Ethanol\,(l)}\cdot cm^3_{React.}}\right]=\frac{\dot{V}_{H_2}\left[\frac{NmL_{H_2(g)}}{min}\right]}{\dot{V}_{Ethanol\,(l)}\left[\frac{mL_{Ethanol\,(l)}}{min}\right]\cdot V_{React.}\,[cm^3_{React.}]} \tag{8.7}$$

8.4.1 ESR performance comparison

The ESR performance comparison between the Si micromonolith ($2.6{\cdot}10^7$ cpsi monolith) and the cordierite monolith ($4{\cdot}10^2$ cpsi monolith), both loaded with the same 1RhPd/CeO_2 catalyst, is shown in figure 8.9. For comparison purposes, tests performed under nearly the same operational conditions and exhibiting full ethanol conversion and similar hydrogen yield (Y_{H_2}=0.57 for 1RhPd/CeO_2//Si versus Y_{H_2}=0.61 for 1RhPd/CeO_2//Mon) were chosen:

- 1RhPd/CeO_2//Si: T= 873 K, P=1 bar and S/C=3 (figure 8.4)
- 1RhPd/CeO_2//Mon: T= 890 K, P=1.5 bar and S/C=3 (figure 5.2).

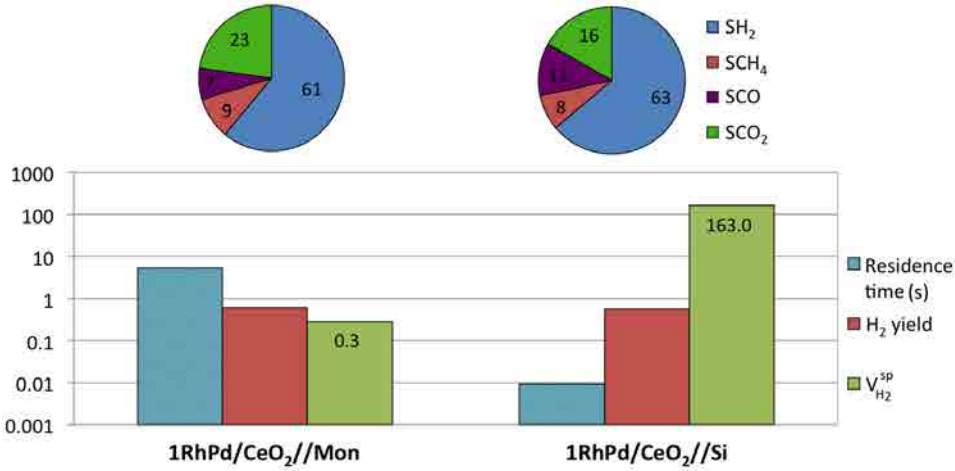

Figure 8.9: ESR performance comparison between 1RhPd/CeO_2//Mon (left) and 1RhPd/CeO_2//Si (right) catalysts. Top row: corresponding selectivities for both catalytic systems at the experimental conditions compared (numbers show the selectivity values). Below are shown the residence time, the H_2 yield and the specific volumetric hydrogen production (given in the specified units, see equation 8.7). Experimental conditions: T=873-890 K, P=1-1.5 bar, S/C=3, χ_{Ethanol}=100%. Liquid feed: Conventional monolith $\dot{V}_{S/C=3}$=0.055 mL/min; Si micromonolith $\dot{V}_{S/C=3}$=0.021 mL/min.

The dramatically superior contact area available in the Si microstructure when compared to the cordierite monolith, $4.1{\cdot}10^5$ m^2/m^3 versus $2.2{\cdot}10^3$ m^2/m^3 respectively, allowed for achieving similar hydrogen yields although residence times were reduced from $\tau{\sim}6$ s to $\tau{\sim}9{\cdot}10^{-3}$ s for the experiments compared, as seen in figure 8.9. Very similar hydrogen and methane selectivities were measured as well. The operation of the silicon micromonolithic system at residence times in the order of milliseconds yielded higher amounts of CO in detriment of CO_2 when compared with the conventional monolith. In fact, as described elsewhere [63] and demonstrated previously in Chapter 5 (section 5.2.2), the water gas shift reaction (equation 5.4) occurs in-series with the ethanol decomposition (equation 5.1). Consequently, extremely reduced residence times diminished the contribution of the WGS reaction. At the operating conditions of the Si micromonolith, H_2, CH_4, CO and CO_2 equilibrium selectivities are 70%, 4%, 7% and 19%, respectively. Specific hydrogen production rates are also reported in figure 8.9. As seen, a noticeable 580-fold increase of $V_{H_2}^{sp}$ was measured for the Si micromonolith when compared with the cordierite monolith. If $V_{H_2}^{sp}$ is multiplied by the reactor volume for each system, then a similar value of $\sim$1.3 $NL_{H_2,gas}/mL_{ethanol,\ in}$ is found, in agreement with the measurement of almost the same hydrogen yield of $\sim$0.6 for both supports, as already mentioned. However, it is important to recall that the catalyst mass of the conventional cordierite monolith was 245 mg, whereas that of the silicon micromonolith was only $\sim$3 mg.

8.4.2 OSR performance comparison

The OSR performance was also compared in both systems. For that purpose, OSR tests were performed over a 1RhPd/CeO_2//Mon loaded with 0.250 g of catalyst. Increasing feed loads were tested at constant temperature (T=923 K), pressure (P=1 bar), S/C (S/C=1) and O_2:ethanol=0.56. For comparison, the experiments performed over the Si micromonolith reported on section 8.3.2.b were chosen.

Even though these experiments were performed at highly reduced residence times over the Si micromonolith, at 923 K complete ethanol conversion was attained for all the experiments and hydrogen yields ranging from 0.58 to 0.61 were achieved. The same values were yielded by the cordierite monolith, highlighting the outstanding performance of the Si micromonolith due to the two orders of magnitude increased contact area. Similar selectivity values were observed for OSR experiments, with almost no variation for the different loads and catalyst supports. Figure 8.10 shows the volumetric hydrogen production attained against the mL of liquid ethanol injected for both the Si micromonolith (1RhPd/CeO_2//Si) and the conventional cordierite monolith (1RhPd/CeO_2//Mon). The residence time of each experiment performed is specified in the plot.

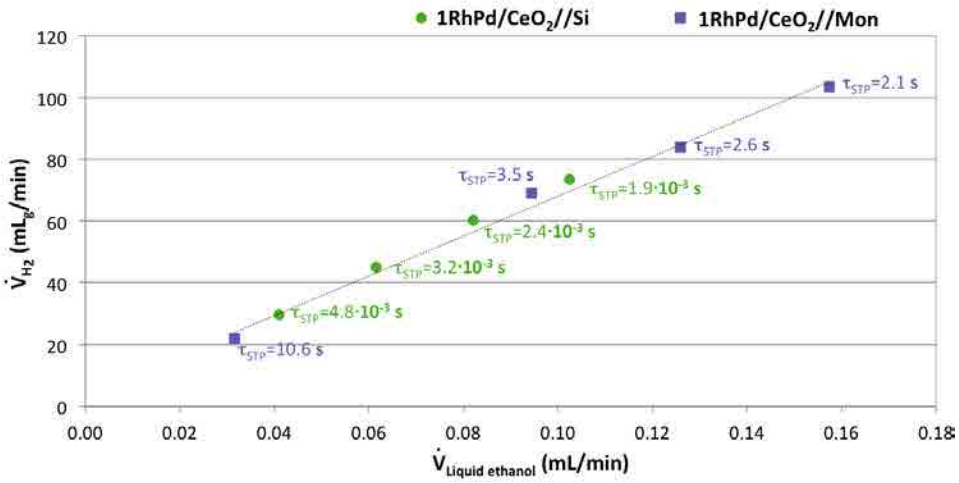

Figure 8.10: OSR performance comparison between 1RhPd/CeO_2//Si and 1RhPd/CeO_2//Mon catalysts. Volumetric hydrogen production as a function of the ethanol injected. The residence time of each test is specified in the plot. Experimental conditions: T=923 K, P=1 bar, S/C=1, O_2:ethanol=0.56, χ_{Ethanol}=100%.

As seen in figure 8.10, the volumetric hydrogen production rate against the mL/min of ethanol injected of both catalytic systems lay in the same line, which indicated the absence of diffusion and mass transfer problems and thus an enormous difference was obtained on the specific hydrogen production rate of both systems:

the 1RhPd/CeO_2//Mon produced 0.24 $NmL_{H_2}/(mL_{liquid\ ethanol} \cdot cm^3)$ on average, whereas the 1RhPd/CeO_2//Si produced 145 $NmL_{H_2}/(mL_{liquid\ ethanol} \cdot cm^3)$ on average or 190 NL_{H_2}/min per cm^3 of micromonolith.

After all these experiments, the Si micromonolith was removed from the reactor housing and was cut in order to analyze the microchannels by SEM. The SEM images obtained were shown in figure 8.3 and revealed that no microchannels were blocked with carbon deposits.

The silicon micromonolith functionalization, its characterization and the catalytic screening tests were published in *N. J. Divins, E. López, Á. Rodríguez, D. Vega and J. Llorca, "Bio-ethanol steam reforming and autothermal reforming in 3-µm channels coated with RhPd/CeO_2 for hydrogen generation", Chemical Engineering and Processing: Process Intensification, 64 (2013), pp. 31* [201] and this is one of the papers of this Thesis.

8.5 Multifuel steam reforming

As excellent performance was exhibited by 1RhPd/CeO_2//Si for the ESR, a new Si micromonolith was coated with 1RhPd/CeO_2 following the above-mentioned method and was tested for steam reforming of high-C-content compounds. The aim of these tests was to investigate the feasibility of reforming compounds with higher C content than ethanol and the stability of the Si micromonoliths towards these types of reactions. Therefore, these analyses do not aim at being a complete investigation of the influence of different reaction parameters on the performance of high-C-content compounds reforming reactions, but a first evaluation of Si microreactors for such reactions.

Initially, ethanol steam reforming tests were performed at S/C=3 and temperatures ranging from 873 K to 923 K, in order to assure the correct performance of the new functionalized 1RhPd/CeO_2//Si. Again, full ethanol conversion was achieved, assuring the absence of bypasses and channels without catalyst.

Subsequently, the multifuel reforming experiments were carried out under the same reaction conditions for all the tests, namely temperatures ranging from 823 K to 1023 K, atmospheric pressure, fixed injection rates of the inlet mixture (feed mixtures were injected by using a syringe pump, Kent Scientific) and the water content of the feed mixtures was fixed at three times the stoichiometric S/C ratio of its equation. The compounds reformed were: acetic acid (equation 8.8), acetone (equation 8.9), isopropanol (equation 8.10) and methoxyethanol (equation 8.11). At the end of these tests, also diesel (of equivalent formula $C_{12}H_{23}$) steam reforming (equation 8.12) at 1023 K was performed for 20 hours. No regeneration treatment was

performed between the different high-C-content compounds tests.

$$\text{Acetic acid SR: } CH_3COOH + 2\,H_2O \longrightarrow 2\,CO_2 + 4\,H_2 \text{ [202]} \tag{8.8}$$

$$\text{Acetone SR: } CH_3COCH_3 + 5\,H_2O \longrightarrow 3\,CO_2 + 8\,H_2 \text{ [203]} \tag{8.9}$$

$$\text{Isopropanol SR: } CH_3CHOHCH_3 + 5\,H_2O \longrightarrow 3\,CO_2 + 9\,H_2 \text{ [203]} \tag{8.10}$$

$$\text{Methoxyethanol SR: } CH_3OCH_2CH_2OH + 4\,H_2O \longrightarrow 3\,CO_2 + 8\,H_2 \tag{8.11}$$

$$\text{Diesel SR: } C_{12}H_{23} + 24\,H_2O \longrightarrow 12\,CO_2 + 35.5\,H_2 \tag{8.12}$$

As seen in equations 8.8 to 8.12, the steam reforming of these compounds yields different number of H_2 moles per mole of fuel fed. Therefore, different hydrogen yields were defined for each of these fuels and, as previously done for ESR (see equation 8.3), the number of H_2 moles per mole of fuel fed was normalized by its maximum theoretical production, hence the hydrogen yields are defined between 0 and 1. The H_2 yields defined for comparison purposes are presented in equations 8.13 - 8.17.

$$\text{Acetic acid SR: } Y_{H_2} = \frac{\dot{n}_{H2}}{4\,\dot{n}_{acetic\,acid,in}} \tag{8.13}$$

$$\text{Acetone SR: } Y_{H_2} = \frac{\dot{n}_{H2}}{8\,\dot{n}_{acetone,in}} \tag{8.14}$$

$$\text{Isopropanol SR: } Y_{H_2} = \frac{\dot{n}_{H2}}{9\,\dot{n}_{isopropanol,in}} \tag{8.15}$$

$$\text{Methoxyethanol SR: } Y_{H_2} = \frac{\dot{n}_{H2}}{8\,\dot{n}_{methoxyethanol,in}} \tag{8.16}$$

$$\text{Diesel SR: } Y_{H_2} = \frac{\dot{n}_{H2}}{35.5\,\dot{n}_{diesel,in}} \tag{8.17}$$

The hydrogen yield achieved for the different compounds tested at 973 K is reported in figure 8.11. The S/C of each experiment is detailed in the plot. In addition, the top row in figure 8.11 shows the selectivity to H_2, CH_4 CO and CO_2 as well as the selectivity to other byproducts categorized as *others* for each test. For all the high-C-content compounds tested, the main byproduct detected was acetone. Only in the case of methoxyethanol, up to ∼1% of other byproducts (C_2 species) was detected together with acetone.

Among the different species examined, methoxyethanol steam reforming yielded the highest hydrogen production per mole of fuel injected, which is the compound with the closest properties to ethanol. However, ESR rendered the highest selectivity to H_2. Acetic acid and acetone steam reforming showed poor hydrogen selectivities (S_{H_2}∼20%); whereas that attained via isopropanol SR was ca. 44%,

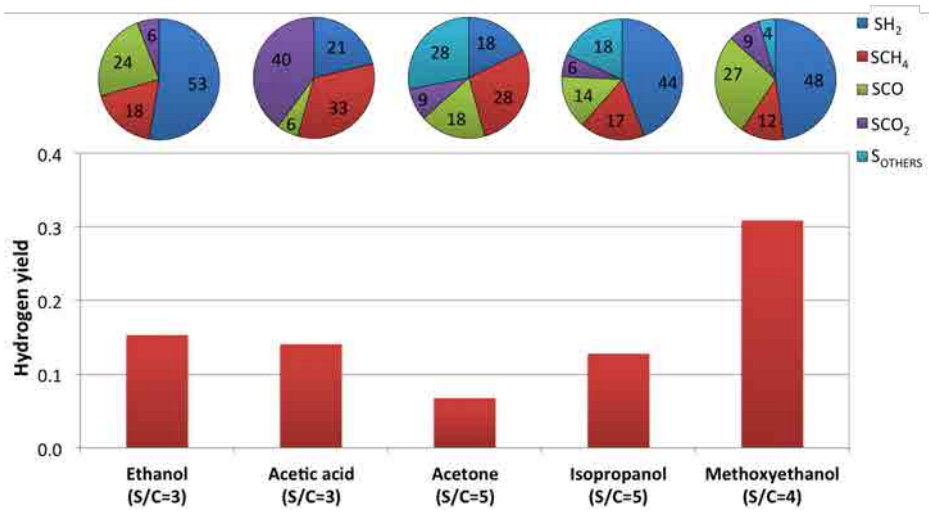

Figure 8.11: Hydrogen yield achieved for the multifuel steam reforming reactions. Experimental conditions: T=973 K. P=1 bar. $\dot{V}_{\text{Liquid fuel}}$=0.020 mL/min.

although large quantities of acetone were produced too. Diesel steam reforming tests showed very low activity and the hydrogen yield attained was <0.01.

After these experiments the Si micromonolith was cut in order to analyze the microchannels by SEM and evaluate the catalyst stability. Representative SEM images of the post-reacted 1RhPd/CeO_2//Si are shown in figure 8.12.

Figure 8.12a shows a frontal view of the Si micromonolith where the microchannels could be distinguished across the monolithic structure. On the micromonolith's upper side (shown in the upper part of figure 8.12a) large carbonaceous deposits were distinguished and confirmed by EDX analyses. A detail of them is given in figure 8.12b; where it is possible to see the compact structure that carbon deposits formed. The microchannels shown in figure 8.12c revealed differences with the microchannels subjected only to ESR tests (see figure 8.3). The severer reactions conditions tested during the reforming of high-C-content compounds provoked changes on the ceria coatings and also C deposits formed over the catalytic layers. However, in spite of the aggressive reaction conditions tested, no blocked microchannels were detected due to carbon deposition nor detached CeO_2 layers. Finally, figures 8.12d and 8.12e show the detail of the inside of a microchannel: figure 8.12d was acquired with the inlens detector and figure 8.12e with the secondary electrons detector. Both SEM images show the well-developed and homogeneous CeO_2 layer deposited and perfectly adhered to the SiO_2 layer. The texture of the CeO_2 layer was also distinguished as well as the formation of some voids on its surface (figure 8.12e).

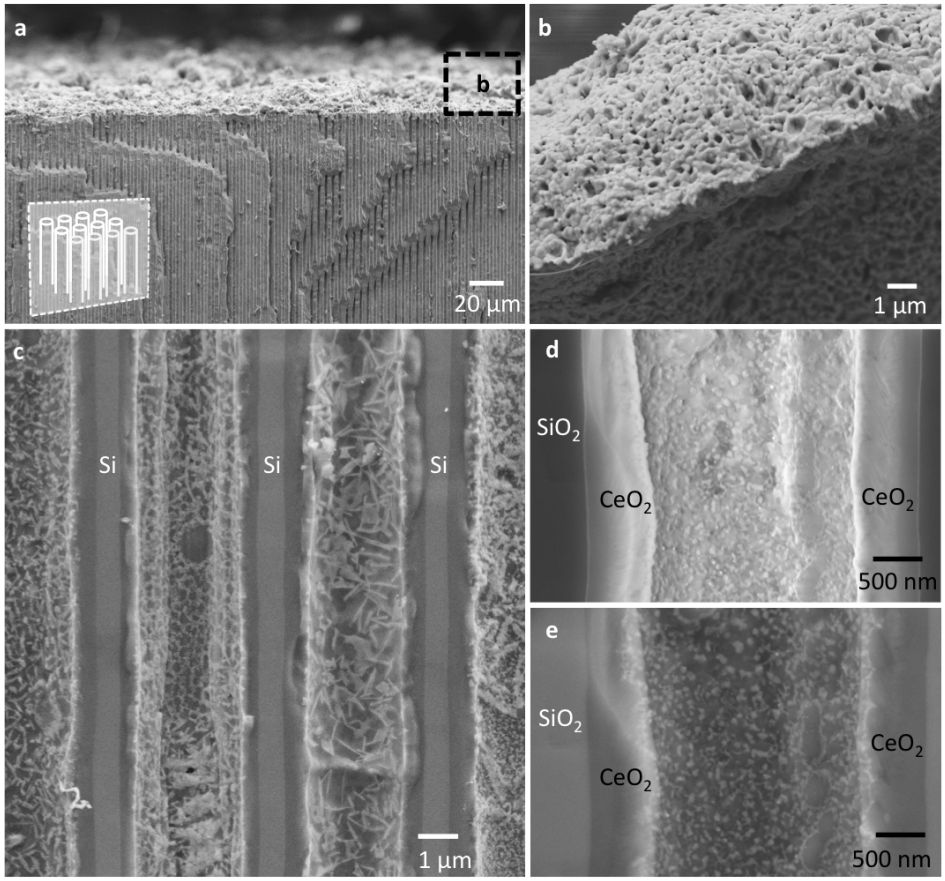

Figure 8.12: 1RhPd/CeO_2//Si SEM images after high-C-content compounds reforming tests. a) Frontal view of the Si micromonolith. b) High magnification image of the area enclosed by black dots in a. Detail of the carbon deposits formed over the Si micromonolith. c) Detail of the post-reaction RhPd/CeO_2 layer developed over the Si microchannels. d) and e) Detail of the post-reaction 1RhPd/CeO_2 layer deposited on the microchannels: d) was acquired with the inlens detector; and e) with the secondary electrons detector.

The characterization of the 1RhPd/CeO_2//Si ended with the fabrication of a TEM lamella of a piece of a reacted microchannel. The purpose was to study the RhPd NPs and to check for sintering. In order to fabricate the TEM lamella of the microreactor, the Si micromonolith surface was grooved with the focused ion beam (FIB) coupled to the SEM microscope (Neon40 crossbeam station equipped with a field emission gun, Zeiss). Figure 8.13 shows SEM images acquired chronologically during the performance of the FIB grooves.

The drawing in figure 8.13a shows the arrangement of the microchannels during the lamella-fabrication process. Initially, a Pt strip was deposited on the desired microchannel in order to protect the subjacent CeO_2 layers and performed a clean-

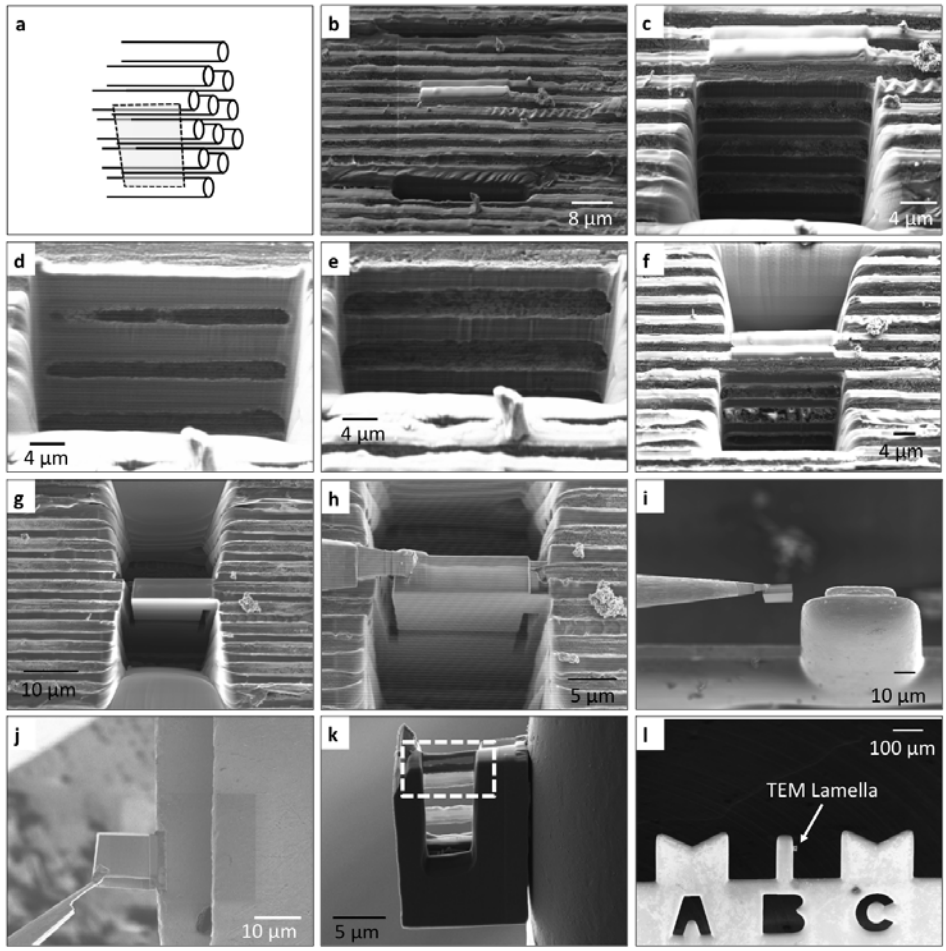

Figure 8.13: SEM images of the lamella fabrication process. a) Schematic representation of the microchannels arrangement. b) to g) SEM images acquired chronologically during the FIB grooving. h) Micromanipulator attached to the isolated channels. i) Extraction of the lamella from the microreactor. j) Lamella attached to a TEM sample holder. k) Lamella after the polishing treatment and ready for TEM observation where the successive deposited layers can be distinguished. l) General view of the TEM sample holder where the lamella was mounted.

FIB cut. The Pt strip coating can be identified in figure 8.13b as the white cylinder laying on one Si wall. Then ∼80 µm-depth grooves were performed on the front and the back side of the Pt strip, as seen in figures 8.13b to 8.13f. During this process, the microchannels at different depths were subsequently cut. The isolated and intact part that was left exposed after this process (central part of image 8.13f) was thinned out until a piece of about one microchannel thickness and four microchannels depth was obtained, as seen in figure 8.13g. Then a micromanipulator was brought close to the isolated channels (figure 8.13h) and its broad tip was attached on the left side of the sample by Pt deposition. The right side of the

lamella was cut with the FIB and the micromanipulator attached to the sample was lifted out. The extracted lamella was subsequently brought close to a TEM sample holder (figure 8.13i) and it was attached to the TEM sample holder again by Pt deposition (figure 8.13j).

Finally, the tip of the micromanipulator was cut with the FIB. The isolated lamella mounted on the TEM sample holder was polished until it was thin enough to be transparent to electrons (∼60 to 70 nm thickness) in order to make possible to examine it in transmission mode (figure 8.13k). The area enclosed by white dots on figure 8.13k shows one microchannel left exposed during the polishing process, where it is possible to distinguish from the top to the bottom, respectively: a SiO_2 layer (black), the Si wall (dark grey), again a SiO_2 layer of the adjacent channel (black) and the CeO_2 layer deposited on top of SiO_2 (light grey). The lamella prepared for TEM observation is shown in figure 8.13k and figure 8.13l shows the lamella mounted on the TEM sample holder. After all this process, the TEM sample holder was removed from the SEM system and it was examined on a TEM microscope (Jeol2010F). Figure 8.14 shows representative TEM images of the RhPd/CeO_2 catalyst identified on the RhPd/CeO_2//Si lamella after reaction.

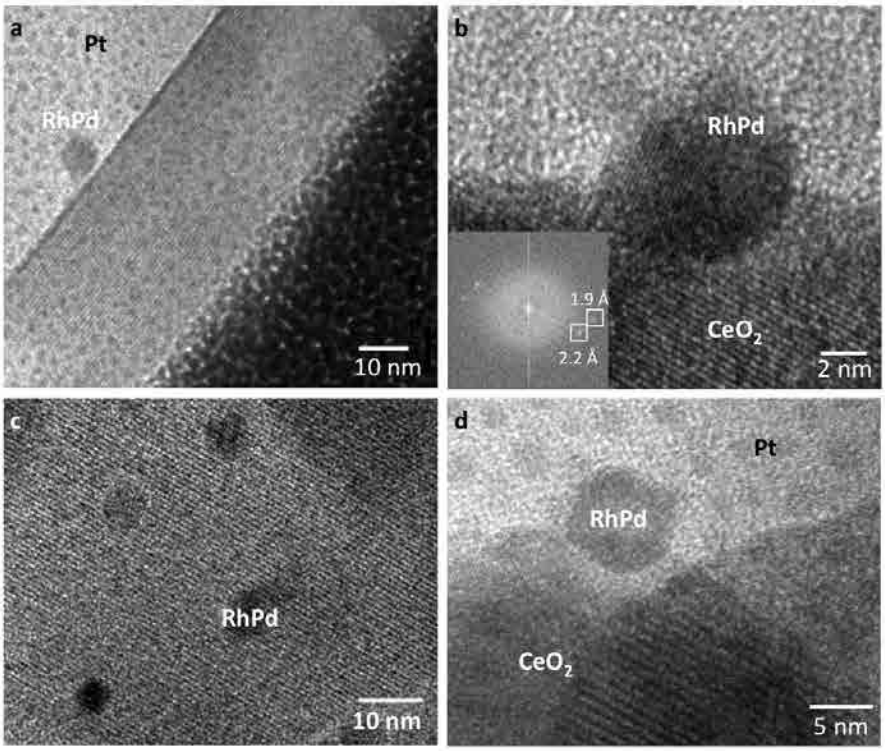

Figure 8.14: HRTEM images of the RhPd/CeO_2//Si lamella. Detail of the RhPd/CeO_2 catalyst.

TEM analyses of the fabricated RhPd/CeO_2//Si lamella allowed to identify some RhPd NPs dispersed over the CeO_2 support. Also, small NPs disseminated around the sample were identified, as seen in figures 8.14a and 8.14d. These NPs are ascribed to Pt NPs deposited during the Pt depositions carried out during lamella fabrication process, as they were homogeneously dispersed over all the catalytic layers (CeO_2 as well as SiO_2) and they were much smaller (they measured ∼2 nm in diameter) than the identified RhPd NPs. After the exposure to acetic acid, acetone, isopropanol, methoxyethanol and finally diesel steam reforming conditions at temperatures ranging from 823 K to 1023 K and the lamella fabrication process (focused Ga^+ ions beam), most of the RhPd NPs identified remained in close contact with the CeO_2 support, as seen in figures 8.14a, 8.14b and 8.14d. Also, NPs underwent moderate sintering as the current mean particle size was 7 ± 2 nm. HRTEM analyses of NPs showing lattice fringes allowed to conclude that, after the reaction conditions tested, Rh and Pd constituting the NPs were still alloyed as they showed reflections at 1.93 and 2.23 Å that can be indexed to (200) and (111) planes (see figure 8.14b), respectively, of a RhPd alloy [119]. Hence, the RhPd/CeO_2 catalyst maintained its fundamental structure. The remarkable conclusion of the lamella fabrication is that it allowed to characterize the catalytic layers, which constituted the active phase of a real microreactor that had been exposed to severe working conditions for ∼80 hours.

Part II.

Au/TiO_2 catalysts for CO preferential oxidation

9 Hydrogen purification with Au/TiO_2 catalysts: An overview

Catalytic hydrogen production by means of ethanol steam reforming has been exhaustively researched in Part I. As described, when hydrogen is produced from reforming processes CO is always present, regardless of the substrate used. Therefore, fuel processing represents a very important aspect of fuel cell (FC) technology and the development of processes devoted to obtain CO-free hydrogen streams is a critical issue and an essential requirement for proton exchange membrane FCs (PEMFCs) feeding [29]. The present Part is dedicated to the investigation of the last catalytic purification stage of the reforming process, the CO abatement, by means of CO preferential oxidation . A new generation of robust Au/TiO_2 catalysts was designed to selectively reduce the carbon monoxide content to a few ppm and to generate almost CO-free H_2 streams suitable for PEMFC feeding.

9.1 Hydrogen purification

As already presented in the Introduction (section 1.3.2), PEMFCs possess numerous attractive features for small-scale electricity generation, which are boosting their research. However, one of their major drawbacks is that the presence of CO traces (>10 ppm) in the feed streams strongly affects the kinetics of their platinum (Pt) anode electrodes. At the PEMFCs working temperatures, CO strongly coordinates with Pt, inhibiting the dissociation (electro-catalytic oxidation) of hydrogen to protons and electrons and, consequently, hampering its activity [204]. Besides, CO is a critical pollutant. Therefore, the production of CO-free hydrogen is essential to feed PEMFC.

In the literature, three catalytic hydrogen purification approaches have been proposed and have been thoroughly investigated, as already described in the Introduction (section 1.4.2), namely methanation, CO preferential oxidation and hydrogen separation with Pd-based membranes. In this Thesis, two routes have been explored to obtain PEMFC-grade hydrogen: purification based on Pd-membrane

separation, which was investigated in Chapter 7, and the carbon monoxide preferential oxidation reaction profiting Au/TiO_2 catalysts, which is the focus of the present Part. These two processes are suitable for powering small-scale stationary units or for on-board H_2 production [205].

9.2 Carbon monoxide preferential oxidation reaction

Among the different methods proposed to selectively eliminate CO to obtain fuel cell grade H_2, its catalytic oxidation is considered as one of the most plausible options, because it is a cheap and effective solution [206]. Carbon monoxide preferential oxidation (CO-PrOx) is particularly appealing when applied to low-scale or portable reformer-PEMFC systems due to its fairly simple implementation, low operation costs and minimal loss of hydrogen [204, 207].

CO-PrOx is an effective method to ideally oxidize with air ∼1% CO (10000 ppm) from the pre-cleaned reformate streams[1] to less than 10 ppm (which is tolerable for the PEMFC anode), without oxidizing almost none of the 40 - 70% of H_2 present in the reformate stream. Therefore, in the CO-PrOx system two oxidation reactions compete for the oxygen consumption and, as a consequence, CO-PrOx catalysts have to exhibit high CO oxidation activity (equation 9.1), while H_2 oxidation (equation 9.2) has to be maintained low in order to avoid fuel losses, at temperatures ranging from 200℃ to 80℃. High selectivity is a critical requirement for CO-PrOx catalysts.

$$\text{Desired reaction:} \quad CO + \frac{1}{2}O_2 \longrightarrow CO_2 \qquad \Delta H^0_{298K} = -285 \text{ kJmol}^{-1} \tag{9.1}$$

$$\text{Undesired reaction:} \quad H_2 + \frac{1}{2}O_2 \longrightarrow H_2O \qquad \Delta H^0_{298K} = -243 \text{ kJmol}^{-1} \tag{9.2}$$

CO-PrOx should be operated in this temperature range in order to efficiently use energy, since the CO-PrOx reactor is placed between the low-temperature WGS reactor (∼200℃) and the PEMFC (∼80℃) [34]. At higher temperatures (150℃-300℃), the oxidation reactions may be accompanied by the reverse water-gas shift and/or methanation reactions [205], resulting in H_2 losses. Also, the presence of CO_2 and H_2O should be considered as, generally, their presence diminishes CO conversion [209].

To summarize, the fundamental requirements of the CO-PrOx process to achieve the target of CO concentration reduction below 10 ppm are [41]:

- High CO oxidation activity and selectivity coupled to low H_2 oxidation.

[1] CO concentration downstream the WGS reactors typically ranges ∼0.5-2% [208].

- Avoidance of undesirable side reactions, such as methanation or reverse WGS.
- Operation within the parameters of the fuel processor, which include temperature, space velocities and high steam and CO_2 concentrations rendered by the preceding reforming and WGS units.
- Long stability and resistance to deactivation.

Hence, the development of an appropriate catalyst to achieve the identified requirements is essential.

9.3 CO-PrOx catalysts

Early in the 1960s, Engelhard patented a commercial CO-PrOx catalyst composed of Fe promoted-Pt supported on γ-alumina to purify hydrogen removing CO to levels acceptable for the ammonia synthesis [41]. Since then, motivated by the increasing attention that hydrogen and fuel cells are receiving as new tools for energy management, a profuse number of studies on the design of suitable catalysts for the competitive oxidation of CO in the presence of H_2 has been published. For instance, in November 2014 the citation database *Scopus* (www.scopus.com, [210]) was employed to search for articles, book's chapters, patents, reviews and conference papers that contained the word *Prox* either in the title or in the author keywords. After the search refinement excluding articles not related with the preferential oxidation of CO, 380 documents were obtained among which there were 283 journal articles, 8 reviews and 11 patents, evidencing the overwhelming effort directed towards the CO-PrOx reaction. Therefore, this Introduction is not intended to be an exhaustive revision of the literature, but a general overview of the different CO-PrOx catalysts developed so far. In addition, due to the large differences in the catalytic conditions tested and preparation procedures (such as gas stream composition, space velocity, metal content, ...), the activity performance comparison of the different formulated catalysts is hardly attainable and a ranking of the different catalyst's formulations is nearly impossible [205].

Many catalytic formulations have been tested for the CO-PrOx reaction so far. In general, a suitable catalyst must adsorb CO and provide activated oxygen, while hydrogen adsorption must be suppressed [211]. Catalysts for the selective oxidation of CO can be classified into three categories according to the active metal used: (i) Pt group metal (PGM) catalysts (mainly Pt, Ru, Rh, Pd and Ir), (ii) transition metal (TM) catalysts and (iii) Au-based catalysts [34, 205]. Liu et al. [34] designed a conceptual illustration (see figure 9.1), where the different categories of CO-PrOx catalysts were organized depending on their CO conversion as a function of the reaction temperature. As seen in figure 9.1, supported Au catalysts

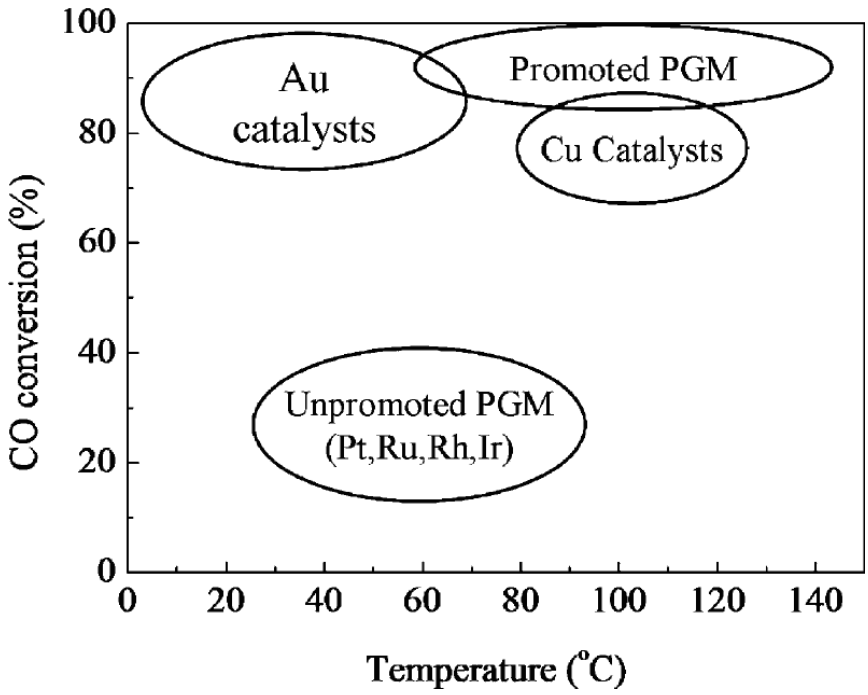

Figure 9.1: Illustration of the catalytic performance of the different types of CO-PrOx catalysts depending on their CO conversion as function of the reaction temperature. Extracted from [34].

exhibit exceptionally high CO oxidation activity in the low-temperature range, whereas Cu-based catalysts and promoted PGM catalysts show similar CO conversion levels at higher temperatures than gold catalysts. Unpromoted PGM catalysts usually show very low activities at temperatures below 100°C. A brief overview of the performance of each of these catalysts's categories is revised in the following sections 9.3.1, 9.3.2 and 9.3.3.

9.3.1 Platinum group metal catalysts

PGM catalysts generally comprise Pt, Rh, Ru, Ir and Pd-supported catalysts. As seen in figure 9.1, unpromoted PGM usually show low CO conversion at temperatures below 100°C and may lack the required selectivity for CO-PrOx.

Platinum-based catalysts are the most studied among PGM-based catalysts. In 1993 in an initial work by Oh and Sinkevitch [212], the authors tested a collection of catalysts composed of noble metals, such as Ru, Rh, Pt and Pd supported on alumina, as well as of base metals such as Co-Cu, Ni-Co-Fe, Ag, Cr, Fe and Mn under a feed stream containing CO, H_2 and O_2 of unrealistic concentration (the gas composition was 900 ppm CO, 800 ppm O_2 and 0.85% H_2 balanced N_2). Among

the catalysts tested, it was found that Pt, Rh and Ru were the most appropriate catalysts for the CO-PrOx reaction: CO was almost completely converted to CO_2 at temperatures ∼100℃ over Ru/Al_2O_3 and Rh/Al_2O_3 and at ∼200℃ over Pt/Al_2O_3, however large H_2 amounts were consumed in the presence of excess oxygen. Ruthenium and Rh catalysts were more selective than Pt/Al_2O_3.

Kahlich et al. performed a kinetic study of the CO oxidation in a H_2-rich gas stream over Pt/Al_2O_3 catalysts [213]. The authors concluded that over 0.5% Pt/Al_2O_3 the highest attainable conversion was 80% of 1% CO with 1% O_2 in the presence of H_2 even at 250℃. The presence of hydrogen was found to increase the CO rate oxidation by a factor of ∼2. They estimated that over a Pt/Al_2O_3 catalyst the optimum temperature range for CO-PrOx is ∼200℃ and CO concentration 2.5 times the stoichiometric amount of O_2. Many synthesis procedures and different formulations were then investigated. By means of a sol-gel method preparation, Manasilp and Gulari [214] synthesized 2% Pt/Al_2O_3 catalysts and obtained 80% CO conversion at 170℃ with a selectivity of ca. 50%. Addition of water vapor had a significant positive effect. However, in the absence of steam, CO_2 in the feed stream decreased the activity significantly. Avgouropoulos et al. [215] reported a stable performance for 110 hours of a 5% Pt/Al_2O_3 catalyst at 100℃ under a reaction mixture containing 1% CO, 1.25% O_2, 50% H_2, 15% CO_2 balanced He.

The effect of other supports has also been investigated. Igarashi et al. [216] and Sebastian et al. [217] supported Pt on different zeolitic materials and found that Pt/zeolites exhibited better selectivities but lower activities than Pt/Al_2O_3. Wootsch et al. [218] studied Pt supported on $Ce_xZr_{1-x}O_2$ (x=0, 0.15, 0.5, 0.68, 1) and found that the ceria-supported catalysts were more active than Pt/Al_2O_3 in both CO and H_2 oxidation. In addition, the effect of the morphology of CeO_2 as a support was investigated and Pt was supported on CeO_2 cubes, rods and octahedra [219]. The catalytic performance of the tested Pt/CeO_2 catalysts in both CO oxidation and CO-PrOx followed the order: $Pt/CeO_{2,\ rods} > Pt/CeO_{2,\ cubes} > Pt/CeO_{2,\ octahedra}$. However, some weak points that may hamper the implementation of Pt-based catalysts have been identified: (i) narrow operating window: Pt catalysts can be efficiently used in a small temperature range (170-200℃) and in the presence of excess oxygen and (ii) low selectivity to CO oxidation [218].

Palladium-supported catalysts have very low activity and selectivity for the CO-PrOx reaction. The strong affinity for hydrogen chemisorption of Pd causes that at higher temperatures metallic Pd preferentially adsorbs hydrogen than CO and the adsorbed H species are more easily oxidized than CO [41, 205]. Although it had been shown that Rh-based catalysts were more selective than Pt/Al_2O_3 catalysts, few papers reported their use for the CO-PrOx reaction. More recently, the performance of Rh supported on Al_2O_3, CeO_2, TiO_2, zeolites and MgO was in-

vestigated [220, 221]. Comparing the performance of Rh/MgO with Ru/γ-Al_2O_3 and Pt/γ-Al_2O_3 catalysts, Han et al. [221] found that Rh/MgO catalysts at 250℃ exhibited better performance than Pt and Ru-based catalysts at their respective optimum working temperatures. Iridium supported on CeO_2 was found to be reasonably active and selective, although less than Pt [41]. Finally, many papers have reported the use of Ru-based catalysts as it is cheaper than other noble metals. After a literature revision, Liu et al. [34] concluded that Ru/Al_2O_3 catalysts appear as the most promising for the CO-PrOx reaction among PGM catalysts based on the catalytic results obtained under realistic operating conditions, however the simultaneous consumption of H_2 reduces its interest. Ruthenium catalysts present several drawbacks for its application in the CO-PrOx process [30], such as (i) optimum operating temperatures between 140-200℃, which is higher than the working temperature of PEMFCs, (ii) Ru is very active for the methanation of both CO and CO_2 and especially at temperatures ∼200℃, thus consuming H_2, and (iii) Ru possesses different oxidation states, therefore its surface composition varies with air exposure and it is not active on its oxidized state.

As a general conclusion, unpromoted PGM catalysts are not considered as promising candidates for the CO-PrOx reaction, therefore in order to increase their activity, the addition of promoters such as reducible metal oxides used either as promoters of the active phases or of the supports, alkali metal ions or a second noble metal has been studied [34]. As seen in figure 9.1, promoted PGM catalysts generally exhibited enhanced CO-PrOx activities and showed interesting performances in the reaction temperature range 60-150℃.

9.3.2 Transition metal oxide catalysts

The first studies reporting the presence of TM oxides in CO-PrOx catalysts concerned its use as promoters of NM-based catalysts [205]. However, driven by the high cost of NM catalysts, catalysts based on transition metal oxides have been researched as a cheap alternative. The first results of CO-PrOx on $CuO\text{-}CeO_2$ catalysts were obtained by Avgouropoulos et al. in 2001 [222], based on the results of a previous work published in 1995 by Liu and Flytzani-Stephanopoulos, where $CuO\text{-}CeO_2$ catalysts were examined for CO and CH_4 total oxidation [223]. $CuO\text{-}CeO_2$ catalysts showed high selectivity to CO oxidation at operating temperatures higher than 140℃, without exhibiting reverse water-gas shift activity.

Since 2001, numerous TM-based catalysts with different active phases and supports have been investigated. Cobalt supported on CeO_2, Al_2O_3, ZrO_2, SiO_2 and TiO_2 was studied by Zhao et al. [224], being the Co/ZrO_2 catalyst the most active of the series of catalysts tested. The same group reported a CoO_x/CeO_2 catalyst which achieved 100% CO conversion under a wide range of reaction conditions [225];

Co/ZrO_2 and Co/CeO_2 catalysts were again recently investigated in [226] and it was found that Co/CeO_2 doped with Mn presented the highest CO conversion at low temperatures. Mariño et al. [227] in 2005 studied a wide range of TM (Co, Cr, Ni, Cu, Zn) supported on oxides with very different acidic, basic and redox properties such as MgO, La_2O_3, SiO_2-Al_2O_3, CeO_2 and $Ce_{0.63}Zr_{0.37}O_2$. An important conclusion extracted was that, among the different metals investigated, only Cu (Ni at temperatures below 200℃ exhibited good activity although it was lower than Cu) presented high CO conversion and selectivity to CO_2, making Cu-based catalysts the most suitable for the CO-PrOx reaction. Also, the authors found that Cu supported on ceria and on $Ce_{0.63}Zr_{0.37}O_2$ showed similar activity to PGM catalysts and were very selective in the 50-150℃ temperature range. Copper-supported catalysts revealed very good activity for CO-PrOx and exhibited higher selectivity to the CO oxidation than Pt-supported catalysts (at similar conversion levels), which paved the way for TM catalysts investigations to mainly focus on copper-ceria systems [205]. Work has been done on variations of this catalytic system to improve its catalytic performance, such as the development of different synthesis routes [42]; the addition of metal promoters for instance Fe [41], La [228], Zn [229]; the addition of different textural supports, such as SBA-15 [230] or Al_2O_3; or the study of different metal loadings in order to favor CO oxidation in detriment of H_2 oxidation activity. Besides, the influence of the metallic substrate on the catalytic activity of structured catalysts has been investigated as well [231].

9.3.3 Gold catalysts

From a general point of view, TM-catalysts and Au-based catalysts exhibit a better activity and selectivity in a larger temperature range than PGM-catalysts. Supported gold catalysts are famous for their exceptionally high and unique activity for CO oxidation [232], even at low temperatures (<100℃). However, they lack of long stability and deactivation needs more investigation.

In an initial work by Haruta et al. [233], written 25 years ago, it was found that when gold is deposited on selected metal oxides as ultra-fine particles, Au chemistry dramatically changes. Previous to this work, gold was seen as the noblest of all the metals and, thus, considered as poorly reactive [234]. The nobility of Au was demonstrated by density-functional calculations addressed on hydrogen dissociation on the surface of Au. Gold showed the highest dissociation energy of the hydrogen molecule and the lowest chemical adsorption energy on its surface when compared to three other metals close to it in the periodic table: Cu, Ni and Pt. Nevertheless, this knowledge came from the chemistry of smooth gold surfaces or of relatively large gold particles with diameters above 10 nm and Haruta et al. revealed that when gold is dispersed as particles with diameters smaller than 5 nm it exhibits surprisingly high activities in the oxidation of CO [235]. Since then,

CO oxidation has been broadly investigated over Au-supported catalysts and the amount of information published is impressive [236]. Moreover, this led to the extensively study of Au nanocatalysts and was found that they are really very active in many reactions of both industrial and environmental importance, such as low-temperature catalytic combustion, partial oxidation of hydrocarbons, reduction of NO to N_2, hydrogenation of unsaturated substrates, propene epoxidation, among others. They have already been commercialized as deodorizers and gas sensors [235] and will find applications in indoor air quality control, pollutant emission control, production of H_2 energy carrier and innovations in chemical processes [237].

The unique catalytic nature of Au-supported catalysts depends on several critical factors, which in some cases are intimately related: such as the gold particle size, oxidation state and morphology; the metal oxide support type and crystalline structure, presence of promoters; and the architecture of the Au-support interaction [235, 238–241]. In these aspects, the preparation method and the activation procedure may play a key role [241]. Controlling these factors, the catalytic character of Au can be tuned.

The performance of Au supported on a wide variety of materials has been tested. Also, the addition of promoters to Au-supported catalysts has been investigated to further enhance the CO-PrOx activity of these catalysts. In a recent review by Lakshmanan et al. [242], the authors described the recent advancements for unsupported and supported Au catalysts for the CO-PrOx reaction. They reviewed the performance of Au catalysts supported on CeO_2-based supports, on Fe_2O_3, on TiO_2-based supports and MnO_2 and Co_3O_4 as reducible supports, as well as, Au supported on Al_2O_3-based supports and other non reducible supports such as MgO, ZnO, ZrO_2, SBA-15, zeolites, MCM-41, SiO_2 and C. Gold supported on TiO_2 catalysts have been widely studied for the CO-PrOx reaction. Some studies have demonstrated that Au/TiO_2 catalysts are very promising for CO-PrOx at low temperature (below 100°C), as they showed high activity for CO oxidation and selectivities ca. 50%, at typical reaction conditions (80°C, 1-2% CO and excess H_2) [243]. Nevertheless, the stability of these catalysts in the presence of H_2O and CO_2 is still an issue.

Despite the differences reported on the performance of Au catalysts supported on different materials, it was observed that Au NPs of 2-4 nm in diameter exhibited a CO oxidation rate two orders of magnitude larger than 20-30 nm NPs [241]. Therefore, a feature directly related with the size of the Au NPs may be the dominant effect in the exceptional catalytic activity of Au NPs in the nanometer range.

However, supported Au NPs can easily sinter at high temperature [244] and, as previously mentioned, there exists a strong dependence between the particle size for

supported Au NPs and their catalytic activity, which is particularly lost at particle sizes above 6-10 nm. Therefore, extreme stability in NP size is required under reaction conditions [245]. Gold NPs typically sinter rapidly under realistic conditions and small highly dispersed NPs eventually convert to thermodynamically preferred larger particles. As a consequence, considerable effort has been directed towards the design and synthesis of *sintering-resistant* Au NPs [245]. As reported elsewhere [246], several approaches have been explored to prepare gold NPs supported on metal oxides, which include incipient wetness impregnation, co-precipitation, deposition-precipitation, ion exchange, gas-phase grafting, co-sputtering, organic capping, and dendrimer and micelle encapsulation. Impregnation and precipitation methods are very simple and scalable, but normally suffer from precise particle size control. In contrast, organic capping and encapsulation methods produce size-controlled gold nanoparticles whose particle size is established before deposition on the metal oxide support. Moreover, the coordinating ligands in the precursor solution and on the oxide surface prevent aggregation of the nanoparticles [247].

In addition, in the literature, two or more elements of the three different categories have been combined in order to profit from the synergic effect of their combination, as in the case of ESR catalysts. Some of the most recent publications where two elements were combined are [229, 248–251]. In these articles Cu-Zn, Au-Cu, Pt-Cu and Pt-Au bimetallic catalysts were studied, respectively. In all these cases, the addition of a second element resulted in enhance activity by different mechanisms: the addition of Zn to CuO decreased H_2 oxidation activity while the CO oxidation activity was maintained. The presence of Au on a CuO_x/CeO_2 catalyst led to higher CO oxidation activity at low temperatures, however for T>140℃ the doped catalyst showed lower activity than CuO_x/CeO_2 [248]. The influence of Au/Cu ratios was studied in [249] and it was shown that lower Cu/Au atomic ratios for calcined catalysts promoted the catalytic behavior at reaction temperatures below 100℃, whereas the catalytic behavior of reduced bimetallic catalysts was enhanced irrespective of the Cu/Au ratio in the temperature range 80-300℃, showing good stability even in the presence of H_2O and CO_2. A mechanically mixed Pt-Cu supported on CeO_2 catalyst showed higher CO conversion than Pt/CeO_2 in the temperature range 100-200℃.

9.4 From words to action

In this scenario, the aim of the present Part is to study the well-known Au/TiO_2 system for the CO-PrOx reaction using novel Au NPs. The novel Au NPs are composed of nanometer-sized Au cores surrounded by a shell of trimethylsilane dendrons, which are radially attached to the core [252], as depicted in figure 9.2, thereby hindering Au cores aggregation. The prevention of Au NPs sintering may improve their thermal stability under reaction conditions, which is the main draw-

back identified for Au/TiO_2 catalysts. Therefore, in this Thesis several catalysts composed of Au NPs capped with different dendrimers generations were synthesized, characterized and tested for CO-PrOx supported on cordierite honeycombs, conventional microreactors and also on our novel Si micromonolith.

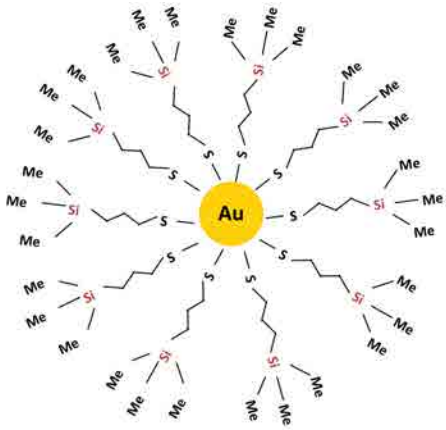

Figure 9.2: Illustration of an Au NP encapsulated in a trimethylsilane dendrimer shell.

9.4.1 Objectives of Part II

The specific objectives of the present Part are:

1. To synthesize Au/TiO_2 catalysts using different generations of encapsulated gold nanoparticles to attain higher stability.

2. To characterize the supported and unsupported Au/TiO_2 catalysts synthesized to assure a successful synthesis.

3. To investigate the thermal stability of the novel Au/TiO_2 catalysts synthesized using encapsulated Au nanoparticles.

4. To examine the reaction performance of all the developed Au/TiO_2 catalysts for the CO preferential oxidation.

5. To evaluate the stability of the best Au/TiO_2 catalyst under a real, precleaned reformate stream.

6. To reduce the CO abatement scale using conventional stainless steel microreactors.

7. To miniaturize the CO purification scale using silicon microreactors.

10 | SYNTHESIS OF Au/TiO_2 CATALYSTS

A new generation of Au/TiO_2 catalysts prepared from performed Au NPs protected with carbosilane dendrimers were tested for the CO-PrOx reaction and compared with conventional Au NPs supported over different structured reactors: cordierite monoliths, stainless steel microreactors and silicon micromonoliths. The structured reactors were functionalized in two steps: first a TiO_2 layer was developed by free impregnation and then the Au NPs where subsequently anchored or grown by incipient wetness impregnation. The same Au/TiO_2 catalysts were also synthesized in powder form for characterization purposes.

10.1 Titania support

The same cordierite honeycombs described in Chapter **3** (of dimensions 1.8x1.8x1.8 cm^3) were used for supporting the Au/TiO_2 catalysts. The TiO_2 layer was prepared using as a precursor Ti^{IV} isopropoxide ($Ti[(OCH(CH_3)_2]_4$, 97+%, Alfa Aesar). The cordierite honeycombs were functionalized by immersing the honeycomb in Ti^{IV} isopropoxide; then the monoliths were dried under axial rotation at 353 K for 1 hour and at 393 K for 1 hour more followed by calcination at 723 K for 4 hours (2 K/min). Following this procedure, approximately, 250 mg of TiO_2 were deposited on the cordierite channels' walls. The monoliths loaded with TiO_2 are referred to as **TiO_2//Mon**, in accordance with the nomenclature method described in Part I for RhPd/CeO_2 catalysts.

The same precursor was used to coat the Si micromonoliths' channels with a thin TiO_2 layer. The procedure described in section **8.2** to functionalize Si micromonoliths with RhPd/CeO_2 catalysts was employed here. Stainless steel microreactors already coated with TiO_2 were supplied by the Mainz Institute of Microtechnology (IMM, Germany).

10.2 Gold nanoparticles

Gold was subsequently anchored or grown over TiO_2 by using five Au NPs precursors:

1. Prepared from $HAuCl_4 \cdot 3H_2O$ (ACS reagent, Sigma-Aldrich).
2. Preformed Au nanoparticles encapsulated in dodecanethiol ligands.
3. Preformed Au nanoparticles encapsulated in three different generations of trimethylsilane dendrons (Au nanoparticle-cored dendrimers, Au NCD).

Conventional gold NPs synthesized using $HAuCl_4$ were grown on TiO_2 by incipient wetness impregnation of a $HAuCl_4$ 0.012 M ethanolic solution, followed by calcination at 723 K for 4 hours (1 K/min). These samples are referred to as **AuC/TiO$_2$** (conventional Au supported on TiO_2).

The preformed nanoparticles were synthesized at the Dendrimers & Molecular Polygons Group (Department of Inorganic Chemistry, UB) [252]. Dodecanethiol- and dendrimer-stabilized core-shell Au NPs were synthesized following the well-known Brust's method [253]. The synthesis of Au NPs protected with an organic shell consisted of two main steps: (i) the synthesis of the corresponding thiol-functionalized ligands and (ii) growing of metallic Au nanoparticles with the simultaneous attachment of the self-assembled ligand monolayers on the growing Au nuclei.

The starting materials for the Au-capped NPs synthesis are thiol-functionalized dendrons and dodecanethiol ligands, which were synthesized at UB and the exact details of the synthesis route are reported elsewhere [252]. In this Thesis, Au NPs protected with three different generations (G0, G1 and G2) of trimethylsilane dendrons and with dodecanethiols (D), schematically depicted in figure 10.1, were studied.

Once the organic shells were synthesized, the gold cores were encapsulated via the Brust's two-phase method: The gold precursor, $HAuCl_4$, was transferred from aqueous solution to toluene using tetraoctylammonium bromide (TOAB) as the phase-transfer reagent. Then, each generation of the previously synthesized dendrons was dissolved in toluene and added to the organic gold solution under vigorous stirring. Aqueous $NaBH_4$ was subsequently added to the stirring mixtures as Au^+ reducing agent. During this process, while Au atoms were agglomerating the different thiol-functionalized dendrimers simultaneously attached to the growing Au nuclei, creating core-shell NPs. This method was repeated for the three dendrimers generations and for the dodecanethiol-stabilized NPs. The nomenclature of the final Au nanoparticle-cored dendrimers is: Au NPs protected with G0 dendrimers are referred to as **Au@G0**; when protected with G1 and G2 dendrimers

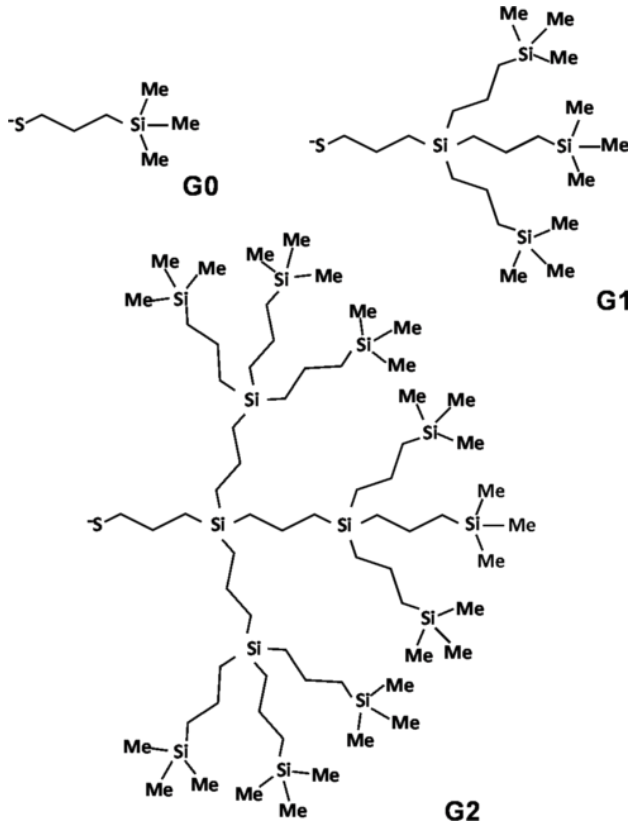

Figure 10.1: Schematic representation of the different generations of investigated dendrons.

as **Au@G1** and **Au@G2**, respectively; and finally gold cores protected with dodecanethiols are referred to as **Au@D**. The synthesis route finished with filtration and purification processes, leading to 40 mM solutions of Au@D, Au@G0, Au@G1 and Au@G2 in toluene. Figure 10.2 shows a schematic representation of the resulting encapsulated Au NCDs.

10.3 Au/TiO_2 catalysts

Preformed gold NPs were deposited on the titania-coated monoliths (TiO_2//Mon) by incipient wetness impregnation of the toluene solutions containing each type of Au NCD and Au@D NPs. The resulting catalysts were **Au@NCD/TiO_2//Mon**, where NCD: G0, G1, G2 and **Au@D/TiO_2//Mon**, respectively. The functionalized monoliths were dried under axial rotation at 353 K for 1 hour and different successive thermal treatments were carried out. The specific thermal treatment performed on each synthesized catalyst is detailed prior to the discussion of their catalytic performance in the Chapter dedicated to catalytic screening (Chapter 12).

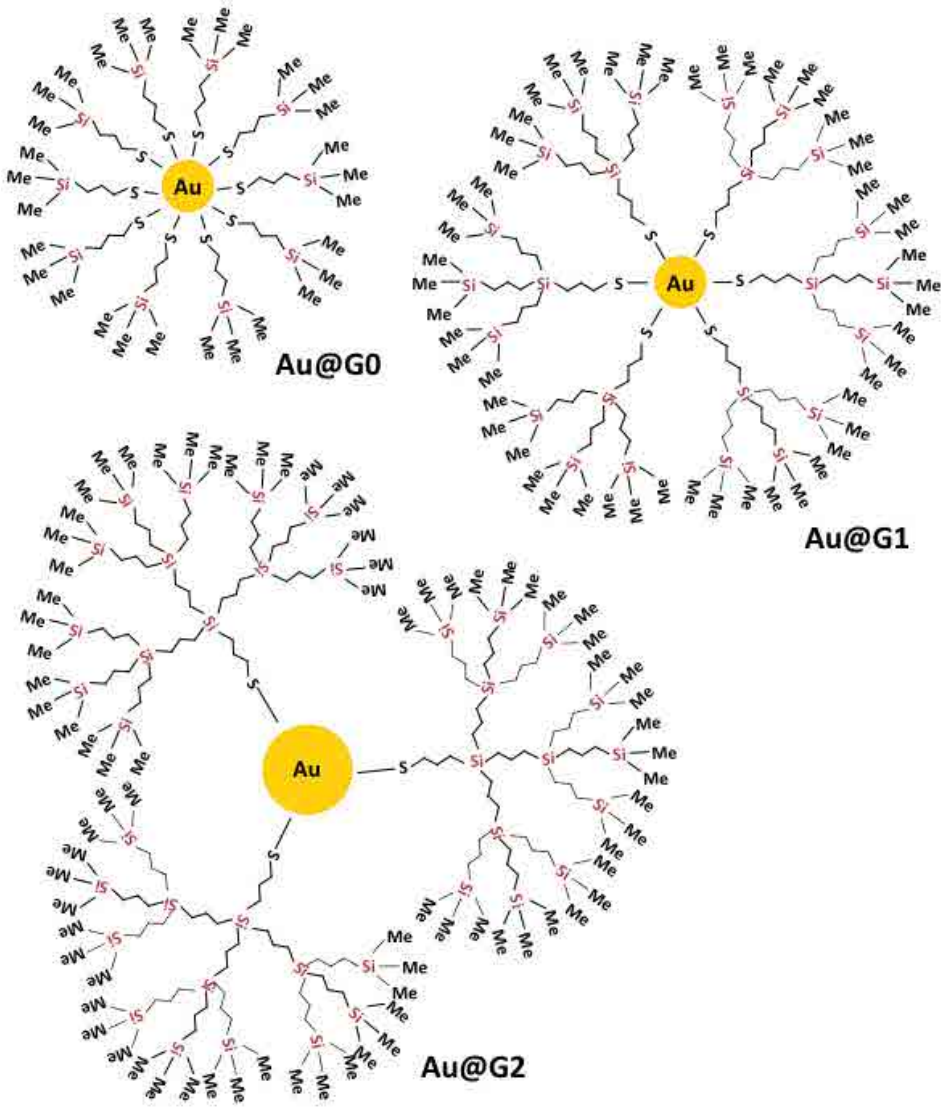

Figure 10.2: Schematic representation of the different encapsulated Au NPs investigated.

The gold metal loading (weight concentration of Au with respect to TiO_2 weight) for all Au/TiO_2 samples was fixed at 2 wt.% Au. Figure **10.3** shows a picture of a cordierite monolith functionalized with $Au@G0/TiO_2$ catalyst (on the right) compared to a bare cordierite monolith (on the left).

Functionalization details of the stainless steel microreactors and the Si micromonolith are given in Chapters **13** and **14**, respectively, which are the chapters where the catalytic tests and functionalization details of these microreactors are addressed.

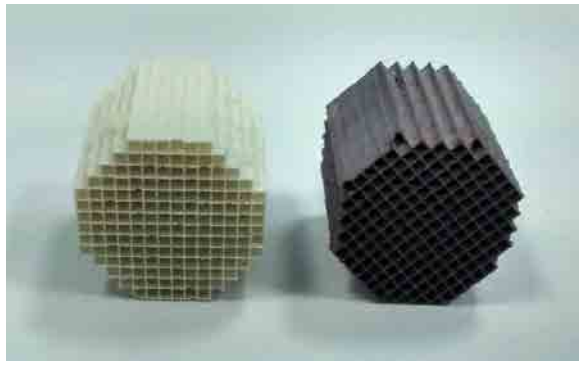

Figure 10.3: Left: Picture of a fresh cordierite monolith. Right: Cordierite monolith coated with $Au@G0/TiO_2$ (sample: $Au@G0/TiO_2//Mon$). The diameter of the monoliths is 1.8 cm.

Table 10.1 lists the nomenclature of Au/TiO_2 catalysts described throughout this Thesis.

Table 10.1: List of Au/TiO_2 synthesized catalysts.

Sample ID	Gold precursor	Substrate
$AuC/TiO_2//Mon$	$HAuCl_4$	CM*
$Au@D/TiO_2//Mon$	Preformed Au@D NPs	CM
$Au@G0/TiO_2//Mon$	Preformed Au@G0 NPs	CM
$Au@G1/TiO_2//Mon$	Preformed Au@G1 NPs	CM
$Au@G2/TiO_2//Mon$	Preformed Au@G2 NPs	CM
$TiO_2//Mon$	-	CM
$Au@G0/TiO_2$	Preformed Au@G0 NPs	-
$Au@D/TiO_2//Micro$	Preformed Au@D NPs	SSM**
$Au@G0/TiO_2//Micro$	Preformed Au@G0 NPs	SSM
$Au@G1/TiO_2//Si$	Preformed Au@G1 NPs	SiM***

*CM: Cordierite monolith. **SSM: Conventional stainless steel microreactor.
***SiM: Silicon micromonolith.

11 | Characterization of Au/TiO_2 catalysts

Gold-titania catalysts developed for the CO-PrOx reaction were characterized before reaction in order to study their fundamental properties, such as morphology, crystalline structure, particle size distribution, Au dispersion and oxidation state, likewise investigated for ESR catalysts.

11.1 Titania support

The first analyses started with the characterization of the bare support, which included the study of the TiO_2 crystalline structure, its porosity and adherence to the cordierite channels' walls.

11.1.1 Crystalline structure

Three different polymorphs of TiO_2 are known: rutile (which is the most common natural form of TiO_2), anatase and brookite. The first two polymorphs are tetragonal minerals, while brookite is orthorhombic. When anatase is heated up in air, a phase transition from anatase to rutile occurs, which has been reported to initiate at temperatures ~973 K [254]. In the literature, it has been reported that the anatase form of titanium dioxide enhances CO oxidation [255], thus the TiO_2 synthesis was focused on the obtention of the anatase polymorph of TiO_2.

Different thermal treatments were performed in order to obtain TiO_2 anatase from Ti^{IV} isopropoxide: (i) 2 mL of Ti^{IV} isopropoxide were dried for 2 hours at 393 K and (ii) 2 mL of Ti^{IV} isopropoxide were dried for 2 hours at 393 K and subsequently calcined in the muffle for 4 hours at 723 K (1 K/min). X-ray diffraction was performed on the sample calcined at 723 K and also on as-deposited Ti^{IV} isopropoxide (dried at room temperature for 30 minutes). Figure 11.1 shows the X-ray diffractograms of both samples collected from 10 to 80°, at step size 0.02° and step time 1s in a conventional XRD apparatus ($\lambda_{Cu K_\alpha}$=1.5406 Å). As seen in figure 11.1, the dried samples were amorphous, whereas the sample calcined at 723 K showed peaks at 25.3°, 37.9°, 48.1°, 54.0°, 55.1° and 62.8°, whose corresponding interplanar

distances (d_{hkl}) are: 3.52 Å, 2.38 Å, 1.89 Å, 1.70 Å, 1.67 Å and 1.48 Å. The Miller indexes of these crystallographic planes are (101), (004), (200), (105), (211) and (204), respectively, of anatase. Therefore, the desired anatase TiO_2 polymorph was formed upon calcination of Ti^{IV} isopropoxide at 723 K.

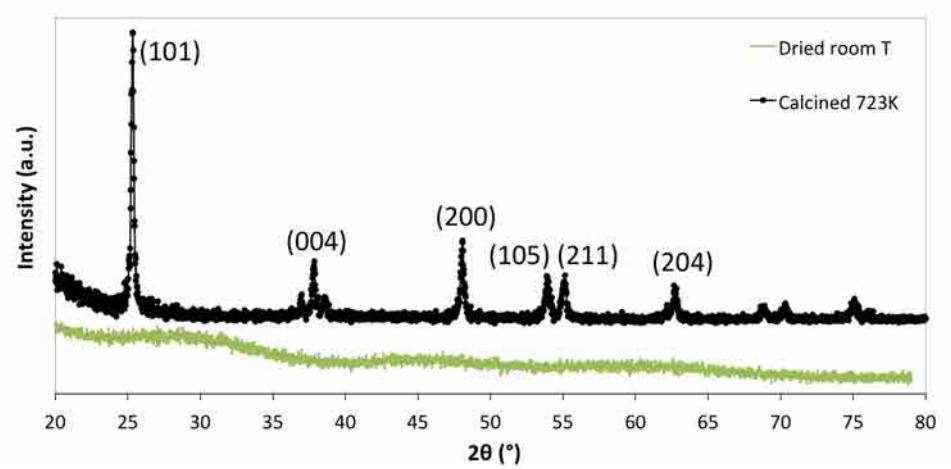

Figure 11.1: Titania X-ray diffractogram pattern acquired with a conventional XRD apparatus (λ=1.5406 Å). Planes indexes of anatase are shown.

11.1.2 Porosity

The porosity of the synthesized anatase powder (after calcination at 723 K) was measured at the Laboratory of Supercritical Fluids sited at MATGAS (Cerdanyola del Vallès). The measurements of nitrogen adsorption/desorption isotherms gave quantitative data on surface area and mean pore diameter following BET (Brunauer, Emmett and Teller) [117] and BJH (Barrett, Joyner and Halenda) [118] models, respectively. The BET surface area obtained was 264 ± 1 m^2/g and the average pore diameter was 3.9 nm.

11.1.3 Adherence

Cordierite monoliths were coated with anatase following the procedure described in Chapter 10. The adherence of the developed titania layers was checked by immersing a TiO_2//Mon in ethanol and placing it into an ultrasounds bath of 40 kHz for increasing periods of time. After each exposure, the TiO_2//Mon was dried at 353 K and weighted in order to check whether the functionalized monolith has lost mass (anatase) or not. The results of the test are shown in figure 11.2, where the evolution of the TiO_2//mon weight versus time exposed to ultrasounds is plotted. The initial mass of the TiO_2-coated monolith was 1.811 g, of which 0.250 g were TiO_2, representing about 14% of the total TiO_2//Mon mass. After

9 minutes exposed to ultrasounds the functionalized TiO_2//Mon weighted 1.797 g, representing a TiO_2 loss ∼5%, which indicated that the TiO_2 layer was well-adhered to the cordierite channel's walls.

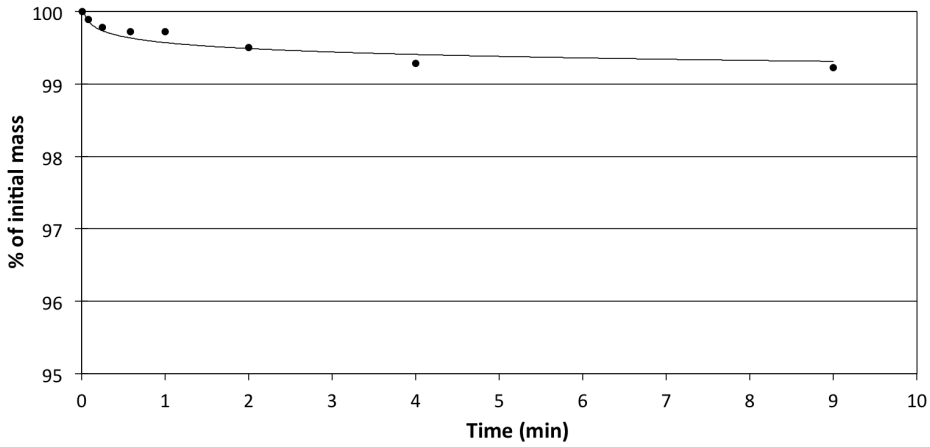

Figure 11.2: TiO_2//Mon mass loss as a function of time exposed to ultrasounds.

11.2 Preformed Au nanoparticles

11.2.1 Transmission electron microscopy characterization

The preformed gold NPs capped with a dodecanethiols shell (Au@D NPs) or with G0, G1 or G2 dendrimers shell (Au@G0, Au@G1 and Au@G2 NPs) were characterized by TEM, XPS and thermogravimetric analyses (TGA). As it is not possible to study unsupported Au NPs synthesized from HAuCl4, these NPs are only described when they are supported on TiO_2 (section **11.3.2**).

Figure **11.3** shows TEM micrographs of unsupported preformed Au NPs. The firsts two columns show low-magnification HRTEM images; well-dispersed Au@NCD and Au@D particles reasonably homogeneous in size were identified, which indicated that the synthesis method used for the different encapsulated Au cores was successful. The analysis of the Au cores size distribution showed that the average diameter of metallic Au@D cores was 1.8 ± 0.6 nm, of Au@G0 2.7± 0.8 nm, of Au@G1 2.5 ± 0.7 nm and of Au@G2 2.6 ± 0.6 nm, which is summarized in table **11.1**. Whereas Au cores in Au@D were clearly smaller than those protected by dendrimers (Au@NCD), there did not exist a clear dependence between the size of the Au cores and the dendrimer generation [252]. The third and fourth columns in figure **11.3** show high-magnification HRTEM micrographs of representative crystalline Au cores identified in each sample and their corresponding Fourier transform

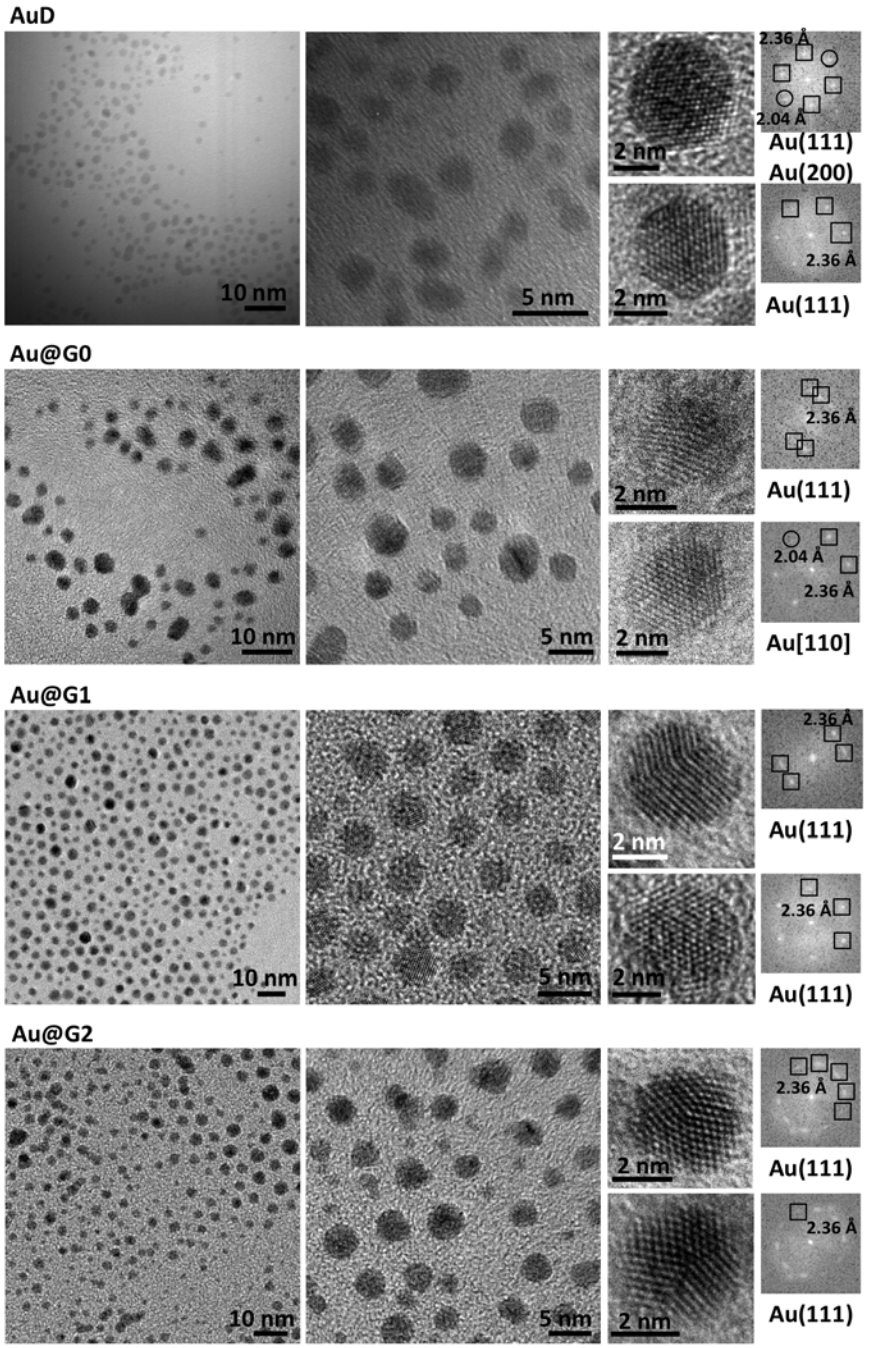

Figure 11.3: HRTEM images of the preformed Au@D, Au@G0, Au@G1 and Au@G2 nanoparticles. For each generation of encapsulated Au NPs are shown from left to right: two low-magnification images, two images showing the detail of two NPs and their corresponding FT image.

(FT) images. In all samples, the Au cores identified exhibited lattice fringes at 2.36 Å and some of them also at 2.04 Å, which were indexed to (111) and (200) crystallographic planes of Au fcc structure, respectively.

Table 11.1: TEM particle size determination of preformed Au NPs.

Preformed Au NP	Particle size (nm)
Au@D	1.8 ± 0.6
Au@G0	2.7 ± 0.8
Au@G1	2.5 ± 0.7
Au@G2	2.6 ± 0.6

11.2.2 Thermogravimetric analyses

The Au NPs protected with carbosilane dendrons were subjected to thermogravimetric analyses (TGA) in order to investigate the temperature at which the dendrimers shells were removed. Figure 11.4 shows the results of the TGA performed.

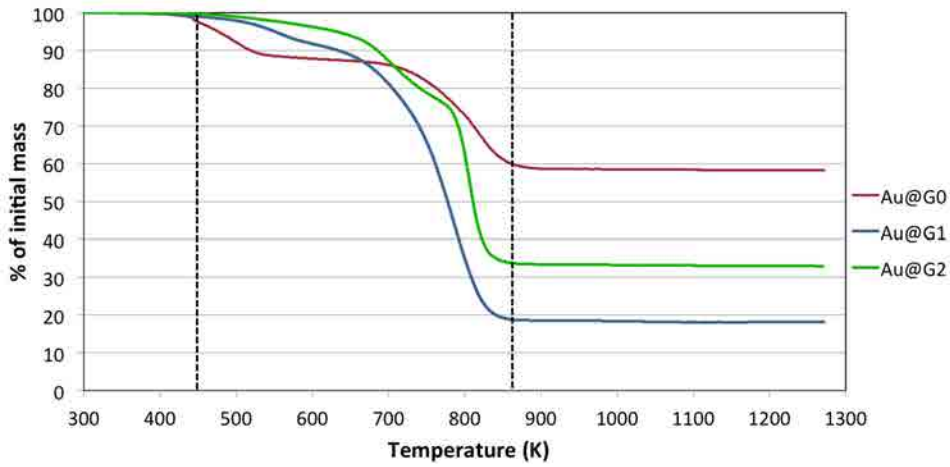

Figure 11.4: Thermogravimetric analyses of Au@G0, Au@G1 and Au@G2.

At temperatures ∼450 K, the samples started to gradually lose the organic shell and at temperatures above 870 K, Au NCDs did not experience any further removal of the organic content.

11.2.3 Thermal stability study

TEM analyses revealed successful synthesis of Au nanoparticles encapsulated in different generations of dendrimers. Thus the studied Au NCDs are suitable for the preparation of nanostructured materials due to size controllability and monodispersity, however whether the Au core under the shell could be made catalytically active, i.e. accessible to reactants and could resist sintering induced by different reactive atmospheres were critical questions, as only Au particles smaller than ∼5 nm are catalytically active (see section **9.3.3**). Therefore, in order to study the preformed Au NPs sintering and monitor the removal of the ligands shell, Au@D and Au@G0 were examined by scanning electron microscopy (SEM), X-ray photoelectron spectroscopy (XPS) and atomic force microscopy (AFM) at the CRnE, UPC. Au@D and Au@G0 were chosen in order to compare the behavior of Au cores protected with dodecanethiol ligands (Au@D), whose use is more spread, with Au cores encapsulated in carbosilane dendrons (Au@G0), which contained Si atoms and haven't been used to stabilize Au cores prior to the publication of [252].

11.2.3.a Scanning electron microscopy characterization

Four samples of Au@D and Au@G0 were prepared by dropcasting: one drop of the toluene solution containing Au@D or Au@G0 was cast over four sloping thermally oxidized Si wafers provided with a SiO_2 layer on its surface. Then, the coated Si wafers were annealed inside the muffle in pairs of Au@D and Au@G0 at 353 K, 773 K, 973 K and 1173 K for 30 minutes. After each oxidation treatment, the samples were examined by SEM. The sequence of SEM images of the Au@D samples is shown in figure **11.5** and the images shown in figure **11.6** correspond to the Au@G0 samples. The particle size distribution of both Au@D and Au@G0 was calculated after each annealing treatment and the results obtained are shown in table **11.2**.

Table 11.2: Particle size distribution determined by SEM after the annealing treatments performed on Au@D and Au@G0 samples.

Annealing temperature (K)	Au@D	Au@G0
773	17 ± 5 nm	9 ± 3 nm
973	18 ± 4 nm	9 ± 3 nm
1173	29 ± 10 nm	22 ± 3 nm

After the first annealing at low temperature (353 K), both Au@D and Au@G0 exhibited a very similar arrangement forming a neuronal-type network structure, indicating that the protecting dendrimers shells had controlled the interparticle distance. The high carbon content still present in both samples after the low temperature oxidation did not allow to measure the particles' diameters.

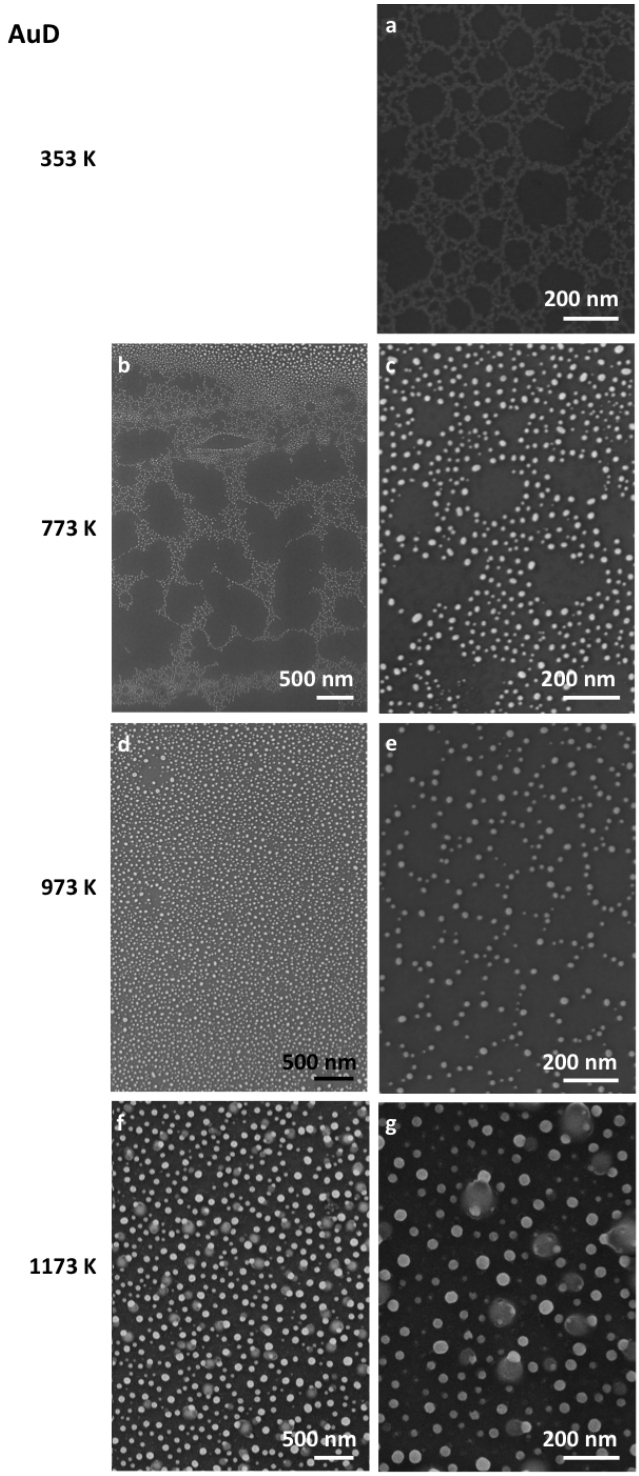

Figure 11.5: Sequence of SEM images of Au@D after the stepwise annealing.

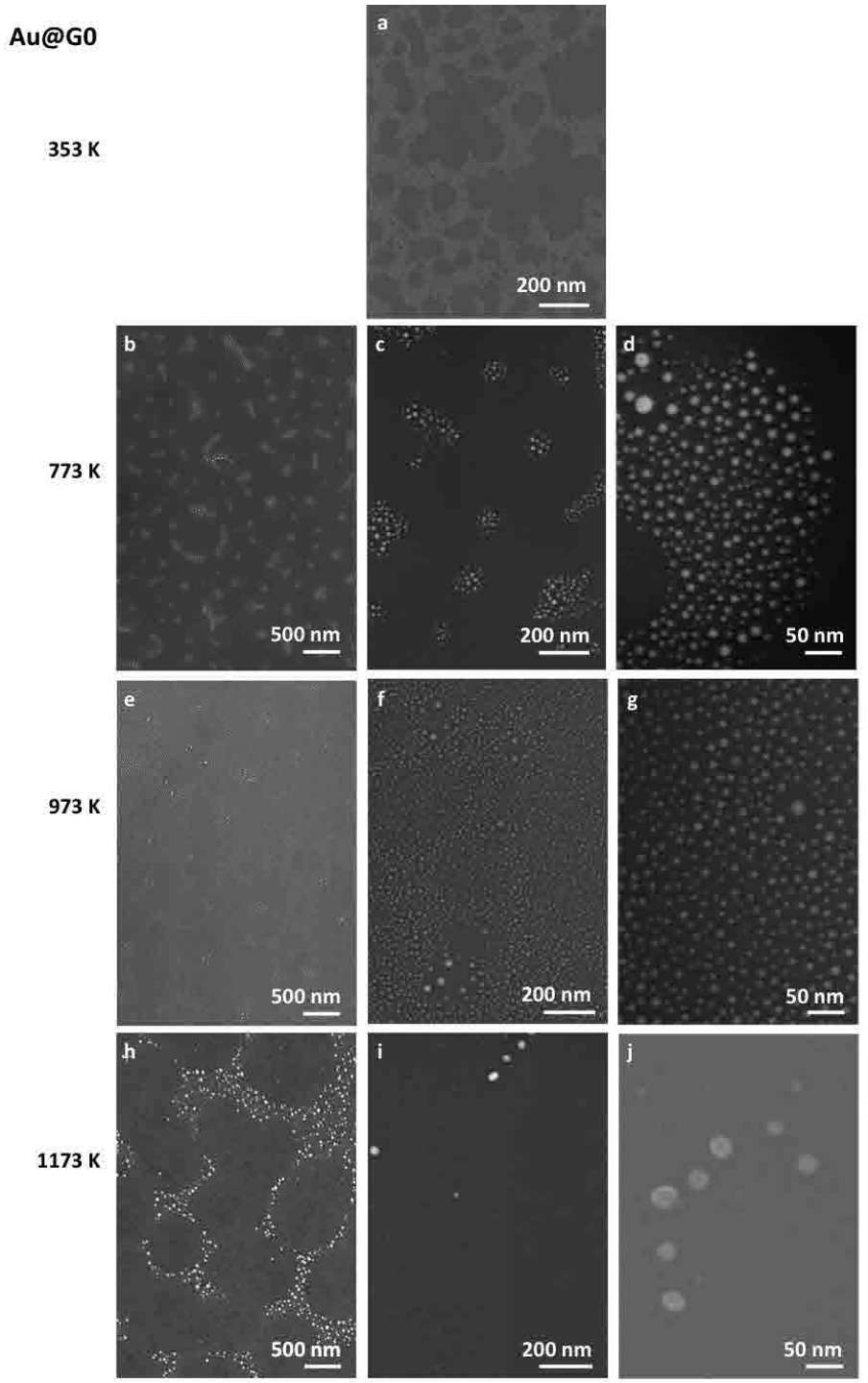

Figure 11.6: Sequence of SEM images of Au@G0 after the stepwise annealing.

The subsequent calcinations at 773 K and 973 K, led to the sintering of both encapsulated Au NPs, but to different degrees. The mean particle size of the Au@G0 after the annealing treatments at 773 K and 973 K was 9.0 nm and 9.2 nm, respectively; and that of Au@D was 17.2 nm and 18.1 nm, respectively.

Therefore, the first differences between both encapsulating systems arose, as the Au cores protected with G0 dendrimers were prevented from the larger agglomeration exhibited by Au@D. The last calcination at 1173 K caused Au@D strong sintering and the mean diameter increased up to 29.1 nm. The same trend was observed for Au@G0, which also sintered after the high temperature annealing, however Au@G0 experienced a milder sintering and their mean diameter was 22.1 nm. After the annealing at 1173 K, only Au@G0 maintained the initial neuronal-type network identified, as observed in figure **11.6**h, indicating that trimethylsilane dendrimers avoided, to some extent, Au@G0 movement under high temperature oxidation conditions as the Au NCDs remained at the same position after annealing. This behavior was not observed for Au@D, as seen in the sequence of images shown in figure **11.5**, and could be one of the reasons why Au@D experienced a stronger sintering. Therefore, the novel carbosilane dendrimers employed to encapsulate Au cores led to the synthesis of Au NCDs with high thermal stability.

11.2.3.b Atomic force microscopy characterization

The thermal stability investigation was completed with AFM studies. Atomic force microscopes are not only sensitive to the position of the Au cores, but also to that of the organic shells and, therefore, AFM measurements allowed for imaging the position of the Au cores and of the protecting dendrimers[1]. Also, AFM has subnanometer resolution on z-axis, which allowed for measuring the particles height with less than 1 nm error. As a result, Au cores smaller than 5 nm surrounded by organic shells, which are below the SEM detection limit, can be imaged by AFM and thus a realistic and more accurate particle size distribution can be obtained. In this study, a Veeco Dimension microscope was used and operated at ambient conditions in dynamic mode (the same tip was used for all measurements).

The topographic AFM measurements and image interpretation were performed at CRnE (UPC) by César Moreno [256]. Au@G0 NPs were placed onto the same oxidized Si wafers and also onto a $SrTiO_3$ (STO) single crystal by dropcasting, following the same procedure described above for the SEM study. All the samples prepared were exposed to annealing treatments at 353 K, 723 K, 823 K, 973 K and 1173 K for 30 minutes and their corresponding AFM images are shown in figures **11.7**a to **11.7**e, respectively. The cellular network structure identified on the SEM images (see figure **11.6**) was also seen by AFM and it was maintained after all the

[1]SEM is only sensitive to the position of the Au cores and the dendrimers can not be imaged.

calcinations performed, as clearly seen in figures 11.7a to 11.7d. After each calcination, the dendrimers were gradually removed, being almost completely removed after the annealing at 1173 K, which left exposed the Au cores. AFM topographic measurements concluded that after the annealing treatment at 1173 K, about 95% were monodisperse Au NPs of ∼2-3 nm, while the other ∼5% of the Au cores sintered and their size was in the range 4-30 nm. A representative profile of the sample calcined at 1173 K scanning two Au cores (acquired between the arrows shown in figure 11.7e) is plotted in figure 11.7f. As seen in the profile, the height of the scanned Au cores was ∼2.5 nm. Therefore, the SEM analyses overestimated the particle size of the calcined Au@G0, probably because the smallest AuNPs could not be detected with this technique.

Deposition of Au@G0 NPs on a STO single crystal led to similar results and, as previously observed for Au@G0 supported on SiO_2, trimethylsilane ligands were progressively removed. Figure 11.7h shows a representative AFM topographic image acquired after the calcination at 1173 K. In this image, the STO terraces can be distinguished with the naked Au cores arranged along them. Figure 11.7g shows the profile acquired between the arrows in figure 11.7h. In this case, the Au NPs ranged from 5 to 7 nm.

For comparison purposes, Au cores encapsulated in dodecanethiol ligands (Au@D) deposited on SiO_2 were studied by AFM, too. After the first low temperature oxidation at 353 K, Au@D exhibited again the cellular network arrangement (see figure 11.7i). After the subsequent annealing at 723 K, the organic shell was removed and Au cores strongly sintered as seen in figure 11.7j, which is in agreement with the SEM observations, where a large Au NPs sintering was detected after calcination at 773 K. Figure 11.7k shows the Au NPs average height with its statistical error as a function of the annealing temperature. $Au@G0//SiO_2$ results indicated that the average Au@G0 height of most particles was nearly constant up to 823 K, while a slight decrease was observed at 973 K due to the removal of the dendrimers shell, which is in agreement with the results of the TGA analysis (see figure 11.4). For Au@G0 supported on $SrTiO_3$ a similar behavior was observed, indicating that the substrate had no influence on the rearrangement and sintering processes of Au@G0. In contrast, Au@D experienced an important increase on their average height after the calcination at 723 K and strongly sintered after the annealing at 1173 K. Therefore, Au@G0 withstood higher temperatures than Au@D maintaining their original size and only ∼5% of Au@G0 formed aggregates of 4-30 nm after calcination at 1173 K. Consequently, Au@G0 appeared attractive as novel encapsulated Au cores that could resist thermal aggregation.

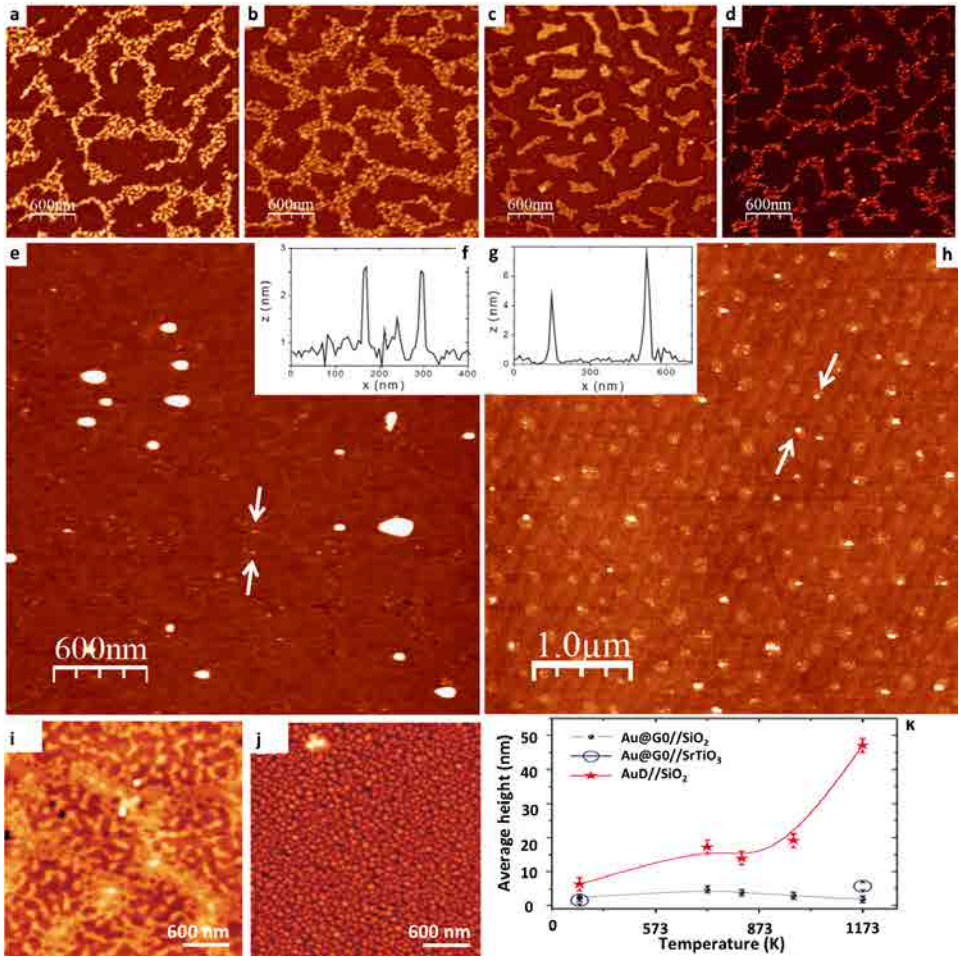

Figure 11.7: Sequence of topographic AFM images of Au@G0 and Au@D after the stepwise annealing. Au@G0//SiO_2 after annealing at: a) 353 K, b) 723 K, c) 823 K, d) 973 K and e) 1173 K. f) Profile acquired between arrows in e). h) Au@G0//$SrTiO_3$ after annealing at 1173 K. g) Profile acquired between arrows in h). Au@D//SiO_2 after annealing at: i) 353 K and j) 1173 K. k) Average height as a function of temperature obtained from topographic images.

11.2.3.c X-ray photoelectron spectroscopy characterization

XPS was performed to monitor the Au/C ratio of the Au cores and the protecting dendrimers shells and to infer the chemical environment of Au nuclei. The XPS equipment located at the CRnE (UPC) described in section **6.2** was used in this study.

An Au@G0 sample was prepared by drop casting the toluene solution onto an STO crystal in order to avoid Si signals originating on the substrate and, thus allowing to distinguish the differences on Si constituting the trimethylsilane ligands.

Before Au@G0 NPs deposition on the STO single crystal, the spectrum of its surface was acquired. Then, Au@G0//STO was oxidized at 353 K for 30 minutes and a spectrum was recorded. In this case, no stepwise annealing was performed, as from AFM measurements small variations were detected at intermediate temperatures and we decided to study directly the sample after calcination at 1173 K. Hence, the sample was removed from the XPS system and calcined into the muffle at 1173 K. This treatment could not be performed *in situ*, because it is not possible to reach 1173 K inside the XPS reaction chamber. Subsequently, the corresponding spectrum was recorded. The results from the deconvolution are listed in table **11.3**.

Table 11.3: XPS results for the Au@G0//STO annealing treatments.

	Relative atomic concentration (%)				
Sample	Si 2p	C 1s	Au 4f	Ti 2p	Sr 3d
STO	0	55.2	0.0	17.4	27.4
Au@G0//STO - 353 K	9.7	65.0	1.1	9.9	14.3
Au@G0//STO - 1173 K	9.9	51.6	0.2	15.7	22.6

Additionally, figure **11.8** shows the Si 2p XP spectra deconvolution after the calcinations at 353 K (figure **11.8**a) and 1173 K (figure **11.8**b). The spectra were calibrated for energy taking into account the position of the Ti $2p_{1/2}$ peak (460.0 eV) [122]. After calcination at 353 K, Si 2p exhibited one component ascribed to carbosilane dendrimers. In contrast, after calcination at 1173 K, Si 2p exhibited an additional component at higher binding energies (102.9 eV), which was ascribed to SiO_2.

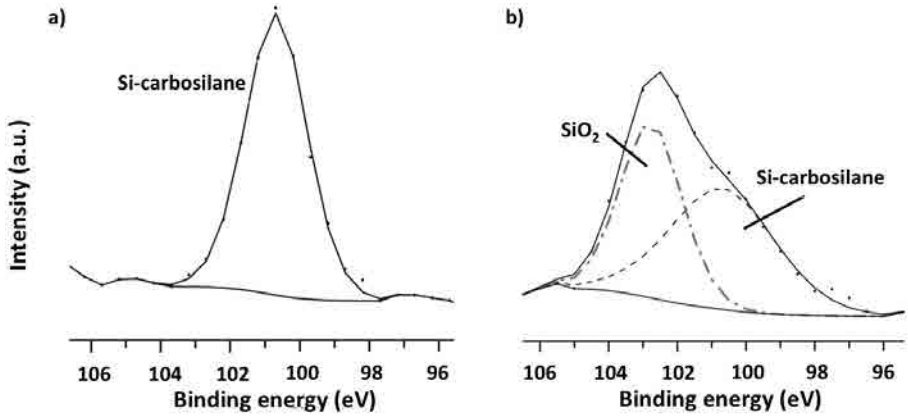

Figure 11.8: Si 2p spectra of Au@G0 NPs after annealing at: a) 353 K and b) 1173 K.

The C/Ti ratio increased from 3.2 to 6.6 after Au@G0 deposition, as expected, and decreased to 3.3 after annealing at 1173 K, which confirmed that the G0 dendrimer was almost completely removed at this calcination temperature. The Si/Ti ratio diminished from 1.0 to 0.6 after the annealing treatments at 353 K and 1173 K, respectively, due to the transformation and agglomeration of the G0 trimethylsilane dendrimer to SiO_2. After the annealing at high temperature, the Au surface relative concentration and the Au/Ti ratio decreased ∼10 times. This reduction could be tentatively ascribed to the mild sintering experienced by the Au cores and also to losses of melted Au, because Au NPs melt at lower temperatures than bulk Au [257].

This study was complemented with STEM analyses of Au@G0 deposited on a Si wafer covered by a SiO_2 layer performed at Oak Ridge National Laboratory by Jaume Gazquez [256]. Annular dark field images allowed to identify a sintered Au NP laying on the SiO_2 substrate, as seen in figure 11.9. Electron energy loss spectra where acquired in the box shown in figure 11.9a, thus obtaining an elemental map of this image, which allowed for the identification of the feature next to the Au NP as SiO_2, confirming the presence of SiO_2 detected by XPS.

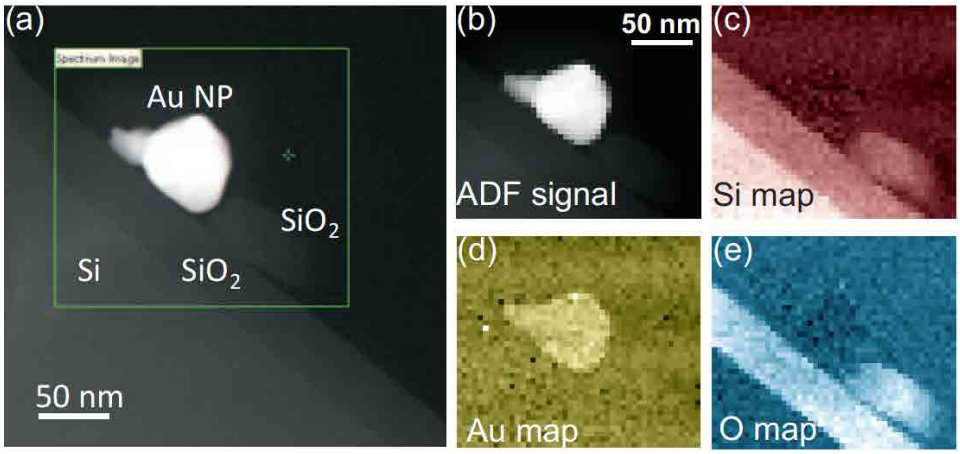

Figure 11.9: Spectrum image of a Au NP after Au@G0//SiO_2 annealing at 1173 K laying on the thermally oxidized Si wafer. a) Low magnification ADF image. The square marks the area where the spectrum image was acquired. b) ADF signal acquired simultaneously with the spectrum image. c), d) and e) are the elemental maps of Si, Au and O, respectively.

These findings allowed to conclude that after calcining at 1173 K the starting Au cores surrounded by trimethylsilane dendrimers, SiO_2 was formed and sat next to Au cores, acting as a pinning center of the resulting Au NPs, consequently immobilizing the naked Au NP and preventing them from sintering. This process is schematically represented in figure 11.10.

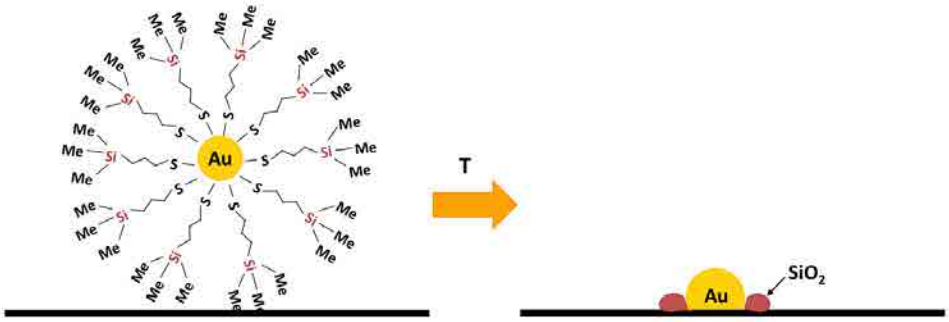

Figure 11.10: Schematic representation of the ligand-assisted pinning mechanism.

Results regarding AFM, STEM and XPS measurements were published in *César Moreno, Núria J. Divins, Jaume Gazquez, Maria Varela, Inma Angurell and Jordi Llorca, "Improved thermal stability of oxide-supported naked gold nanoparticles by ligand-assisted pinning", Nanoscale 4 (2012), pp. 2278* [256].

As Au@G0 NPs showed outstanding thermal stability, NPs protected with dendrimers shells were used to synthesize Au/TiO_2 catalysts for CO-PrOx reaction. These novel Au NPs opened the possibility to calcine them in order to promote the Au-TiO_2 interaction while limiting Au NPs aggregation, which is a critical issue of Au-based catalysts, and also to operate CO-PrOx at high temperature, if required.

11.3 Powdered Au/TiO_2 catalysts

Following the characterization of Au active phases and the TiO_2 support separately, the different types of Au NPs enumerated in Chapter 10, namely Au@G0, Au@G1, Au@G2, Au@D and AuC, were supported on TiO_2, following the synthesis methods aforementioned, and the resulting catalysts were subsequently characterized.

11.3.1 Preformed Au nanoparticles supported on TiO_2

11.3.1.a Transmission electron microscopy characterization

Initially, the microstructure of Au@NCD/TiO_2 catalysts was analyzed by TEM. For TEM characterization, the Au@G1/TiO_2 catalyst was chosen as a representative catalyst of preformed Au NCDs supported on TiO_2. Au@G1 NPs were anchored to powdered anatase and calcined at 673 K for 2 hours.

Representative HRTEM images of 2Au@G1/TiO_2 are shown in figure 11.11. Figure 11.11a shows a low-magnification TEM image of Au@G1 supported on TiO_2. The mean particle size of the identified Au@G1 NPs was 2.5 ± 0.7 nm, which are the

same values found before deposition (see table 11.1). Figure 11.11b shows a representative Au@G1 in close contact with TiO_2, exposing Au (111) crystallographic planes, as measured on its corresponding FT image (figure 11.11c). Au@G1 NPs identified showed lattice fringes at 2.36 Å and 2.04 Å, corresponding to (111) and (200) crystallographic planes of the Au fcc structure, respectively, as measured in the FT images shown in figures 11.11c and 11.11f.

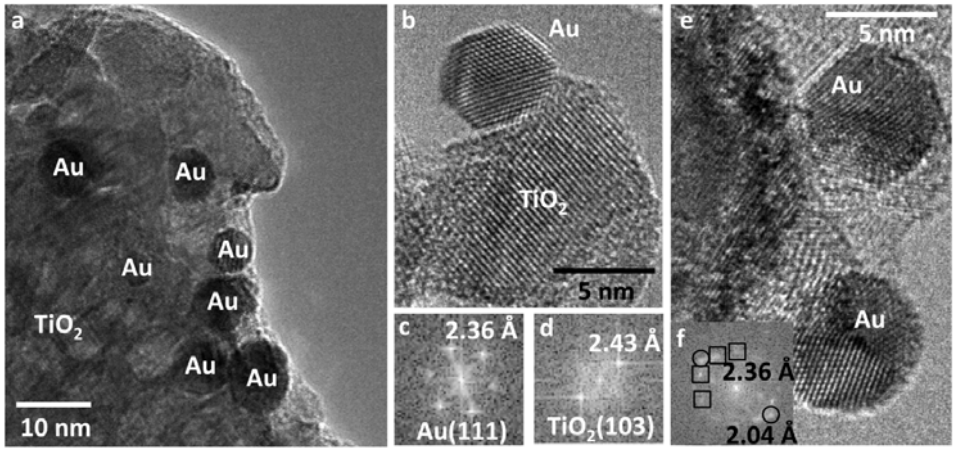

Figure 11.11: HRTEM images of the 2Au@G1/TiO_2 catalyst. a) Low-magnification image. b) Detailed HRTEM image of an individual Au NP anchored to a TiO_2 crystallite. The corresponding FT images are shown in figures c) and d), respectively. e) Detail of two Au@G1 NPs anchored to TiO_2. f) corresponding FT image of the Au NP.

11.3.1.b *In situ* X-ray photoelectron spectroscopy characterization

The ease of removing the protecting organic shells of Au@D, Au@G1 and Au@G2 NPs supported on TiO_2 was monitored by XPS. The samples were prepared by coating thermally oxidized Si wafers with TiO_2 anatase synthesized from Ti^{IV} isopropoxide, as previously reported (see section 10.1). Once the TiO_2 layers were developed, Au@D, Au@G1 and Au@G2 were deposited. The sequence of *in situ* XPS analyses performed on the three catalysts was: 1) catalyst as prepared and thermal treatments at 2) 398 K, 3) 523 K, 4) 598 K, 5) 673 K and 6) 773 K. In this case, the Si wafers coated with the investigated catalysts were thermally treated directly inside the analysis chamber under ultrahigh vacuum (UHV) conditions. Table 11.4 lists the Au/C atomic ratio calculated at each temperature for these experiments.

As a general trend, after each annealing treatment, the Au/C ratio increased following the sequence Au@G2/TiO_2 < Au@G1/TiO_2 < Au@D/TiO_2, as expected. On the other hand, the Au/C ratio progressively increased up to 673 K for the three samples, indicating that the ligands shells were progressively removed at in-

Table 11.4: XPS results for $Au@D/TiO_2$, $Au@G1/TiO_2$ and $Au@G2/TiO_2$ annealing treatments.

	Au/C atomic ratio (%)		
Annealing temperature (K)	$Au@D/TiO_2$	$Au@G1/TiO_2$	$Au@G2/TiO_2$
1. 298	25.6	6.8	0.6
2. 398	44.8	7.9	2.6
3. 523	43.5	9.5	5.1
4. 598	40.0	12.5	9.1
5. 673	41.9	17.9	10.4
6. 773	41.0	13.8	8.1

creasing temperatures. However, at 773 K the Au/C ratio diminished, indicating that the Au surface signal decreased which suggested that at this T mild Au NPs sintering occurred. These results showed that the mass of organic ligand lost at each temperature was similar for Au@G1 and Au@G2 NPs; whereas the loss of dodecanethiol ligands was remarkably higher. As previously deduced from AFM results, dodecanethiol ligands were more easily eliminated than G1 and G2 dendrons. Finally, at 773 K, a large quantity of C still remained on the surface of the three samples. This was due to the absence of a gas stream able to eliminate the residues, as these treatments were directly performed in the analysis chamber under UHV conditions. As a consequence, in these static experiments, where the residues were only partially eliminated by the vacuum, the absolute values were not significant, and only the comparison of the trends of the three samples is meaningful. The spectra were calibrated for energy taking into account the position of the adventitious C 1s signal at 284.8 eV. In all cases, the BE of Au 4d photoelectrons were recorded at 334.8 eV and 352.8 eV, which corresponded to metallic Au.

11.3.2 Conventional Au nanoparticles supported on TiO_2

The microstructure of a $2\%AuC/TiO_2$ powdered catalyst was analyzed by TEM as synthesized, i.e. after the calcination at 673 K of the synthesis procedure. Figure 11.12a shows a low-magnification TEM image of a region of the AuC/TiO_2 catalyst. The detail of an Au NP in close contact with TiO_2 is shown in figures 11.12b, 11.12c and 11.12d. The inset in figure 11.12b shows the FT image corresponding to the identified Au NP. The FT image exhibited spots at 2.04 Å, which were ascribed to (200) planes of the Au fcc structure, forming a 90-degree angle, indicating that the Au NP was oriented along the [100] axis. The HRTEM micrograph shown in figure 11.12c shows the detail of an Au NP exhibiting lattice fringes at 2.36 Å, which were ascribed to (111) planes of the Au fcc structure. The mean particle size determined by TEM analyses was 3.6 ± 1.0 nm.

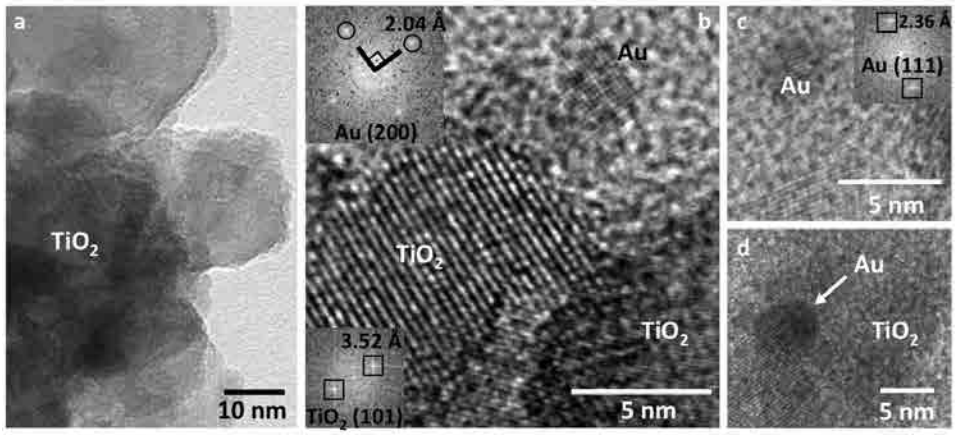

Figure 11.12: HRTEM images of the AuC/TiO_2 catalyst. a) Low-magnification image. b) Detailed HRTEM image of an individual Au NP anchored to TiO_2. The inset shows the corresponding FT images. c) and d) Detail of two AuC NPs anchored to TiO_2.

11.3.3 Functionalized monoliths

The titania coating developed over the cordierite channels of a Au@G2/TiO_2//Mon was examined by SEM. The functionalized monolith was longitudinally cut, as previously performed on section 4.4, and cut again perpendicularly to the channel's direction. In order to perform the cross-sectional cut of the channels, the monolith was embedded in a resin from BUEHLER©. After an aging process at 310 K for 2 hours, the resin harden and it was possible to polish the embedded Au@G2/TiO_2//Mon perpendicularly to its channels. Figure 11.13 shows the SEM images obtained.

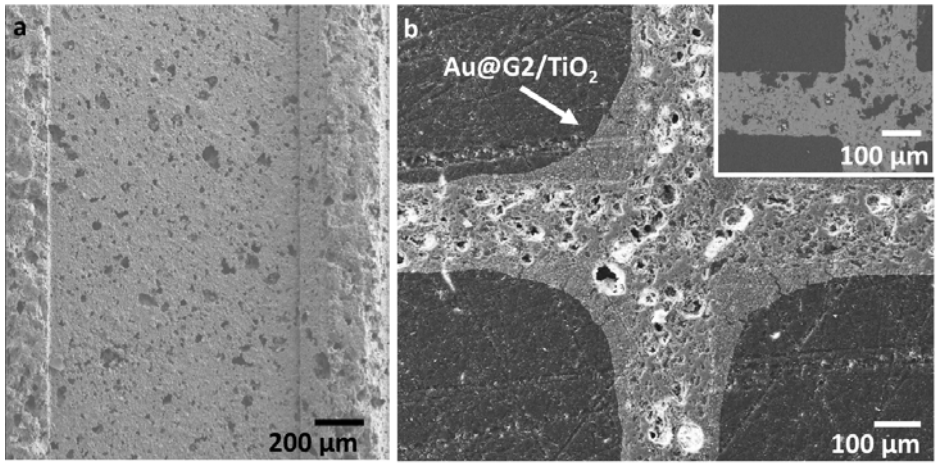

Figure 11.13: SEM images of the Au@G2/TiO_2//Mon. a) Longitudinal view of a channel. b) Cross-section of the embedded monolith.

Figure **11.13**a shows the detail of a coated channel with a homogeneous TiO_2 layer that completely covered the cordierite channels. The subjacent cordierite pores were still visible. Figure **11.13**b shows the cross section view of the Au@G2/TiO_2//Mon. On the channels' corners, the TiO_2 layer accumulated, as expected, but then it was uniformly distributed along the channels. In order to make easier the TiO_2 coating identification in the cross section view, the inset in figure **11.13**b shows a corner of an embedded cordierite monolith without coating. Comparing both images, the TiO_2 layers accumulated on the channels' corners are clearly distinguishable.

12 CO PREFERENTIAL OXIDATION CATALYTIC TESTS

12.1 Reaction setup

CO preferential oxidation catalytic tests were performed in the lab-scale setup schematically represented in figure 12.1. The functionalized monoliths were fitted in a tubular stainless steel reactor (21 mm internal diameter). The reactor was then placed inside a tubular electric furnace (Carbolite) governed with a PID electronic controller (Fuji PXR4). The reaction performance of the developed catalysts was evaluated for three gaseous inlet mixtures containing CO and O_2 at fixed molar ratio and different concentrations of H_2 balanced in Ar, as listed in table 12.1.

Table 12.1: Inlet mixtures composition.

	Concentration (%)			
Mixture	CO	O_2	H_2	Ar
A	2	2	0	96
B	2	2	2	94
C	2	2	50	46

The inlet mixtures were provided by independent mass flow controllers (M+W Instruments) and were introduced into the reactor at atmospheric pressure. The total inlet flow was fixed at 100 mL/min for the three mixtures. Experiments performed with mixture A, which did not contain H_2, corresponded to CO total oxidation (TOX) tests; whereas mixture C contained 50% H_2, representing a realistic amount of the H_2 present in a reformate stream. The O_2/CO molar ratio was fixed at 1 for all mixtures, as it has been previously reported that this could be an optimum value balancing CO oxidation activity and selectivity [258]. CO levels in the off-gas of WGS reactors typically lie between 0.5 and 2 vol.% and, accordingly,

CO concentration in our experiments was fixed at its upper limit (2%), representing the most unfavorable situation. The effect of H_2O and CO_2 was not tested in these experiments.

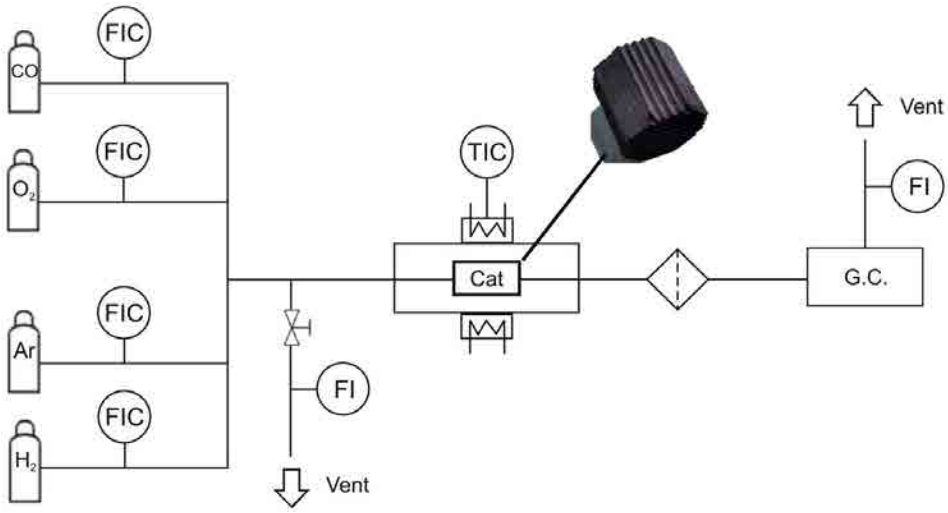

Figure 12.1: Schematic representation of the experimental setup.

Reaction products were analyzed online every 5 minutes with an Agilent 3000A gas micro-chromatograph equipped with MS 5Å, Plot U and Stabilwax capillary columns and TCD detectors. Three to six measurements were acquired at each operation condition once the steady-state was achieved.

12.2 Catalytic screening of $Au/TiO_2//Mon$ catalysts

The catalytic activity of cordierite monoliths coated with Au/TiO_2 catalysts synthesized using ligands-stabilized Au NPs or the conventional $HAuCl_4$ precursor (AuC/TiO_2) was systematically evaluated. The inlet mixtures were introduced into the reactor following the sequence B, A, C at the increasing temperatures 363 K, 398 K, 433 K and 473 K, in this order. The contact time of these experiments at standard temperature and pressure was τ=2.75 s and the gas hourly space velocity GHSV=$1.3{\cdot}10^3$ h^{-1}. Table 12.2 summarizes the experimental conditions evaluated.

The reaction performance evaluation of $Au/TiO_2//Mon$ catalysts is discussed in terms of CO conversion (χ_{CO}, equation 12.2), O_2 conversion (χ_{O_2}, equation 12.3) and selectivity to CO oxidation or selectivity to CO_2 (S_{CO_2}, equation 12.4).

Table 12.2: Experimental conditions tested.

Temperature (K)	363, 398, 433, 473
Absolute pressure (bar)	1
Inlet mixture (100 mL/min)	A, B, C
GHSV (h^{-1})	$1.3{\cdot}10^3$
O_2/CO molar ratio	1, λ=2 (equation 12.1)

$$\lambda = 2\,\frac{\dot{n}_{O_2,in}}{\dot{n}_{CO,in}} = 2 \tag{12.1}$$

$$\chi_{CO} = \frac{\dot{n}_{CO,in} - \dot{n}_{CO,out}}{\dot{n}_{CO,in}} \cdot 100, \quad \text{where } [\dot{n}] = \frac{mol}{s} \tag{12.2}$$

$$\chi_{O_2} = \frac{\dot{n}_{O_2,in} - \dot{n}_{O_2,out}}{\dot{n}_{O_2,in}} \cdot 100 \tag{12.3}$$

$$S_{CO_2} = \frac{\dot{n}_{CO,in} - \dot{n}_{CO,out}}{(\dot{n}_{CO,in} - \dot{n}_{CO,out}) + (\dot{n}_{H_2,in} - \dot{n}_{H_2,out})} \cdot 100 \tag{12.4}$$

12.2.1 Au@D/TiO_2//Mon

The first experiments were carried out with an Au@D/TiO_2//Mon loaded with 0.194 g of 2Au@D/TiO_2, representing a catalyst loading of 1.9 $mg_{catalyst}/cm^2$. The weight hourly space velocity (WHSV) of these experiments was 32 $L/(h{\cdot}g_{catalyst})$. Catalytic tests were directly performed over the as-synthesized Au@D/TiO_2//Mon, i.e. without calcination after Au@D NPs deposition on the anatase coating. Mixture B was directly introduced into the reactor at 363 K. At these reaction conditions the catalyst exhibited poor catalytic activity, as CO conversion was lower than 1%. Hence, the reaction temperature was increased to 473 K (5 K/min) in order to favor CO and H_2 oxidation reactions. At this temperature, the catalyst exhibited full CO conversion and selectivity to CO conversion ~48%. After 1 hour under these reactions conditions, the reaction temperature was lowered to 363 K and CO conversion only decreased to χ_{CO}=97.3%, while selectivity to CO conversion increased up to S_{CO_2}=76%, indicating that the presence of mixture B at 473 K had a positive effect on the catalyst by creating active sites. The beneficial effect of H_2 in Au/TiO_2 catalysts for CO removal has been widely reported in the literature [259, 260]. Maintaining the reaction temperature at 363 K, the inlet mixture was switched to mixture A and all the CO present was consumed. Finally, the effect of high H_2 concentration was evaluated and mixture C was dosed. The catalyst converted ~65% of the CO present while H_2 concentration in the outlet stream diminished from 50% to 47.4%, representing a selectivity to CO_2 ~30%.

After this reaction cycle at 363 K, the reaction temperature was increased to 398 K and the catalytic activity for mixtures B, A and C was investigated. This sequence was repeated at 433 K and 473 K.

Following this study, the catalyst was oxidized (20% O_2 balanced in N_2) at 573 K for 1 hour. Then, the aforementioned reaction cycles were repeated: the catalyst's performance for mixtures B, A and C was tested at 363 K, 398 K, 433 K and 473 K. Once the second reaction cycle was finished, the catalyst was subjected to a new oxidation at 673 K for 1 hour and the catalytic tests were performed again. The process finished with an oxidation at 773 K followed by the sequence of catalytic tests. Figure 12.2 summarizes the chronological sequence of catalytic tests and oxidation treatments performed over the Au@D/TiO_2//Mon. The results of the catalytic tests performed with mixtures B, A and C, comprising CO conversion (χ_{CO}), O_2 conversion (χ_{O_2}) and selectivity to CO oxidation (S_{CO_2}), are compiled for each mixture in figures 12.3, 12.4 and 12.5, respectively.

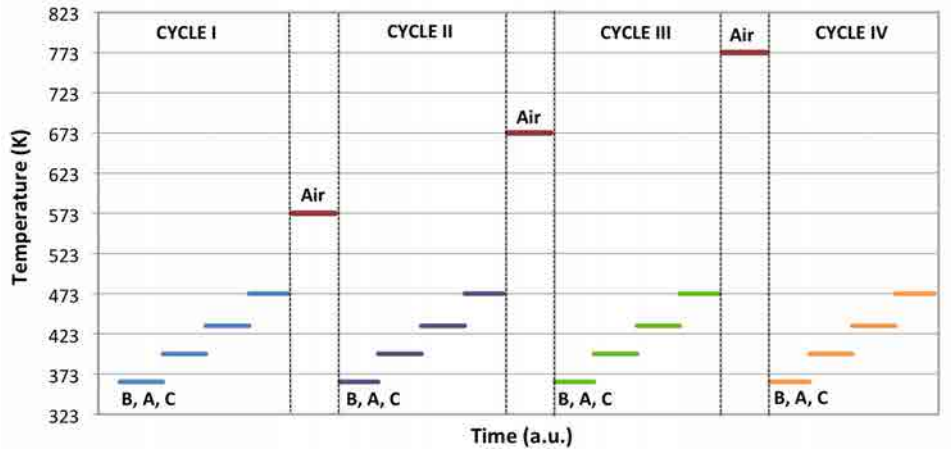

Figure 12.2: Sequence of experimental conditions tested and oxidations performed.

The catalyst was subjected to stepwise oxidations after each reaction cycle in order to elucidate the best combination of activation treatments. As reported in the preceding Chapter, the dodecanethiol shell was gradually removed at increasing temperature, being almost completely removed at 673 K (see table 11.4) and leaving exposed the Au core, which, in principle, made the Au NP accessible to reactants. However other important factors may influence the catalyst's behavior, such as the particle size or the formation of a Au-TiO_2 interface and, precisely for this reason, the catalyst's activity was checked after each oxidation performed.

Results presented in figures 12.3 and 12.5 clearly show that oxidation at 773 K resulted in enhanced catalytic activity in terms of selectivity to CO oxidation for mixture B and in enhanced CO conversion and selectivity to CO_2 for mixture C,

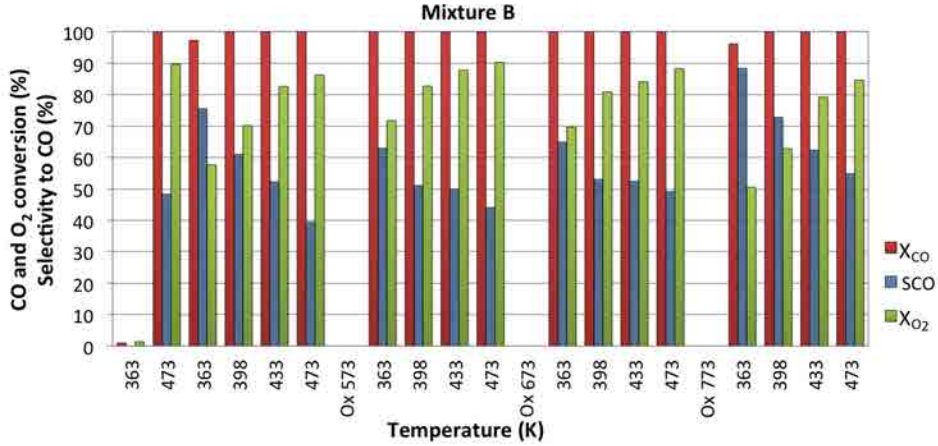

Figure 12.3: Catalytic results of Au@D/TiO_2//Mon for mixture B experiments.

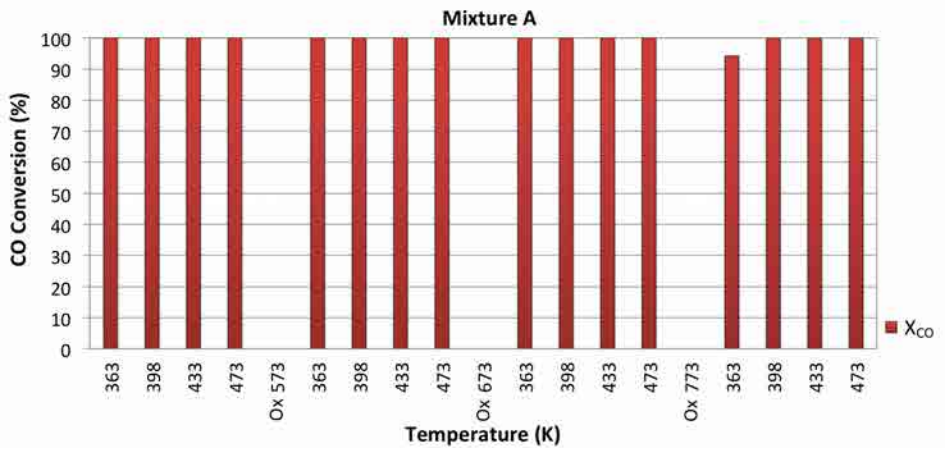

Figure 12.4: Catalytic results of Au@D/TiO_2//Mon for mixture A experiments.

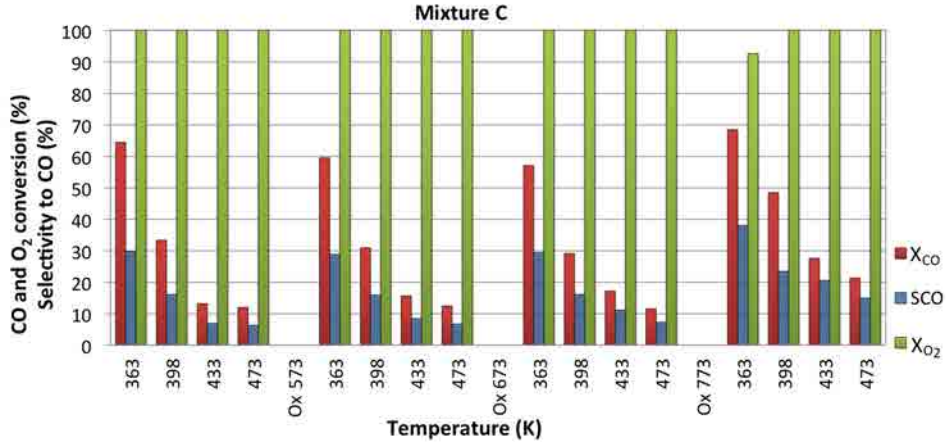

Figure 12.5: Catalytic results of Au@D/TiO_2//Mon for mixture C experiments.

respectively. This behavior may be ascribed not only to the removal of the dodecanethiol shell, but also to the formation of a stronger interaction between Au and TiO_2. As deduced from XPS results (see table **11.4**), the organic shell was removed after the oxidation at 673 K. However, the catalyst exhibited superior activity after the oxidation at 773 K than after the one at 673 K, in spite of the slight increase in particle size, also inferred from XPS. This suggested that the better catalytic performance is likely related to a specific architecture of the Au-TiO_2 contact area, as it has been previously reported that CO oxidation occurs at the perimeter sites of the Au-TiO_2 interface [243, 261]. After the high temperature oxidation, for mixture B experiments, the catalyst exhibited at 363 K ca. 96% CO conversion with 88% selectivity, resulting in an outlet stream composition of 1.49% H_2 and 0.08 % CO (800 ppm). At 398 K, 433 K and 473 K, complete CO oxidation was attained (CO concentration <5 ppm), nevertheless selectivity to CO oxidation progressively decreased at increasing temperature, demonstrating that H_2 oxidation was enhanced at higher temperature, as previously reported [262, 263]. Even so, at high reaction temperature, not all the O_2 supplied was consumed, as seen in figure **12.3**. At 398 K, the lowest temperature at which 100% CO conversion was attained and, consequently, with highest selectivity to CO oxidation (S_{CO_2}=73%), the outlet stream still contained 0.96% of H_2. These values represented better CO-PrOx activity than the ones reported in other works for Au/TiO_2 catalysts and collected in reviews by Lakshmanan et al. [242] and Bion et al. [205].

Concerning CO total oxidation experiments (corresponding to the tests performed with mixture A, figure **12.4**), the catalyst exhibited full CO conversion for all the conditions tested, except for the experiment performed at 363 K after the oxidation at 773 K, at which χ_{CO}=94%.

As regards mixture C experiments, the oxidations also improved the catalyst's performance and the best CO-PrOx activity was recorded again after the oxidation at 773 K. As seen in figure **12.5**, at 363 K the catalyst attained its highest CO conversion and selectivity to CO_2, χ_{CO}=68% and S_{CO_2}=38%, while ∼2% H_2 was oxidized. This resulted in an O_2 conversion of 93%, however for the rest of mixture C experiments, all the O_2 dosed was consumed. Hydrogen oxidation followed the previously observed trend and at higher temperatures, higher H_2 conversions were recorded. This led to a reduction of CO conversion at increasing temperatures, as both CO and H_2 oxidation reactions competed for O_2. As a consequence, the highest CO conversions for mixture C experiments were attained at the lowest temperature tested (363 K), where CO conversion was promoted at the expense of H_2 conversion.

Comparing the catalytic performance for mixtures B and C, it can be concluded that, while dosing mixture B at 473 K had a positive effect on the catalyst activity

improving CO conversion, the presence of 50% H_2 in the inlet was detrimental to CO conversion, as O_2 mainly oxidized H_2. The direct comparison of the catalytic performance of $Au@D/TiO_2$//Mon with the one attained by other catalysts reported in the open literature is hardly attainable due to the differences in reaction conditions tested, Au metal loading and catalysts' properties. Nevertheless, in Rossignol et al. [262], the reaction conditions tested were very similar to ours (1.47% Au loading and reaction mixture composition 2% CO, 2% O_2, 48% H_2 balanced in He). Under these reaction conditions, their best Au/TiO_2 catalyst showed its maximum CO conversion χ_{CO}∼60% at 469 K with a S_{CO_2}∼38%. The reported values were very close to the ones exhibited by our $Au@D/TiO_2$//Mon, but at lower temperature (363 K).

12.2.2 Au@NCD/TiO_2//Mon catalysts

The catalytic performance of $Au@G0/TiO_2$, $Au@G1/TiO_2$ and $Au@G2/TiO_2$ supported on cordierite monoliths was investigated following exactly the same procedure as for the $Au@D/TiO_2$//Mon and the reaction cycles shown in figure 12.2.

12.2.2.a Au@G0/TiO_2//Mon

The first catalytic tests of dendrimer-based Au/TiO_2 catalysts were performed over an $Au@G0/TiO_2$//Mon as-synthesized (loaded with 0.198 g of $2Au@G0/TiO_2$ catalyst). The corresponding WHSV of these experiments was 30 $L/(h{\cdot}g_{catalyst})$. The functionalized monolith was directly activated by dosing mixture B at 473 K. As seen in figure 12.6, under these reaction conditions, the $Au@G0/TiO_2$//Mon exhibited full CO conversion accompanied by a selectivity to CO oxidation of 60%, which was superior to that attained by $Au@D/TiO_2$//Mon at the same temperature (compare with figure 12.3). In contrast to the operation of the $Au@D/TiO_2$//Mon, the $Au@G0/TiO_2$//Mon only reached complete CO conversion at the highest reaction temperature (473 K), however larger selectivities to CO oxidation were achieved. At 433 K, CO was almost completely oxidized (χ_{CO}=97%, i.e. 540 ppm of CO were still present on the outlet stream) and selectivity to CO_2 increased up to S_{CO_2}=73%. As expected, the downward trend observed on selectivity to CO_2 as the reaction temperature increased was also observed for these experiments.

For this catalyst, the oxidation at 673 K was detrimental to the catalytic performance and resulted in lower CO conversion. Furthermore, after the final oxidation at 773 K, the catalytic activity was depleted. In clear contrast with the catalytic behavior exhibited by the $Au@D/TiO_2$//Mon, the oxidation treatments of $Au@G0/TiO_2$//Mon at high temperature (673 K and 773 K) had a marked negative effect on the catalyst's performance. This was a surprising result given that

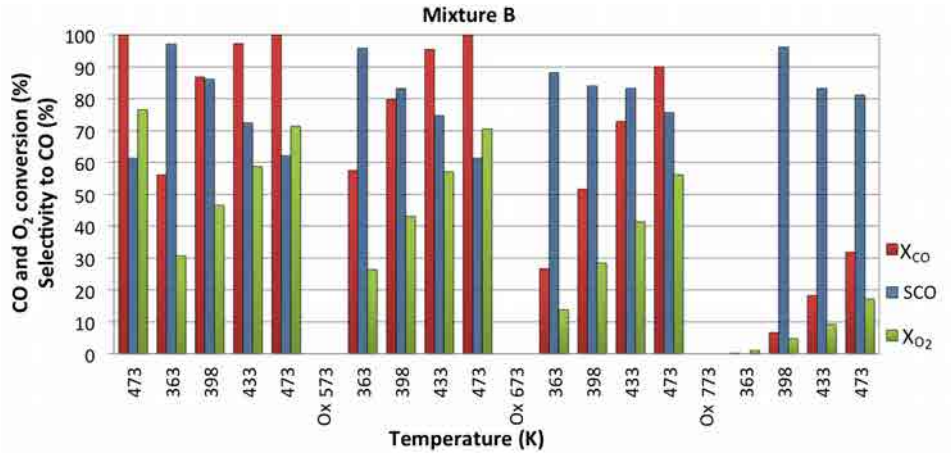

Figure 12.6: Catalytic results of Au@G0/TiO_2//Mon for mixture B experiments.

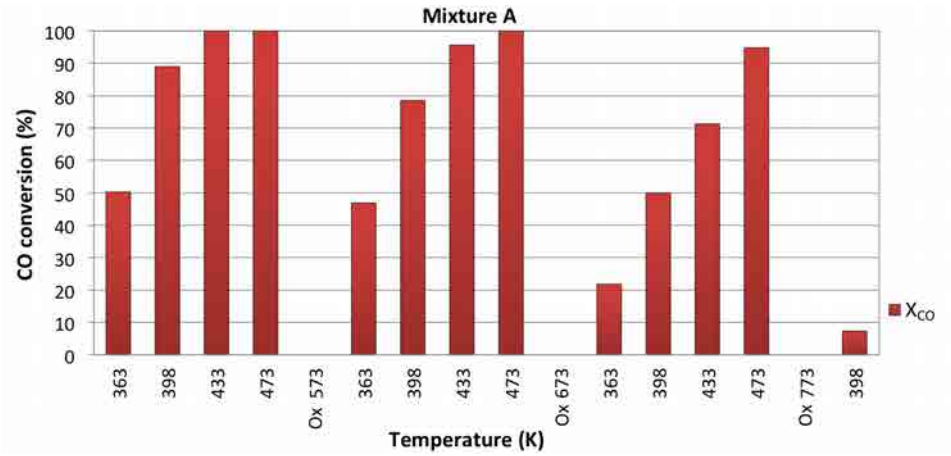

Figure 12.7: Catalytic results of Au@G0/TiO_2//Mon for mixture A experiments.

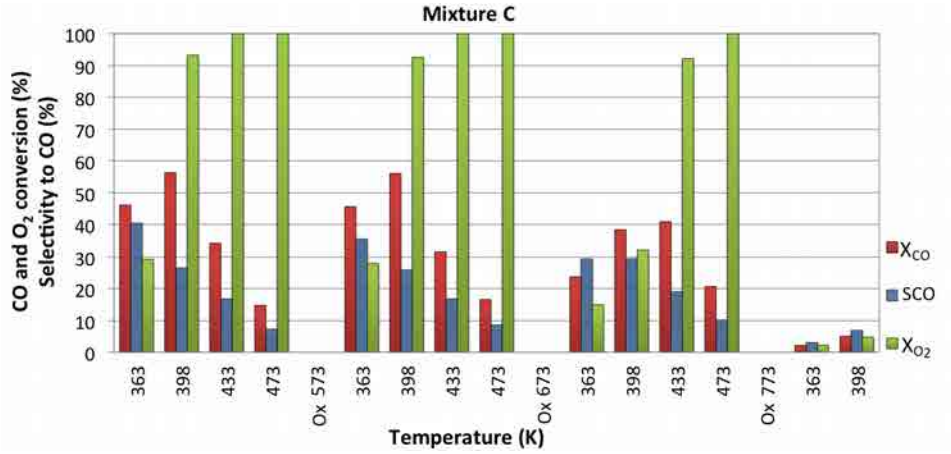

Figure 12.8: Catalytic results of Au@G0/TiO_2//Mon for mixture C experiments.

unsupported Au@G0 NPs showed better thermal stability and resisted particle aggregation at higher temperatures than Au@D NPs, as deduced from the results of the thermal stability study (see section **11.2.3**). This catalytic behavior indicated that while the presence of carbosilane dendrimers residues (produced during the oxidations) served as pinning centers of Au cores and prevented them from large sintering, their presence surrounding the Au nuclei was detrimental to the catalytic activity. This effect could be ascribed to a weaker Au-TiO_2 interaction or to a hindering of the reactants' access to the Au-TiO_2 perimeter sites.

Results regarding CO total oxidation (mixture A experiments) are reported in figure **12.7**. Conversely to the catalytic performance of the $Au@D/TiO_2//Mon$, $Au@G0/TiO_2//Mon$ only attained complete CO oxidation at 433 K and 473 K after the activation treatment and at 473 K after oxidation at 573 K. The activity depletion observed for mixture B experiments after the high temperature oxidations was also clearly observed for these tests. As shown in figure **12.8**, under large H_2 concentration, the $Au@G0/TiO_2//Mon$ exhibited the highest CO conversions ($\sim$50%) only in the low temperature range 363-398 K, but with higher selectivity to CO oxidation than the $Au@D/TiO_2//Mon$.

The catalytic performance examination of Au@D- and Au@G0-based catalysts revealed that, in spite of the lower thermal stability of Au@D NPs, they were more active under mixture B conditions and only slightly superior for mixture C, demonstrating that not only the particle size plays an important role on Au-based catalysts, but other factors such as the chemical environment or the Au-TiO_2 architecture can determine their catalytic activity.

12.2.2.b $Au@G1/TiO_2//Mon$

The catalytic screening tests of $Au@G1/TiO_2//Mon$ yielded a very similar catalytic performance to that of $Au@G0/TiO_2//Mon$ for mixtures A (figure not shown) and B under nearly the same space velocity (WHSV=32 $L/(h{\cdot}g_{catalyst})$). Figure **12.9** reports CO and O_2 conversions and selectivity to CO oxidation for mixture B experiments; where complete CO conversion was again achieved solely at 473 K. The best CO-PrOx activity in terms of full CO conversion accompanied by a high selectivity to CO oxidation were obtained after the oxidation at 573 K, where S_{CO_2}=65%. The oxidation treatments at the highest temperatures (673 K and 773 K) also caused a reduction of the catalytic performance, although it was better than that attained by $Au@G0/TiO_2//Mon$ after the same oxidations. However, the effect of 50% H_2 in the inlet caused a dramatic diminution of CO oxidation, as seen in figure **12.10**.

For mixture C experiments only the tests performed at 363 K and 473 K are reported, as the best CO-PrOx performance was achieved at 363 K. The maximum

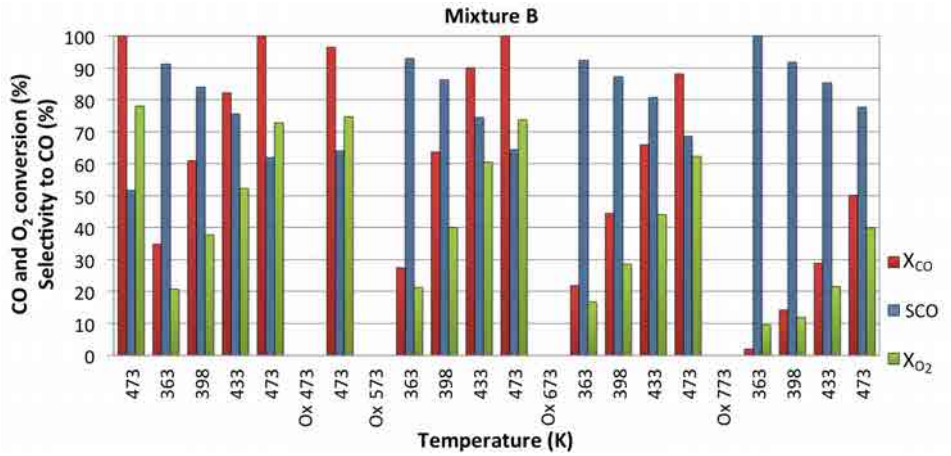

Figure 12.9: Catalytic results of Au@G1/TiO_2//Mon for mixture B experiments.

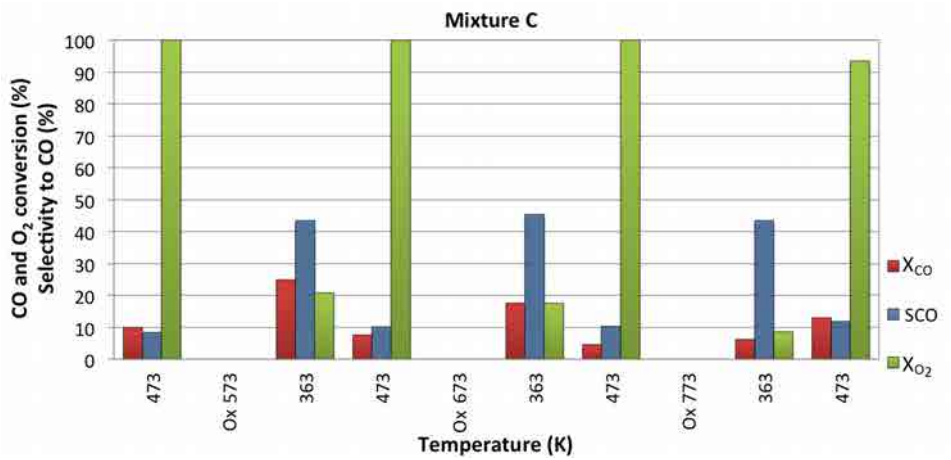

Figure 12.10: Catalytic results of Au@G1/TiO_2//Mon for mixture C experiments.

CO conversion attained was χ_{CO}=25% along with a selectivity S_{CO_2}∼45% (363 K after the oxidation at 573 K); these values were noticeably lower than the ones obtained for Au@D/TiO_2//Mon and Au@G0/TiO_2//Mon (compare with figures 12.5 and 12.8). This marked catalytic activity depletion for high H_2 concentrations, which was larger than the previously observed for Au@D/TiO_2//Mon and Au@G0/TiO_2//Mon, pointed to a reduction of the extension of CO-PrOx reaction provoked by the presence of the longer G1 dendrimers, which contained more Si atoms than G0 dendrimers encapsulating the Au core.

12.2.2.c Au@G2/TiO_2//Mon

Finally, the catalytic activity of a freshly synthesized Au@G2/TiO_2//Mon was examined with a cordierite monolith loaded with 0.247 g of catalyst (WHSV=24

L/(h·$g_{catalyst}$)). Results concerning mixture B experiments at 473 K are plotted in figure 12.11. During the activation treatment (mixture B at 473 K), the catalytic

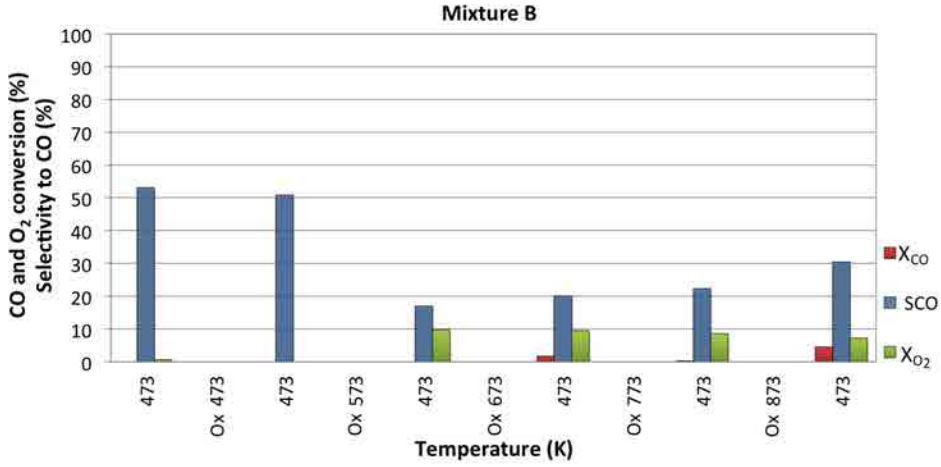

Figure 12.11: Catalytic results of Au@G2/TiO_2//Mon for mixture B experiments.

activity was inexistent and, accordingly, an oxidation at 473 K was directly performed in order to remove the G2-dendrimers shell. For the whole reaction cycle, almost no CO oxidation was recorded and the highest O_2 conversion attained was ∼10%. Thus, an extra oxidation at 873 K was added after the whole sequence in order to further remove the dendrimer shell, but the catalyst only reached 5% CO conversion. These results showed that the Au@G2/TiO_2//Mon was not a suitable catalyst for the CO-PrOx reaction, possibly because the perimeter of Au NPs was totally covered by Si, thus preventing the creation of active sites in the Au-TiO_2 interface and obstructing the interaction of the reactants with the catalyst.

Results of Au@D- and Au@NCD-based catalysts evidenced that the larger the dendrimer shell, the lower the catalytic activity. Consequently, it seemed that a compromise existed between the amount of carbosilane dendrons and Au cores. Whereas carbosilane dendrons hindered Au agglomeration by the formation of SiO_2 at the surface of Au NPs (see the thermal stability study performed in section 11.2.3), an excess of Si (such in the case of Au@G2/TiO_2//Mon and to a lesser extent in Au@G1/TiO_2//Mon) had a detrimental effect on the CO-PrOx reaction, probably because it blocked the catalytic active sites at the Au-TiO_2 interface. This phenomenon is schematically represented in figure 12.12. Hence, an optimum carbosilane dendron for CO-PrOx is found in Au@G0.

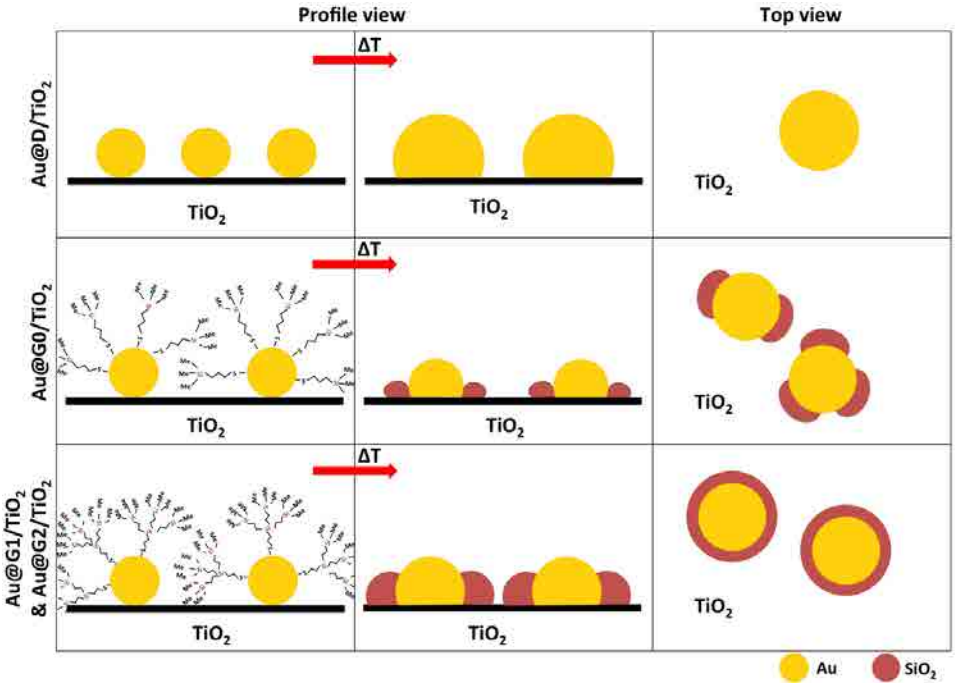

Figure 12.12: Schematic representation of the Au-TiO_2 interface coverage for the different generations of encapsulated Au nanoparticles studied after thermal annealing.

12.2.3 AuC/TiO_2 catalysts

After the comparison between catalysts synthesized using preformed Au NPs, the catalytic activity of a conventional AuC/TiO_2//Mon (loaded with 0.229 g of catalyst) was screened after the synthesis calcination in the muffle at 673 K for 2 hours. The series of catalytic tests started directly dosing mixture B at 473 K; under these reaction conditions the catalyst only converted 20% CO and O_2 conversion reached 30%. The reaction temperature was lowered and the catalytic performance was tested at 363 K, 398 K and 433 K. These results are plotted in figure 12.13. However, at lower temperatures, also the catalytic activity was lower. Consequently, the temperature of the reaction medium was risen to 573 K, at which complete CO conversion was attained, however complete H_2 conversion was also recorded. As the catalyst seemed to be activated, in order to obtain better selectivity to CO oxidation, the reaction temperature was lowered, but no activity improvement was noticed at 398 K and 433 K. At 473 K, the activity improved with respect to the initial values exhibited, but it was still low, χ_{CO}=40%. The catalyst was subjected to several activation treatments under mixture B conditions at increasing temperatures, however no improvement for the CO-PrOx reaction was detected and full CO conversion was only attained at T=573 K, with an associated selectivity to CO_2 close to 50%. As regards mixture A experiments, total CO oxidation was

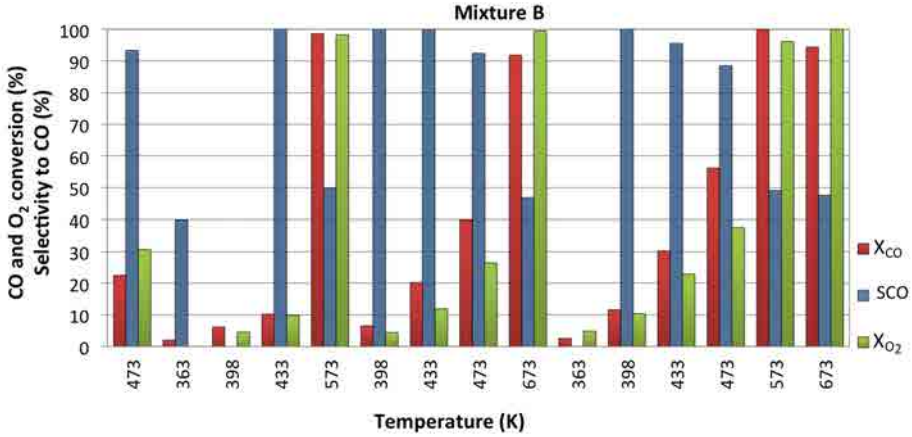

Figure 12.13: Catalytic results of AuC/TiO_2//Mon for mixture B experiments.

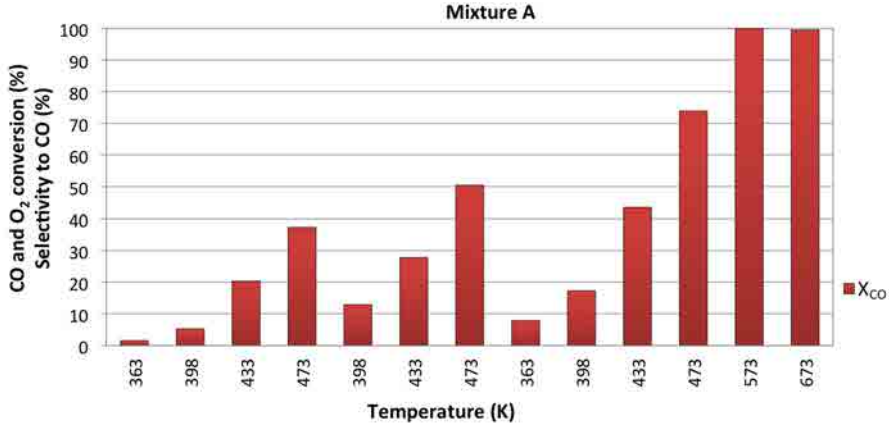

Figure 12.14: Catalytic results of AuC/TiO_2//Mon for mixture A experiments.

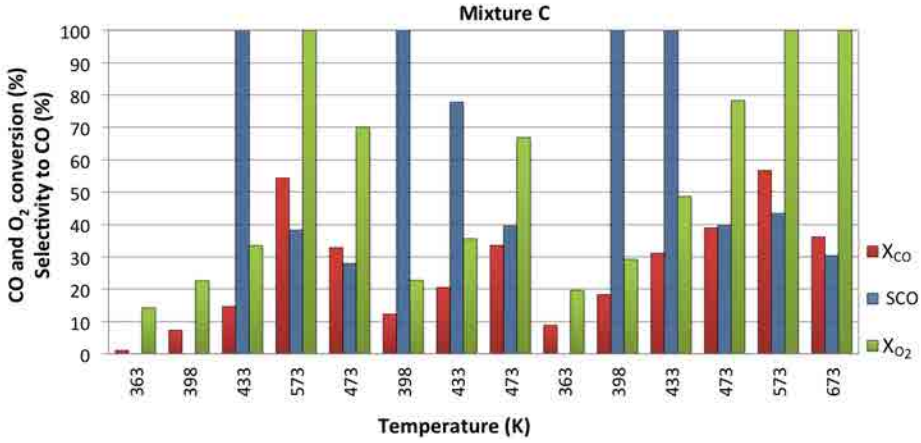

Figure 12.15: Catalytic results of AuC/TiO_2//Mon for mixture C experiments.

solely achieved at 573 K and 673 K, as seen in figure **12.14**, revealing that the AuC/TiO_2//Mon had a very low CO oxidation activity. Finally, experiments with mixture C were performed; figure **12.15** summarizes the obtained results. The best performance was attained at 573 K, at which CO conversion recorded its maximum (χ_{CO}=57%) and it was accompanied by a high selectivity to CO_2 (S_{CO_2}=43%), taking into account the high reaction temperature. In the 363-473 K temperature range the best CO-PrOx catalytic results were attained at 433 K, where the catalyst achieved 100% selectivity to CO_2 with CO conversion close to 30%; and at 473 K, where both CO oxidation and selectivity to CO oxidation were ∼40%. Therefore, the CO-PrOx performance of the conventional catalyst was clearly inferior to that of Au@D/TiO_2//Mon and Au@G0/TiO_2//Mon.

12.2.4 Catalytic screening of the TiO_2 support

The catalytic performance of a cordierite monolith coated with 0.232 g of TiO_2 (calcined at 723 K) was evaluated in order to study the activity of the bare titania support, without gold NPs. The reaction sequence shown in figure **12.2** was followed again and the space velocity of these tests was fixed at GHSV=$1.3{\cdot}10^3$ h^{-1}. During the first reaction cycle, the TiO_2//Mon exhibited poor catalytic performance. Thus, the temperature was raised to 573 K under mixture B and the catalyst attained ca. 90% CO conversion. Subsequently, the temperature was lowered and the second cycle was started. Nevertheless, the CO conversion did not increase and the catalyst only converted CO at temperatures higher than 573 K. At these temperatures all the O_2 dosed was consumed and the selectivity to CO_2 was ∼50%. Results obtained for mixture B experiments are shown in figure **12.16**. Results concerning mixture A and C experiments are not shown, because the CO conversion was only significant at 573 K and 673 K.

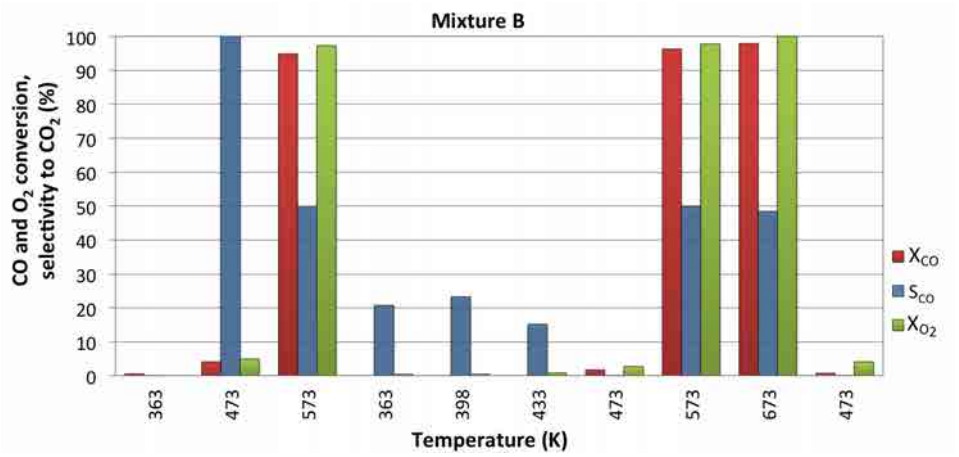

Figure 12.16: Catalytic results of TiO_2//Mon for mixture B experiments.

12.3 *In situ* XPS characterization of the Au@G0/TiO_2 catalyst

The surface properties of an as-synthesized Au@G0/TiO_2 catalyst after the oxidations and reaction conditions tested in the laboratory was followed by *in situ* XPS in order to try to correlate the catalytic behavior observed with the surface organization of the catalyst and to monitor the removal of the dendrimer shell. A pellet of a freshly synthesized 10Au@G0/TiO_2 catalyst was dried for 10 minutes under an IR lamp and it was subsequently introduced into the XPS system located at the CRnE (UPC) (see section 6.2 for details of the XPS equipment). The analyses started with the acquisition of a survey spectrum and Au 4f, C 1s, Ti 2p and Si 2s spectral regions of the as-synthesized sample. Then, the pellet was subjected to different treatments after each of which the same regions were acquired. The sequence of *in situ* XPS analyses performed on the Au@G0/TiO_2 catalyst was: 1) catalyst as-prepared, oxidations for 10 minutes with 20 mL/min of air at: 2) 473 K, 3) 573 K, 4) 673 K, 5) CO-PrOx performance at 673 K (reaction mixture: 3 mL/min H_2 + 3 mL/min CO + 15 mL/min air), 6) oxidation at 773 K and 7) oxidation at 873 K. Gold 4f spectra were deconvoluted constraining the distance between $Au4f_{7/2}$ and $Au4f_{5/2}$ components at 3.65 eV [122] and the ratio between their areas. All spectra were referred to the adventitious C 1s signal at 284.8 eV. The results of the spectra deconvolution are compiled in table 12.3, where the percentage atomic ratios of the surface elements present at the catalyst's surface are listed.

Table 12.3: XPS results for the sequence of *in situ* treatments of the Au@G0/TiO_2 catalyst.

	Atomic ratio (%)			
Treatment	Au/Ti	Au/C	Si/Au	Si/Ti
1. As-synthesized	38	48	215	82
2. Oxidation at 473 K	34	55	227	78
3. Oxidation at 573 K	30	65	261	78
4. Oxidation at 673 K	29	129	133	39
5. CO-PrOx at 673 K	29	296	154	44
6. Oxidation at 773 K	27	239	220	58
7. Oxidation at 873 K	26	289	1389	363

As deduced from the results listed in table 12.3, Au@G0 NPs slightly agglomerated after each step of the sequence of treatments performed, as the Au/Ti ratio gradually decreased. On the other hand, the Au/C ratio progressively increased

until the sample was oxidized at 673 K, which caused a large increment of the Au/C ratio, denoting that the organic part of the dendrimer shell was mostly removed. This result is in agreement with the XPS results obtained under UHV conditions for Au@D/TiO_2, Au@G1/TiO_2 and Au@G2/TiO_2 catalysts studied in section **11.3.1.b**. Nevertheless, the Au@G0/TiO_2 treatments were carried out with air at atmospheric pressure in the reaction chamber coupled to the XPS analysis chamber, which led to a remarkably higher C removal than that attained on the UHV-XPS experiments previously reported. Interestingly, after the experiment under CO-PrOx reaction conditions (3 mL/min H_2 + 3 mL/min CO + 15 mL/min air), the Au/C ratio suffered its major increment and Au surface concentration was three times that of C. This result indicated that the presence of H_2 and CO enhanced carbosilane dendrimers removal, as the reaction mixture caused a larger dendrimers removal than the pure oxidation performed at the same temperature (673 K) in the previous step. Furthermore, the Si/Au ratio registered one of its lower values. This effect may be the origin of the improved catalytic activity observed for the catalysts after dosing mixture B at 473 K. Subsequent oxidations at 773 K and 873 K almost did not cause changes on Au/Ti and Au/C ratios, evidencing that the organic shell was removed during the reaction performance. However, that was not the case for Si/Au and Si/Ti ratios, which experienced a significance increase after the oxidation at 873 K, indicating that carbosilane residues covered part of the Au/TiO_2 catalyst.

13 CO PREFERENTIAL OXIDATION IN CONVENTIONAL MICROREACTORS

The catalytic performance of the best Au/TiO_2 catalysts tested in Chapter 12 was evaluated in conventional microreactors in order to take advantage of the better thermal management attained in microreactors, which is a critical issue for efficient CO-PrOx reaction operation. Also the effect of the presence of CO_2 and steam was evaluated in long-term stability tests.

13.1 Introduction

In the literature it has been reported that bringing CO levels to below 50 ppm does not only require an active catalyst but also a good reactor design [264]. The ability of the reactor design to eliminate the heat released by CO and H_2 oxidation reactions from the reaction medium to maintain adequate selectivity levels is of crucial importance. The control of the reaction temperature and, thus avoidance of temperature gradients or hot spot formation, results in improved CO selectivity as parasitic reactions such as H_2 oxidation, methanation and reverse WGS are prevented as much as possible [42]. Consequently, thermal and also mass transport management have been identified as key issues for practical CO-PrOx reactor designs and efficient reactor operation to obtain highly selective CO abatement to levels acceptable for PEMFC [265]. In this context, the thin catalytic coatings directly developed on the channel walls of microreactors [266], the higher surface area and higher heat and mass transfer efficiency of microreactors in addition to lower pressure drops offer advantages over conventional packed-bed reactors to run the highly exothermic CO-PrOx reaction, as previously reported in a number of papers [265]. Kolb et al. in [207] evaluated the performance of CO-PrOx-heat-exchanger reactors based on microreaction technology and on fixed-bed technology designed for 0.1 and 5 kW_e power output units and, in both cases, the microreactor

designs outperformed the conventional fixed-bed designs, resulting in lower reactor volumes and weights.

Therefore, the performance of our best CO-PrOx catalysts, namely Au@G0/TiO_2 and Au@D/TiO_2, was tested in conventional microreactors in order to evaluate their suitability for small-scale and portable applications. For comparison purposes, the performance of AuC/TiO_2 was also evaluated in a microreactor.

13.2 Microreactor functionalization

The microreactors used in these experiments were provided by the Mainz Institute of Microtechnology (IMM, Germany). The microreactors have a sandwich-type design where two microstructured platelets are attached face to face by laser welding [267]. Each of the stainless steel platelets has 14 semicylindrical channels of 500 µm width, 250 µm depth and 25 mm length. The microchannels were manufactured by means of commercial photoetching based on wet chemical etching with aqueous $FeCl_3$ solutions [266]. Inlet and outlet conduits were attached to the platelets by laser welding [268]. Each couple of platelets was coated with anatase TiO_2 at IMM following a well-established procedure. Subsequently, at UPC the gold precursors were added dropwise over the microchannels to obtain a nominal gold loading of 2 wt.%. One couple of platelets containing 15 mg of TiO_2 was impregnated with Au@D toluene solution and calcined at 773 K for 2 hours (2 K/min) leading to the Au@D/TiO_2//Micro sample. Another couple coated with 16 mg of TiO_2 was impregnated with Au@G0 preformed NPs solution and calcined at 673 K for 2 hours (2 K/min), constituting the Au@G0/TiO_2//Micro sample. Finally, another platelets couple coated with 15 mg of TiO_2 was impregnated with $HAuCl_4$ ethanolic solution ($12{\cdot}10^{-3}$ M) and then it was calcined at 673 K for 2 hours (sample AuC/TiO_2//Micro). Figure 13.1 shows a picture of the microchannels after catalyst deposition.

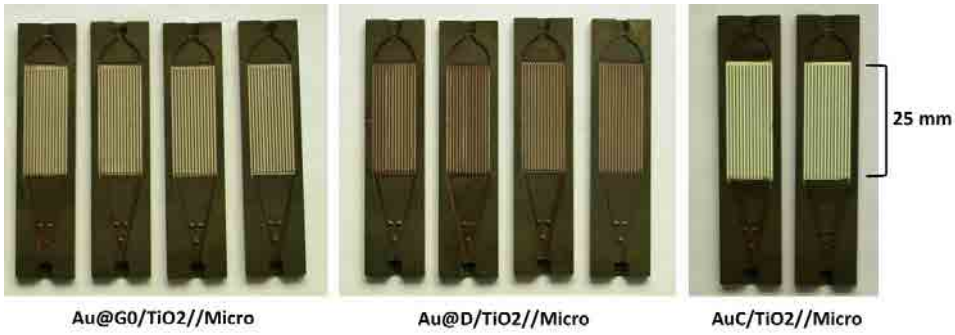

Figure 13.1: Microchannels of the stainless steel microreactors coated with different Au precursors. From left to right coated with: Au@G0, Au@D and AuC gold precursors.

The calcination temperature of each sample was chosen according to the catalytic results exhibited by the samples loaded on cordierite monoliths (Chapter 12). Therefore, the thermal treatments that resulted in the best performance of each catalytic system were directly performed on the functionalized microreactors.

Once the catalyst was deposited, both platelets of a couple were sealed by laser welding at IMM, which allowed for leak-tightness of the reactors at operation temperatures above 1023 K [267]. Figure 13.2 shows a picture of the microreactor.

Figure 13.2: Welded platelets constituting a microreactor. The scale is shown in cm.

13.3 Catalytic activity screening

To screen the catalytic performance of conventional microreactors, the same setup used for testing functionalized cordierite monoliths (see figure12.1) was used. The needle valve placed after the mass flow controllers was employed to regulate the total flux injected without varying the gases concentration. Initially, the effect of mixtures A, B and C was evaluated on the microreactors performance. Table 13.1 recalls the concentration of each of these mixtures.

Table 13.1: Inlet mixtures concentration.

	Concentration (%)			
Mixture	CO	O_2	H_2	Ar
A	2	2	0	96
B	2	2	2	94
C	2	2	50	46

13.3.1 Catalytic screening of the Au@D/TiO_2//Micro

The firsts experiments carried out concerned the influence of the feed load or the space velocity on CO conversion and selectivity to CO oxidation. The feed loads tested corresponded to gas hourly space velocities (GHSV) ranging from $1.2{\cdot}10^4$ to $9.2{\cdot}10^4$ h^{-1}, which represented weight hourly space velocities (WHSV) from 52.4 to 390.2 $L/(h{\cdot}g_{catalyst})$. The GHSV of these experiments was calculated taking into account the volume of the 14 microchannels.

As previously established for cordierite monoliths, the series of catalytic tests started dosing mixture B at 473 K in order to activate the catalyst. Au@D/TiO_2//Mon experienced a slow activation, where CO conversion gradually increased. Once the steady state was achieved, the reaction temperature was lowered to 363 K and the catalyst performance for mixture B was tested at different space velocities. Afterwards, the inlet was switched to mixture A and finally to mixture C. The same procedure was repeated at 398 K, 433 K and 473 K.

Figure **13.3** shows the CO conversions attained for mixture B experiments at the different temperatures and GHSV tested, while figure **13.6** shows the associated selectivities to CO oxidation.

The expected trends were observed for both parameters, CO conversion and selectivity to CO_2: the higher the space velocity, the lower the CO conversion; while the opposite was true for the selectivity to CO oxidation: the higher the space velocity the higher the CO_2 selectivity, as previously reported by Reina et al. [258]. Another common trend observed for all the experiments was that the higher the temperature, the higher the CO conversion and the lower the selectivity to CO oxidation, which was also observed for the tests carried out on cordierite monoliths. At 363 K and 398 K, selectivities higher than 90% were recorded for all the GHSV tested; at 398 K up to 94% CO_2 selectivity was obtained with χ_{CO}=80%. In the high temperature range, full CO conversion was achieved with selectivities to CO oxidation of 80% and 63% at 433 K and 473 K, respectively.

As seen in figure **13.4**, for mixture A experiments complete CO conversion was achieved at 473 K almost for all the space velocities tested. However, when temperature was lowered to 433 K, it was only achieved for the lowest GHSV. Interestingly, as seen in figure **13.4**, the trends recorded at 363 K, 398 K and 433 K were very similar to those recorded for mixture B, indicating that the presence of 2% H_2 had a minor effect on χ_{CO}.

However, when the inlet was switched to mixture C (figures **13.5** and **13.7**), CO conversion decreased for all temperatures, except for 363 K, as seen in figure **13.5**. At

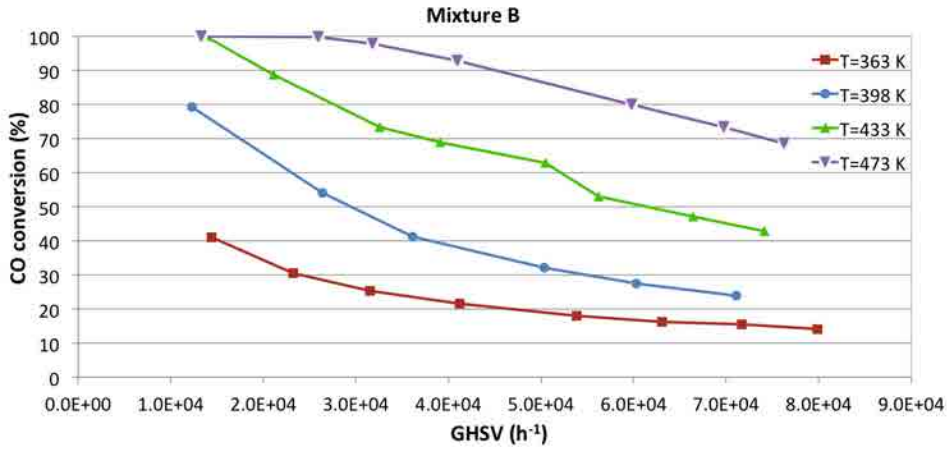

Figure 13.3: CO conversion for mixture B experiments. Sample: Au@D/TiO_2//Micro.

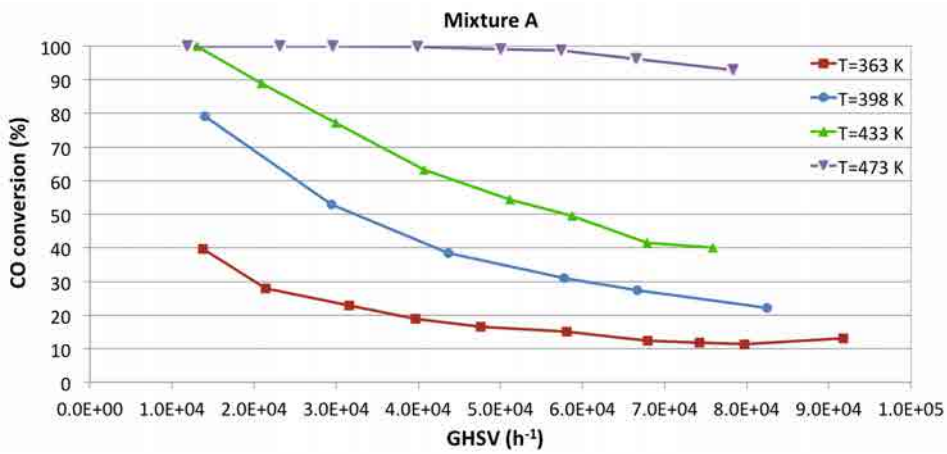

Figure 13.4: CO conversion for mixture A experiments. Sample: Au@D/TiO_2//Micro.

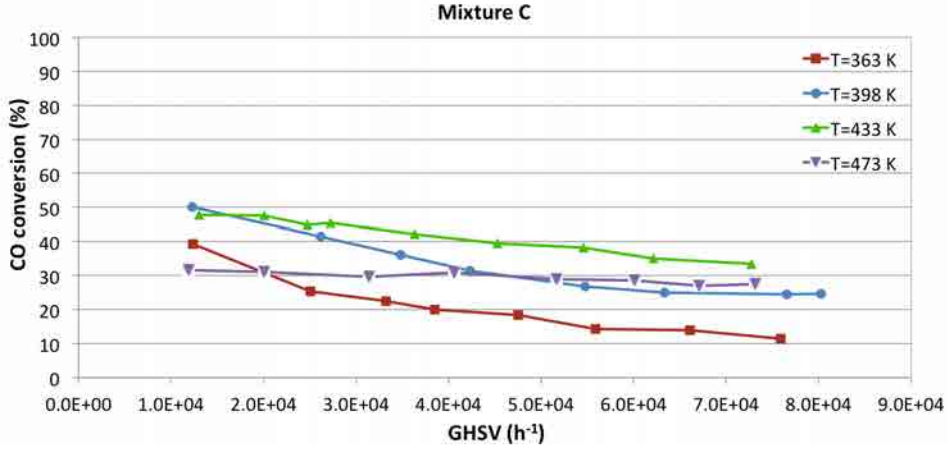

Figure 13.5: CO conversion for mixture C experiments. Sample: Au@D/TiO_2//Micro.

the lowest temperature, practically the same CO conversion as for mixture B was attained (compare with figure **13.3**). At the lowest GHSV, ∼50% CO conversion was achieved at 398 K and 433 K. Both CO conversion and selectivity to CO oxidation (see figure **13.7**) experienced smooth variations for the range of GHSV tested.

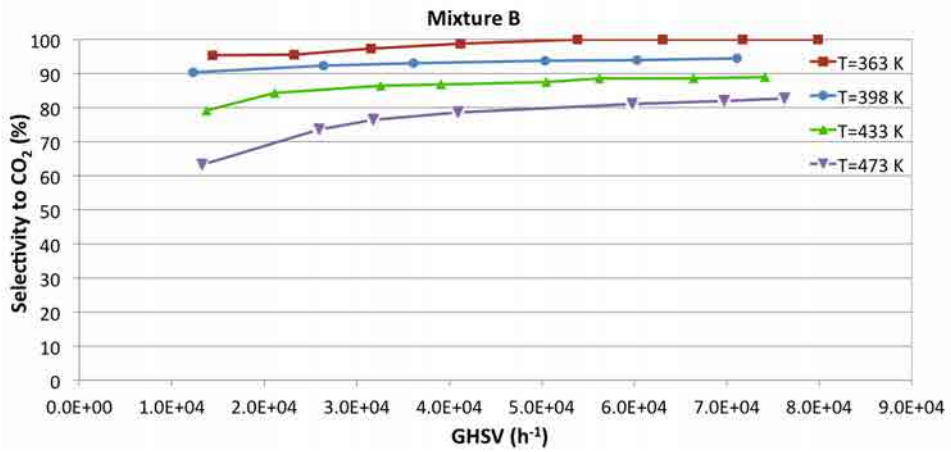

Figure 13.6: Selectivity to CO oxidation for mixture B experiments. Sample: Au@D/TiO_2//Micro.

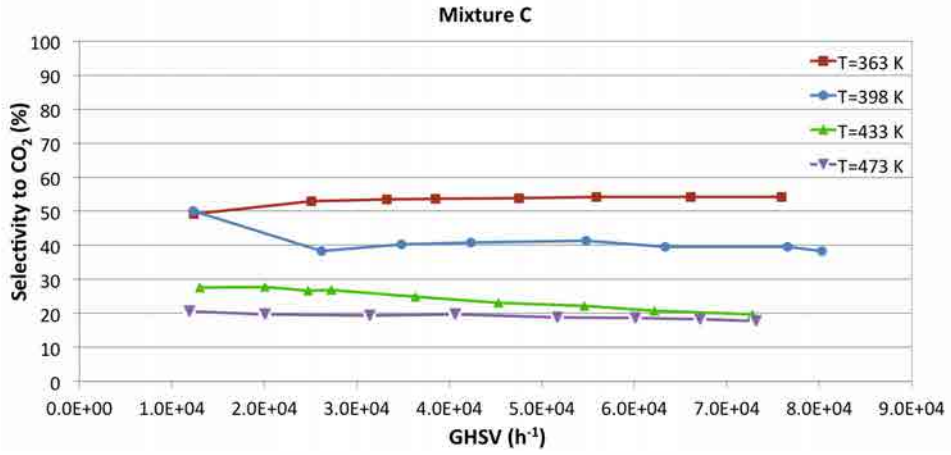

Figure 13.7: Selectivity to CO oxidation for mixture C experiments. Sample: Au@D/TiO_2//Micro.

This initial screening of the Au@D/TiO_2//Micro allowed for elucidating the reaction conditions that resulted in enhanced CO-PrOx performance of the microreactor. Accordingly, the subsequent tests of the microreactors Au@G0/TiO_2//Micro and AuC/TiO_2//Micro were performed only at the lowest GHSV studied.

13.3.2 Catalytic screening of the Au@G0/TiO_2//Micro

Au@G0/TiO_2//Micro tests started directly performing the activation treatment (mixture B at 473 K). However, when the reaction temperature was lowered to 363 K, the microreactor exhibited very low CO oxidation and this trend was maintained for the first cycle of temperatures and mixtures tested, namely 363 K, 398 K, 433 K and 473 K and mixtures B, A and C (see figure 12.2). Consequently, as the catalyst was already calcined, in order to improve the catalytic activity and in accordance with the XPS results discussed in section 12.3, the reaction temperature was increased stepwise to 673 K under mixture B atmosphere. Results concerning mixture B experiments are presented chronologically in figure 13.8. At 623 K and 673 K, the catalyst attained complete CO conversion. In this graph, the extra steps performed at higher temperatures are highlighted with stripped bars. Following the treatment with mixture B at 673 K, reaction temperature was lowered to 363 K and a regular reaction cycle was performed again. This cycle finished dosing again mixture B and increasing the reaction temperature to 773 K. Afterwards, the last regular reaction cycle was performed.

As seen in figure 13.8, after each exposure to mixture B at increasing temperature, both CO conversion and selectivity to CO_2 improved, which most probably could be related to further removal of the dendrimer shell. After exposure to mixture B at 773 K, the best CO-PrOx performance was registered: χ_{CO}=82% along with a selectivity to CO_2 S_{CO_2}=85% was obtained at 473 K.

Regarding CO total oxidation (TOX) experiments, the microreactor could not attain complete CO oxidation for the reaction conditions tested. Figure 13.9 shows the results obtained for these experiments. In this figure, CO conversion at the same reaction temperature for the successive cycles is group together and the different colors of the bars denote the temperature of the previous treatment performed with mixture B. For instance, the red bar shown at 398 K corresponds to the CO conversion achieved for TOX at 398 K after dosing mixture B at 673 K. As clearly seen in figure 13.9, the higher the temperature of the activation treatment with mixture B, the higher the CO oxidation activity, as previously observed for mixture B experiments. The maximum CO conversion was achieved again at the highest reaction temperature (473 K), where χ_{CO}=94%.

Finally, experiments performed with mixture C are plotted in figure 13.10. In this figure, CO conversion trends are group together in the same way as for mixture A. In this case, the selectivity of each experimental condition is also included and it is represented next to its corresponding χ_{CO}. At 363 K and 398 K, the CO conversion recorded was nearly the same as for mixture B experiments and the presence of larger H_2 concentration only affected the selectivity to CO_2 , which was

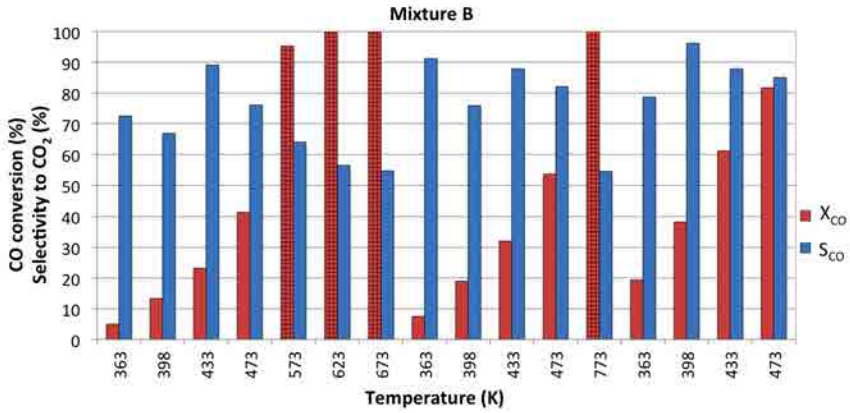

Figure 13.8: CO conversion for mixture B experiments. Experimental conditions: GHSV=$1.2{\cdot}10^4$ h^{-1}. Sample: Au@G0/TiO_2//Micro.

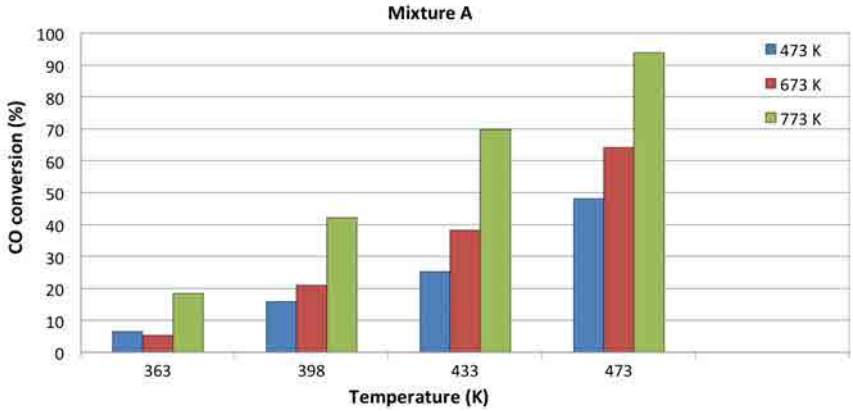

Figure 13.9: CO conversion for mixture A experiments. Experimental conditions: GHSV=$1.2{\cdot}10^4$ h^{-1}. Sample: Au@G0/TiO_2//Micro.

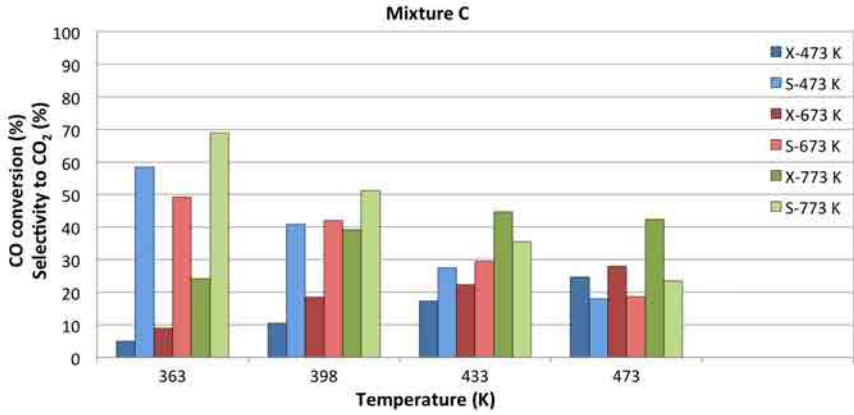

Figure 13.10: CO conversion for mixture C experiments. Experimental conditions: GHSV=$1.2{\cdot}10^4$ h^{-1}. Sample: Au@G0/TiO_2//Micro. χ and S refer to CO conversion and S_{CO_2}, respectively.

reduced by ~10%. However, experiments performed at higher temperatures (433 K and 473 K) showed a reduction on both the CO oxidation and its selectivity, with respect to mixture B experiments.

13.3.3 Catalytic screening of the AuC/TiO_2//Micro

The catalytic activity of the AuC/TiO_2//Micro was evaluated following the same sequence as for Au@G0/TiO_2//Mon. Thus, mixture B was also dosed at high temperature in the order shown in figure 13.8. The AuC/TiO_2//Micro exhibited a surprisingly low activity for all the mixtures tested as demonstrated in figures 13.11 to 13.13, where the results obtained for mixtures B, A and C, respectively, are shown. The highest CO conversion attained by the AuC/TiO_2//Micro during the regular cycles was <10% for the three mixtures. As seen in figure 13.11, it was only for the extra experiments carried out with mixture B at high temperatures that the microreactor achieved $\chi_{CO} \geq 30\%$. However, as high reaction temperatures were essayed, their selectivity to CO oxidation was low, as expected.

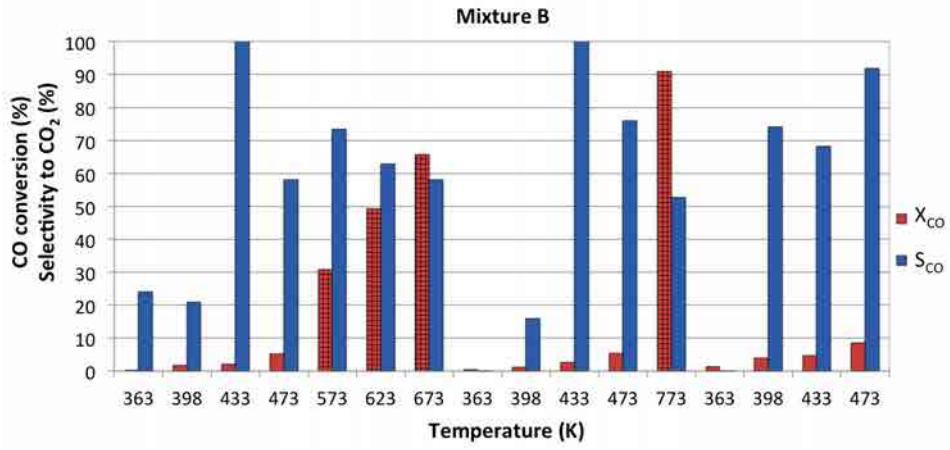

Figure 13.11: CO conversion for mixture B experiments. Experimental conditions: GHSV=$1.2 \cdot 10^4$ h^{-1}. Sample: AuC/TiO_2//Micro.

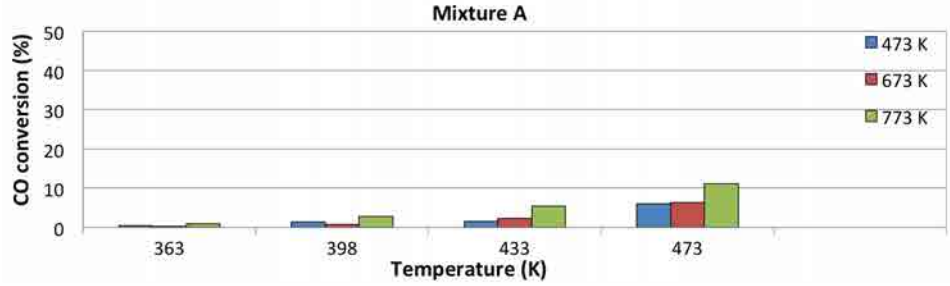

Figure 13.12: CO conversion for mixture A experiments. Experimental conditions: GHSV=$1.2 \cdot 10^4$ h^{-1}. Sample: AuC/TiO_2//Micro.

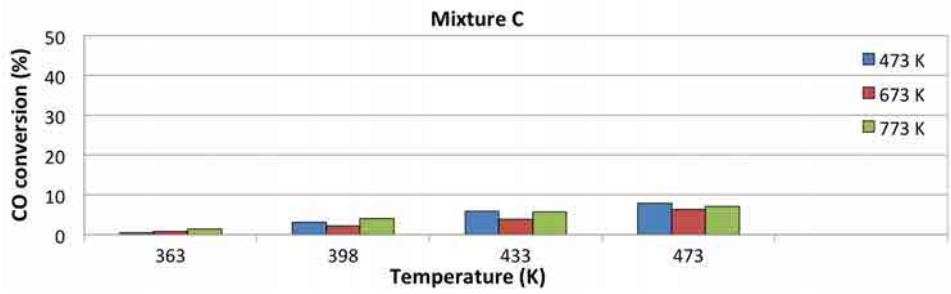

Figure 13.13: CO conversion for mixture C experiments. Experimental conditions: GHSV=$1.2{\cdot}10^4$ h^{-1}. Sample: AuC/TiO_2//Micro.

13.4 Performance comparison with cordierite monoliths

This section aims at comparing the catalytic activity exhibited by the same catalyst supported on cordierite monoliths and on stainless steel microreactors. To do so, the best CO-PrOx performance exhibited by the Au@G0/TiO_2//Mon, the Au@G0/TiO_2//Micro, the Au@D/TiO_2//Mon and Au@D/TiO_2//Micro for mixture C (which is the mixture that more closely modeled real reformate streams) was chosen for comparison.

As the amount of catalyst loaded on cordierite monoliths was one order of magnitude higher than that of microreactors (200 mg on cordierite monoliths versus 15 mg on stainless steel microreactors), a specific activity a (equation **13.2**) was defined normalizing the corresponding activity, A, (mL of CO converted per unit time, equation **13.1**) by the amount of catalyst used.

$$A = \frac{2}{100} \cdot \Phi \cdot \chi_{CO} \cdot \frac{1}{100} \tag{13.1}$$

$$a = \frac{A}{m};\ [a] = \frac{mL_{COconverted}}{min \cdot g_{catalyst}} \tag{13.2}$$

where Φ stands for the total inlet flux and it is multiplied by $\frac{2}{100}$ as the inlet contained 2% CO.

Figure **13.14** shows the results of the performance comparison for both structured catalysts. The specific activity of both Au@G0/TiO_2 and Au@D/TiO_2 catalysts was almost identical when supported on cordierite monoliths and microreactors: the microreactors converted about 1 $mL_{CO}/(min{\cdot}g_{catalyst})$ more than monoliths, in spite of the higher space velocities essayed both in terms of reactor volume (GHSV: 10^3 versus 10^4 h^{-1}) and catalyst mass (WHSV: 32 versus 52 $L{\cdot}h^{-1}{\cdot}g^{-1}_{catalyst}$). Therefore, also for our experiments the microreactors outperformed conventional

cordierite monoliths (400 cpsi). The comparison of the different catalytic systems also revealed slightly superior catalytic activity of the Au@D/TiO_2 catalyst, no matter the structural support. The highest specific activity achieved by our gold catalysts was obtained by the Au@D/TiO_2//Micro during the tests of space velocity (section **13.3.1**): up to 35 $mL_{CO}/(min \cdot g_{catalyst})$ were converted at 433 K and GHSV=$7.3 \cdot 10^4$ h^{-1}.

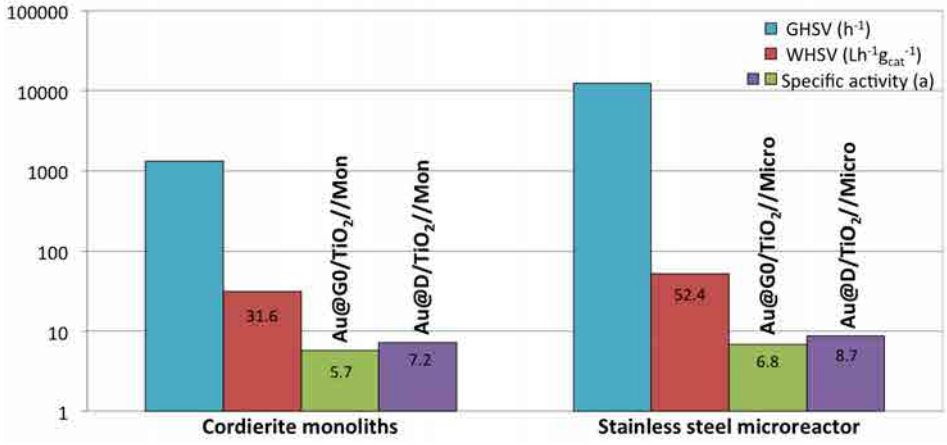

Figure 13.14: CO-PrOx performance comparison between functionalized cordierite monoliths and conventional microreactors.

13.5 Long-term run

The catalytic screening of functionalized microreactors ended with a 500-hours stability test of Au@G0/TiO_2//Micro and Au@D/TiO_2//Micro, which was performed under real post-reformate conditions at the laboratories of the IMM. In these long-term runs, the influence of steam and CO_2 was evaluated. Table **13.2** lists the operating conditions tested and table **13.3** the composition of the inlet mixture.

Table 13.2: Operating conditions evaluated for the stability test.

Temperature (K)	453
Absolute pressure (bar)	1
Total inlet flux (mL/min)	30
GHSV (h^{-1})	$2.6 \cdot 10^4$
λ	2

Two new microreactors were functionalized with Au@D/TiO_2 and Au@G0/TiO_2 catalysts, following the same procedure explained at beginning of this Chapter

Table 13.3: Inlet mixture composition evaluated on the stability test.

Species	Concentration (%)
H_2	48.5
CO	0.85
O_2	0.85
N_2	3.4
CO_2	18
H_2O	29

(section 13.2). The microreactors were tested under reaction conditions without performing any activation treatment.

Figures 13.15 and 13.16 report the concentration of the species detected at the outlet of the Au@D/TiO_2//Micro and Au@D/TiO_2//Micro, respectively. The concentration of the inlet mixture was measured for ca. 20 hours in order to assure a constant injection during the 500-hours stability test. The concentration of the species analyzed during this period of time is reported at the beginning of both graphs and its end is marked with the word *Bypass*. Concentrations recorded during this period were used as a reference of $\dot{n}_{CO,in}$ to calculate CO conversion.

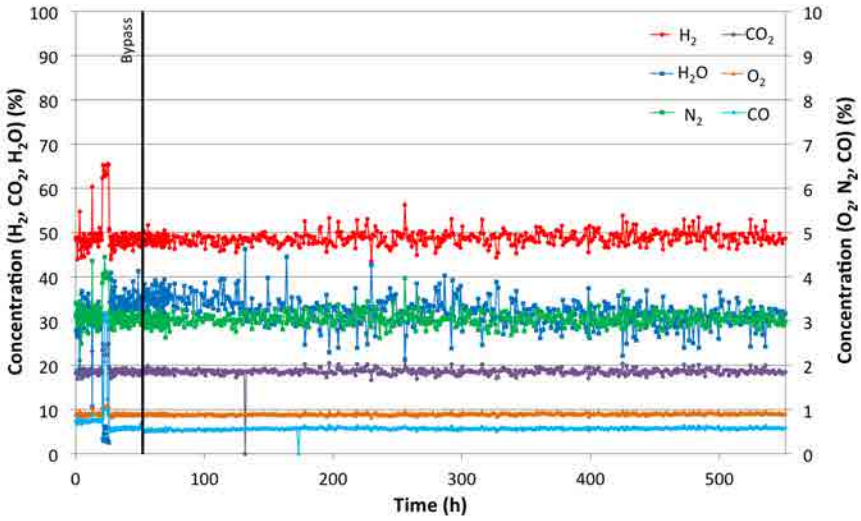

Figure 13.15: Species detected at the outlet of the Au@D/TiO_2//Micro.

Trends reported in figures 13.15 and 13.16 show stable operation of both microreactors, without fluctuations of species concentration in the outlet; only some spikes were recorded. The corresponding CO conversion of these tests for both microreactors is presented in figure 13.17.

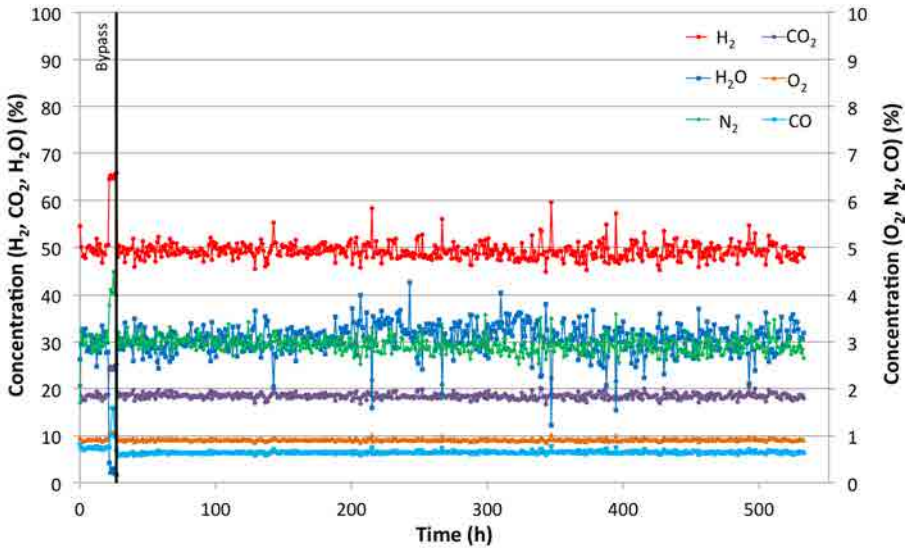

Figure 13.16: Species detected at the outlet of the Au@G0/TiO_2//Micro.

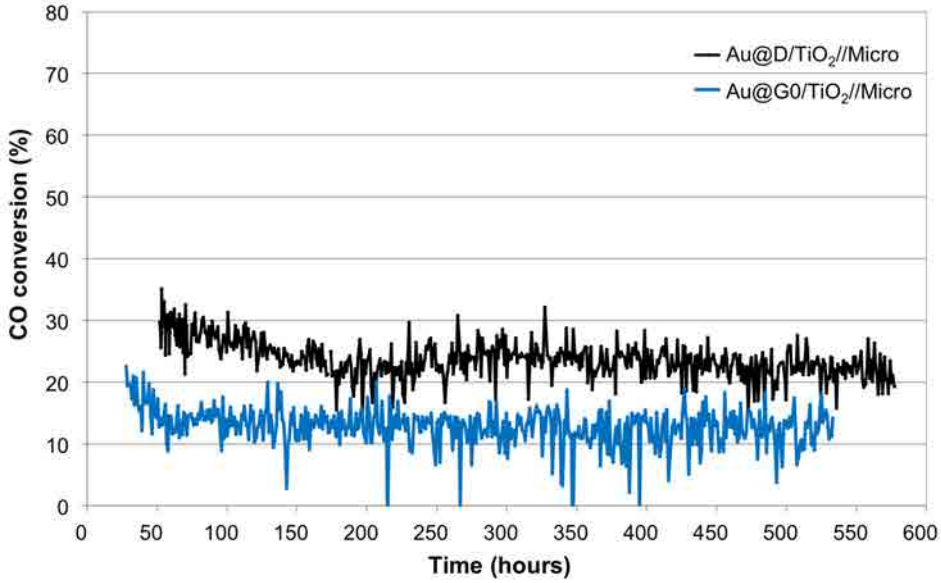

Figure 13.17: CO conversion achieved by Au@D/TiO_2//Micro and Au@G0/TiO_2//Micro during the stability test under a real CO-PrOx mixture.

Both microreactors experienced a transient operation at the beginning of the test, but after this period, its performance was stable and no deactivation signs were noticed. In addition, no traces of methane were detected. As evidenced by results presented in figure **13.17**, CO_2 and H_2O caused a decrease of CO catalytic oxidation for both microreactors. In the case of the Au@D/TiO_2//Micro, CO con-

versions obtained in this temperature range for mixture C experiments (see figure **13.5**, GHSV=$2.6 \cdot 10^4$ h^{-1}) were 45% at 433 K and 30% at 473 K, whereas the mean CO conversion achieved during the stability test was 24% at 453 K. This value is lower than the previously recorded, but the presence of steam and CO_2 did not entail a dramatic diminution of the catalytic activity.

As regards Au@G0/TiO_2//Micro performance, the averaged CO conversion for the 500-hours stability test was 13%, whereas previously CO conversion ranged 40-45% in the 433-473 K temperature range (see figure **13.10**, GHSV=$1.2 \cdot 10^4$ h^{-1}). Therefore, CO_2 and H_2O had a more pronounced effect on the Au@G0/TiO_2//Micro performance, as they caused an activity diminution of one third. However, the Au@G0/TiO_2//Micro reached stable performance in ca. 30 hours (hour number 50 in figure **13.17**), while it took ca. 110 hours (hour number 150) for the Au@D/TiO_2//Micro.

These tests showed an outstanding stable performance of the gold-based catalysts developed for 500 hours, thus overcoming one of the major drawbacks recognized in the literature for these type of catalysts.

14 | CO PREFERENTIAL OXIDATION IN SILICON MICROCHANNELS

The last Chapter of Part II is dedicated to the miniaturization of the CO clean-up scale. In this Chapter, a further scale reduction of CO abatement in the presence of hydrogen is explored by using the novel Si micromonoliths already tested for ESR in Chapter 8. The micromonolith was successfully functionalized with Au@G1/TiO_2, and then its catalytic activity for the CO preferential oxidation reaction was tested.

The outstanding geometrical and physical properties of the Si micromonoliths, previously reported in sections 1.5.1.a and 8.2, lead to specific surface areas of $4.1{\cdot}10^5$ m^2/m^3, low pressure drops and good thermal conductivity, which make of Si micromonoliths appealing supports for the CO-PrOx reaction, because isothermal operation is feasible and the formation of hot spots can be prevented.

14.1 Silicon micromonolith functionalization

For these experiments a gold precursor consisting of Au NPs encapsulated by dendrimers was chosen, as Au@NCD NPs showed superior stable performance under real CO-PrOx conditions. In this case, the performance of Au@G1 NPs deposited on the Si micromonolith was investigated.

In order to successfully functionalize the 3.3 µm channels with Au@G1/TiO_2 catalyst, a variation of the method developed to coat the Si microchannels with RhPd/CeO_2 catalyst, which is described in section 8.2, was followed here. Therefore, once the SiO_2 layer was developed over the Si microchannels, the hydroxyl groups attached to the SiO_2 surface were exchanged at room temperature with titanium isopropoxide ($Ti[OCH(CH_3)_2]_4$) (Panreac). Ti^{IV} isopropoxide was force to pass through the micromonolith channels applying a pressure gradient at both ends of 75 kPa. The thermal decomposition of Ti^{IV} isopropoxide upon calcination at 723 K for 4 hours (1 K/min), led to the development of a layer of anatase, as previously

described in section 11.1.1. Finally, preformed Au@G1 NPs (2 wt.%) were deposited onto the TiO_2 support by free impregnation of the Au@G1-containing toluene solution, which also was force to pass through the TiO_2-coated microchannels by applying a pressure gradient. Then the functionalized micromonolith was calcined at 673 K for 2 hours (2 K/min). This sample is referred to as Au@G1/TiO_2//Si.

The catalytic coating was analyzed by SEM, however as previously described in section 8.2, in order to investigate the channels' interior, the micromonolith had to be cut and thus the SEM analyses were performed after reaction performance. Nevertheless, the images of the post-reacted microchannels are shown here in order to have the entire characterization together and, hence, have the full picture of the catalyst coating. Figure 14.1 shows representative SEM images of the functionalized and post-reacted Au@G1/TiO_2//Si.

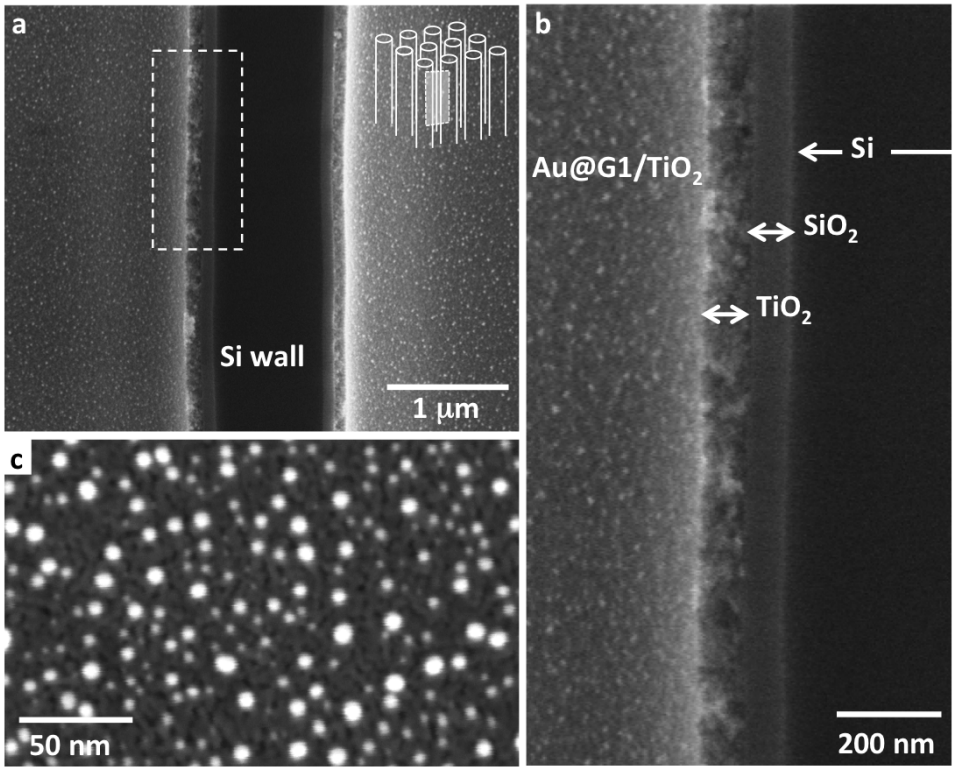

Figure 14.1: Representative SEM images of the Au@G1/TiO_2 layer developed over the oxidized Si microchannels. a) Profile view of two adjacent coated microchannels. Silicon microchannels are arranged as depicted in the drawing. b) High magnification image of the enclosed area in a. Detail of the different layers developed over the Si substrate. From right to left: Si wall, SiO_2 and Au@G1/TiO_2. c) High magnification image of the Au@G1/TiO_2 layer in planar view.

Figure 14.1a shows a profile view of two adjacent microchannels. The black zone in the center of the image corresponded to the Si matrix. At both sides of it, the channels were completely covered with a homogeneous and well-adhered layer of Au@G1/TiO_2. A higher magnification image of the area enclosed by the white square is shown in figure 14.1b. In figure 14.1b the different developed layers can be clearly distinguished: the black area corresponded to the Si matrix, which was covered by a compact, homogenous and well-defined SiO_2 layer of about 60 nm thickness (dark grey). At the same time, the SiO_2 layer was completely covered by a homogeneous and perfectly anchored TiO_2 layer of about 80 nm thickness (light grey). Au@G1 NPs appeared as the bright dots dispersed over the TiO_2 support, as seen in more detail in figure 14.1c. During the SEM observation, channels without catalyst were not identified, nor gold aggregates. Therefore, the synthesis method resulted in successfully coated microchannels that withstood reaction conditions. The estimate amount of catalyst incorporated to the Si micromonolith assuming a TiO_2 layer thickness of ca. 0.1 µm and 1.54 millions of channels coated is ∼1 mg.

14.2 Catalytic activity screening

The procedure described for catalytic testing of 1RhPd/CeO_2//Si (section 8.3) was reproduced for Au@G1/TiO_2//Si. In short, the 8-mm functionalized micromonolith was glued onto a stainless steel washer and this system was then sealed in a stainless steel reactor (21 mm internal diameter). The experimental setup described in Chapter 12 (figure 12.1) used for the catalytic testing of functionalized cordierite monoliths was implemented for catalytic testing of the Si micromonolith too. Again, the needle valve was employed to regulate the total flow injected without varying the gases concentration. In this case, the inlet flow was passed at 5 NmL/min, leading to a contact time of 0.09 s. The reaction performance of Au@G1/TiO_2//Si was tested for the previously defined mixtures A, B and C and a new mixture, D. However, in these experiments, oxygen was supplied from an air stream and, thus, in order to differentiate these mixtures from the previously tested, a "$\star$" was added to the name of the mixture. Table 14.1 lists the concentrations of the mixtures essayed. All mixtures kept the O_2:CO ratio constant at λ=2 as well as the residence time, because H_2 concentration was increased at the expense of that of Ar.

Initially, the catalytic activity of the Au@G1/TiO_2//Si was tested for mixture A* at 473 K. The Si micromonolith showed a slow stabilization and after ca. 4 hours, CO conversion stabilized at 45%. Then the temperature was lowered and the first experiment, consisting of a light-off curve of pure CO oxidation (mixture A* experiment) to test for proper activity of the Au@G1/TiO_2//Si, was carried out. These results are reported in figure 14.2. Low CO conversions were measured in the usual range of operating temperatures of the CO-PrOx reaction over

Table 14.1: Inlet mixtures composition.

	Concentration (%)				Ratio
Mixture	CO	Air	H_2	Ar	H_2/CO
A*	2	10	0	88	0
B*	2	10	2	86	1
C*	2	10	41	47	20
D*	2	10	21	67	10

Au-based catalysts: CO conversion reached ca. 5% at T<393 K and 9% at 423 K. The light-off temperature (defined as the temperature where χ_{CO}=50% is reached) obtained was $T_{\chi_{CO}=50\%}$∼473 K. Finally, complete CO conversion was obtained at T≥673 K, which assured absence of bypasses in the micromonolith-washer-reactor assembly and of channels without catalyst coverage.

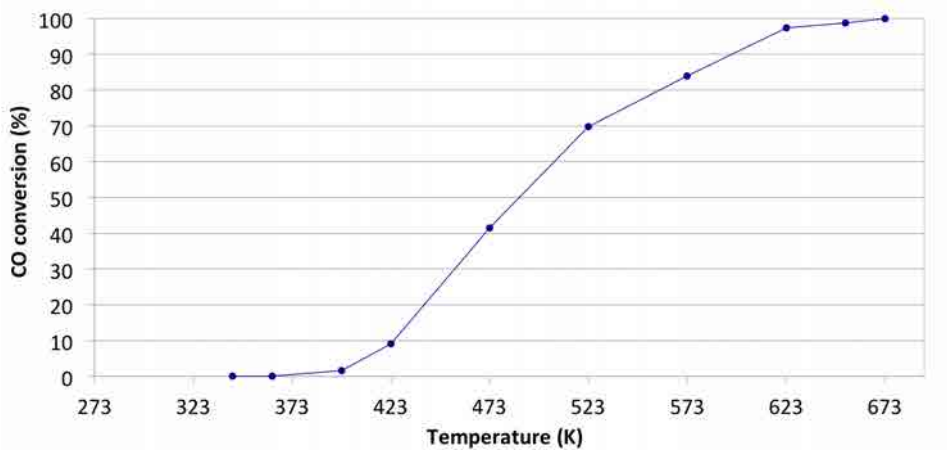

Figure 14.2: Light-off curve of pure CO oxidation for the Au@G1/TiO_2//Si catalyst.

The influence of different H_2 amounts in the inlet was tested at 363 K, 398 K and 433 K. At each reaction temperature evaluated, first mixture A* was dosed, then B*, D* and finally C*. Subsequently, the reaction temperature was risen and the same sequence of mixtures was tested. At 363 K, the maximum CO conversion was attained with mixture B*, but it was <2%. Therefore, these results are omitted and only the results obtained at 398 K and 433 K are presented in figure **14.3**.

As previously observed for cordierite monoliths and stainless steel microreactors (Chapters **12** and **13**, respectively), higher temperatures rendered higher CO conversions. For the Si micromonolith, the beneficial effect of dosing H_2 was also noticed and CO conversion increased when the inlet mixture was switched from

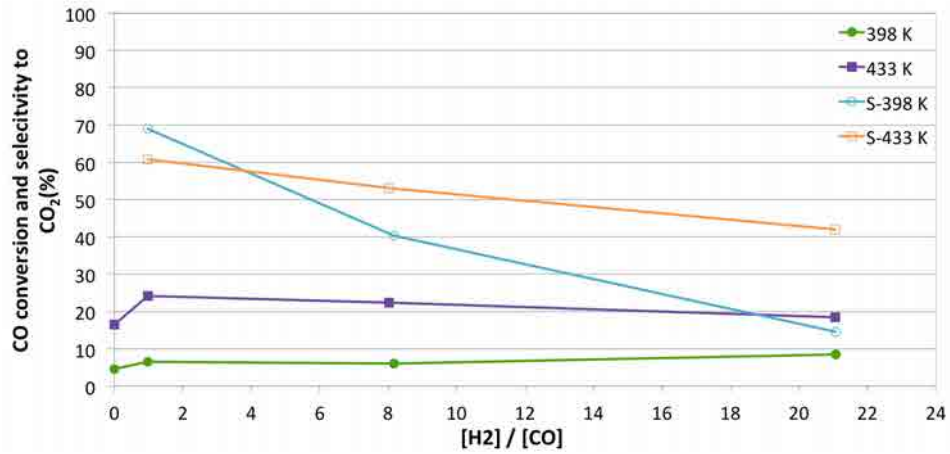

Figure 14.3: Influence of the H_2/CO ratio on CO conversion and selectivity to CO_2 for the Au@G1/TiO_2//Si.

mixture A* (0% H_2) to mixture B* (2% H_2). Conversely, when higher H_2 amounts were dosed, CO conversion progressively dropped. As regards selectivity to CO_2, a lot of error was noticed, as only 0.5% difference on H_2 conversion caused a 5% change on selectivity to CO_2. However, the general trends are correct. As seen in figure **14.3**, when the temperature was increased from 398 K to 433 K, the selectivity dropped from ∼70% to ∼60%, as expected and previously experienced with the stainless steel microreactors and cordierite monoliths. Also, higher amounts of hydrogen, led to lower selectivities to CO oxidation for both reaction temperatures.

14.3 Performance comparison of Au-based catalysts deposited on different substrates

As several CO abatement scales employing the same catalysts are explored in this Thesis, this section aims at comparing the catalytic performance of the Au-based catalysts deposited on different structural supports, namely cordierite monoliths, stainless steel microreactors and silicon micromonoliths.

As already mentioned in previous sections dedicated to the performance comparison between different functionalized substrates (see section **8.4** for the ESR performance comparison between the Si micromonolith and cordierite monoliths and section **13.4** for the CO-PrOx performance comparison between conventional stainless steel microreactors and cordierite monoliths), the direct comparison of their performances is unviable as the enormous differences between the dimensions of the substrates prevented the use of the same operating conditions. In this context, as the total mass of catalyst incorporated on Si microchannels could not be

unambiguously calculated and it could only be estimated, the activity attained by each functionalized substrate is normalized by reactor volume, defining a specific activity in terms of reactor volume, a* (see equation 14.2).

$$A = \frac{2}{100} \cdot \Phi \cdot \chi_{CO} \cdot \frac{1}{100} \tag{14.1}$$

$$a^\star = \frac{A}{V};\ [a^\star] = \frac{mL_{COconverted}}{min \cdot cm^3} \tag{14.2}$$

Two definitions can be considered for the reactor volume: the volume of the substrate occupied by the catalyst coating ($V_{Reactor}$) or the volume of the functionalized channels were the gases actually flow ($V_{Channels}$). Table 14.2 lists the reactor and channels volume of all the substrates tested.

Table 14.2: Reactor and channels' volume of the different substrates.

Substrate	Reactor dimensions	$V_{Reactor}$ (cm^3)	$V_{Channels}$ (cm^3)
CM[1]	ϕ[4]=1.8; L[5]=1.8 cm	4.58	2.27
SSM[2]	2.5 x 1.4 x 0.4 cm	1.40	$6.9 \cdot 10^{-2}$
SiM[3]	ϕ=0.7; L:0.2 mm	$7.7 \cdot 10^{-3}$	$2.6 \cdot 10^{-3}$

[1]CM: Cordierite monolith. [2]SSM: Stainless steel microreactor. [3]SiM: Silicon micromonolith. [4]ϕ: Diameter. [5]L: Length

The reaction performance of a freshly synthesized Au@G1/TiO_2//Mon (0.250 g catalyst) was evaluated for mixtures A*, B* and C* at 398 K and GHSV=$1.3 \cdot 10^3$ h^{-1}, and their corresponding specific activity was calculated. During these tests, CO conversions up to 80% were achieved. Besides, the specific activity exhibited by the Au@G0/TiO_2//Micro at 398 K and 433 K for mixtures A, B and C was calculated aiming to have a complete comparison. Figure 14.4 shows the specific activity in terms of reactor volume (a*) attained by Au@G1/TiO_2//Si, Au@G0/TiO_2//Micro and Au@G1/TiO_2//Mon catalysts for mixture C* (or C in the case of the conventional microreactor). In this plot, both GHSV and a* were calculated considering $V_{Reactor}$.

As seen in figure 14.4, the specific activity achieved by the micromonolithic structures outperformed that of cordierite monoliths; moreover, each scale reduction implied a specific activity increment. Operating at the same temperature, the Si micromonolith (SiM) showed an outstanding difference of specific activity of ca. 2 orders of magnitude higher when compared to the cordierite monoliths (CM) (even though CO conversion attained by the SiM was lower than that of the CM) and 1 order of magnitude higher than that of the stainless steel microreactors (SSM). As already pointed out in section 8.4, the increase in contact area when reducing the

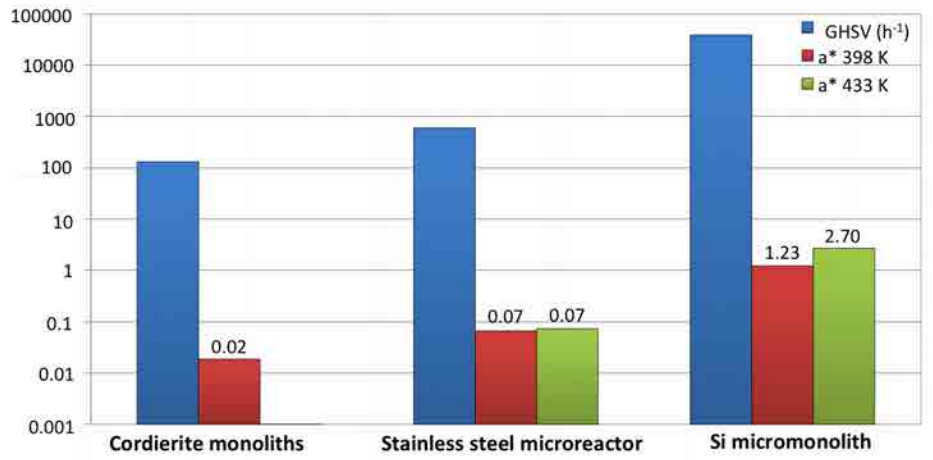

Figure 14.4: CO-PrOx performance comparison between Au@G1/TiO_2//Mon, Au@G0/TiO_2//Micro and Au@G1/TiO_2//Si. The specific activity is given at 398 K and 433 K; the corresponding units are shown in equation **14.2**.

scale from 400 cpsi CM to SiM enhances the specific activity, even if the reactor operates at higher space velocities (ca. 300-fold higher). The specific surface area or the area-to-volume ratio, calculated as the area of the channels divided by its volume, increased from $4.4{\cdot}10^3$ to $8.0{\cdot}10^3$ m^2/m^3, when reducing the scale from CM to SSM and it dramatically increased up to $1.2{\cdot}10^6$ m^2/m^3, when downscaling to the SiM. The higher specific surface area available in the microreactors led to higher specific activities.

Results presented in this Chapter were published in *N. J. Divins, E. López, M. Roig, T. Trifonov, A. Rodríguez, F. González de Rivera, L. I. Rodríguez, M. Seco, O. Rossell, J. Llorca, "A million-channel CO-PrOx microreactor on a fingertip for fuel cell application", Chemical Engineering Journal, 167 (2011), pp. 597* [269] and this one of the papers of this Thesis.

Figure **14.5** outlines the specific surface area, catalyst loading and specific activities achieved by the substrates investigated in this Thesis: 400 cpsi cordierite monoliths, stainless steel microreactors and silicon micromonoliths. As seen in this summarizing illustration, the reduction on the channels dimension brings along an increment on the specific surface area (m^2/m^3) of the structured substrates. This also involves a reduction of the catalyst mass used per substrate's surface, allowing for the usage of less catalyst. The increment in the surface area finally results in the improved specific activities attained by the silicon micromonoliths functionalized with Au/TiO_2 catalysts, as reported in this Chapter, as well as in the superior performance exhibited by the Si micromonolith functionalized with RhPd/CeO_2 catalyst, reported in Chapter 8.

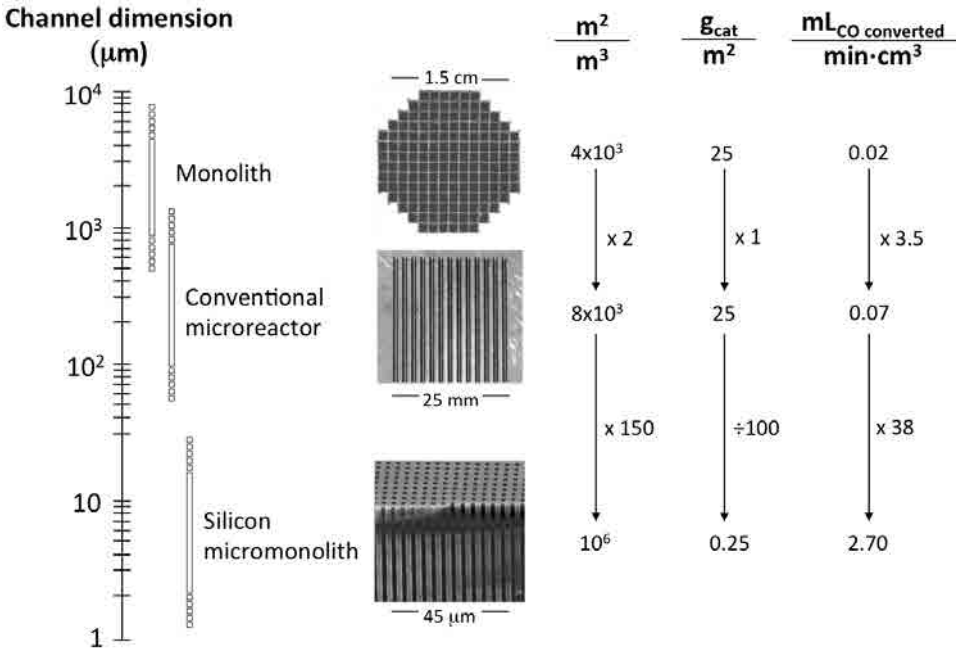

Figure 14.5: Comparison of the different structured reactors studied in this Thesis.

15 | Conclusions

The main objectives of this Thesis were the production of hydrogen through the ethanol steam reforming and the carbon monoxide abatement of reformate streams via its preferential oxidation. From the results described in this dissertation, the main conclusions extracted are:

PART I:

1. An effective washcoating method was established to prepare and functionalize cordierite monoliths with RhPd/CeO_2 catalysts prepared by precipitation and incipient wetness impregnation.

2. The characterization of RhPd/CeO_2 catalysts by TEM, SEM and XPS revealed a successful synthesis and the catalysts developed withstood the reaction conditions tested.

3. The catalytic activity of the RhPd/CeO_2 catalysts developed for the ethanol steam reforming reaction (ESR) was screened under realistic operational conditions. The results of the catalytic tests showed that *working* 1RhPd/CeO_2 catalysts were the most active for the ESR reaction, yielding the highest hydrogen productions without forming byproducts, such as coke precursors. 1RhPd/CeO_2 catalysts generated up to 3.7 moles of hydrogen per mole of ethanol fed at 950 K, S/C=3 and P=1.5 bar.

4. The *working* 1RhPd/CeO_2//Mon catalyst deactivated after 67 hours of operation with bioethanol, which contained sulfur and high-carbon-content compounds. However, only additional chlorine and C were detected on its surface after the bioethanol test by XPS. The usual catalytic activity of the catalyst was completely recovered by oxidizing the catalyst with air and without performing any activation treatment.

5. Stable performance for more than 100 hours was achieved by a modified *working* RhPd/CeO_2 catalyst feeding a commercial bioethanol.

6. The catalytic screening of the active phase, RhPd nanoparticles (NPs), and the CeO_2 support separately showed that a synergic effect existed between both. The catalytic activity of the 1RhPd/CeO_2 system was superior to the

addition of the activities attained by RhPd NPs and the CeO_2 support separately, both in terms of hydrogen yield and products distribution. Moreover, the formation of coke precursors was suppressed over the 1RhPd/CeO_2 catalyst.

7. The 1.5Pd@Rh/CeO_2 catalyst (Pd:Rh=75:1.3) showed a hydrogen production normalized by exposed area of noble metals close to the one attained by the 1RhPd/CeO_2 catalyst (Pd:Rh=1). However, the coke build-up of the 1.5Pd@Rh/CeO_2 catalyst (5 times the catalyst's mass) derived in a deficient ESR catalyst. Coke deposition could be related to the low amount of Rh in the catalyst, which is the element responsible for the C-C scission.

8. After the ESR conditions tested, RhPd NPs grew from 1-2 nm to 3.1± 1.2 nm, nevertheless they kept their bimetallic nature. Also, scarce carbon deposits were detected surrounding both RhPd NPs and the ceria support. Besides, after the hydrogen reduction at high temperature (1050 K), RhPd NPs and 3RhPd@D NPs experienced a similar growth up to ∼4 nm.

9. After *in situ* ESR tests, the 1RhPd/CeO_2 exhibited more oxidized Rh and Pd than after a reduction at the same temperature, in spite of the large amount of H_2 generated during the ESR reaction, as inferred by XPS.

10. *In situ* and *operando* XPS results of supported and unsupported RhPd@D NPs showed different oxidation states, indicating that the ceria support altered the oxidation states of Rh and Pd.

11. Ceria also altered the rearrangement of Rh and Pd, by limiting their segregation. Therefore, the metal-support interaction played an important role in the reorganization of the metal atoms.

12. *In situ* and *operando* XPS studies of the same catalytic systems (RhPd@D NPs and RhPd@D/CeO_2 catalyst) showed different results, denoting that some species only exist during the presence of the reactive atmosphere.

13. Pure hydrogen streams (H_2 purity>99.999%) were obtained coupling the RhPd/CeO_2//Mon catalyst to a Pd-Ag membrane. Permeate flows up to 110 mL_{H_2}/min, which represented ca. 3.6 $mL_{H_2}/(min{\cdot}cm^2{}_{membrane})$, were attained. Hydrogen recuperations ca. 70% were achieved at the highest permeate pressure tested (11 bar).

14. A successful methodology was established to functionalize Si micromonoliths, composed of more than 1.5 million channels of diameter 3.3 µm, with homogenous, thin and well-adhered layers of RhPd/CeO_2 catalyst. The appropriate periphery was implemented to perform ESR and oxidative steam reforming (OSR) tests.

15. Complete ethanol conversion was achieved by the 1RhPd/CeO_2//Si at temperatures higher than 873 K at a residence time of only 8.5 milliseconds (GHSV=$4.2{\cdot}10^5$ h^{-1}).

16. Hydrogen production rates up to 26 mL_{H_2}/min and 41 mL_{H_2}/min were achieved for ESR (S/C=3) and OSR (S/C=1, O/ethanol=0.56), respectively, at 873 K and at atmospheric pressure.

17. The Si micromonolith outperformed the cordierite monoliths for both ESR and OSR. The Si micromonolith exhibited specific hydrogen productions (hydrogen production normalized by reactor volume and ethanol fed) ∼160 $mL_{H_2}/(mL_{Ethanol}{\cdot}cm^3_{Reactor})$, which was two orders of magnitude higher than that attained by 400-cpsi monoliths.

18. The 1RhPd/CeO_2 catalyst deposited on the Si microchannels withstood reaction conditions. As inferred from the microfabricated TEM lamella, after the reaction conditions tested, RhPd NPs were still in close contact with the ceria support and maintained their alloyed nature.

PART II:

1. A synthesis method based on an alkoxide decomposition followed by impregnation was established to prepare and functionalize cordierite monoliths with Au/TiO_2 catalysts using the different generations of encapsulated gold NPs.

2. Gold NPs encapsulated in G0 dendrimers showed higher thermal stability than NPs encapsulated in dodecanethiols, as inferred by SEM and AFM.

3. By combining AFM, XPS and STEM analyses, it was possible to conclude that calcining at 1173 K Au@G0 NPs, the Si constituting the trimethylsilane dendrimers was oxidized to form SiO_2. The formed SiO_2 sat next to the Au cores, immobilizing them and preventing them from sintering.

4. Each Au-based catalyst exhibited a different optimum oxidation temperature that led to improved CO-PrOX performance. This effect could be related with the removal of the dodecanethiol and dendrimers shell and to the formation of a specific architecture of the Au-TiO_2 interface.

5. The Au@D/TiO_2//Mon exhibited the best CO-PrOX performance for a mixture containing 50% H_2 and 2% CO (λ=2) at 363 K, where 68% CO conversion and 38% selectivity to CO oxidation were achieved. On the other hand, for the Au@G0/TiO_2//Mon, the best performance for this mixture was recorded at 363 K and 398 K, where ∼50% CO conversion and 40% selectivity to CO oxidation were achieved.

6. The addition of 2% H_2 to a CO and O_2 mixture resulted in enhanced CO oxidation.

7. There existed a compromise between the length of the trimethylsilane dendrimers and the Au core: larger dendrimers shell led to lower catalytic activity.

8. The CO abatement scale was reduced by coating stainless steel microreactors with the catalysts that showed the best CO-PrOx performance supported on cordierite monoliths.

9. Au@G0/TiO_2//Micro and Au@D/TiO_2//Micro outperformed their counterparts supported on cordierite monoliths. The functionalized microreactors showed the same activity per gram of catalyst as cordierite monoliths; however the gas hourly space velocities were one order of magnitude higher and 10 times less catalyst was used on microreactors.

10. Au@G0/TiO_2//Micro and Au@D/TiO_2//Micro showed stable performance for ca. 500 hours of operation under a real, pre-cleaned reformate stream, containing 48.5% H_2, 0.85 % CO (λ=2), 18% CO_2 and 29% H_2O at 453 K.

11. A successful methodology was established to functionalize Si micromonoliths with a thin, homogeneous and well-adhered layer of Au/TiO_2 catalyst. Complete CO conversion was attained by the Au@G1/TiO_2//Si catalyst at temperatures higher than 673 K, assuring the absence of bypasses and channels without catalyst.

12. Up to 20% CO conversion was attained at a residence time of only 90 milliseconds for a mixture containing 50% H_2 with the Si micromonolith.

13. The scale reduction involved in the miniaturization of the substrates from 400-cpsi monoliths, to conventional stainless steel microreactors to, finally, the Si micromonoliths entailed several advantages. The specific activity (in terms of reactor volume) achieved by the micromonolithic structures outperformed that of cordierite monoliths and each scale reduction resulted in a specific activity increment. The Au@G1/TiO_2//Si showed a specific activity two orders of magnitude higher than the cordierite monoliths and one order of magnitude higher than conventional microreactors, despite that the Si micromonoliths were operated at much higher space velocities.

BIBLIOGRAPHY

[1] United Nations, "Millennium Development Goals and beyond 2015." http://www.un.org/millenniumgoals. Accessed 2014-09-16.

[2] International Energy Agency, "Key World Energy Statistics 2014," 2014.

[3] C. Song, "Fuel processing for low-temperature and high-temperature fuel cells: Challenges, and opportunities for sustainable development in the 21st century," *Catalysis Today*, vol. 77, pp. 17–49, Jan. 2002.

[4] British Petroleum (BP), "Statistical Review of World Energy June 2014," tech. rep., 2014.

[5] S. Dunn, "Hydrogen futures: toward a sustainable energy system," *International Journal of Hydrogen Energy*, vol. 27, pp. 235–264, Mar. 2002.

[6] E. Dlugokencky and P. Tans, "NOAA/ESRL." www.esrl.noaa.gov/gmd/ccgg/trends. Accessed 2015-02-02.

[7] Population Reference Bureau, "World Population Data Sheet 2012." http://www.prb.org/Publications/Datasheets/2012/world-population-data-sheet/data-sheet.aspx. Accessed 2015-02-02.

[8] S. K. Ritter, "Global warming and climate change," *Chemical Engineering News*, vol. 87, no. 51, pp. 11–21, 2009.

[9] Council of the European Union, "Climate Change Strategies 2005," Tech. Rep. March, European Union, 2005.

[10] J. Hansen, M. Sato, P. Kharecha, D. Beerling, R. Berner, V. Masson-Delmotte, M. Pagani, M. Raymo, D. L. Royer, and J. C. Zachos, "Target atmospheric CO_2: Where should humanity aim?," *The Open Atmospheric Science Journal*, vol. 2, pp. 217–231, Nov. 2008.

[11] L. M. Gandía, G. Arzamendi, and P. M. Diéguez, "Renewable hydrogen energy: An overview," in *Renewable Hydrogen Technologies* (L. M. Gandía, G. Arzamendi, and P. M. Diéguez, eds.), pp. 1–17, Amsterdam: Elsevier, 2013.

[12] International Energy Agency, "World Energy Statistics," 2013.

[13] European Climate Foundation, "Roadmap 2050: A pratical guide to a prosperous, low-carbon Europe," 2010.

[14] R. Gorham, "Air pollution from ground transportation. An assessment of causes, strategies and tactics, and proposed actions for the international community," *The Global Initiative on Transport Emissions Division for Sustainable Development*, 2002.

[15] D. R. Bohi and M. A. Toman, *The economics of energy security*. Springer, 1996.

[16] R. M. Navarro, M. A. Peña, and J. L. G. Fierro, "Hydrogen production reactions from carbon feedstocks: fossil fuels and biomass," *Chemical reviews*, vol. 107, pp. 3952–91, Oct. 2007.

[17] S. Sorrell, J. Speirs, R. Bentley, R. Miller, and E. Thompson, "Shaping the global oil peak: A review of the evidence on field sizes, reserve growth, decline rates and depletion rates," *Energy*, vol. 37, pp. 709–724, Jan. 2012.

[18] OPEC, "OPEC." http://www.opec.org/opec_web/en/data_graphs/330.htm. Accessed 2014-01-16.

[19] M. Ball and M. Wietschel, "The future of hydrogen - opportunities and challenges," *International Journal of Hydrogen Energy*, vol. 34, pp. 615–627, Jan. 2009.

[20] J. O. Bockris, "The hydrogen economy: Its history," *International Journal of Hydrogen Energy*, vol. 38, pp. 2579–2588, Feb. 2013.

[21] M. W. Jensen and M. Ross, "The ultimate challenge: Developing an infrastructure for fuel cell vehicles," *Environment*, vol. 42, pp. 10–22, Sept. 2000.

[22] J. Emsley, *Nature's Building Blocks: An A-Z Guide to the Elements*. Oxford Pakistan Paperbacks Series, Oxford University Press, 2001.

[23] N. Armaroli and V. Balzani, "The Hydrogen Issue," *ChemSusChem*, vol. 4, no. 1, pp. 21–36, 2011.

[24] G. A. Olah, A. Goeppert, and G. K. S. Prakash, "The hydrogen economy and its limitations," in *Beyond Oil and Gas: The Methanol Economy*, pp. 143–178, Wiley-VCH Verlag GmbH & Co. KGaA, 2009.

[25] G. A. Deluga, J. R. Salge, L. D. Schmidt, and X. E. Verykios, "Renewable hydrogen from ethanol by autothermal reforming.," *Science (New York, N.Y.)*, vol. 303, pp. 993–997, Feb. 2004.

[26] J. Llorca, *El hidrógeno y nuestro futuro energético*. Edicions de la Universitat Politecnica de Catalunya, S.L., 2010.

[27] G. Ertl, "Gerhard Ertl- Facts." http://www.nobelprize.org/nobel_prizes/chemistry/laureates/2007/ertl-facts.html. Accessed 2015-02-02, 2007.

[28] Fuel Cells 2000, "Fuel Cells." http://www.fuelcells.org. Accessed 2014-01-21.

[29] T. V. Choudhary and D. W. Goodman, "CO-free fuel processing for fuel cell applications," *Catalysis Today*, vol. 77, pp. 65–78, Jan. 2002.

[30] R. Farrauto, S. Hwang, L. Shore, W. Ruettinger, J. Lampert, T. Giroux, Y. Liu, and O. Ilinich, "New material needs for hydrocarbon fuel processing: Generating Hydrogen for the PEM Fuel Cell," *Annual Review of Materials Research*, vol. 33, pp. 1–27, Aug. 2003.

[31] A. J. Martín, A. Hornés, A. Martínez-Arias, and L. Daza, "Chapter 15 - Recent advances in fuel cells for transport and stationary applications," in *Renewable Hydrogen Technologies* (L. M. Gandía, G. Arzamendi, and P. M. Diéguez, eds.), pp. 361–380, Amsterdam: Elsevier, 2013.

[32] G. Kolb, *Fuel processing for fuel cells*. Wiley-VCH Verlag GmbH & Co. KGaA, 2008.

[33] A. Haryanto, S. Fernando, N. Murali, and S. Adhikari, "Current status of hydrogen production techniques by steam reforming of ethanol: A review," *Energy & Fuels*, vol. 19, pp. 2098–2106, Sept. 2005.

[34] K. Liu, A. Wang, and T. Zhang, "Recent advances in preferential oxidation of CO reaction over platinum group metal catalysts," *ACS Catalysis*, vol. 2, no. 6, pp. 1165–1178, 2012.

[35] F. Gallucci and A. Basile, "Pd-Ag membrane reactor for steam reforming reactions: A comparison between different fuels," *International Journal of Hydrogen Energy*, vol. 33, pp. 1671–1687, Mar. 2008.

[36] A. Basile, "Hydrogen production using Pd-based membrane reactors for fuel cells," *Topics in Catalysis*, vol. 51, no. 1-4, pp. 107–122, 2008.

[37] D. Mendes, S. Tosti, F. Borgognoni, A. Mendes, and L. M. Madeira, "Integrated analysis of a membrane-based process for hydrogen production from ethanol steam reforming," *Catalysis Today*, vol. 156, pp. 107–117, Oct. 2010.

[38] E. López, N. J. Divins, and J. Llorca, "Hydrogen production from ethanol over Pd-Rh/CeO_2 with a metallic membrane reactor," *Catalysis Today*, vol. 193, pp. 145–150, Oct. 2012.

[39] J. Llorca, V. Cortés Corberán, N. J. Divins, R. O. Fraile, and E. Taboada, "Chapter 7 - Hydrogen from bioethanol," in *Renewable Hydrogen Technologies* (L. M. Gandía, G. Arzamendi, and P. M. Diéguez, eds.), pp. 135–169, Amsterdam: Elsevier, 2013.

[40] M. Vadrucci, F. Borgognoni, A. Moriani, A. Santucci, and S. Tosti, "Hydrogen permeation through Pd-Ag membranes: Surface effects and Sieverts' law," *International Journal of Hydrogen Energy*, vol. 38, pp. 4144–4152, Apr. 2013.

[41] R. J. Farrauto, Y. Liu, W. Ruettinger, O. Ilinich, L. Shore, and T. Giroux, "Precious metal catalysts supported on ceramic and metal monolithic structures for the hydrogen economy," *Catalysis Reviews*, vol. 49, pp. 141–196, Mar. 2007.

[42] S. Ivanova, O. H. Laguna, M. A. Centeno, A. Eleta, M. Montes, and J. A. Odriozola, "Chapter 10 - Microprocess technology for hydrogen purification," in *Renewable Hydrogen Technologies* (L. M. Gandia, G. Arzamendi, and P. M. Dieguez, eds.), pp. 225–243, Amsterdam: Elsevier, 2013.

[43] J. D. Holladay, Y. Wang, and E. Jones, "Review of developments in portable hydrogen production using microreactor technology.," *Chemical reviews*, vol. 104, pp. 4767–89, Oct. 2004.

[44] K. F. Jensen, "Microreaction engineering: is small better?," *Chemical Engineering Science*, vol. 56, pp. 293–303, Jan. 2001.

[45] G. Kolb and V. Hessel, "Micro-structured reactors for gas phase reactions," *Chemical Engineering Journal*, vol. 98, pp. 1–38, Mar. 2004.

[46] J. Llorca, A. Casanovas, T. Trifonov, A. Rodriguez, and R. Alcubilla, "First use of macroporous silicon loaded with catalyst film for a chemical reaction: A microreformer for producing hydrogen from ethanol steam reforming," *Journal of Catalysis*, vol. 255, no. 2, pp. 228–233, 2008.

[47] V. Lehmann, "The physics of macropore formation in low doped n-type silicon," *Journal of The Electrochemical Society*, vol. 140, pp. 2836–2843, Oct. 1993.

[48] G. Barillaro and F. Pieri, "A self-consistent theoretical model for macropore growth in n-type silicon," *Journal of Applied Physics*, vol. 97, no. 11, p. 116105, 2005.

[49] S. Roy, R. Raju, H. F. Chuang, B. A. Cruden, and M. Meyyappan, "Modeling gas flow through microchannels and nanopores," *Journal of Applied Physics*, vol. 93, no. 8, p. 4870, 2003.

[50] D. Pimentel, "Ethanol Fuels: Energy balance, economics and environmental impacts are negative," *Natural resources research*, vol. 12, no. 2, pp. 127–134, 2003.

[51] M. Galbe and G. Zacchi, "A review of the production of ethanol from softwood.," *Applied microbiology and biotechnology*, vol. 59, pp. 618–28, Sept. 2002.

[52] S. Cavallaro, "Ethanol Steam Reforming on Rh/Al_2O_3 Catalysts," - *Energy & Fuels*, no. 6, p. 1195, 2000.

[53] F. Auprêtre, C. Descorme, and D. Duprez, "Bio-ethanol catalytic steam reforming over supported metal catalysts," *Catalysis Communications*, vol. 3, no. 6, pp. 263–267, 2002.

[54] J. P. Breen, R. Burch, and H. M. Coleman, "Metal-catalysed steam reforming of ethanol in the production of hydrogen for fuel cell applications," *Applied Catalysis B: Environmental*, vol. 39, pp. 65–74, Aug. 2002.

[55] C. Diagne, H. Idriss, and A. Kiennemann, "Hydrogen production by ethanol reforming over Rh/CeO_2-ZrO_2 catalysts," *Catalysis Communications*, vol. 3, no. 12, pp. 565–571, 2002.

[56] F. Romero-Sarria, J. C. A. Vargas, A.-C. A. Roger, and A. Kiennemann, "Hydrogen production by steam reforming of ethanol: Study of mixed oxide catalysts $Ce_2Zr_{1.5}Me_{0.5}O_8$: Comparison of Ni/Co and effect of Rh," *Selected Contributions of the XX Ibero-American Symposium of Catalysis*, vol. 133-135, no. 0, pp. 149–153, 2008.

[57] M. Dömök, A. Oszkó, K. Baán, I. Sarusi, and A. Erdöhelyi, "Reforming of ethanol on Pt/Al_2O_3-ZrO_2 catalyst," *Applied Catalysis A: General*, vol. 383, pp. 33–42, July 2010.

[58] D. K. Liguras, D. I. Kondarides, and X. E. Verykios, "Production of hydrogen for fuel cells by steam reforming of ethanol over supported noble metal catalysts," *Applied Catalysis B: Environmental*, vol. 43, no. 4, pp. 345–354, 2003.

[59] I. A. C. Ramos, T. Montini, B. Lorenzut, H. Troiani, F. C. Gennari, M. Graziani, and P. Fornasiero, "Hydrogen production from ethanol steam reforming on $M/CeO_2/YSZ$ (M=Ru, Pd, Ag) nanocomposites," *Recent developments in the characterization and application of nanostructured ceria based catalysts-Prof. Serafin Bernal Festschrift*, vol. 180, no. 1, pp. 96–104, 2012.

[60] B. Zhang, W. Cai, Y. Li, Y. Xu, and W. Shen, "Hydrogen production by steam reforming of ethanol over an Ir/CeO_2 catalyst: Reaction mechanism and stability of the catalyst," *International Journal of Hydrogen Energy*, vol. 33, no. 16, pp. 4377–4386, 2008.

[61] J.-Y. Siang, C.-C. Lee, C.-H. Wang, W.-T. Wang, C.-Y. Deng, C.-T. Yeh, and C.-B. Wang, "Hydrogen production from steam reforming of ethanol using a ceria-supported iridium catalyst: Effect of different ceria supports," *International Journal of Hydrogen Energy*, vol. 35, no. 8, pp. 3456–3462, 2010.

[62] M. C. Sanchez-Sanchez, R. M. Navarro Yerga, D. I. Kondarides, X. E. Verykios, and J. L. G. Fierro, "Mechanistic aspects of the ethanol steam reforming reaction for hydrogen production on Pt, Ni, and PtNi catalysts supported on γ-Al_2O_3," *The Journal of Physical Chemistry A*, vol. 114, no. 11, p. 3873, 2010.

[63] H. Idriss, M. Scott, J. Llorca, S. Chan, W. Chiu, P.-Y. Sheng, A. Yee, M. Blackford, S. Pas, A. Hill, F. Alamgir, R. Rettew, C. Petersburg, S. Senanayake, and M. Barteau, "A phenomenological study of the metal-oxide interface: The role of catalysis in hydrogen production from renewable resources," *ChemSusChem*, vol. 1, no. 11, pp. 905–910, 2008.

[64] M. Scott, M. Goeffroy, W. Chiu, M. Blackford, and H. Idriss, "Hydrogen production from ethanol over $RhPd/CeO_2$ catalysts," *Topics in Catalysis*, vol. 51, no. 1, pp. 13–21, 2008.

[65] H. Idriss, "Ethanol reactions over the surfaces of noble metal/cerium oxide catalysts," *Platinum Metals Rev.*, vol. 48, no. 3, pp. 105–115, 2004.

[66] A. Simson, R. Farrauto, and M. Castaldi, "Steam reforming of ethanol/gasoline mixtures: Deactivation, regeneration and stable performance," *Applied Catalysis B: Environmental*, vol. 106, pp. 295–303, Nov. 2011.

[67] M. Cobo, D. Pieruccini, R. Abello, L. Ariza, L. F. Córdoba, and J. a. Conesa, "Steam reforming of ethanol over bimetallic $RhPt/La_2O_3$: Long-term stability under favorable reaction conditions," *International Journal of Hydrogen Energy*, vol. 38, pp. 5580–5593, May 2013.

[68] V. Palma, F. Castaldo, P. Ciambelli, G. Iaquaniello, and G. Capitani, "On the activity of bimetallic catalysts for ethanol steam reforming," *International Journal of Hydrogen Energy*, vol. 38, pp. 6633–6645, May 2013.

[69] S. M. de Lima, R. C. Colman, G. Jacobs, B. H. Davis, K. R. Souza, A. F. de Lima, L. G. Appel, L. V. Mattos, and F. B. Noronha, "Hydrogen production from ethanol for PEM fuel cells. An integrated fuel processor comprising ethanol steam reforming and preferential oxidation of CO," *Catalysis Today*, vol. 146, pp. 110–123, Aug. 2009.

[70] S. M. de Lima, A. M. Silva, U. M. Graham, G. Jacobs, B. H. Davis, L. V. Mattos, and F. A. B. Noronha, "Ethanol decomposition and steam reforming

of ethanol over $CeZrO_2$ and $Pt/CeZrO_2$ catalyst: Reaction mechanism and deactivation," *Applied Catalysis A: General*, vol. 352, no. 1-2, pp. 95–113, 2009.

[71] Y. Chen, Z. Shao, and N. Xu, "Ethanol Steam Reforming over Pt Catalysts Supported on $Ce_xZr_{1-x}O_2$ Prepared via a Glycine Nitrate Process," *Energy & Fuels*, vol. 22, pp. 1873–1879, May 2008.

[72] M. a. Goula, S. K. Kontou, and P. E. Tsiakaras, "Hydrogen production by ethanol steam reforming over a commercial Pd/γ-Al_2O_3 catalyst," *Applied Catalysis B: Environmental*, vol. 49, pp. 135–144, May 2004.

[73] V. Galvita, G. Semin, V. Belyaev, V. Semikolenov, P. Tsiakaras, and V. Sobyanin, "Synthesis gas production by steam reforming of ethanol," *Applied Catalysis A: General*, vol. 220, pp. 123–127, Oct. 2001.

[74] V. Galvita, V. Belyaev, V. Semikolenov, P. Tsiakaras, A. Frumin, and V. Sobyanin, "Ethanol decomposition over Pd-based catalyst in the presence of steam," *Reaction Kinetics and Catalysis Letters*, vol. 76, pp. 343–351, July 2002.

[75] E. Gucciardi, V. Chiodo, S. Freni, S. Cavallaro, A. Galvagno, and J. C. J. Bart, "Ethanol and dimethyl ether steam reforming on Rh/Al_2O_3 catalysts for high-temperature fuel-cell feeds," *Reaction Kinetics, Mechanisms and Catalysis*, vol. 104, pp. 75–87, June 2011.

[76] S. M. de Lima, A. M. da Silva, L. O. da Costa, U. M. Graham, G. Jacobs, B. H. Davis, L. V. Mattos, and F. B. Noronha, "Study of catalyst deactivation and reaction mechanism of steam reforming, partial oxidation, and oxidative steam reforming of ethanol over Co/CeO_2 catalyst," *Journal of Catalysis*, vol. 268, pp. 268–281, Dec. 2009.

[77] H. Song and U. Ozkan, "Ethanol steam reforming over Co-based catalysts: Role of oxygen mobility," *Journal of Catalysis*, vol. 261, pp. 66–74, Jan. 2009.

[78] J. A. Rodriguez, S. Ma, P. Liu, J. Hrbek, J. Evans, and M. Pérez, "Activity of CeO_x and TiO_x nanoparticles grown on Au(111) in the water-gas shift reaction.," *Science (New York, N.Y.)*, vol. 318, pp. 1757–60, Dec. 2007.

[79] A. Trovarelli, "Catalytic properties of ceria and CeO_2-containing materials," *Catalysis Reviews*, vol. 38, pp. 439–520, Nov. 1996.

[80] M. S. Scott and H. Idriss, "Heterogeneous catalysis for hydrogen production," in *Handbook of Green Chemistry*, Wiley-VCH Verlag GmbH & Co. KGaA, 2010.

[81] P. Ciambelli, V. Palma, and A. Ruggiero, "Low temperature catalytic steam reforming of ethanol. 2. Preliminary kinetic investigation of Pt/CeO_2 catalysts," *Applied Catalysis B: Environmental*, vol. 96, no. 1-2, pp. 190–197, 2010.

[82] A. Erdöhelyi, J. Raskó, T. Kecskés, M. Tóth, M. Dömök, and K. Baán, "Hydrogen formation in ethanol reforming on supported noble metal catalysts," *Catalysis Today*, vol. 116, pp. 367–376, Aug. 2006.

[83] A. Birot, F. Epron, C. Descorme, and D. Duprez, "Ethanol steam reforming over $Rh/CexZr1\text{-}xO_2$ catalysts: Impact of the $CO\text{-}CO_2\text{-}CH4$ interconversion reactions on the H_2 production," *Applied Catalysis B: Environmental*, vol. 79, no. 1, pp. 17–25, 2008.

[84] H.-S. Roh, Y. Wang, D. King, A. Platon, and Y.-H. Chin, "Low temperature and H_2 selective catalysts for ethanol steam reforming," *Catalysis Letters*, vol. 108, no. 1, pp. 15–19, 2006.

[85] N. R. Peela, A. Mubayi, and D. Kunzru, "Steam reforming of ethanol over $Rh/CeO_2/Al_2O_3$ catalysts in a microchannel reactor," *Chemical Engineering Journal*, vol. 167, pp. 578–587, Mar. 2011.

[86] L. De Rogatis, T. Montini, M. F. Casula, and P. Fornasiero, "Design of $Rh/Ce_{0.2}Zr_{0.8}O_2\text{-}Al_2O_3$ nanocomposite for ethanol steam reforming," *Journal of Alloys and Compounds*, vol. 451, pp. 516–520, Feb. 2008.

[87] H.-S. Roh, Y. Wang, and D. L. King, "Selective Production of H_2 from Ethanol at Low Temperatures over $Rh/ZrO_2–CeO_2$ Catalysts," *Topics in Catalysis*, vol. 49, pp. 32–37, May 2008.

[88] J. S. Moura, M. O. Souza, J. D. A. Bellido, E. M. Assaf, M. Opportus, P. Reyes, and M. d. C. Rangel, "Ethanol steam reforming over rhodium and cobalt-based catalysts: Effect of the support," *International Journal of Hydrogen Energy*, vol. 37, pp. 3213–3224, Feb. 2012.

[89] M. Dömök, K. Baán, T. Kecskés, and A. Erdőhelyi, "Promoting Mechanism of Potassium in the Reforming of Ethanol on Pt/Al_2O_3 Catalyst," *Catalysis Letters*, vol. 126, pp. 49–57, Sept. 2008.

[90] S. M. de Lima, A. M. da Silva, G. Jacobs, B. H. Davis, L. V. Mattos, and F. B. Noronha, "New approaches to improving catalyst stability over Pt/ceria during ethanol steam reforming: Sn addition and CO_2 co-feeding," *Applied Catalysis B: Environmental*, vol. 96, pp. 387–398, June 2010.

[91] P. Yaseneva, S. Pavlova, V. Sadykov, G. Alikina, A. Lykashevich, V. Rogov, S. Belochapkine, and J. Ross, "Combinatorial approach to the preparation

and characterization of catalysts for biomass steam reforming into syngas," *Catalysis Today*, vol. 137, pp. 23–28, Aug. 2008.

[92] J. Kaspar and P. Fornasiero, "Structural properties and thermal stability of ceria-zirconia and related materials," in *Catalysis by Ceria and Related Materials*, vol. Volume 2 of *Catalytic Science Series*, pp. 217–241, Imperial College Press, Jan. 2002.

[93] F. Can, A. Le Valant, N. Bion, F. Epron, and D. Duprez, "New active and selective Rh-REO x-Al_2O_3 catalysts for ethanol steam reforming," *The Journal of Physical Chemistry C*, vol. 112, pp. 14145–14153, 2008.

[94] A. Le Valant, F. Can, N. Bion, D. Duprez, and F. Epron, "Hydrogen production from raw bioethanol steam reforming : Optimization of catalyst composition with improved stability against various impurities," *International Journal of Hydrogen Energy*, vol. 35, no. 10, pp. 5015–5020, 2010.

[95] A. Le Valant, A. Garron, N. Bion, F. Epron, and D. Duprez, "Hydrogen production from raw bioethanol over $Rh/MgAl_2O_4$ catalyst," *Catalysis Today*, vol. 138, pp. 169–174, Nov. 2008.

[96] A. Le Valant, A. Garron, N. Bion, D. Duprez, and F. Epron, "Effect of higher alcohols on the performances of a $1\%Rh/MgAl_2O_4/Al_2O_3$ catalyst for hydrogen production by crude bioethanol steam reforming," *International Journal of Hydrogen Energy*, vol. 36, pp. 311–318, Jan. 2011.

[97] F. Frusteri, S. Freni, V. Chiodo, L. Spadaro, O. Di Blasi, G. Bonura, and S. Cavallaro, "Steam reforming of bio-ethanol on alkali-doped Ni/MgO catalysts: hydrogen production for MC fuel cell," *Applied Catalysis A: General*, vol. 270, pp. 1–7, Aug. 2004.

[98] J. Kugai, S. Velu, and C. Song, "Low-temperature reforming of ethanol over CeO_2-supported Ni-Rh bimetallic catalysts for hydrogen production," *Catalysis Letters*, vol. 101, pp. 255–264, June 2005.

[99] M. Li, X. Wang, S. Li, S. Wang, and X. Ma, "Hydrogen production from ethanol steam reforming over nickel based catalyst derived from Ni/Mg/Al hydrotalcite-like compounds," *International Journal of Hydrogen Energy*, vol. 35, pp. 6699–6708, July 2010.

[100] W. Wang, "Production of Hydrogen by Steam Reforming of Bio-Ethanol Over Nickel-Copper Bimetallic Catalysts," *International Journal of Green Energy*, vol. 6, pp. 92–103, Feb. 2009.

[101] Y. Yang, J. Ma, and F. Wu, "Production of hydrogen by steam reforming of ethanol over a Ni/ZnO catalyst," *International Journal of Hydrogen Energy*, vol. 35, pp. 877–882, June 2006.

[102] A. Bshish, Z. Yaakob, B. Narayanan, R. Ramakrishnan, and A. Ebshish, "Steam-reforming of ethanol for hydrogen production," *Chemical Papers*, vol. 65, pp. 251–266, Apr. 2011.

[103] M. H. Youn, J. G. Seo, P. Kim, J. J. Kim, H.-I. Lee, and I. K. Song, "Hydrogen production by auto-thermal reforming of ethanol over Ni/γ-Al_2O_3 catalysts: Effect of second metal addition," *Journal of Power Sources*, vol. 162, pp. 1270–1274, Nov. 2006.

[104] M. H. Youn, J. G. Seo, P. Kim, and I. K. Song, "Role and effect of molybdenum on the performance of Ni-Mo/γ-Al_2O_3 catalysts in the hydrogen production by auto-thermal reforming of ethanol," *Journal of Molecular Catalysis A: Chemical*, vol. 261, pp. 276–281, Jan. 2007.

[105] A. Vizcaino, P. Arena, G. Baronetti, A. Carrero, J. Calles, M. Laborde, and N. Amadeo, "Role and effect of molybdenum on the performance of Ni-Mo/γ-Al_2O_3 catalysts in the hydrogen production by auto-thermal reforming of ethanol," *International Journal of Hydrogen Energy*, vol. 33, pp. 3489–3492, July 2008.

[106] D. Sahoo, S. Vajpai, S. Patel, and K. Pant, "Kinetic modeling of steam reforming of ethanol for the production of hydrogen over Co/Al_2O_3 catalyst," *Chemical Engineering Journal*, vol. 125, pp. 139–147, Jan. 2007.

[107] A. M. Karim, Y. Su, J. Sun, C. Yang, J. J. Strohm, D. L. King, and Y. Wang, "A comparative study between Co and Rh for steam reforming of ethanol," *Applied Catalysis B: Environmental*, vol. 96, pp. 441–448, June 2010.

[108] H. Song, L. Zhang, and U. S. Ozkan, "Investigation of the Reaction Network in Ethanol Steam Reforming over Supported Cobalt Catalysts," *Industrial & Engineering Chemistry Research*, vol. 49, pp. 8984–8989, Oct. 2010.

[109] J. Llorca, P. Ramírez de la Piscina, J.-A. Dalmon, and N. Homs, "Transformation of Co 3 O 4 during Ethanol Steam-Re-forming. Activation Process for Hydrogen Production," *Chemistry of Materials*, vol. 16, pp. 3573–3578, Sept. 2004.

[110] B. Bayram, I. I. Soykal, D. von Deak, J. T. Miller, and U. S. Ozkan, "Ethanol steam reforming over Co-based catalysts: Investigation of cobalt coordination environment under reaction conditions," *Journal of Catalysis*, vol. 284, pp. 77–89, Nov. 2011.

[111] P. Bichon, G. Haugom, H. J. Venvik, A. Holmen, and E. A. Blekkan, "Steam Reforming of Ethanol Over Supported Co and Ni Catalysts," *Topics in Catalysis*, vol. 49, pp. 38–45, Apr. 2008.

[112] Y. Men, G. Kolb, R. Zapf, V. Hessel, and H. Löwe, "Ethanol steam reforming in a microchannel reactor," *Process Safety and Environmental Protection*, vol. 85, pp. 413–418, Jan. 2007.

[113] X. Peng, Q. Pan, G. L. Rempel, and S. Wu, "Synthesis, characterization, and application of PdPt and PdRh bimetallic nanoparticles encapsulated within amine-terminated poly(amidoamine) dendrimers," *Catalysis Communications*, vol. 11, pp. 62–66, Oct. 2009.

[114] J. C. Garcia-Martinez and R. M. Crooks, "Extraction of Au nanoparticles having narrow size distributions from within dendrimer templates," *Journal of the American Chemical Society*, vol. 126, pp. 16170–16178, Nov. 2004.

[115] N. J. Divins, I. Angurell, C. Escudero, V. Pérez-Dieste, and J. Llorca, "Influence of the support on surface rearrangements of bimetallic nanoparticles in real catalysts," *Science (New York, N.Y.)*, vol. 346, pp. 620–623, 2014.

[116] M. Friederici, I. Angurell, O. Rossell, M. Seco, N. J. Divins, and J. Llorca, "Facile synthesis of palladium nanoparticles protected with alkanethiolates functionalized with organometallic fragments," *Organometallics*, vol. 31, pp. 722–728, Jan. 2012.

[117] S. Brunauer, P. H. Emmett, and E. Teller, "Adsorption of gases in multimolecular layers," *Journal of the American Chemical Society*, vol. 60, pp. 309–319, Feb. 1938.

[118] E. P. Barrett, L. G. Joyner, and P. P. Halenda, "The determination of pore volume and area distributions in porous substances. I. Computations from nitrogen isotherms," *Journal of the American Chemical Society*, vol. 73, pp. 373–380, Jan. 1951.

[119] Y. Qi, J. Wu, H. Zhang, Y. Jiang, C. Jin, M. Fu, H. Yang, and D. Yang, "Facile synthesis of Rh-Pd alloy nanodendrites as highly active and durable electrocatalysts for oxygen reduction reaction," *Nanoscale*, vol. 6, no. 12, pp. 7012–7018, 2014.

[120] E. Aneggi, J. Llorca, M. Boaro, and A. Trovarelli, "Surface-structure sensitivity of CO oxidation over polycrystalline ceria powders," *Journal of Catalysis*, vol. 234, pp. 88–95, Aug. 2005.

[121] D. R. Mullins, S. H. Overbury, and D. R. Huntley, "Electron spectroscopy of single crystal and polycrystalline cerium oxide surfaces," *Surface Science*, vol. 409, no. 2, pp. 307–319, 1998.

[122] C. Wagner, W. Riggs, and L. Davis, "Handbook of X-ray photoelectron spectroscopy," *PerkinElmer, Waltham*, 1979.

[123] J. Xu and G. F. Froment, "Methane steam reforming, methanation and water-gas shift: I. Intrinsic kinetics," *AIChE Journal*, vol. 35, pp. 88–96, Jan. 1989.

[124] E. López, G. Kolios, and G. Eigenberger, "Preferential oxidation of CO in a folded-plate reactor," *Chemical Engineering Science*, vol. 62, no. 18-20, pp. 5598–5601, 2007.

[125] J. Comas, F. Mariño, M. Laborde, and N. Amadeo, "Bio-ethanol steam reforming on Ni/Al_2O_3 catalyst," *Chemical Engineering Journal*, vol. 98, pp. 61–68, Mar. 2004.

[126] A. Fatsikostas and X. E. Verykios, "Reaction network of steam reforming of ethanol over Ni-based catalysts," *Journal of Catalysis*, vol. 225, pp. 439–452, July 2004.

[127] E. López, N. J. Divins, A. Anzola, S. Schbib, D. Borio, and J. Llorca, "Ethanol steam reforming for hydrogen generation over structured catalysts," *International Journal of Hydrogen Energy*, vol. 38, pp. 4418–4428, Apr. 2013.

[128] C. Wheeler, "The water-gas shift reaction at short contact times," *Journal of Catalysis*, vol. 223, pp. 191–199, Apr. 2004.

[129] J. A. Farmer and C. T. Campbell, "Ceria maintains smaller metal catalyst particles by strong metal-support bonding," *Science*, vol. 329, pp. 933–936, Aug. 2010.

[130] Y. Suchorski, L. Rihko-Struckmann, F. Klose, Y. Ye, M. Alandjiyska, K. Sundmacher, and H. Weiss, "Evolution of oxidation states in vanadium-based catalysts under conventional XPS conditions," *Applied Surface Science*, vol. 249, pp. 231–237, Aug. 2005.

[131] I. Lopez-Salido, D. C. Lim, and Y. D. Kim, "Ag nanoparticles on highly ordered pyrolytic graphite (HOPG) surfaces studied using STM and XPS," *Surface Science*, vol. 588, pp. 6–18, Aug. 2005.

[132] J. Radnik, C. Mohr, and P. Claus, "On the origin of binding energy shifts of core levels of supported gold nanoparticles and dependence of pretreatment and material synthesis," *Physical Chemistry Chemical Physics*, vol. 5, pp. 172–177, Dec. 2003.

[133] J. Moulder, W. Stickle, P. Sobol, and K. Bomben, "Handbook of XPS," *Perkin Elmer Corporation, Eden Prairie, Minnesota*, 1992.

[134] A. Gayen, K. R. Priolkar, P. R. Sarode, V. Jayaram, M. S. Hegde, G. N. Subbanna, and S. Emura, "$Ce_{1-x}Rh_xO_{2-\delta}$ solid solution formation in combustion-synthesized Rh/CeO_2 catalyst studied by XRD, TEM, XPS and EXAFS," *Chemistry of Materials*, vol. 16, no. 11, pp. 2317–2328, 2004.

[135] P. S. Bagus, E. S. Ilton, and C. J. Nelin, "The interpretation of XPS spectra: Insights into materials properties," *Surface Science Reports*, vol. 68, pp. 273–304, June 2013.

[136] J. Kugai, V. Subramani, C. Song, M. Engelhard, and Y. Chin, "Effects of nanocrystalline CeO_2 supports on the properties and performance of Ni–Rh bimetallic catalyst for oxidative steam reforming of ethanol," *Journal of Catalysis*, vol. 238, pp. 430–440, Mar. 2006.

[137] A. Talo, J. Lahtinen, and P. Hautojärvi, "An XPS study of metallic three-way catalysts: The effect of additives on platinum, rhodium, and cerium," *Applied Catalysis B: Environmental*, vol. 5, pp. 221–231, Feb. 1995.

[138] K. Sun, W. Lu, M. Wang, and X. Xu, "Characterization and catalytic performances of La doped Pd/CeO_2 catalysts for methanol decomposition," *Applied Catalysis A: General*, vol. 268, pp. 107–113, 2004.

[139] K. Otto, L. Haack, and J. DeVries, "Identification of two types of oxidized palladium on γ-alumina by X-ray photoelectron spectroscopy," *Applied Catalysis B: Environmental*, vol. 1, pp. 1–12, Feb. 1992.

[140] E. J. Peterson, A. T. DeLaRiva, S. Lin, R. S. Johnson, H. Guo, J. T. Miller, J. Hun Kwak, C. H. F. Peden, B. Kiefer, L. F. Allard, F. H. Ribeiro, and A. K. Datye, "Low-temperature carbon monoxide oxidation catalysed by regenerable atomically dispersed palladium on alumina.," *Nature communications*, vol. 5, p. 4885, Jan. 2014.

[141] D. I. Kondarides and X. E. Verykios, "Effect of chlorine on the chemisorptive properties of Rh/CeO_2 catalysts studied by XPS and temperature programmed desorption techniques," *Journal of Catalysis*, vol. 174, pp. 52–64, 1998.

[142] *User manual for the X-ray source XR-50.* Berlin, Germany: SPECS GmbH - Surface Analysis and Computer Technology, 2006.

[143] C. J. Powell and A. Jablonski, *NIST Electron Inelastic-Mean-Free-Path database - Version 1.2.* Gaithersburg, MD: National Institute of Standards and Technology, 2010.

[144] F. Tao, M. E. Grass, Y. Zhang, D. R. Butcher, J. R. Renzas, Z. Liu, J. Y. Chung, B. S. Mun, M. Salmeron, and G. A. Somorjai, "Reaction-driven restructuring of Rh-Pd and Pt-Pd core-shell nanoparticles," *Science (New York, N.Y.)*, vol. 322, no. November, pp. 932–934, 2008.

[145] F. Aksoy, M. E. Grass, S. H. Joo, N. Jabeen, Y. P. Hong, Z. Hussain, B. S. Mun, and Z. Liu, "Study of electro-chemical properties of metal-oxide interfaces using a newly constructed ambient pressure X-ray photoelectron spectroscopy endstation," *Nuclear Instruments and Methods in Physics Research*

Section A: Accelerators, Spectrometers, Detectors and Associated Equipment, vol. 645, pp. 260–265, July 2011.

[146] K. Mudiyanselage, S. D. Senanayake, L. Feria, S. Kundu, A. E. Baber, J. Graciani, A. B. Vidal, S. Agnoli, J. Evans, R. Chang, S. Axnanda, Z. Liu, J. F. Sanz, P. Liu, J. a. Rodriguez, and D. J. Stacchiola, "Importance of the metal-oxide interface in catalysis: In situ studies of the water-gas shift reaction by ambient-pressure X-ray photoelectron spectroscopy.," *Angewandte Chemie (International ed. in English)*, vol. 52, pp. 5101–5105, May 2013.

[147] C. Wen, Y. Zhu, Y. Ye, S. Zhang, F. Cheng, Y. Liu, P. Wang, and Feng Tao, "Water-gas shift reaction on metal nanoclusters encapsulated in mesoporous ceria studied with photoelectron ambient-pressure X-ray photoelectron spectroscopy," *ACS Nano*, vol. 6, no. 10, pp. 9305–9313, 2012.

[148] A. Caballero, J. P. Holgado, V. M. Gonzalez-delaCruz, S. E. Habas, T. Herranz, and M. Salmeron, "In situ spectroscopic detection of SMSI effect in a Ni/CeO_2 system: hydrogen-induced burial and dig out of metallic nickel.," *Chemical Communications*, vol. 46, pp. 1097–1099, Feb. 2010.

[149] C. Mattevi, C. T. Wirth, S. Hofmann, R. Blume, M. Cantoro, C. Ducati, C. Cepek, A. Knop-gericke, S. Milne, C. Castellarin-cudia, S. Dolafi, A. Goldoni, R. Schloegl, and J. Robertson, "In situ x-ray photoelectron spectroscopy study of catalyst-support interactions and growth of carbon nanotube forests," *Journal of Physical Chemistry C*, vol. 112, pp. 12207–12213, 2008.

[150] A. Bruix, J. A. Rodriguez, P. J. Ram, S. D. Senanayake, J. Evans, J. B. Park, D. Stacchiola, P. Liu, J. Hrbek, and F. Illas, "A new type of strong metal-support interaction and the production of H_2 through the transformation of water on $Pt/CeO_2(111)$ and $Pt/CeO(x)/TiO_2(110)$ catalysts," *Journal of the American Chemical Society*, vol. 134, pp. 8968–8974, May 2012.

[151] F. Tao and M. Salmeron, "In situ studies of chemistry and structure of materials in reactive environments," *Science (New York, N.Y.)*, vol. 331, pp. 171–174, Jan. 2011.

[152] S. Zafeiratos, T. Dintzer, D. Teschner, R. Blume, M. Hävecker, a. Knop-Gericke, and R. Schlögl, "Methanol oxidation over model cobalt catalysts: Influence of the cobalt oxidation state on the reactivity," *Journal of Catalysis*, vol. 269, pp. 309–317, Feb. 2010.

[153] D. E. Starr, Z. Liu, M. Hävecker, A. Knop-Gericke, and H. Bluhm, "Investigation of solid/vapor interfaces using ambient pressure X-ray photoelectron spectroscopy," *Chemical Society reviews*, vol. 42, pp. 5833–5857, July 2013.

[154] D. E. Starr, H. Bluhm, Z. Liu, A. Knop-Gericke, and M. Hävecker, "Application of Ambient-Pressure X-ray Photoelectron Spectroscopy for the in-situ investigation of heterogeneous catalytic reactions," in *In-situ characterization of heterogeneous catalysts*, pp. 315–343, John Wiley & Sons, Inc., 2013.

[155] C. Escudero and M. Salmeron, "From solid-vacuum to solid-gas and solid-liquid interfaces: In situ studies of structure and dynamics under relevant conditions," *Surface Science*, vol. 607, pp. 2–9, Jan. 2013.

[156] V. Pérez-Dieste, L. Aballe, S. Ferrer, J. Nicolàs, C. Escudero, A. Milán, and E. Pellegrin, "Near ambient pressure XPS at ALBA," *Journal of Physics: Conference Series*, vol. 425, p. 072023, Mar. 2013.

[157] D. F. Ogletree, H. Bluhm, G. Lebedev, C. S. Fadley, Z. Hussain, and M. Salmeron, "A differentially pumped electrostatic lens system for photoemission studies in the millibar range," *Review of Scientific Instruments*, vol. 73, no. 11, pp. 3872–3877, 2002.

[158] Y. Zhu, S. Zhang, J.-j. Shan, L. Nguyen, S. Zhan, X. Gu, and F. F. Tao, "In situ surface chemistries and catalytic performances of ceria doped with palladium, platinum, and rhodium in methane partial oxidation for the production of syngas," *ACS Catalysis*, vol. 3, pp. 2627–2639, Nov. 2013.

[159] M. M. Natile and A. Glisenti, "Nanostructured CeO_2 powders by XPS," *Surface Science Spectra*, vol. 13, no. 1, pp. 17–30, 2006.

[160] C. Force, E. Roman, J. M. Guil, and J. Sanz, "XPS and 1H NMR study of thermally stabilized Rh/CeO_2 catalysts submitted to reduction/oxidation treatments," *Langmuir: the ACS journal of surfaces and colloids*, vol. 23, pp. 4569–4574, Apr. 2007.

[161] A. Iulianelli and A. Basile, "Hydrogen production from ethanol via inorganic membrane reactors technology: a review," *Catalysis Science & Technology*, vol. 1, p. 366, May 2011.

[162] F. Gallucci, A. Basile, S. Tosti, A. Iulanelli, and D. E, "Methanol and ethanol steam reforming in membrane reactors: An experimental study," *International Journal of Hydrogen Energy*, vol. 32, pp. 1201–1210, June 2007.

[163] A. Basile, F. Gallucci, A. Iulianelli, and S. Tosti, "CO-free hydrogen production by ethanol steam reforming in a Pd-Ag membrane reactor," *Fuel Cells*, vol. 8, no. 1, pp. 62–68, 2008.

[164] S. Tosti, A. Basile, F. Borgognoni, V. Capaldo, S. Cordiner, S. Di Cave, F. Gallucci, C. Rizzello, A. Santucci, and E. Traversa, "Low temperature ethanol steam reforming in a Pd-Ag membrane reactor. Part 1: Ru-based catalyst," *Journal of Membrane Science*, vol. 308, pp. 250–257, Feb. 2008.

[165] A. Iulianelli, T. Longo, S. Liguori, P. Seelam, R. Keiski, and A. Basile, "Oxidative steam reforming of ethanol over Ru-Al_2O_3 catalyst in a dense Pd-Ag membrane reactor to produce hydrogen for PEM fuel cells," *International Journal of Hydrogen Energy*, vol. 34, pp. 8558–8565, Oct. 2009.

[166] S. Tosti, A. Basile, R. Borelli, F. Borgognoni, S. Castelli, M. Fabbricino, F. Gallucci, and C. Licusati, "Ethanol steam reforming kinetics of a Pd-Ag membrane reactor," *International Journal of Hydrogen Energy*, vol. 34, pp. 4747–4754, June 2009.

[167] S. Tosti, M. Fabbricino, A. Moriani, G. Agatiello, C. Scudieri, F. Borgognoni, and A. Santucci, "Pressure effect in ethanol steam reforming via dense Pd-based membranes," *Journal of Membrane Science*, vol. 377, pp. 65–74, July 2011.

[168] S. Tosti, F. Borgognoni, and A. Santucci, "Multi-tube Pd-Ag membrane reactor for pure hydrogen production," *International Journal of Hydrogen Energy*, vol. 35, pp. 11470–11477, Oct. 2010.

[169] A. Santucci, M. C. Annesini, F. Borgognoni, L. Marrelli, M. Rega, and S. Tosti, "Oxidative steam reforming of ethanol over a Pt/Al_2O_3 catalyst in a Pd-based membrane reactor," *International Journal of Hydrogen Energy*, vol. 36, pp. 1503–1511, Jan. 2011.

[170] A. Iulianelli and A. Basile, "An experimental study on bio-ethanol steam reforming in a catalytic membrane reactor. Part I: Temperature and sweep-gas flow configuration effects," *International Journal of Hydrogen Energy*, vol. 35, pp. 3170–3177, Apr. 2010.

[171] A. Iulianelli, S. Liguori, T. Longo, S. Tosti, P. Pinacci, and A. Basile, "An experimental study on bio-ethanol steam reforming in a catalytic membrane reactor. Part II: Reaction pressure, sweep factor and WHSV effects," *International Journal of Hydrogen Energy*, vol. 35, pp. 3159–3164, Apr. 2010.

[172] A. Basile, P. Pinacci, A. Iulianelli, M. Broglia, F. Drago, S. Liguori, T. Longo, and V. Calabrò, "Ethanol steam reforming reaction in a porous stainless steel supported palladium membrane reactor," *International Journal of Hydrogen Energy*, vol. 36, pp. 2029–2037, Feb. 2011.

[173] P. K. Seelam, S. Liguori, A. Iulianelli, P. Pinacci, V. Calabrò, M. Huuhtanen, R. Keiski, V. Piemonte, S. Tosti, M. De Falco, and A. Basile, "Hydrogen production from bio-ethanol steam reforming reaction in a Pd/PSS membrane reactor," *Catalysis Today*, vol. 193, pp. 42–48, Oct. 2012.

[174] W.-H. Lin, C.-S. Hsiao, and H.-F. Chang, "Effect of oxygen addition on the hydrogen production from ethanol steam reforming in a Pd-Ag membrane reactor," *Journal of Membrane Science*, vol. 322, pp. 360–367, Sept. 2008.

[175] W.-H. Lin, Y.-C. Liu, and H.-F. Chang, "Autothermal reforming of ethanol in a Pd-Ag/Ni composite membrane reactor," *International Journal of Hydrogen Energy*, vol. 35, pp. 12961–12969, Dec. 2010.

[176] D. D. Papadias, S. H. Lee, M. Ferrandon, and S. Ahmed, "An analytical and experimental investigation of high-pressure catalytic steam reforming of ethanol in a hydrogen selective membrane reactor," *International Journal of Hydrogen Energy*, vol. 35, pp. 2004–2017, Mar. 2010.

[177] M. Domínguez, E. Taboada, E. Molins, and J. Llorca, "Ethanol steam reforming at very low temperature over cobalt talc in a membrane reactor," *Catalysis Today*, vol. 193, pp. 101–106, Oct. 2012.

[178] R. Espinal, A. Anzola, E. Adrover, M. Roig, R. Chimentao, F. Medina, E. López, D. Borio, and J. Llorca, "Durable ethanol steam reforming in a catalytic membrane reactor at moderate temperature over cobalt hydrotalcite," *International Journal of Hydrogen Energy*, vol. 39, pp. 10902–10910, July 2014.

[179] C.-Y. Yu, D.-W. Lee, S.-J. Park, K.-Y. Lee, and K.-H. Lee, "Ethanol steam reforming in a membrane reactor with Pt-impregnated Knudsen membranes," *Applied Catalysis B: Environmental*, vol. 86, pp. 121–126, Feb. 2009.

[180] H. Lim, Y. Gu, and S. T. Oyama, "Reaction of primary and secondary products in a membrane reactor: Studies of ethanol steam reforming with a silica-alumina composite membrane," *Journal of Membrane Science*, vol. 351, pp. 149–159, Apr. 2010.

[181] A. Caravella, F. Scura, G. Barbieri, and E. Drioli, "Sieverts law empirical exponent for Pd-based membranes: Critical analysis in pure H_2 permeation," *The Journal of Physical Chemistry B*, vol. 114, pp. 6033–6047, Apr. 2010.

[182] R. Buxbaum and H. Lei, "Power output and load following in a fuel cell fueled by membrane reactor hydrogen," *Journal of Power Sources*, vol. 123, pp. 43–47, Sept. 2003.

[183] H.-F. Chang, W.-J. Pai, Y.-J. Chen, and W.-H. Lin, "Autothermal reforming of methane for producing high-purity hydrogen in a Pd/Ag membrane reactor," *International Journal of Hydrogen Energy*, vol. 35, pp. 12986–12992, Dec. 2010.

[184] J. Tong and Y. Matsumura, "Effect of catalytic activity on methane steam reforming in hydrogen-permeable membrane reactor," *Applied Catalysis A: General*, vol. 286, pp. 226–231, June 2005.

[185] L. Coronel, J. Múnera, E. Lombardo, and L. Cornaglia, "Pd based membrane reactor for ultra pure hydrogen production through the dry reforming of

methane. Experimental and modeling studies," *Applied Catalysis A: General*, vol. 400, pp. 185–194, June 2011.

[186] R. Koch, E. López, N. J. Divins, M. Allué, A. Jossen, J. Riera, and J. Llorca, "Ethanol catalytic membrane reformer for direct PEM FC feeding," *International Journal of Hydrogen Energy*, vol. 38, pp. 5605–5615, May 2013.

[187] A. Hedayati, O. Le Corre, B. Lacarrière, and J. Llorca, "Exergetic study of catalytic steam reforming of bio-ethanol over Pd–Rh/CeO_2 with hydrogen purification in a membrane reactor," *International Journal of Hydrogen Energy*, Sept. 2014.

[188] D. R. Palo, R. A. Dagle, and J. D. Holladay, "Methanol steam reforming for hydrogen production.," *Chemical reviews*, vol. 107, pp. 3992–4021, Oct. 2007.

[189] J. Llorca, "Microreactors for the generation of hydrogen from ethanol," in *Handbook of sustainable energy* (W. H. Lee and V. G. Cho, eds.), ch. 22, pp. 693–699, Nova Science Publishers, 2010.

[190] A. Casanovas, M. Saintgerons, F. Griffon, and J. Llorca, "Autothermal generation of hydrogen from ethanol in a microreactor," *International Journal of Hydrogen Energy*, vol. 33, pp. 1827–1833, Apr. 2008.

[191] O. Görke, P. Pfeifer, and K. Schubert, "Kinetic study of ethanol reforming in a microreactor," *Applied Catalysis A: General*, vol. 360, pp. 232–241, June 2009.

[192] W. Cai, F. Wang, A. van Veen, C. Descorme, Y. Schuurman, W. Shen, and C. Mirodatos, "Hydrogen production from ethanol steam reforming in a micro-channel reactor," *International Journal of Hydrogen Energy*, vol. 35, pp. 1152–1159, Feb. 2010.

[193] N. R. Peela and D. Kunzru, "Oxidative steam reforming of ethanol over Rh based catalysts in a micro-channel reactor," *International Journal of Hydrogen Energy*, vol. 36, pp. 3384–3396, Mar. 2011.

[194] N. R. Peela and D. Kunzru, "Steam reforming of ethanol in a microchannel reactor: Kinetic study and reactor simulation," *Industrial & Engineering Chemistry Research*, vol. 50, pp. 12881–12894, Dec. 2011.

[195] M. Domínguez, G. Cristiano, E. López, and J. Llorca, "Ethanol steam reforming over cobalt talc in a plate microreactor," *Chemical Engineering Journal*, vol. 176-177, pp. 280–285, Dec. 2011.

[196] M. A. Rahman, F. R. García-García, and K. Li, "On-board H_2 generation by a catalytic hollow fibre microreactor for portable device applications," *Catalysis Communications*, vol. 16, pp. 128–132, Nov. 2011.

[197] M. A. Rahman, F. R. García-García, and K. Li, "Development of a catalytic hollow fibre membrane microreactor as a microreformer unit for automotive application," *Journal of Membrane Science*, vol. 390-391, pp. 68–75, Feb. 2012.

[198] G. Kolb, Y. Men, K.-P. Schelhaas, D. Tiemann, R. Zapf, and J. Wilhelm, "Development work on a microstructured 50 kW ethanol fuel processor for a small-scale stationary hydrogen supply system," *Industrial & Engineering Chemistry Research*, vol. 50, pp. 2554–2561, Mar. 2011.

[199] W. Cai, F. Wang, E. Zhan, A. Vanveen, C. Mirodatos, and W. Shen, "Hydrogen production from ethanol over Ir/CeO_2 catalysts: A comparative study of steam reforming, partial oxidation and oxidative steam reforming," *Journal of Catalysis*, vol. 257, pp. 96–107, July 2008.

[200] "Bioanalytical microfluidics program." http://navier.engr.colostate.edu/~dandy/code/code-4/index.html.

[201] N. J. Divins, E. López, A. Rodríguez, D. Vega, and J. Llorca, "Bio-ethanol steam reforming and autothermal reforming in 3-μm channels coated with $RhPd/CeO_2$ for hydrogen generation," *Chemical Engineering and Processing: Process Intensification*, vol. 64, pp. 31–37, Feb. 2013.

[202] E. C. Vagia and A. A. Lemonidou, "Investigations on the properties of ceria-zirconia-supported Ni and Rh catalysts and their performance in acetic acid steam reforming," *Journal of Catalysis*, vol. 269, pp. 388–396, Feb. 2010.

[203] A. A. Lemonidou and E. C. Vagia, "Hydrogen production via steam reforming of bio-oil components over calcium aluminate supported nickel and noble metal catalysts," *Applied Catalysis A: General*, vol. 351, pp. 111–121, Dec. 2008.

[204] O. Korotkikh and R. Farrauto, "Selective catalytic oxidation of CO in H_2: fuel cell applications," *Catalysis Today*, vol. 62, pp. 249–254, Oct. 2000.

[205] N. Bion, F. Epron, M. Moreno, F. Mariño, and D. Duprez, "Preferential oxidation of carbon monoxide in the presence of hydrogen (PROX) over noble metals and transition metal oxides: Advantages and drawbacks," *Topics in Catalysis*, vol. 51, pp. 76–88, Oct. 2008.

[206] Y. Choi and H. G. Stenger, "Kinetics, simulation and insights for CO selective oxidation in fuel cell applications," *Journal of Power Sources*, vol. 129, pp. 246–254, Apr. 2004.

[207] G. Kolb, V. Hessel, V. Cominos, C. Hofmann, H. Löwe, G. Nikolaidis, R. Zapf, A. Ziogas, E. Delsman, M. de Croon, J. Schouten, O. de la Iglesia, R. Mallada, and J. Santamaria, "Selective oxidations in micro-structured catalytic

reactors - For gas-phase reactions and specifically for fuel processing for fuel cells," *Catalysis Today*, vol. 120, pp. 2–20, Jan. 2007.

[208] F. Mariño, G. Baronetti, M. Laborde, N. Bion, A. L. Valant, F. Epron, and D. Duprez, "Optimized CuO-CeO_2 catalysts for COPROX reaction," *International Journal of Hydrogen Energy*, vol. 33, pp. 1345–1353, Feb. 2008.

[209] T. Reina, E. Papadopoulou, S. Palma, S. Ivanova, M. Centeno, T. Ioannides, and J. Odriozola, "Could an efficient WGS catalyst be useful in the CO-PrOx reaction?," *Applied Catalysis B: Environmental*, vol. 150-151, pp. 554–563, May 2014.

[210] "Scopus citation database." www.scopus.com. Accessed: 2014-11-11.

[211] O. Pozdnyakova, D. Teschner, a. Wootsch, J. Krohnert, B. Steinhauer, H. Sauer, L. Toth, F. Jentoft, a. Knopgericke, and Z. Paal, "Preferential CO oxidation in hydrogen (PROX) on ceria-supported catalysts, part I: Oxidation state and surface species on Pt/CeO_2 under reaction conditions," *Journal of Catalysis*, vol. 237, pp. 1–16, Jan. 2006.

[212] S. Oh and R. Sinkevitch, "Carbon Monoxide Removal from Hydrogen-Rich Fuel Cell Feedstreams by Selective Catalytic Oxidation," *Journal of Catalysis*, vol. 142, pp. 254–262, July 1993.

[213] M. Kahlich, H. Gasteiger, and R. Behm, "Kinetics of the Selective CO Oxidation in H_2-Rich Gas on Pt/Al_2O_3," *Journal of Catalysis*, vol. 171, pp. 93–105, Oct. 1997.

[214] A. Manasilp and E. Gulari, "Selective CO oxidation over Pt/alumina catalysts for fuel cell applications," *Applied Catalysis B: Environmental*, vol. 37, pp. 17–25, Apr. 2002.

[215] G. Avgouropoulos, T. Ioannides, C. Papadopoulou, J. Batista, S. Hocevar, and H. Matralis, "A comparative study of Pt/γ-Al_2O_3, Au/α-Fe_2O_3 and CuO-CeO_2 catalysts for the selective oxidation of carbon monoxide in excess hydrogen," *Catalysis Today*, vol. 75, pp. 157–167, July 2002.

[216] H. Igarashi, H. Uchida, M. Suzuki, Y. Sasaki, and M. Watanabe, "Removal of carbon monoxide from hydrogen-rich fuels by selective oxidation over platinum catalyst supported on zeolite," *Applied Catalysis A: General*, vol. 159, pp. 159–169, Oct. 1997.

[217] V. Sebastian, S. Irusta, R. Mallada, and J. Santamaría, "Selective oxidation of CO in the presence of H_2, CO_2 and H_2O, on different zeolite-supported Pt catalysts," *Applied Catalysis A: General*, vol. 366, pp. 242–251, Sept. 2009.

[218] A. Wootsch, C. Descorme, and D. Duprez, "Preferential oxidation of carbon monoxide in the presence of hydrogen (PROX) over ceria-zirconia and alumina-supported Pt catalysts," *Journal of Catalysis*, vol. 225, pp. 259–266, July 2004.

[219] Y. Gao, W. Wang, S. Chang, and W. Huang, "Morphology Effect of CeO_2 Support in the Preparation, Metal-Support Interaction, and Catalytic Performance of Pt/CeO_2 Catalysts," *ChemCatChem*, vol. 5, pp. 3610–3620, Dec. 2013.

[220] C. Galletti, S. Fiorot, S. Specchia, G. Saracco, and V. Specchia, "Activity of rhodium-based catalysts for CO preferential oxidation in H_2-rich gases," *Topics in Catalysis*, vol. 45, pp. 15–19, Aug. 2007.

[221] Y.-F. Han, M. Kahlich, M. Kinne, and R. Behm, "CO removal from realistic methanol reformate via preferential oxidation-performance of a Rh/MgO catalyst and comparison to Ru/γ-Al_2O_3, and Pt/γ-Al_2O_3," *Applied Catalysis B: Environmental*, vol. 50, pp. 209–218, July 2004.

[222] G. Avgouropoulos, T. Ioannides, H. K. Matralis, J. Batista, and S. Hocevar, "CuO-CeO_2 mixed oxide catalysts for the selective oxidation of carbon monoxide in excess hydrogen," *Catalysis Letters*, vol. 73, pp. 33–40, Apr. 2001.

[223] W. Liu and M. Flytzani-Stephanopoulos, "Total Oxidation of Carbon Monoxide and Methane over Transition Metal Fluorite Oxide Composite Catalysts I. Catalyst Composition and Activity," *Journal of Catalysis*, vol. 153, pp. 304–316, May 1995.

[224] Z. Zhao, M. M. Yung, and U. S. Ozkan, "Effect of support on the preferential oxidation of CO over cobalt catalysts," *Catalysis Communications*, vol. 9, pp. 1465–1471, Mar. 2008.

[225] P. Gawade, B. Bayram, A.-M. C. Alexander, and U. S. Ozkan, "Preferential oxidation of CO (PROX) over CoO_x/CeO_2 in hydrogen-rich streams: Effect of cobalt loading," *Applied Catalysis B: Environmental*, vol. 128, pp. 21–30, Nov. 2012.

[226] L. E. Gómez, A. V. Boix, and E. E. Miró, "Co/ZrO_2, Co/CeO_2 and MnCoCe structured catalysts for COPrOx," *Catalysis Today*, vol. 216, pp. 246–253, Nov. 2013.

[227] F. Mariño, C. Descorme, and D. Duprez, "Supported base metal catalysts for the preferential oxidation of carbon monoxide in the presence of excess hydrogen (PROX)," *Applied Catalysis B: Environmental*, vol. 58, pp. 175–183, June 2005.

[228] J. S. Moura, J. d. S. L. Fonseca, N. Bion, F. Epron, T. d. F. Silva, C. G. a. Maciel, J. M. Assaf, and M. d. C. Rangel, "Effect of lanthanum on the properties of copper, cerium and zirconium catalysts for preferential oxidation of carbon monoxide," *Catalysis Today*, vol. 228, pp. 40–50, June 2014.

[229] A. L. Cámara, V. C. Corberán, L. Barrio, G. Zhou, R. Si, J. C. Hanson, M. Monte, J. C. Conesa, J. A. Rodriguez, and A. Martínez-Arias, "Improving the CO-PROX performance of inverse CeO_2/CuO catalysts: Doping of the CuO component with Zn," *The Journal of Physical Chemistry C*, vol. 118, pp. 9030–9041, May 2014.

[230] C. Tang, J. Sun, X. Yao, Y. Cao, L. Liu, C. Ge, F. Gao, and L. Dong, "Efficient fabrication of active CuO-CeO_2/SBA-15 catalysts for preferential oxidation of CO by solid state impregnation," *Applied Catalysis B: Environmental*, vol. 146, pp. 201–212, Mar. 2014.

[231] M. I. Domínguez, A. Pérez, M. A. Centeno, and J. A. Odriozola, "Metallic structured catalysts: Influence of the substrate on the catalytic activity," *Applied Catalysis A, Genera*, vol. 478, pp. 45–57, 2014.

[232] A. S. K. Hashmi and G. J. Hutchings, "Gold catalysis," *Angewandte Chemie-International Edition*, vol. 45, no. 47, pp. 7896–7936, 2006.

[233] M. Haruta, N. Yamada, T. Kobayashi, and S. Iijima, "Gold catalysts prepared by coprecipitation for low-temperature oxidation of hydrogen and of carbon monoxide," *Journal of Catalysis*, vol. 309, pp. 301–309, 1989.

[234] B. Hammer and J. K. Norskov, "Why gold is the noblest of all the metals," *Nature*, vol. 376, pp. 238–240, July 1995.

[235] M. Haruta, "Size- and support-dependency in the catalysis of gold," *Catalysis Today*, vol. 36, no. 1, pp. 153–166, 1997.

[236] M. Boronat and A. Corma, "Oxygen activation on gold nanoparticles: separating the influence of particle size, particle shape and support interaction.," *Dalton transactions (Cambridge, England : 2003)*, vol. 39, pp. 8538–46, Sept. 2010.

[237] M. Haruta, "When gold is not noble: catalysis by nanoparticles," *The Chemical record*, vol. 3, pp. 75–87, Jan. 2003.

[238] M. Haruta, "Gold as a novel catalyst in the 21st century: Preparation, working mechanism and applications," *Gold Bulletin*, vol. 37, pp. 27–36, Mar. 2004.

[239] M. Valden, X. Lai, and D. Goodman, "Onset of catalytic activity of gold clusters on titania with the appearance of nonmetallic properties," *Science (New York, N.Y.)*, vol. 281, pp. 1647–50, Sept. 1998.

[240] M. Chen and D. W. Goodman, "Catalytically active gold: from nanoparticles to ultrathin films," *Accounts of chemical research*, vol. 39, pp. 739–46, Oct. 2006.

[241] N. Lopez, "On the origin of the catalytic activity of gold nanoparticles for low-temperature CO oxidation," *Journal of Catalysis*, vol. 223, pp. 232–235, Apr. 2004.

[242] P. Lakshmanan, J. E. Park, and E. D. Park, "Recent Advances in Preferential Oxidation of CO in H_2 Over Gold Catalysts," *Catalysis Surveys from Asia*, vol. 18, pp. 75–88, June 2014.

[243] D. Widmann, E. Hocking, and R. Behm, "On the origin of the selectivity in the preferential CO oxidation on Au/TiO_2 - Nature of the active oxygen species for H_2 oxidation," *Journal of Catalysis*, vol. 317, pp. 272–276, Aug. 2014.

[244] Z. Ma and S. Dai, "Development of novel supported gold catalysts: A materials perspective," *Nano Research*, vol. 4, pp. 3–32, Oct. 2010.

[245] M. Chen and D. W. Goodman, "Catalytically active gold on ordered titania supports.," *Chemical Society reviews*, vol. 37, pp. 1860–70, Sept. 2008.

[246] J. Llorca, M. Domínguez, C. Ledesma, R. Chimentao, F. Medina, J. Sueiras, I. Angurell, M. Seco, and O. Rossell, "Propene epoxidation over TiO_2-supported Au-Cu alloy catalysts prepared from thiol-capped nanoparticles," *Journal of Catalysis*, vol. 258, pp. 187–198, Aug. 2008.

[247] A. Taketoshi and M. Haruta, "Size- and Structure-specificity in Catalysis by Gold Clusters," *Chemistry Letters*, vol. 43, no. 4, pp. 380–387, 2014.

[248] O. Laguna, W. Hernández, G. Arzamendi, L. Gandía, M. Centeno, and J. Odriozola, "Gold supported on CuO_x/CeO_2 catalyst for the purification of hydrogen by the CO preferential oxidation reaction (PROX)," *Fuel*, vol. 118, pp. 176–185, Feb. 2014.

[249] X. Liao, W. Chu, X. Dai, and V. Pitchon, "Bimetallic Au-Cu supported on ceria for PROX reaction: Effects of Cu/Au atomic ratios and thermal pretreatments," *Applied Catalysis B: Environmental*, vol. 142-143, pp. 25–37, Oct. 2013.

[250] J. Kugai, T. Moriya, S. Seino, T. Nakagawa, Y. Ohkubo, H. Nitani, and T. A. Yamamoto, "Active metal-oxide interfaces in supported Pt-Cu/CeO_2 and mechanically mixed Pt-$Cu+CeO_2$ catalysts synthesized by an electron beam irradiation method for selective CO oxidation," *Catalysis Letters*, vol. 143, pp. 1182–1187, July 2013.

[251] Y. Liu, B. Liu, Y. Liu, Q. Wang, W. Hu, P. Jing, L. Liu, S. Yu, and J. Zhang, "Improvement of catalytic performance of preferential oxidation of CO in H_2-rich gases on three-dimensionally ordered macro- and meso-porous Pt-Au/CeO_2 catalysts," *Applied Catalysis B: Environmental*, vol. 142-143, pp. 615–625, Oct. 2013.

[252] F. Gonzàlez de Rivera, L.-I. Rodríguez, O. Rossell, M. Seco, N. J. Divins, I. Casanova, and J. Llorca, "Carbosilane dendrons as stabilizing agents for the formation of gold nanoparticles," *Journal of Organometallic Chemistry*, vol. 696, pp. 2287–2293, June 2011.

[253] M. Brust, M. Walker, and D. Bethell, "Synthesis of thiol-derivatised gold nanoparticles in a two-phase liquid-liquid system," *Chemical Communications*, pp. 801–802, 1994.

[254] M. Kotobuki, R. Leppelt, D. Hansgen, D. Widmann, and R. Behm, "Reactive oxygen on a Au/TiO_2 supported catalyst," *Journal of Catalysis*, vol. 264, pp. 67–76, May 2009.

[255] Y. Denkwitz, B. Schumacher, G. Kučerová, and R. J. Behm, "Activity, stability, and deactivation behavior of supported Au/TiO_2 catalysts in the CO oxidation and preferential CO oxidation reaction at elevated temperatures," *Journal of Catalysis*, vol. 267, pp. 78–88, Oct. 2009.

[256] C. Moreno, N. J. Divins, J. Gázquez, M. Varela, I. Angurell, and J. Llorca, "Improved thermal stability of oxide-supported naked gold nanoparticles by ligand-assisted pinning," *Nanoscale*, vol. 4, no. 7, p. 2278, 2012.

[257] P. Buffat and J.-P. Borel, "Size effect on the melting temperature of gold particles," *Physical Review A*, vol. 13, pp. 2287–2298, June 1976.

[258] T. Reina, S. Ivanova, M. Centeno, and J. Odriozola, "Catalytic screening of Au/CeO_2-MOx/Al_2O_3 catalysts (M = La, Ni, Cu, Fe, Cr, Y) in the CO-PrOx reaction," *International Journal of Hydrogen Energy*, vol. 40, pp. 1782–1788, Jan. 2015.

[259] L. Piccolo, H. Daly, A. Valcarcel, and F. C. Meunier, "Promotional effect of H_2 on CO oxidation over Au/TiO_2 studied by operando infrared spectroscopy," *Applied Catalysis B: Environmental*, vol. 86, pp. 190–195, Feb. 2009.

[260] B. Schumacher, Y. Denkwitz, V. Plzak, M. Kinne, and R. Behm, "Kinetics, mechanism, and the influence of H_2 on the CO oxidation reaction on a Au/TiO_2 catalyst," *Journal of Catalysis*, vol. 224, pp. 449–462, June 2004.

[261] I. X. Green, W. Tang, M. Neurock, and J. T. Yates, "Spectroscopic observation of dual catalytic sites during oxidation of CO on a Au/TiO_2 catalyst," *Science*, vol. 333, pp. 736–739, Aug. 2011.

[262] C. Rossignol, S. Arrii, F. Morfin, L. Piccolo, V. Caps, and J.-L. Rousset, "Selective oxidation of CO over model gold-based catalysts in the presence of H_2," *Journal of Catalysis*, vol. 230, pp. 476–483, Mar. 2005.

[263] O. Laguna, M. Domínguez, S. Oraá, A. Navajas, G. Arzamendi, L. Gandía, M. A. Centeno, M. Montes, and J. Odriozola, "Influence of the O_2/CO ratio and the presence of H_2O and CO_2 in the feed-stream during the preferential oxidation of CO (PROX) over a CuO_x/CeO_2-coated microchannel reactor," *Catalysis Today*, vol. 203, pp. 182–187, Mar. 2013.

[264] V. Cominos, V. Hessel, C. Hofmann, G. Kolb, R. Zapf, a. Ziogas, E. R. Delsman, and J. C. Schouten, "Selective oxidation of carbon monoxide in a hydrogen-rich fuel cell feed using a catalyst coated microstructured reactor," *Catalysis Today*, vol. 110, pp. 140–153, 2005.

[265] D. Potemkin, P. Snytnikov, V. Belyaev, and V. Sobyanin, "Preferential CO oxidation over Cu/CeO_{2-x} catalyst: Internal mass transport limitation," *Chemical Engineering Journal*, vol. 176-177, pp. 165–171, Dec. 2011.

[266] P. Snytnikov, M. Popova, Y. Men, E. Rebrov, G. Kolb, V. Hessel, J. Schouten, and V. Sobyanin, "Preferential CO oxidation over a copper–cerium oxide catalyst in a microchannel reactor," *Applied Catalysis A: General*, vol. 350, pp. 53–62, Nov. 2008.

[267] G. Kolb, R. Zapf, V. Hessel, and H. Löwe, "Propane steam reforming in micro-channels - results from catalyst screening and optimisation," *Applied Catalysis A: General*, vol. 277, pp. 155–166, Dec. 2004.

[268] M. O'Connell, G. Kolb, R. Zapf, Y. Men, and V. Hessel, "Bimetallic catalysts for the catalytic combustion of methane using microreactor technology," *Catalysis Today*, vol. 144, pp. 306–311, June 2009.

[269] N. J. Divins, E. Lopez, M. Roig, T. Trifonov, A. Rodriguez, F. Gonzalez de Rivera, L. I. Rodriguez, M. Seco, O. Rossell, and J. Llorca, "A million-channel CO-PrOx microreactor on a fingertip for fuel cell application," *Chemical Engineering Journal*, vol. 167, no. 2-3, pp. 597–602, 2011.

List of Publications

Part of the original work presented in this Thesis is reported in the following publications:

1. **Núria J. Divins**, Inma Angurell, Carlos Escudero, Virginia Pérez-Dieste and Jordi Llorca, "Influence of the support on surface rearrangements of bimetallic nanoparticles in real catalysts", *Science (New York, N.Y.)*, vol. 346, pp. 620-623, 2014.

2. E. López, **N. J. Divins**, A. Anzola, S. Schbib, D. Borio, and J. Llorca, "Ethanol steam reforming for hydrogen generation over structured catalysts", *International Journal of Hydrogen Energy*, vol. 38, pp. 4418-4428, 2013.

3. **N. J. Divins**, E. López, Á. Rodríguez, D. Vega and J. Llorca, "Bio-ethanol steam reforming and autothermal reforming in 3-μm channels coated with $RhPd/CeO_2$ for hydrogen generation", *Chemical Engineering and Processing: Process Intensification*, vol. 64, pp. 31-37, 2013.

4. C. Moreno, **N. J. Divins**, J. Gázquez, M. Varela, I. Angurell, and J. Llorca, "Improved thermal stability of oxide-supported naked gold nanoparticles by ligand-assisted pinning", *Nanoscale*, vol. 4, no. 7, p. 2278-2280, 2012.

5. E. López, **N. J. Divins**, and J. Llorca, "Hydrogen production from ethanol over $Pd\text{-}Rh/CeO_2$ with a metallic membrane reactor", *Catalysis Today*, vol. 193, pp. 145-150, 2012.

6. **N. J. Divins**, E. López, M. Roig, T. Trifonov, A. Rodríguez, F. Gonzàlez de Rivera, L. I. Rodríguez, M. Seco, O. Rossell, J. Llorca, "A million-channel CO-PrOx microreactor on a fingertip for fuel cell application", *Chemical Engineering Journal*, vol. 167, no. 2-3, pp. 597-602, 2011.

And in the book chapter:

7. J. Llorca, V. Cortés Corberán, **N. J. Divins**, R. O. Fraile, and E. Taboada, "Chapter 7 - Hydrogen from bioethanol", in Renewable Hydrogen Technologies (Editors L. M. Gandía, G. Arzamendi, and P. M. Diéguez), pp. 135-169, Amsterdam: Elsevier, 2013.

Complementary work performed during my PhD Thesis, which has not been included in this Thesis, is listed in the following publications:

1. **N. J. Divins**, A. Casanovas, W. Xu, S.D. Senanayake, D. Wiater, A. Trovarelli, J. Llorca, "The influence of nano-architectured CeO_x supports in $RhPd/CeO_2$ for the catalytic ethanol steam reforming reaction", *Catalysis Today*, 2015, in press, corrected proof. doi:10.1016/j.cattod.2014.12.042.

2. Aristizábal, S. Contreras, **N. J. Divins**, J. Llorca, and F. Medina, "Effect of impregnation protocol in the metallic sites of Pt-Ag/activated carbon catalysts for water denitration", *Applied Surface Science*, vol. 298, pp. 75-89, 2014.

3. E. Aneggi, **N. J. Divins**, C. de Leitenburg, J. Llorca, and A. Trovarelli, "The formation of nanodomains of Ce_6O_{11} in ceria catalyzed soot combustion", *Journal of Catalysis*, vol. 312, pp. 191-194, 2014.

4. R. Koch, E. López, **N. J. Divins**, M. Allué, A. Jossen, J. Riera, and J. Llorca, "Ethanol catalytic membrane reformer for direct PEM FC feeding", *International Journal of Hydrogen Energy*, vol. 38, pp. 5605-5615, 2013.

5. F. Gonzàlez de Rivera, I. Angurell, M. D. Rossell, R. Erni, J. Llorca, **N. J. Divins**, G. Muller, M. Seco, and O. Rossell, "A general approach to fabricate Fe_3O_4 nanoparticles decorated with Pd, Au, and Rh: Magnetically recoverable and reusable catalysts for Suzuki C-C cross-coupling reactions, hydrogenation, and sequential reaction", *Chemistry: a European journal*, vol. 19, pp. 11963-11974, 2013.

6. Aristizábal, S. Contreras, **N. J. Divins**, J. Llorca, and F. Medina, "Pt-Ag/activated carbon catalysts for water denitration in a continuous reactor: Incidence of the metal loading, Pt/Ag atomic ratio and Pt metal precursor", *Applied Catalysis B: Environmental*, vol. 127, pp. 351-362, 2012.

7. M. Friederici, I. Angurell, O. Rossell, M. Seco, **N. J. Divins**, and J. Llorca, "Facile synthesis of palladium nanoparticles protected with alkanethiolates functionalized with organometallic fragments", *Organometallics*, vol. 31, pp. 722-728, 2012.

8. F. Gonzàlez de Rivera, L.-I. Rodríguez, O. Rossell, M. Seco, **N. J. Divins**, I. Casanova, and J. Llorca, "Carbosilane dendrons as stabilizing agents for the formation of gold nanoparticles", *Journal of Organometallic Chemistry*, vol. 696, pp. 2287-2293, 2011.

9. C. Ledesma, M. Domínguez, **N. J. Divins**, E. López, and J. Llorca, "Hydrogen generation from renewables. Steam reforming of ethanol and dimethyl eter over structured catalysts", *Chemistry Today*, vol. 27, no. 5, p. 40, 2009.

PUBLISHED PAPERS

ATTENTION ¡

Pages 298 to 372 of the thesis are available at the editor's web